Modelling and Interpretation of Venusian Channels.

by

David Benjamin John Bussey

A thesis submitted to the University of London for the degree of Doctor of Philosophy.

University of London Observatory Annexe,

University College London,

33 - 35 Daws Lane,

Mill Hill Park,

London NW7 4SD

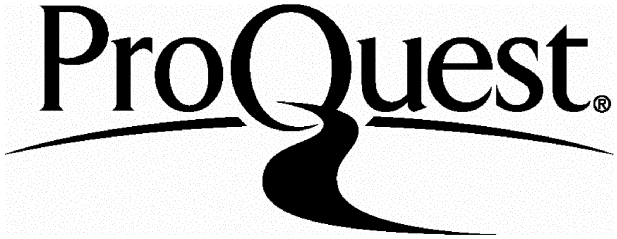

To Mum & Fa

I stood upon that silent hill

And stared into the sky until

My eyes were blind with stars and still

I stared into the sky.

Ralph Hodgson

Acknowledgements

There are many people to whom I would like to express my gratitude for their help whilst I have been doing my PhD. I would like to thank my supervisor, Professor John Guest, for his guidance, field work experience and anecdotes. Thanks go to all the postgrads at the annexe; Mark Bulmer, Mike Lancaster, Duncan Copp for their general help and Charles Wiles for all the computing knowledge, sometimes asked for, that he passed on. I am most grateful to Mike Gray for producing all the photographic products in the thesis. My time at the annexe would have been a much duller experience without Valerie Peerless and Maureen Evans and my warm thanks go to them. For his wit and invaluable assistance I'd particularly like to thank Soren Sörensen. For reading the manuscript, grateful thanks go to Wyn Hughes and John Woodcock. I would like also to thank Ed Syson, Martin Summers and Claire Robins for their help in keeping me sane throughout the PhD. Thanks go to Paul Spudis for providing the incentive for finishing. Finally I'd like to thank my family for their continuous encouragement and support.

A global view of Venus consisting of cycle 1 synthetic imaging radar data. The image is centred at 180°E longitude. The orange hue is based on colour data collected by the Venera 13 & 14 landers. The bright feature along the centre of the image is the highland region Aphrodite Terra. The dark area, lower centre, is a plains region which contains the channels studied in this thesis. Image P-39225.

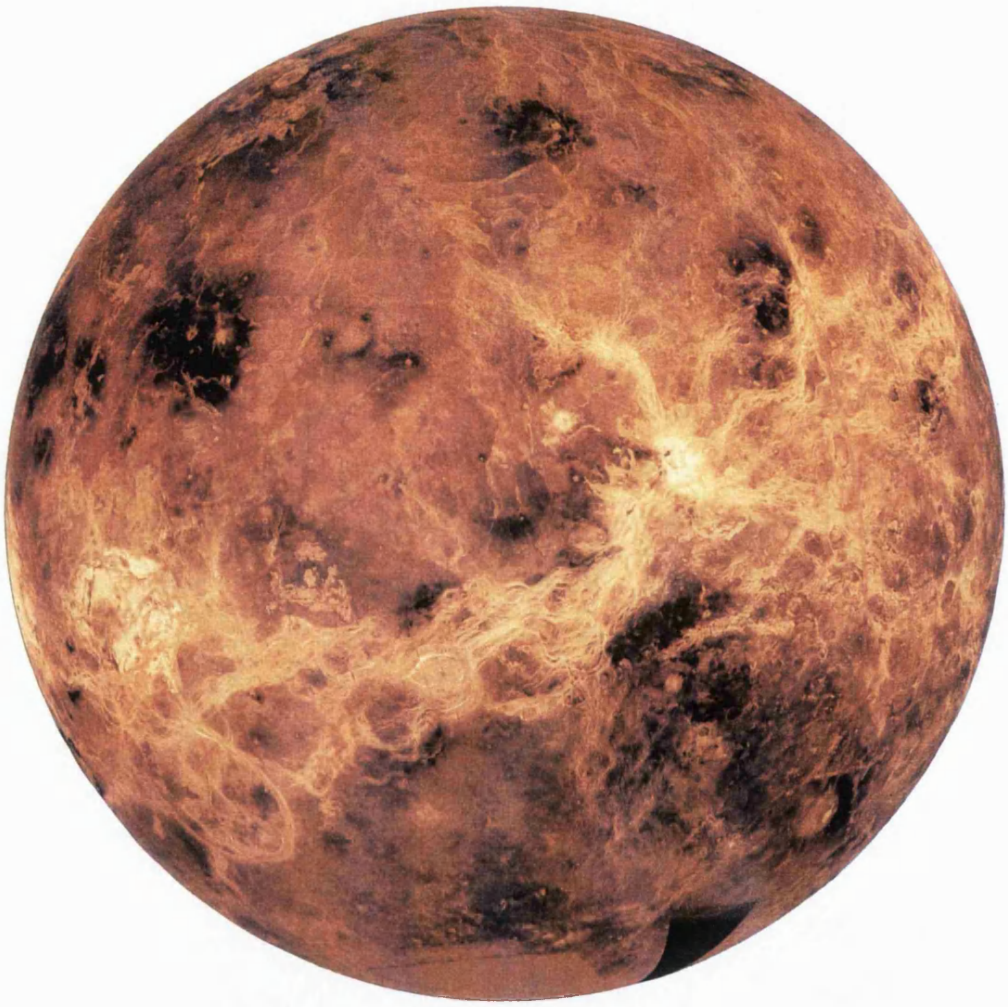

Abstract

The Magellan high resolution radar mapping of Venus discovered several different types of channels on the surface of the planet. Some closely resemble the sinuous rilles on the moon whilst the most spectacular type of channel, referred to as 'canali', are simple channels, up to several thousand kilometres long. One of the most remarkable features of the canali is that they often appear to have undergone erosional processes during their formation. Ambient conditions on Venus make any association with water unlikely, and point to a volcanic origin.

A preliminary study of the venusian surface indicated an unusually high density of canali type channels in a region roughly 30° latitude by 30° longitude to the south east of Aphrodite Terra and to the east of Artemis Chasma. Twelve channels were found and a detailed study of them undertaken. This included measurements of length and present day slope as well as determination of cross-sectional profile. Part of this study involved consideration of their origin with particular reference to erosion by lava. As lava erosion is uncommon on Earth it was decided to consider under what conditions lava might be able to erode, either thermally or mechanically, on Venus.

A numerical model is derived to investigate the sensitivity of the erosion process to various thermal and physical parameters of the lava and substrate, placing constraints on the physical characteristics required to obtain a suitably rapid erosion rate. The model allows for the effects of latent heat and also considers the presence of a liquid substrate boundary layer between the lava and solid substrate. In the model, the higher initial substrate temperature results in a calculated venusian erosion rate approximately 1.5 times greater than the equivalent terrestrial one.

Table of Contents

List of Figures

List of Tables

Notation

A	Cross sectional area
c	Specific Heat Capacity
E	Energy
k	Thermal Conductivity
L	Latent Heat
$\dot{Q}$	Rate of Heat Flow
t	Time
α	Thermal Diffusivity
ρ	Density
θ	Temperature
θ_s	Initial Substrate Temperature
θ_l	Lava Temperature
θ_m	Melting Temperature
θ_{surf}	Surface Temperature

Chapter 1
Introduction

1.1 Introduction.

The Magellan mission has produced an extensive data set which can be used to study Venus in unprecedented detail. One of the unexpected results from the high resolution radar mapping part of the mission was the discovery that channels are abundant on the surface of the planet. The high surface temperature on Venus (~468°C) precludes the presence of water, and there are no features currently present to indicate that water has ever played a major role in resurfacing the planet's surface. Therefore, another source for these channels must be found, the most likely being that they are of volcanic origin.

There are several different types of channel on Venus. Some closely resemble the sinuous rilles on the moon whilst the most spectacular type of channel, referred to as 'canali' (Italian for channels), are simple channels that retain a relatively constant width throughout their length. Canali often display many features that one associates with river valleys on Earth, including a meandering profile and inner terraced walls. In addition, one of the most remarkable features of the canali is that they often appear to have undergone erosional processes during their formation.

This chapter describes missions to Venus before Magellan, the Magellan mission including the data products produced and a description of venusian topography. It ends with a brief chapter by chapter summary of the rest of the thesis.

1.2 Previous Missions.

Venus is the nearest planet to Earth, coming to within 39 million kilometres of the Earth at inferior conjunction. Apart from the Sun and the moon, Venus is the brightest feature in the sky and is clearly visible to the naked eye, depending on the time of year, either around sunset or sunrise. It is for this reason that Venus is known as the evening or morning star. A list of the basic physical characteristics of the planet is shown in Table 1.1.

Until the second half of this century, the study of Venus had consisted solely of telescopic observations. These were disappointing in the sense that they failed to reveal any surface detail, due to the venusian atmosphere. However they were important for other reasons. Venus displays a full cycle of phases, which disproved the Ptolemaic theory of the Universe (Moore and Hunt 1983). Telescopic observations also proved the presence of an atmosphere as the disc of the planet appeared blurred when transiting in front of the Sun. It was also possible to calculate approximate values for the orbital period as well as the mass and size of the planet.

It wasn't until the 1960s that it became possible to study the surface of the planet. This was achieved using radar at the radio telescopes at Goldstone, California; Haystack, Massachusetts; and Arecibo, Puerto Rico. These were able to identify persistent features on the surface of the planet and so for the first time a rotational period could be calculated. This is equal to 243 days, and also Venus was found to rotate in a retrograde sense, i.e. east to west. One problem with Earth based radar is that the highest resolution (~1 km) is obtained when Venus is closest to earth and the orbital mechanics of the planet are such that when this occurs Venus is always displaying the same hemisphere towards Earth.

Table 1.1. A list of basic physical characteristics for Venus (Briggs and Taylor, 1982).

Parameter	Value
Mass	4.87×10^{24} kg
Radius	6051 km
Density	5.2×10^{3} kg m^{-3}
Equatorial gravity	8.87 m s^{-2}
Rotation period	243 days
Orbital period	224.7 days
Obliquity	3°
Orbital eccentricity	0.007
Mean distance from the sun	108.2×10^{6} km

In order to obtain a detailed global study of Venus it is necessary to send spacecraft to the planet. There have been a total of twenty missions to Venus before Magellan; a full list including a mission summary is shown in Table 1.2. The first spacecraft to visit Venus was Mariner 2 in August 1962. This was a flyby mission which discovered the surface temperature to be ~468°C and that Venus does not have a magnetic field. There then followed a number of atmospheric probe missions by the USSR before the American Mariner 10 mission in 1974 which encountered Venus en route to Mercury. It took images of the planet in both the visible and the ultraviolet range of the spectrum. From these images it was found that the rotation rate of the clouds in the upper atmosphere is much faster, at 5 days, than the rotation period of the planet.

The first panoramic pictures of the surface of the planet were returned by Venera 9 lander in 1975 (Figure 1.1). Other Venera landers conducted chemical analyses of the surface, discovering that some of the rocks were basaltic in composition. The first orbiter to obtain radar images of the surface was Pioneer 12 (also known as Pioneer Venus Orbiter) which between 1978 and 1981 obtained images in the central latitudes at a resolution of approximately 30 km and also produced the first topographical map of the planet by acquiring altimetry data with a footprint size of 100 km and a vertical accuracy of about 100 m. The first orbital synthetic aperture radar images of the surface were obtained in 1983 and 1984 by Venera 15 and 16. These spacecraft imaged approximately half the northern hemisphere at a resolution of 1 to 2 km. The accompanying altimetry data had a footprint size of 40 to 50 km and a vertical resolution of 50 m. The last missions to Venus before Magellan were Vega 1 and 2 which released balloon probes into the atmosphere.

Table 1.2. A list of the twenty missions to Venus before Magellan (Young, 1990).

Mission	Launch Date	Mission Summary
Mariner 2	27/8/62	Flyby 14/12/62. Found 468°C surface temperature and an absence of a magnetic field.
Venera 4	12/6/67	Atmospheric probe. Entered on 18/10/67.
Mariner 5	14/6/67	Flyby 19/10/67. Provided data on surface temperature and atmospheric composition.
Venera 5	5/1/69	Atmospheric probe. Entered on 16/5/69. Confirmed high CO_2 & lack of water vapour.
Venera 6	10/1/69	Similar to Venera 5. Entered on 17/5/69.
Venera 7	17/8/70	Lander. Entered atmosphere on 15/12/70.
Venera 8	27/3/72	Lander. Recorded surface temperature and pressure on 22/7/72.
Mariner 10	3/11/73	Flyby 5/2/74. Studied atmosphere in visible and ultraviolet wavelengths.
Venera 9	8/6/75	Orbiter-lander. Sent back first view of the surface.
Venera 10	14/6/75	Orbiter-lander. Sent back view of the surface.
Pioneer 12	20/5/78	Orbiter. Entered orbit on 4/12/78. Performed radar mapping of the surface.
Pioneer 13	8/8/78	Atmospheric probes. Four probes entered atmosphere on 9/12/78. Obtained temperature and pressure readings, and wind data.
Venera 11	9/9/78	Flyby-lander. Lander reached surface on 25/12/78. Detected electrical and acoustical events in the atmosphere.
Venera 12	14/9/78	Similar to Venera 11. Landed 21/12/78.
Venera 13	31/10/81	Orbiter-lander. Landed 3/3/82. First colour pictures of the surface.
Venera 14	4/11/81	Orbiter-lander. Colour surface pictures, soil samples, seismic study.
Venera 15	2/6/83	Orbiter. Performed radar mapping of the surface.
Venera 16	7/6/83	Similar to Venera 15. Also performed atmospheric analysis.
Vega 1	15/12/84	Venus-Comet Halley mission. Carried descent vehicle and balloon probe.
Vega 2	21/12/84	Similar to Vega 1.

Figure 1.1. A view of the venusian surface taken by Venera 9 in 1975.

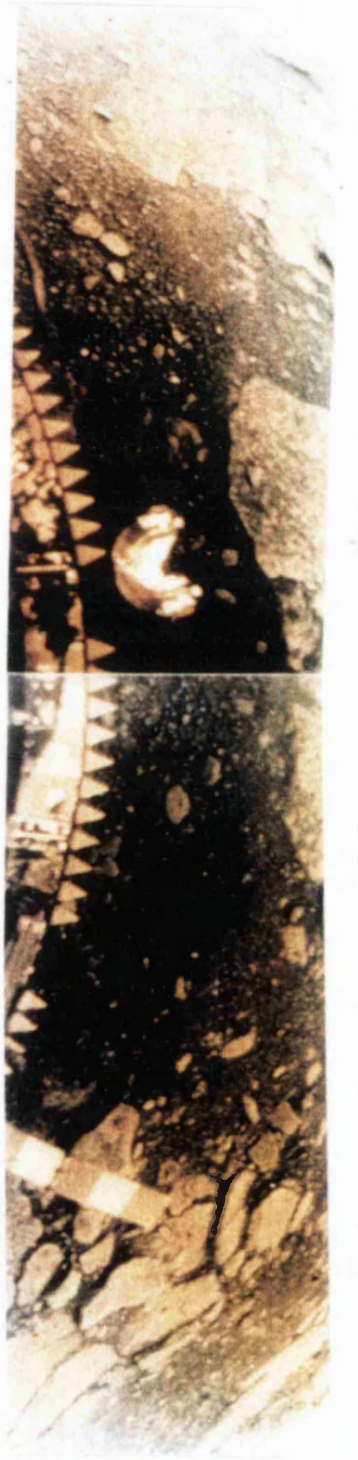

1.3 Magellan Mission.

1.3.1 The Magellan Spacecraft.

In 1984 NASA announced it was planning a mission to Venus. The spacecraft to conduct this mission was called VOIR (Venus Orbiting Imaging Radar) and was to have been a highly complex custom built spacecraft. VOIR was cancelled due to budgetary pressures, but as a result the Magellan mission was commissioned to conduct a radar mapping mission of the venusian surface but at a much reduced cost. This was to be achieved by utilising mission proven technologies and spare components from previous missions. A list of Magellan components that were in fact spares from other spacecraft is shown in Table 1.3.

Figure 1.2 shows a diagram of the Magellan spacecraft. The most prominent component is the 3.7 m diameter parabolic high-gain antenna. This is used to acquire the radar data, transmit these data back to Earth, receive commands from Earth and to transmit engineering data about the spacecraft back to Earth. Attached to the high-gain antenna is the altimeter antenna which is used solely for the acquisition of radar altimetry data. Situated below the high-gain antenna is the forward equipment module which contains the radar electronics, radio telecommunications equipment, attitude-control equipment, batteries and the power-conditioning unit. The forward equipment module sits above the equipment bus which holds the flight computers, tape recorders, solar array controls and pyrotechnic control electronics. Attached to the side of the spacecraft are the two solar panels, capable of providing up to 1200 watts. Below the equipment bus is the propulsion module and the solid rocket motor used for orbit insertion. Magellan measured 6.4 m in length, and at launch it was attached to a inertial upper stage which was used to drive the spacecraft out of Earth orbit and en route to Venus.

Table 1.3. A list of Magellan components that were spares from previous missions (Young, 1990).

Figure 1.2. A diagram of the Magellan spacecraft including the inertial upper stage (Young, 1990).

Component	Source
Medium-gain antenna	Mariner Mars 1971
High and low-gain antennas	Voyager
Equipment bus	Voyager
Star-scanner design	Inertial Upper Stage
Radio-frequency travelling-wave tube assemblies	Ulysses
Altitude-control computer	Galileo
Command and data subsystem	Galileo
Thruster rockets (small)	Voyager
Electric-power distribution unit	Galileo
Power control unit	P-80 Satellite
Pyrotechnic control	Galileo
Solid-rocket motor design	Space shuttle payload assist module
Propellant-tank design	Space shuttle auxiliary power unit

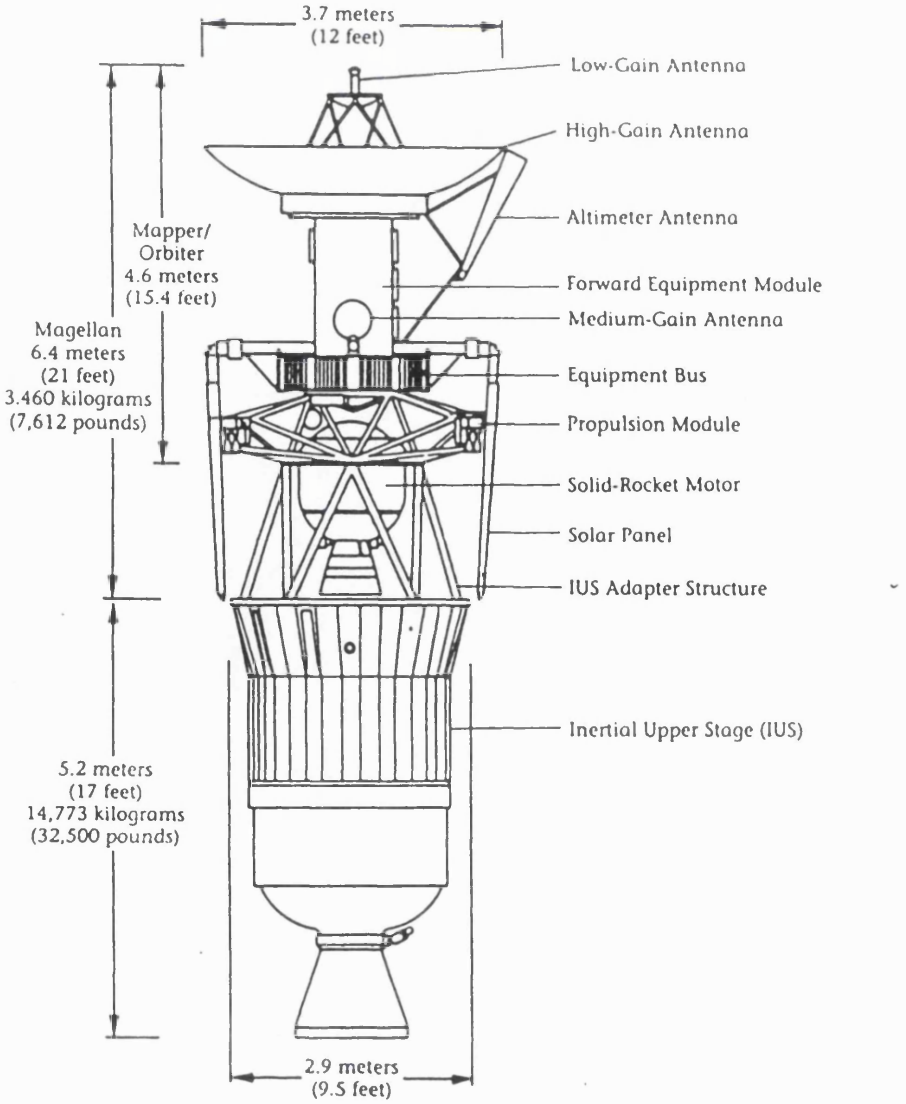

1.3.2 Mission Requirements.

The Magellan mission to Venus began on May 4th 1989, with the launch of the shuttle Atlantis (Figure 1.3). Magellan was the first planetary mission to be launched by a shuttle. After an interplanetary cruise of 15 months Magellan reached Venus on August 10th 1990 (Saunders and Pettengill, 1991). Magellan was inserted into a near-polar elliptical orbit, the details of which are shown in Table 1.4. After 4 weeks of in-orbit tests, during which contact was lost with the spacecraft twice, mapping began on 15th September 1990.

The scientific objectives of the mission were (Ford et al, 1993),

1. To provide a global characterisation of landforms and tectonic features.
2. To distinguish and understand impact processes.
3. To define and explain erosion, deposition, and chemical processes.
4. To model the interior density distribution.

In order to accomplish this the primary mission requirements were to map at least 70% of the planet at a resolution better than 300 m (Saunders et al., 1992) and to determine the global relief at a horizontal resolution of about 10 km and a vertical accuracy of 80 m or better (Ford and Pettengill, 1992). The time during which this was to be achieved was called Cycle 1 and was set to last 243 days, equal to the time it takes for Venus to complete one full rotation beneath the spacecraft. During Cycle 1 Magellan was able to map about 83.7% of the surface, thus surpassing the mission requirements.

The extended mission consisted of two further 243 day mapping sessions (Cycles 2 & 3), and a period devoted to gravity measurements (Cycle 4). The mission was terminated on the 11th October 1994 by aerobraking the spacecraft

Table 1.4. Details of Magellan's orbit, after insertion on August 10th 1990 (Ford et al., 1993).

Parameter	Value
Periapsis altitude	289 km
Periapsis latitude	9.5°N
Altitude at pole	2000 km
Inclination	85.5°
Period	3.259 Hours
Repeat cycle	243 days

Figure 1.3. A stunning view of Magellan being ejected from the cargo bay of the space shuttle Atlantis on May 5 1989, before beginning its 15 month interplanetary cruise to Venus.


USA

into the atmosphere to gather data on the possible use of this technique to achieve orbit insertion for future missions to the planet.

1.3.3 Mapping.

The Magellan radar sensor performed three separate roles.

1. Synthetic Aperture Radar (SAR) imaging.
2. Radiometry.
3. Altimetry.

To carry out the first two, the sensor is connected to the high gain antenna which is oriented at 25° off the nadir in a direction normal the spacecraft trajectory. This was done in order to improve the azimuth resolution. During cycle 1 the spacecraft was operated in a left looking configuration. During altimetry operations the sensor was connected to the nadir oriented altimeter horn antenna. Figure 1.4 shows the observing geometry during an orbit. Due to Magellan being in an elliptical orbit, combined with the antennas' being in a fixed position relative to the spacecraft, it was necessary to alter the alignment of Magellan during the mapping part of an orbit in order to obtain the maximum surface coverage possible. This was achieved using three electrically driven reaction wheels, to cut down on the amount of hydrazine that had to be carried.

As Magellan only had one high-gain antenna, this had to be used for both transmitting radar pulses and receiving the radar echoes. Thus mapping operations were carried out using a process known as burst mode data collection, in which SAR, altimetry and radiometer data were acquired in batches several times a second, (Figure 1.5). Initially between 150 and 800 pulses of SAR energy

Figure 1.4. A diagram showing the observing geometry for Magellan whilst mapping (Young, 1990).

Figure 1.5. A diagram showing how Magellan used the burst mode method to collect SAR, altimetry and radiometer data (Ford et al., 1993, adapted from Pettengill et al., 1991).

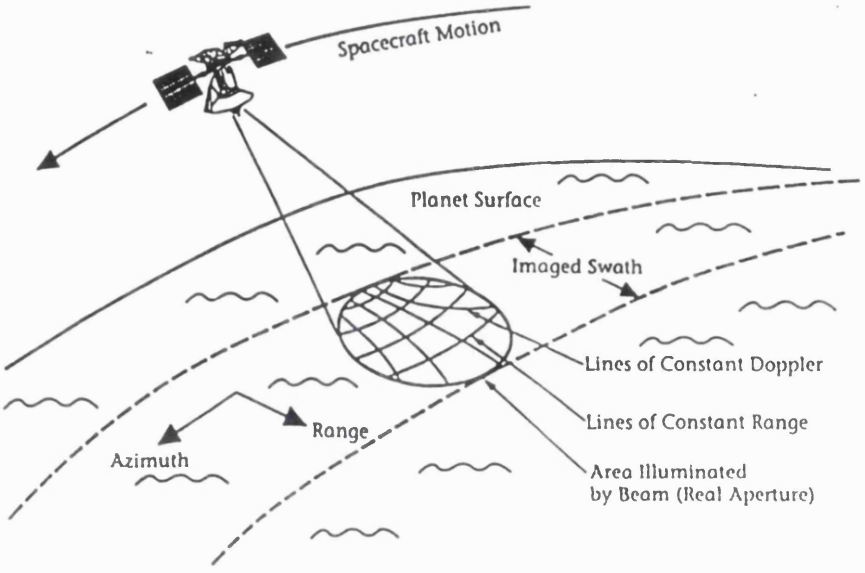
Spacecraft Motion
Planet Surface
Imaged Swath
Lines of Constant Doppler
Lines of Constant Range
Range
Azimuth
Area Illuminated
by Beam (Real Aperture)

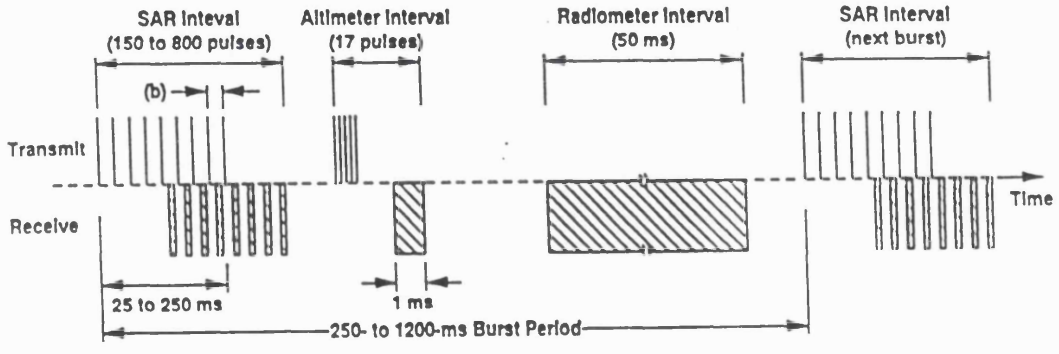
SAR Inteval
(150 to 800 pulses)
Altimeter Interval
(17 pulses)
Radiometer Interval
(50 ms)
SAR Interval
(next burst)
(b)
Transmit
Receive
Time
25 to 250 ms
1 ms
250- to 1200-ms Burst Period

was transmitted, the received echoes being interleaved with the outward pulses. Next the sensor was switched to altimetry mode, and 17 pulses were emitted using the horn antenna. The last pulse was sent before the first altimetry echo was received. Finally the sensor used the high-gain antenna to receive the microwave energy naturally emitted from the planet surface.

During an orbit, mapping began when Magellan was above the north pole of the planet. This continued for 37.2 minutes, with the collected data being stored on tape recorders. The high-gain antenna was then pointed towards Earth and the data played back, via the Deep Space Network (DSN). The playback period was divided into two almost equal sections either side of apoapsis, with the intervening time being used for a star scan and desaturation of the three reaction wheels. After the playback of data was finished Magellan was then oriented again for mapping operations. A diagram showing the orbit profile is shown in Figure 1.6.

Due to the elliptical orbit of the spacecraft, the area of the surface imaged for the first time per orbit was greater at higher latitudes. Thus it was possible to map these latitudes only on alternating orbits without losing the required amount of overlap. This allowed more southerly latitudes to be mapped by delaying the beginning of mapping on alternate orbits until the spacecraft was at about 70°N. This meant that mapping finished on these "delayed" orbits at 74°S compared to 57°S for the orbits when mapping had begun at the north pole.

Figure 1.6. The Magellan mapping orbit profile (Ford et al., 1993).

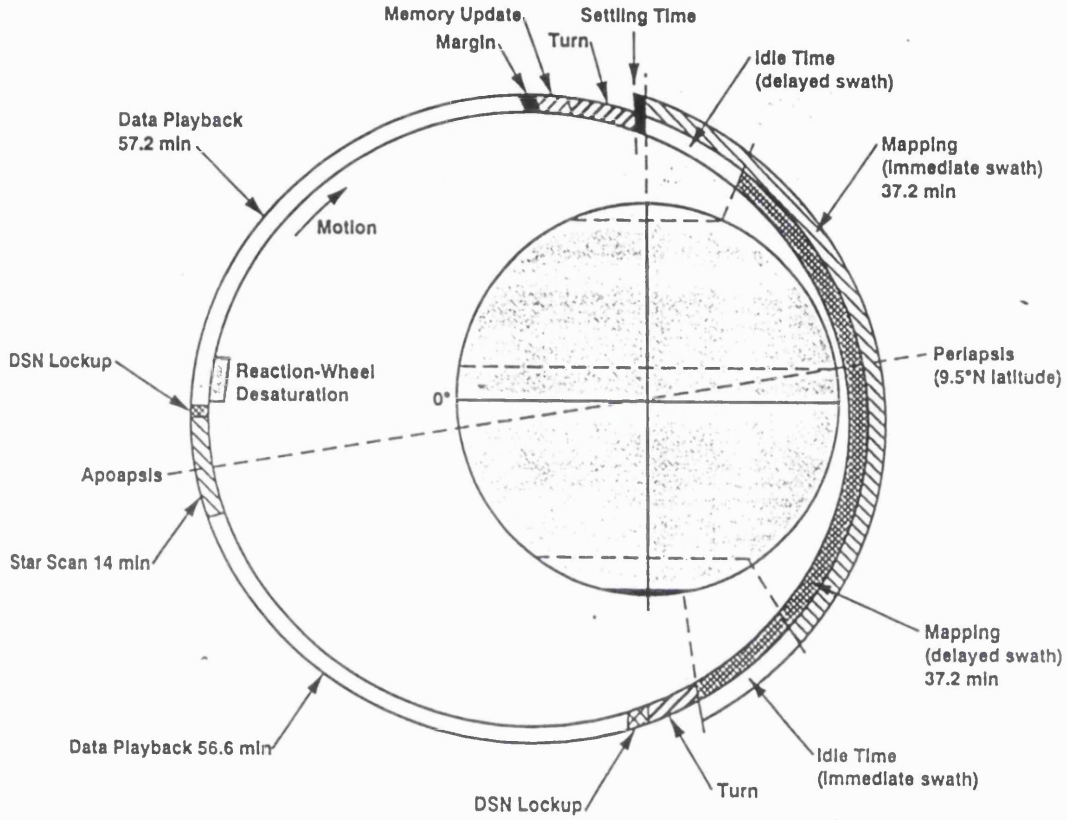
Memory Update Margin
Turn
Settling Time
Idle Time (delayed swath)
Data Playback 57.2 min
Mapping (immediate swath) 37.2 min
Motion
DSN Lockup
Reaction-Wheel Desaturation
0°
Periapsis (9.5°N latitude)
Apoapsis
Star Scan 14 min
Mapping (delayed swath) 37.2 min
Data Playback 56.6 min
Idle Time (immediate swath)
DSN Lockup
Turn

1.4 Synthetic Aperture Radar Imaging.

Radar imaging consists of transmitting pulses of electromagnetic radiation and analysing the returned echoes (Ford et al., 1989). Cross-track (range) information is acquired by considering the time delay between the different echoes from a pulse, as the early echoes come from reflections from the terrain closest to the transmitter whilst the later returns come from further away. This is why the radar pulses are emitted in a direction perpendicular to the spacecraft track. Along-track (azimuth) information is obtained by looking at the Doppler shift of the returned echoes. Echoes received from the terrain in front of the spacecraft have a higher frequency than the transmitted pulse whilst those from behind the spacecraft have a lower frequency. During one orbit each point on the ground is illuminated a number of times. Synthetic aperture radar imaging produces a resolution much higher than what would normally be achieved, by multiple sampling of the echoes for a particular point, thus synthesising the spatial resolution of a much larger antenna. The resolution produced by this technique varied with latitude, due to the elliptical orbit of Magellan. A list of both azimuth and range resolutions is shown in Table 1.5.

Before trying to interpret the images produced, it is useful to define some of the terms that are associated with a side-looking radar (Figure 1.7) The angle between the antenna boresight and the nadir is called the look angle. The complement of the look angle is the depression angle. The incidence angle is the angle between the incoming radar and the surface normal. For a flat surface the look and incidence angles are not the same, due to planetary curvature which slightly increases the incidence angle. Figure 1.8 shows how the nominal incidence angle varied with latitude for the different mapping cycles.

Table 1.5. A list showing how both the range and azimuth resolutions varied with latitude (Saunders et al., 1992).

Figure 1.7. Definition of some of the terms associated with side looking radar (Ford et al., 1989).

Latitude	Range Resolution /m	Azimuth Resolution /m
90°	250	110
82°	211	110
60°	155	110
45°	125	110
30°	108	110
10°	101	110
-10°	108	110
-25°	125	110
-40°	155	110
-62°	211	110
-70°	250	110

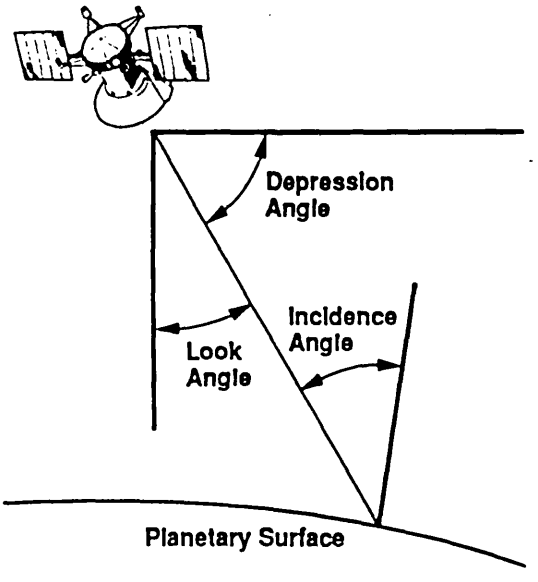

Figure 1.8. A graph showing how the nominal incidence angle varied with latitude for the three mapping cycles of the Magellan mission (Ford et al., 1993).

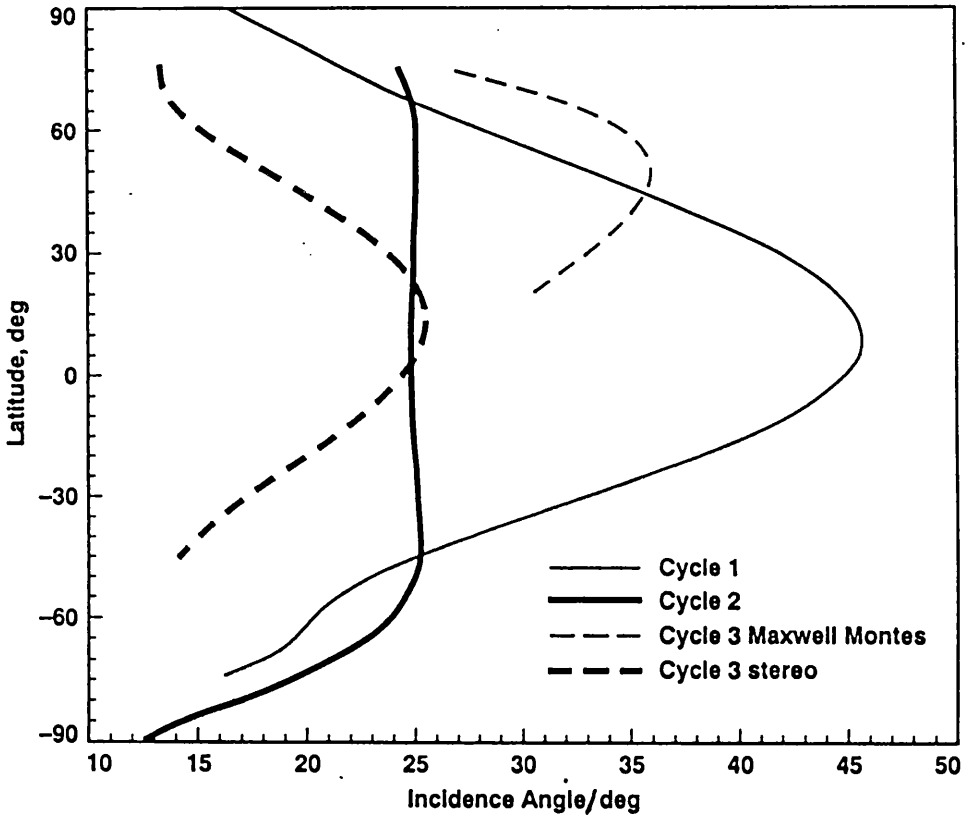
90
60
30
0
-30
-60
-90
Latitude, deg
10
15
20
25
30
35
40
45
50
Incidence Angle/deg
Cycle 1
Cycle 2
Cycle 3 Maxwell Montes
Cycle 3 stereo

The main factors that affect the brightness in radar images are, in decreasing order of importance,

- surface slope
- surface roughness
- dielectric constant.

If the surface is oriented so that the radar has a very small incidence angle, then the radar return will be strong, resulting in a bright feature being seen in a radar image. Conversely, if an area slopes away from the incoming radar (large incidence angle) then there will be a weak echo and a dark region on any image. Radar waves incident upon a surface are scattered. The nature of this scattering depends on the smoothness of the surface (Figure 1.9). If the surface is smooth, relative to the radar wavelength, then specular reflection occurs with very little energy being scattered in the direction of the incident pulse. The rougher a surface is, the more energy is scattered randomly until there is a diffuse distribution of the reflected energy. Whether a surface appears bright or dark in a Magellan image depends on both the roughness (relative to the Magellan radar wavelength of 12.6 cm) and the incident angle. Figure 1.10 shows how radar backscatter varies with incidence for a smooth, moderately rough and rough surface. A smooth surface is more sensitive to the incident angle than a rough surface which tends to scatter the incident radar in all directions. One important feature of the graphs to note is that for small incident angles, a smooth surface may give a higher radar return than a rough one. Of relative minor importance in affecting the strength of the radar backscatter is the value for the dielectric constant of the surface. On Earth wet soil has a higher dielectric constant and is consequently a better radar reflector than dry soil. The value of the dielectric constant is similar for dry geologic materials except metallic compounds, which may be present at high venusian elevations.

Figure 1.9. A diagram showing how the amount of scattering depends upon the roughness of the surface relative to the wavelength of the incident radar (Ford et al., 1993).

Figure 1.10. A diagram showing how the amount of radar backscatter varies with incidence angle for a smooth, moderately rough and rough surface (Ford et al., 1993).

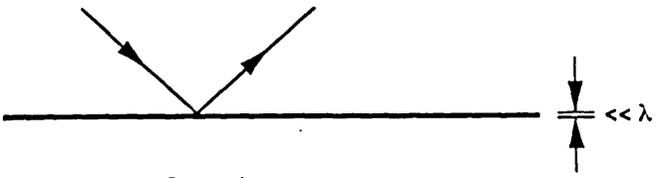

Smooth: no return

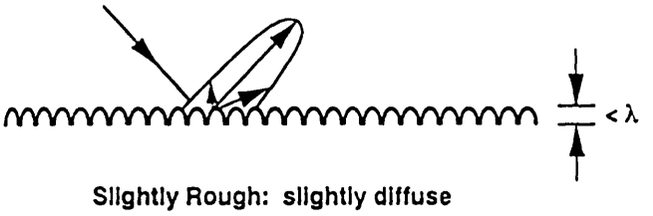

Slightly Rough: slightly diffuse

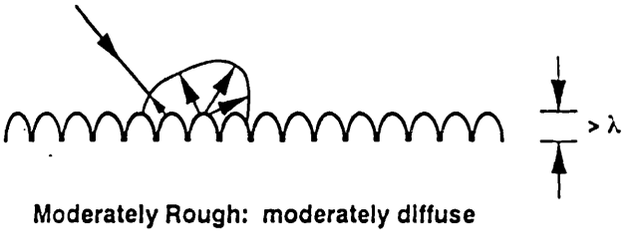

Moderately Rough: moderately diffuse

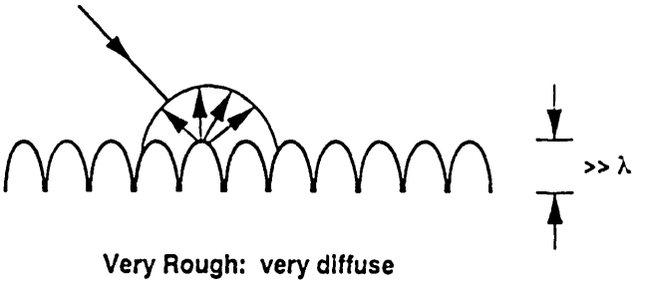

Very Rough: very diffuse

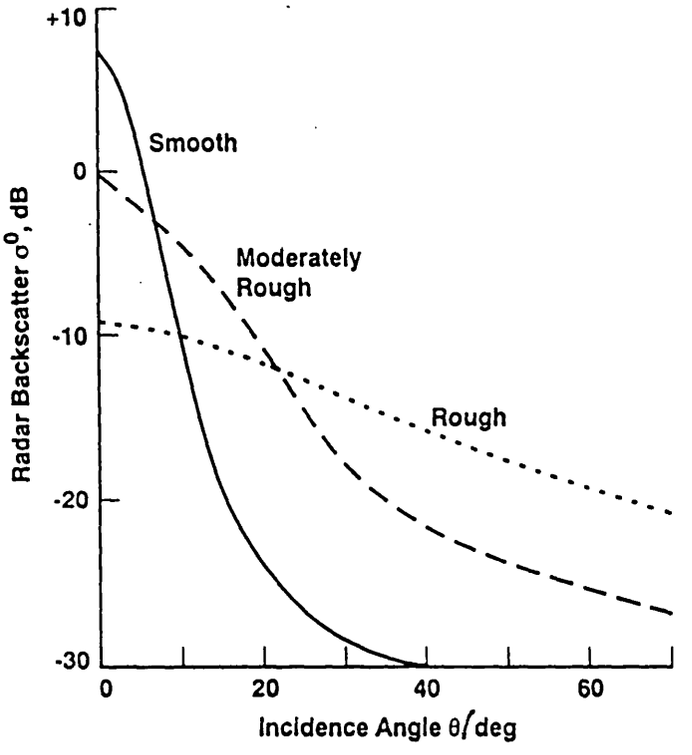

1.5 Data Products.

The Magellan mission produced several different types of data sets. The primary analysis tool was the SAR imagery, (at various resolutions) which was used to interpret channel morphology, whilst the topography data were used to obtain approximate figures for the gradients of the channels.

1.5.1 SAR Data Products.

The raw SAR data returned to the spacecraft during each orbit consisted of a narrow strip, approximately 20 km wide and 17000 km long. This was converted into basic image data records (BIDRs). Accompanying each BIDR is the altimeter/radiometer composite data record (ARCDR) also obtained during the same orbital sweep. Processing of the raw SAR data results in the production of a full resolution basic image data record (F-BIDR). The pixel size of a F-BIDR is 75 m. Each consecutive orbit maps slightly westwards of the previous orbit. However, due to the elliptical orbit of the Magellan spacecraft, the degree of overlap is not uniform but varies with latitude, being greatest at high latitude. Nevertheless the science requirements for Magellan specified that each geographical point on the venusian surface should be imaged by a minimum of four orbital passes, or "looks". In actual fact the number of looks varied from five to fifteen (Table 1.6).

Due to their narrow field of view, BIDRs are not a useful product when analysing a large region. For this reason other products were produced by mosaicking adjacent BIDRs to produce mosaicked image data records (MIDRs). The basic MIDR is a full resolution MIDR, or F-MIDR. This consists of 7168

Table 1.6. A table showing how the number of looks varied with latitude (Saunders et al., 1992).

Latitude	Number of Looks
90°	14
82°	15
60°	9
45°	8
30°	6
10°	5
-10°	5
-25°	5
-40°	11
-62°	15
-70°	14

lines x 8192 samples, and has the same pixel size as the F-BIDRs, i.e. 75 m per pixel. Each F-MIDR covers a region approximately 5° in latitude and longitude.

Whilst it is normally advantageous to work with the highest resolution data possible, it is sometimes useful to be able to study a larger area on one image. Mosaics of larger regions were obtained by compressing the original BIDRs. There are three types of compressed MIDR (C-MIDR). A C1-MIDR is produced by replacing arrays of 3 x 3 pixels with one pixel, the value being the average of the nine pixels being substituted. Thus the pixel size of a C1-MIDR is 225 m, and a C1-MIDR covers an area approximately 15° by 15° in size. Similar compression of a C1-MIDR produces a C2-MIDR (C2 meaning compressed twice), with a pixel size of 675 m and covering 45° by 45°. Compression of a C2-MIDR produces a C3-MIDR, which covers an area 120° by 80° at a pixel size of 2025m. A diagram of the different image data products is shown in Figure 1.11. The initial science requirement for Magellan called for global image coverage to be produced as quickly and cheaply as possible. To this end the production of C1-MIDRs was given priority over F-MIDRs, and therefore there are times when one is forced to use C1-MIDRs as they are the only coverage available.

MIDRs are available in both digital and photographic form. The initial study to identify the location of the channels primarily involved the study of the photographic products as they have the advantage of being easy and quick to use. More detailed analysis of the images requires manipulation of the digital data to pick out features not readily visible on the photographs. In digital form a F-MIDR consists of 57 separate images. The full MIDR is divided up into 56 framelets, each one 1024 x 1024 pixels, with a pixel size of 75 m. The whole region covered by a F-MIDR is shown on a browse image, 1024 x 896 pixels, which is produced by compressing the original MIDR 8 times. The pixel size of a browse image is therefore 600 m. Thus it is useful to picture the browse image as being made up

Figure 1.11. A diagram showing the areas covered by the different Magellan image data products (Ford et al., 1993).

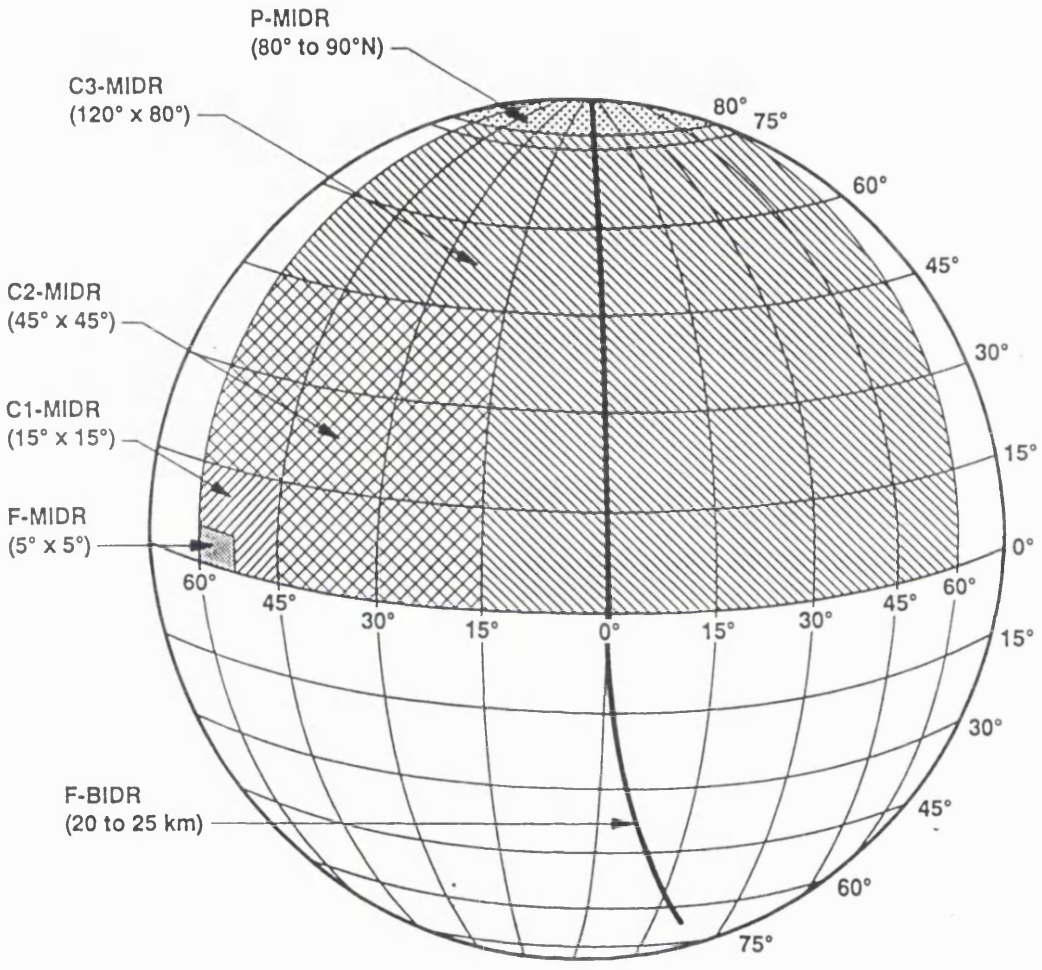

F-BIDR	Full-Resolution Basic Image Data Record
F-MIDR	Full-Resolution Mosaicked Image Data Record
C1-MIDR	Compressed-Once Mosaicked Image Data Record
C2-MIDR	Compressed-Twice Mosaicked Image Data Record
C3-MIDR	Compressed-Thrice Mosaicked Image Data Record
P-MIDR	Polar Mosaicked Image Data Record

of 56 mini-framelets, each one 128 x 128 pixels formed by reducing the original framelet by a factor of eight. This is shown in Figure 1.12. It was found that in order for measurements to be taken it was desirable to have F-MIDR coverage for the channels wherever possible. If this was not available then it was almost always necessary to work from the C1-MIDR framelets as opposed to the C1-MIDR browse image. The size of the channels means that C2 and C3 MIDRs were not used in the study.

1.5.2 Altimetry Data Set.

The altimetry data come in two different forms. The altimetry-radiometry composite data record (ARCDR) consists of individual footprints of data obtained at the same time as the BIDRs were being taken. The global topography data record (GTDR) is formed by processing of the planetary radius measurements from the ARCDR data to produce a more useful data product which can be used to study the topography of a region.

The altimeter footprint dimension varies with the latitude of the spacecraft (Table 1.7). The size of the channels, combined with the spatial resolution of the altimetry data (i.e. the footprint size) means that it is not possible to get channel profile information directly from the altimetry data. The data are useful however in their GTDR form to obtain approximate values for the slope of the channels, although the problem arises that regional deformation may have changed the slope of the channels in places since their formation. The possibility of looking at individual footprint echoes to resolve channel detail was considered, but rejected, as it was unreliable due to the complexity of the returned echoes making it difficult to ascertain which echo corresponded to a particular feature within the area covered by the altimetry footprint.

Figure 1.12. A diagram showing how a browse image is made up of a number of compressed framelets.

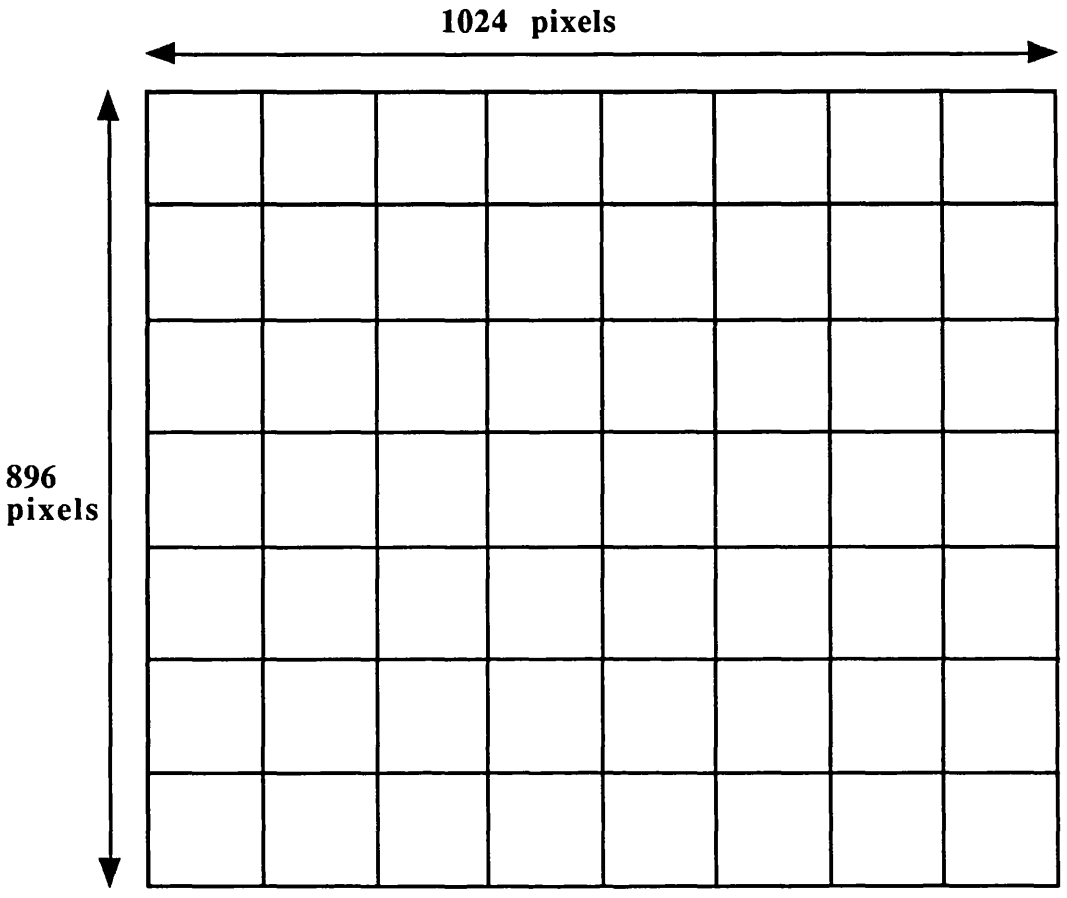
1024 pixels
896
pixels

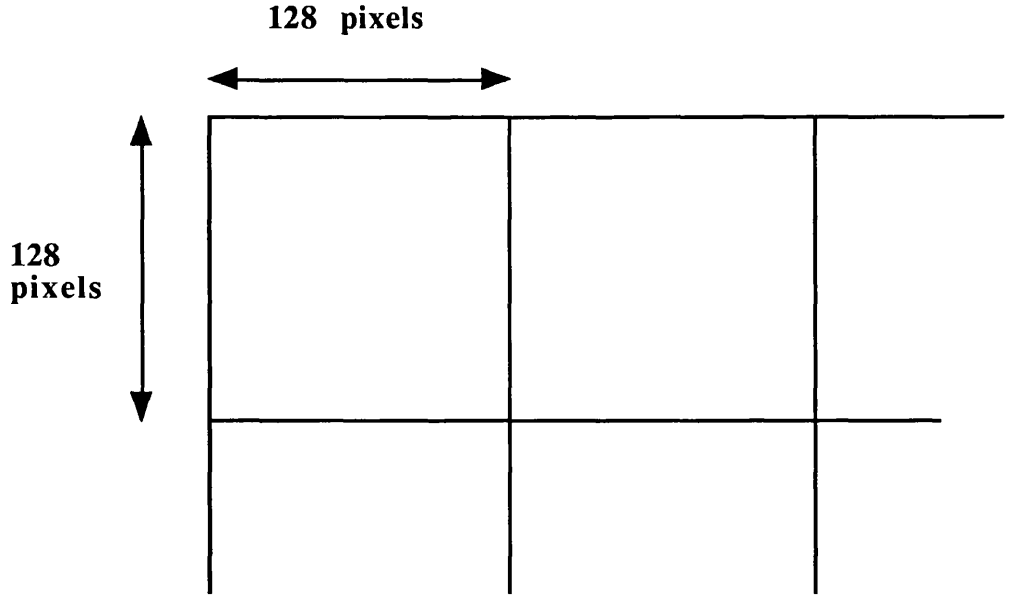
128 pixels
128
pixels

Table 1.7. A table showing how the altimeter footprint dimensions varied with latitude (Ford et al., 1993).

Latitude	Cross-track dimension (E-W) /km	Along-track dimension (N-S) /km
80°, -60°	27	15
70°, -50°	24	11
60°, -40°	21	8
50°, -30°	19	11
40°, -20°	16	8
30°, -10°	14	9
20°, 0°	13	9
10°	12	8

The GTDR data are available in different cartographic projections. Planetary coverage up to ±66.5° latitude is available in Mercator and sinusoidal projections, whilst polar projection images are available centred on either pole and extending to ±32° latitude. Both the sinusoidal and mercator GTDRs are made up of 32 framelets, arranged in four rows of eight. Each framelet consists of 1024 x 1024 pixels at a resolution of approximately 4.641 km per pixel. Figure 1.13 shows the latitude and longitude coverage of the framelets. A browse image, similar in format to a MIDR's browse image, is also available. This is produced by averaging 8 x 8 groups of pixels to produce a final image 512 lines by 1024 samples in size.

This section has described the data products used to study the venusian canali. A description of this study is presented in chapters 3 & 4.

1.6 Global Topography.

Pioneer Venus mapped 93% of Venus at a vertical resolution of 150 m and an average sampling interval of 60 km. From these data the first near-global map of venusian topography was produced. This showed that 60% of the surface lay within 500 m of the mean planetary radius of 6051.5 km (Pettengill et al., 1980). It also indicated that Venus was made up of three primary physiographic units, the main unit (65% of the surface) being rolling plains, with the rest of the terrain consisting of highland (8%) and lowland (27%) areas.

A goal of the Magellan mission was to map the whole of Venus at a vertical resolution of 80 m and a horizontal resolution of approximately 10 km

Figure 1.13. The latitude and longitude coverage of the GTDR framelets.

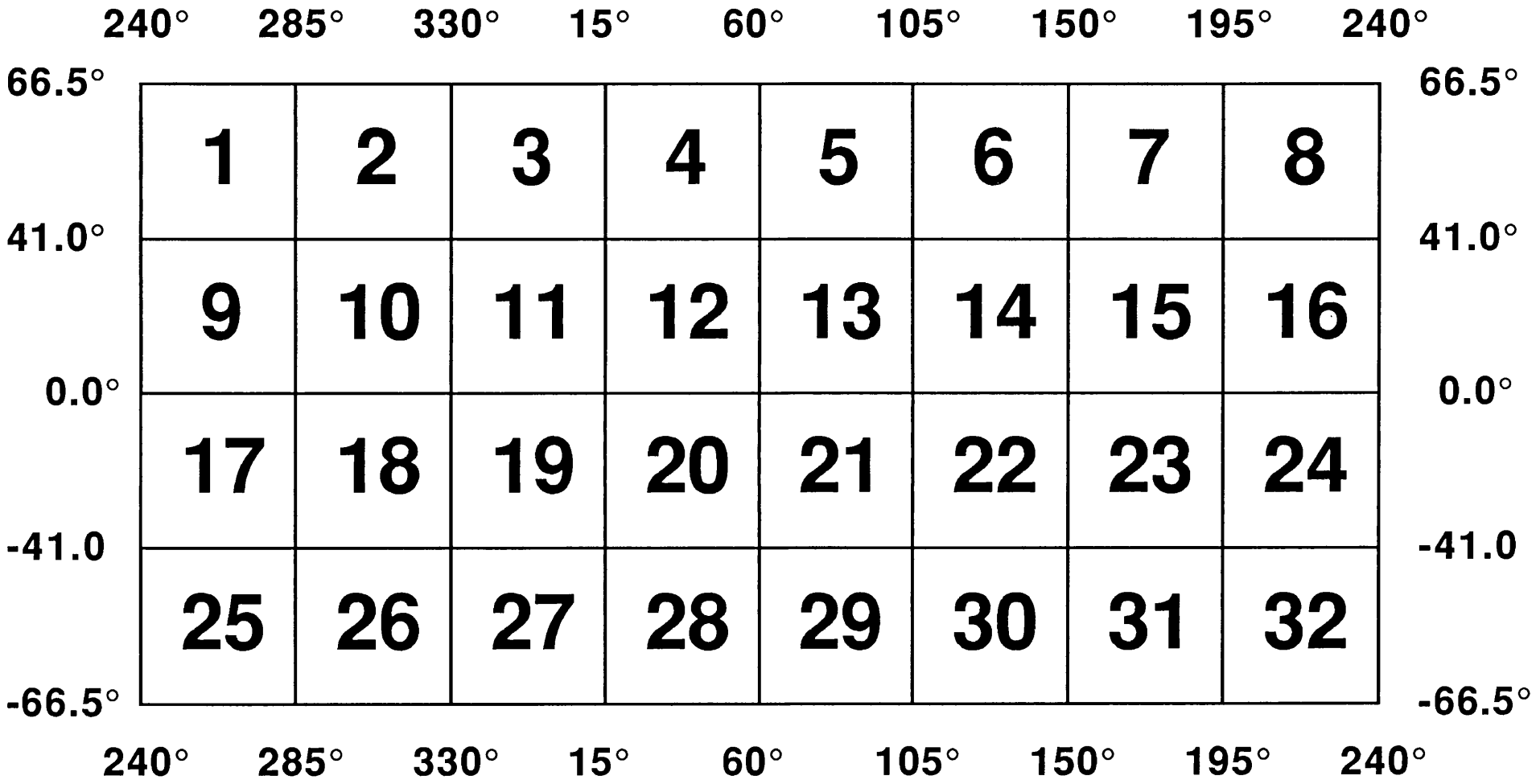
240° 285° 330° 15° 60° 105° 150° 195° 240°
66.5°
41.0°
0.0°
-41.0
-66.5°
1 2 3 4 5 6 7 8
9 10 11 12 13 14 15 16
17 18 19 20 21 22 23 24
25 26 27 28 29 30 31 32
240° 285° 330° 15° 60° 105° 150° 195° 240°

(Ford & Pettengill, 1992). As described in section 1.3.3, data were collected using the nadir pointing horn antenna.

The Magellan results show that more than 80% of the venusian surface lies within 1 km of the mean planetary radius of 6051.84 km. They also confirm that Venus has a unimodal elevation histogram, already known from the Pioneer and Venera altimetry data, compared with the Earth's bimodal and Mars' trimodal hypsometric distributions. A global topography map for Venus, giving a selection of named features, is shown in Figure 1.14.

The most prominent highland feature in the northern hemisphere is Ishtar Terra. This plateau lies 3 to 4 km above the mean planetary radius, and is approximately the size of Australia. It contains the highest feature on Venus, Maxwell Montes, a 12 km high mountain. Ishtar Terra is surrounded by a number of lowland areas, namely Atalanta Planitia to the east and Sedna and Guinevere planitiae to the south. One remarkable feature of the plains is that they have very low slopes. Within Guinevere Planitia are a number of more modest highlands, Alpha, Bell and Eistla regiones. Eistla Regio contains the twin volcanoes Sif and Gula montes, 3.5 and 4.4 km high respectively. To the east of Guinevere lie a number of equatorial highland regions known collectively as Aphrodite Terra. This feature, the size of Africa, is surrounded by a network of chasmata including Diana Chasma which contains the lowest point on the venusian surface, some 4 km below the mean planetary radius.

Figure 1.14. A map of Venus topography, including a selection of named features.

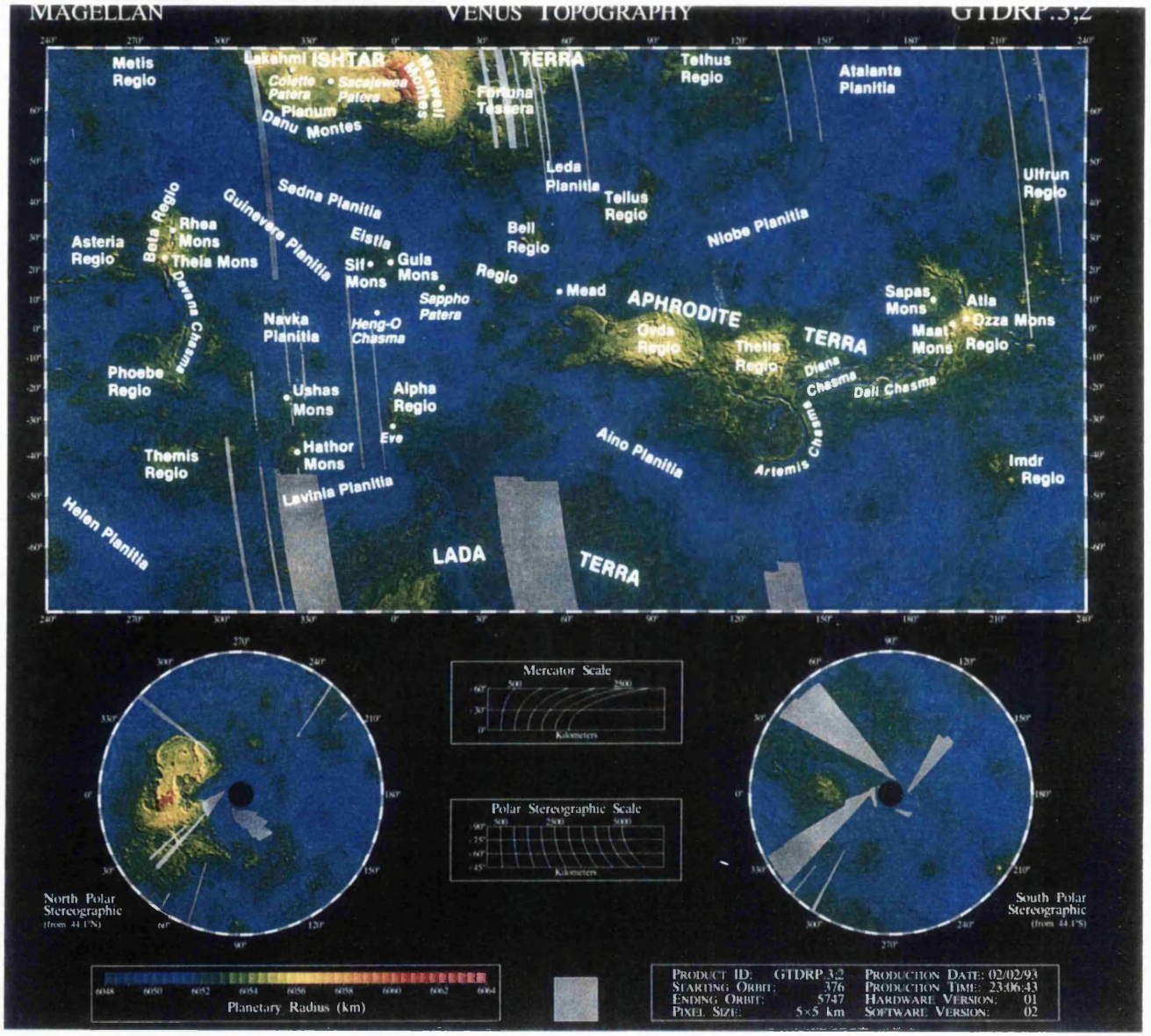
MAGELLAN
VENUS TOPOGRAPHY
GTDRP.3;2
Metis Regio
Lakshmi
ISHTAR
Maxwell Montes
TERRA
Colette Patera
Sacajawea Patera
Piganum
Danu Montes
Fortuna Tessera
Tethus Regio
Atalanta Planitia
Leda Planitia
Ulfrun Regio
Sedna Planitia
Guinevere Planitia
Beta Regio
Rhea Mons
Asteria Regio
Thetis Mons
Eistla
Sif Mons
Gula Mons
Bell Regio
Tellus Regio
Niobe Planitia
Devana Chasma
Seppho Patera
Mead
APHRODITE
TERRA
Sapas Mons
Atla
Ozza Mons
Maat Mons
Regio
Navka Planitia
Heng-O Chasma
Onda Regio
Thetis Regio
Diana Chasma
Dali Chasma
Phoebe Regio
Ushas Mons
Alpha Regio
Eve
Hathor Mons
Themis Regio
Aino Planitia
Artemis Chasma
Imdr Regio
Lavinia Planitia
Helen Planitia
LADA
TERRA
Mercator Scale
Kilometers
Polar Stereographic Scale
Kilometers
North Polar Stereographic
(from 44°N)
South Polar Stereographic
(from 44°S)
Planetary Radius (km)
PRODUCT ID: GTDRP.3;2
STARTING ORBIT: 376
ENDING ORBIT: 5747
PIXEL SIZE: 5×5 km
PRODUCTION DATE: 02/02/93
PRODUCTION TIME: 23:06:43
HARDWARE VERSION: 01
SOFTWARE VERSION: 02

1.7 Thesis Overview.

Chapter 2 reviews Venus volcanism, channels on the moon and Venus, and several models that have been proposed to describe their formation. A preliminary study of the venusian surface indicated an unusually high density of canali type channels in a region roughly 30° latitude by 30° longitude to the south east of Aphrodite Terra and to the east of Artemis Chasma. Twelve channels were found and it was decided to make a detailed study of these channels. The first part of this study consisted of measuring physical parameters of the channels such as their length and width, and also inferring the cross-sectional profile from the radar images. This work is described in chapter 3. The next step in the analysis of the channels is described in chapter 4. This involved producing maps of the channels showing the determined cross-sectional profiles as well as trying to calculate the direction in which they were emplaced by looking for features such as branching and flows from the end of channels. For channels for which it was possible to find an emplacement direction, present day slopes were measured to try to see if the region in which the channels were formed had undergone any kind of vertical deformation since they were created. Many of the channels studied showed evidence that erosive processes had affected their formation. As lava erosion is uncommon on Earth it was decided to consider under what conditions lava might be able to erode, either thermally or mechanically, on Venus. This took the form of the development of a mathematical model that allows for factors such as latent heat, and allows lava parameters to be varied to see how sensitive the erosion process is to them. The theory behind the thermal erosion model is described in chapter 5. Details of the experiments carried out using the model as well as the results from the experiments are shown in chapter 6. A description of the erosional model as well as some of the results from chapter 6 have been published in Bussey et al. (1995). My contribution to this paper consisted of development of the model with advice on finite differences by S-A Sörensen and comments on lava flow

processes based on field experience from J.E. Guest. A summary of the conclusions drawn from the work presented in this thesis as well as ideas for future work are displayed in chapter 7.

Chapter 2
Review of Venus, Channels and Erosional Models

Volcanic processes have played a major role on Venus. This chapter reviews venusian volcanism, channels on the moon and Venus,and models that have been proposed for their formation.

2.1 Venus Overview.

2.1.1 Surface Geology.

During the 1970's seven Soviet spacecraft successfully landed on the venusian surface (Nikolayeva, 1990). These landers provided both physical and chemical data about their surroundings. Four of the landers (Veneras 9, 10, 13 and 14) sent back images of the surrounding terrain.

All the landers contained instruments to allow them to measure the composition of the surface on which they landed (Keldysh, 1977). Five of the landers (Veneras 9, 10, 14 and Vegas 1 & 2) determined that they landed on rock similar in composition to tholeiitic basalt (Nikolayeva, 1990; Saunders et al., 1991). The Venera 13 site appears to be similar to terrestrial alkaline basalt whilst the composition of the Venera 8 landing site indicates that it is one of a number of possibilities including granite, shoshonite or syenite rock (Nikolayeva, 1990).

The first panoramas of the venusian surface were returned by the Venera 9 & 10 spacecraft (Florensky et al., 1977) The images were taken using optical-mechanical TV cameras similar to those used on Soviet lunar missions.

Panoramic views were obtained by scanning a mirror capable of rotating about both it s horizontal and vertical axes.

Venera 9 landed on a steep slope densely covered by slab shaped rocks. These rocks had a maximum width of about 70 cm and a height of between 15 and 20 cm. The images also showed there to be loose soil type material between the rocks. Venera 10 landed in a plains region and revealed the surrounding surface to consist of smooth bedrock material surrounded by unconsolidated fines.

The Venera 9 & 10 landers also collected other data. They showed the temperature to be between 730 and 740 K, the pressure to be 88 - 94 bars and the wind velocity to be 0.5 - 1.0 m s^{-1}. Venera 10 used a gamma densitometer to measure the density of the rock at the landing site., the value being 2800 kg m^{-3}. Having found the density, the densitometer was used to determine an approximate target strength for the rock. This was achieved by dropping the 2 kg instrument onto the surface, striking the rock with the force of a sledge hammer. The rock suffered no visible effect and it was inferred that the struck material was "hard" (Florensky et al., 1977). The final piece of information that the landers were able to obtain was that the venusian surface has an orange hue when viewed at visible wavelengths (Pieters et al., 1986). This is due to the thick atmosphere filtering out the shorter wavelength blue radiation.

2.1.2 Venus Volcanism.

Volcanic processes have been the most widespread and important geologic phenomenon on the surface of Venus (Saunders et al., 1992). The most widespread terrain is the lowland volcanic plains which largely consist of flood

lava flows. Whilst the global distribution of volcanic features is not random, there are no linear concentrations of features from which one could infer the existence of plate tectonics.

A study of Magellan data covering more than 90% of the venusian surface has revealed more than 1600 volcanic landforms (Head et al., 1992). There is a diverse variety of features including shield fields, intermediate and large volcanoes, coronae, novae, flood type flow fields and lava channels. These will be discussed in more detail below. There is little evidence for explosive volcanism on Venus. This is as was predicted by Head and Wilson (1986) who stated that the high atmospheric pressure (~98 bar) will inhibit the exsolution of volatiles from a rising magma, hence reducing the amount of explosive volcanism that will occur.

The term shield field is used to describe a region with a concentration higher than the regional average of shield volcanoes. Shield volcanoes are small volcanoes, typically <20 km in diameter. The morphology of individual shields is diverse (Guest et al., 1992) with the majority having convex slopes rising to a summit pit. They have been interpreted as being of basaltic composition. More than 550 shield fields of various sizes have been identified, although more than 50% of the fields have a diameter in the range 100 - 200 km. These fields are widely distributed globally and are probable evidence of hot spots or mantle plumes.

Intermediate volcanoes are defined as landforms 20 - 100 km in diameter. More than 270 such features have been mapped on Venus, of various morphologies. Anemone type volcanoes are characterised by having radar bright petal shaped radial lava flows associated with them. Steep-sided domes, also known as "pancake" domes, are another type of intermediate volcano. These have been interpreted to be silicic lava domes (Head et al., 1991) as they are very similar in morphology to terrestrial dacite and rhyolite domes. The venusian domes are

larger than their counterparts on Earth having diameters in the range of 10 - 70 km and heights of the order of 300 m. Fink et al. (1993) suggest that they are formed by episodic emplacement and also mention that they provide evidence of evolved magmas on Venus. A third class of intermediate volcano are known as scalloped margin domes and are characterised by having a circular interior (either flat of slightly depressed), surrounded by a rim and radial ridges. They tend to be 20 - 30 km in size and appear morphologically similar to some terrestrial sea floor volcanoes.

Large volcanoes (> 100 km in diameter) have positive topography and radial, both radar dark and light, lava flows. More than 150 large volcanoes have been identified, having a fairly equal size density in the range 100 - 700 km (Head et al., 1992). The global distribution for these features is not random. Whilst there is a high density in Atla Regio, Beta/Phoebe/Themis regiones and along Eistla Regio, there is a distinct lack of large volcanoes in the plains regions. In general these features seem to occur at higher elevations, which might be related to altitude effects on neutral buoyancy zones and edifice growth (Head and Wilson, 1992).

Coronae are circular or ovoidal structures with an annulus of concentric fractures. Their interiors can be topographically positive or negative, they have a peripheral moat and it is common to observe volcanic or tectonic features within the main structure. There are different types of coronae and they have been characterised by the type and distribution of fractures associated with them (Stofan et al., 1992). More then 170 coronae have been mapped, and they range in size from 200 - 2600 km although the most common size is between 200 and 250 km. Their spatial distribution is not random; they are concentrated into a few groups and chains. There is a lack of them in plains regions but this may be due

to resurfacing of these areas. It has been suggested that they are the surface manifestations of mantle plumes (Stofan et al., 1992; Squyers et al., 1992).

More than 50 major lava flood type flow fields have been identified on Venus. Each flow can cover large areas, for example the Mylitta Fluctus flow field in southern Lavinia Planitia covers an area approximately equal to $3x10^5$ km^3 (Roberts et al., 1992). Therefore it is possible that these flows have played a major role in the resurfacing of the planet, particularly the lowland plains where these flows are most common possibly because the low altitude promotes flood type volcanism (Head and Wilson, 1992).

2.2 Channels.

2.2.1 Lunar Sinuous Rilles.

Sinuous rilles are a common feature in the mare regions of the moon. They consist of a meandering channel of remarkably constant width often originating from a roughly circular depression at the topographic high of the feature. There has been much debate as to the processes that formed them. Whilst it is now generally accepted that they are of volcanic origin, when they were first observed there were a number of other emplacement mechanisms proposed including water erosion (Urey, 1967), nuées ardentes (Cameron, 1964) and gas emissions along lines of crustal fractures (McCall, 1970).

Sample returns of lunar rock by the Apollo program showed that it was volcanic and had a very low volatile content making it extremely unlikely that water had ever been present on the surface of the moon in sufficient quantities to produce the rilles seen, or that gas could have been the formational medium. Carr

(1974) and Greeley (1971) cite extensive physical evidence supporting lava rather than water as the source for the rilles. The rilles have a discrete source where as rivers tend to have a diffuse source made up of a number of tributaries. If water had formed the rilles, one would expect to see fluvial depositional features which are not present on the lunar surface. Also proposals for water erosion require short flow durations which in turn need an easily eroded lunar regolith. Apollo field results show that the regolith is compacted below the top 15 cm and that it is only 3 to 16 m deep, much less than that required by water erosion of short duration.

The main question associated with the origin of the sinuous rilles is whether they were formed predominantly by erosional (either thermal or mechanical) or constructional processes.

The constructional argument is put forward by Oberbeck et al. (1969) and Greeley (1971). The meanders of sinuous rilles suggest an origin by fluid flow. Lunar basaltic lavas were very fluid, permitting long lava flows and hence long lava tubes. Some lunar sinuous rilles such as Hadley Rille, in a valley of the Apennine mountains east of Mare Imbrium, may be collapsed lava tubes. Hadley Rille is about 135 km long, has an average width of 1.2 km and an average depth of about 370 m. It appears to originate from a depression at the highest point of the channel. This may represent the vent for the lava that formed the channel. Hadley Rille is situated along the crest of a ridge, a position not normally associated as the likely course of a flowing liquid. It is proposed (Greeley, 1971), that this ridge was actually formed at the same time as the rille and is the result of constructional processes associated with the formation of a lava tube. These processes include overflow of the main channel onto the surrounding terrain and also distributary tubes which branch out radially from the primary structure and deposit lava parallel to the main channel/tube forming broad ridges. Once the

source of lava terminates, the flow soon stops resulting in the lava tube draining, to leave a hollow structure. The roof subsequently collapses, due to a mixture of gravitational forces and meteoritic bombardment, resulting in the structure seen today. A possible terrestrial analogue is a collapsed lava tube system originating from Modoc crater in California (Oberbeck et al., 1969).

An alternative to the constructional hypothesis is that the rilles were formed by lava erosion, either melting away the underlying substrate (thermal erosion), scraping it away (mechanical erosion), or more probably a combination of the two. Several models on this topic have been put forward and of key significance is whether the flow that produced the rilles was laminar (Carr, 1974) or turbulent (Hulme, 1973, 1982; Hulme and Fielder, 1977, Head and Wilson, 1980, 1981; Wilson and Head, 1980) in nature. The character of a flow is determined by the Reynolds number which expresses the relative importance of the inertial and viscous forces. If viscous forces are dominant then the flow will have a low Reynolds number and have a laminar profile where the velocity is a function of depth. As inertial forces become more important the Reynolds number increases until a critical value of the Reynolds number when the laminar flow regime breaks down and the flow becomes turbulent.

In fluids such as water the rate of strain is proportional to the applied stress, the constant of proportionality being viscosity. Fluids that exhibit this behaviour are called Newtonian fluids. Lava shows non-Newtonian behaviour, such as stopping on a slope and having a steep flow front (Hulme, 1982). It is the crystals and vesicles within a lava that make it a non-Newtonian fluid. Instead it behaves approximately like a Bingham plastic (Robson, 1967), or possibly a pseudo plastic. The difference between a Bingham plastic and a Newtonian fluid is that the former has a finite yield stress (Hulme, 1974, 1982; Dragoni et al.,

1986) which must be overcome before any flow occurs. Bingham plastics tend to have a higher critical Reynolds number than Newtonian fluids.

Basalt flows on Earth tend to be laminar (Hulme, 1973), although they may show signs of approaching the change to turbulent flow. Some lunar basalts are between one and two orders of magnitude less viscous than their terrestrial counterparts (Murase and McBirney, 1970). Hulme (1973) argues that this has two effects; it reduces the Reynolds number and also means that the lunar basalts will reach the surface faster than basalts on Earth. They will therefore have cooled less and so contain fewer crystals. Thus they will behave more like Newtonian fluids, having a lower critical Reynolds number. In conclusion, Hulme (1973) states that the reduced viscosity of the lunar basalts results in their having a higher Reynolds number and a lower critical Reynolds number, both of which point to lunar flows being turbulent rather than laminar. More generally, the Reynolds number is directly proportional to the flow velocity. Clearly a low viscosity fluid will flow relatively rapidly thus having a high Reynolds number and therefore a turbulent nature.

Thermal erosion of the underlying substrate consists of heating this material until its melting temperature is reached, then supplying latent heat until the rock finally enters the liquid phase. At this point the fluid substrate actually becomes part of the flow. In practice this may not occur as the substrate has a melting range bordered by its solidus and liquidus temperatures. As the underlying rock reaches its solidus temperature it becomes a mixture of liquid and solid, enabling the lava to remove it by scraping it away, i.e. mechanical erosion. Hulme (1974) argues that lunar basalts will be emplaced as turbulent flows and also that turbulent flows will be more effective at both thermal and mechanical erosion than laminar ones. Carr (1974) states that turbulent flow is not a prerequisite to erosion taking place. He argues that the nature of the flow will not

affect thermal erosion but agrees that turbulent flows will be more effective at mechanical erosion. Part of the justification for his statements comes from occurrences of lava erosion on Earth e.g. lava tubes in Hawaii, in which erosion took place under conditions where laminar flow was most likely to be occurring. Carr (1974) also mentions lava channels on Mars. Whilst the large martian outflow channels are associated with aqueous processes, there are a number of channels which have been interpreted as having a volcanic origin. Many of these are associated with volcanic constructs such as shield volcanoes.

2.2.2 Venusian Channels.

2.2.2.1 Description.

Channels of different types are common on Earth, Mars and the Moon and have now been observed on Venus. Over 200 channels have now been found on Venus (Baker et al., 1992), with a diverse range of morphologies. Some of them appear similar to the lunar sinuous rilles whilst others have similarities with river channels on Earth. Many of the channels seen have meandering sections at some point along their length. A study of the meandering properties of the channels (Komatsu and Baker, 1994) has shown them to generally have the same ratio of meander wavelength to channel width as terrestrial rivers. The surface temperature on Venus precludes the presence of water and an alternative origin must be sought. As volcanism has played a primary role in shaping the venusian surface, the most likely explanation for the channels seen is that they were formed by low viscosity lava (Baker et al., 1992; Gregg and Greeley, 1993; Komatsu et al., 1993). Baker et al. (1992) classify the different types of channel into four groups, simple, complex, compound and integrated.

Simple channels are characterised by consisting of one single main channel with very few, if any, branches. Simple channels can be divided into two subcategories, sinuous rilles and canali.

Sinuous rilles appear morphologically similar to their lunar counterparts. They consist of a single channel which narrows and shallows towards its terminus. They often originate from roughly circular depressions which may represent the drained source vent for the lava which formed them. They tend to be several tens to hundreds of kilometres long and about 1 - 2 km wide. Sinuous rilles are widely distributed globally (Komatsu et al., 1993) with approximately half of them being associated with coronae type structures suggesting that the formation process for the sinuous rilles may be closely related to coronae evolution i.e. with mantle plumes. They have been interpreted as erosional features by Komatsu et al. (1993).

Canali type channels are arguably the most impressive because they are relatively long. The largest mapped canale is approximately 6800 km long (Baker et al., 1992). Canali tend to be larger and longer than sinuous rilles and whilst they too consist of a main channel it is not uncommon for them to contain subsidiary channels which branch off the main one. Unlike sinuous rilles a canale tends to maintain a relatively constant width (of roughly 1 - 5 km) throughout its entire length. Baker et al. (1992) propose an erosional origin for the canali where as Gregg and Greeley (1993) argue that they were formed by constructional processes. Canali are concentrated in several plains regions including southern Guinevere Planitia, Helen Planitia and the plains north of Rusalka Planitia. A detailed study of canali located in an area south east of Aphrodite Terra and to the east of Artemis Chasma is described in chapters 3 and 4 of this thesis.

Complex channel structures consist of a number of interlinked channels making up an anastomosing or braided pattern. The individual channels, often separated by radar bright "islands", tend to be about 3 km wide whilst the width of the complex feature as a whole is of the order of 20 to 30 km. Complex channels are up to 100 km in length. Complex channels are widely distributed on the venusian surface, partly due to the circumstances under which they occur. Channels emanating from the fluidised ejecta blanket of craters tend to be of the complex type, as do channels located on flow deposits.

Compound channels consist of both simple and complex sections. Compound channels tend to be simple initially, forming in mountainous areas and thus being topographically constrained, becoming complex when the channel reaches a plains region. There are often significant flow deposits along the channel's length or at the terminus. There is a large width variation along the length of a compound channel, with widths ranging from tens of kilometres in complex regions down to the limit of Magellan resolution for the simple parts. Only a handful of compound channels have been found (Komatsu et al., 1993) and thus a study of global distribution is not possible.

Integrated channel networks consist of a main channel with small tributary channels at right angles to it. They differ from the other types of channel described in that it is hypothesised that they weren't formed by lava flowing down a slope (Baker et al., 1992). Instead it is mooted that they have formed by the undermining and subsequent collapse of surface material by the extrusion of low viscosity subsurface lava. Some valley networks are associated with coronae structures. Here magma rises up through fractures already present, thermal and mechanical erosion occurs enlarging the structure, and then sapping occurs leaving the features as they are today.

2.2.2.2 Channel Forming Fluids.

There are a number of candidates for fluids that may have formed the channels seen on the venusian surface. Criteria for the physical properties of any formational fluid can be determined from the morphologies of the channels. Many of the channels have features associated with rivers on Earth. Whilst it is extremely unlikely that water has played any role in the formation of the venusian channels it is likely that the fluid that did had certain aqueous properties such as a low viscosity. Some channels appear to have been roofed over at points along their length and therefore must have been formed by a fluid with a solidification temperature greater than the ambient venusian temperature. It is unlikely that one fluid is responsible for all the different types of channel. Indeed it may be that each individual type of channel has its own unique lava composition. A description of possible lavas is shown below.

Silicate lavas are common on Earth but channels of the canali type seen on Venus are not. This is because the commonest lavas on Earth are basalts which have a high silicate content and are therefore too viscous to produce channels of the type seen on Venus. It is likely that if silicate lavas are responsible for venusian channels then they will be exotic ultramafic or highly alkaline mafic lavas such as komatiite or picrite in order to have the low viscosity required. Another possibility are high Fe-Ti lunar type basalts which have a viscosity one or two orders of magnitude smaller than terrestrial basalts. Komatiite lavas are an attractive proposition for a number of reasons. They have relatively very high eruption temperatures, ~1850 K, low viscosities (Huppert at al., 1984), and there is field evidence of komatiite flows eroding the substrate on which they were flowing (Huppert and Sparks, 1985). One problem with komatiites forming

that
venusian channels is that as they are so hot they will cool quickly and therefore extremely high eruption rates are required.

Sulphur volcanism is very common on the Galilean satellite Io. However despite sulphur being abundant on Earth there has been very little sulphur volcanism on Earth, due to the Earth's crust and mantle being depleted in the element (Baker at al., 1992). The venusian crust and mantle may also be depleted in sulphur; however the venusian atmosphere contains abundant sulphurous gases and the Venera landers discovered several weight percent of sulphur in surface samples. Sulphur exhibits a wide range of viscosities from the viscosity of water to that of tholeiitic basalt, the viscosity being a function of both temperature and degree of polymerisation. Sulphur could form on the surface of Venus from the melting of sulphides such as pyrite. Sulphur has a solidification temperature of about 388 K and therefore a sulphur flow on Venus would be similar to water flowing on Earth in the sense that it would have a cut and carry role, depositing any material accumulated during the flow at the end of the channel. Clearly sulphur could not have formed any of the channels which display roofing.

Carbonatite lavas are locally abundant on Earth, the most famous occurrence probably being the carbonatite volcano Oldoinyo Lengai in Tanzania (Dawson et al., 1968). Carbonatites have a low viscosity, an eruption temperature of about 863 K and a solidification temperature approximately equal to 753 K (Pinkerton et al., 1990). As the melting temperature is just above the ambient temperature on Venus it is possible for carbonatite flows to remain fluid for a long time, producing long channels, but equally solidification to form a crust on the surface of the flow is also possible. Gregg and Greeley (1993) stated that, like sulphur, carbonatites have melting temperatures below the ambient venusian temperature but according to Treiman (1994) they used incorrect values. There is field evidence for carbonatite flows eroding their substrate, particularly close to

the source (Pinkerton et al., 1990). Kargel et al. (1994) state that carbonatite lava could heve produced many of the features one associates with canali.

2.3 Thermal Erosion Models.

Several mathematical models have been published to look at thermal erosion by lava. Early models were developed to try to understand the origin of lunar sinuous rilles (Hulme, 1973; Carr, 1974). Later models have considered erosion on Earth (Huppert et al., 1984) and Venus (Gregg and Greeley, 1993).

2.3.1 Hulme (1973).

Hulme (1973) proposes that the low viscosity of lunar high Fe-Ti basalts resulted in turbulent lava flows on the surface of the moon. The erosion process is treated as being similar to the ablation process described in Osizik (1968). The erosion rate is given by

$$\frac{h(\theta_l - \theta_m)}{\rho L} \cdot \frac{N}{(1+N)} \tag{2.1}$$

where h is the heat transfer coefficient and N is a ratio of the heat required to melt the substrate to the heat required to raise the substrate from it s initial temperature to the melting temperature:

$$N = \frac{L}{c(\theta_m - \theta_s)} \tag{2.2}$$

where c is the specific heat capacity of the substrate. A full list of notation for the equations used can be found at the beginning of the thesis (p18). The value used in the model for the heat transfer coefficient is an empirical one for turbulent flow in a pipe:

$$h = 0.023\frac{k}{D}\mathrm{Pr}^{0.4}\,\mathrm{Re}^{0.8} \qquad (2.3)$$

where Pr is the Prandtl number for the flow, Re is the Reynolds number and D is the diameter of the pipe. Hulme (1973) states that in a turbulent flow the temperature of the interface between the lava and the ground may be above the solidus temperature of the ground and that therefore some of the rock will be partially melted. This newly melted rock will be removed and mixed with the flowing lava.

2.3.2 Carr (1974).

Carr (1974) considers thermal erosion by lava in laminar flows on the moon. His model consists of solving the two dimensional heat equation

$$\frac{\partial^2\theta}{\partial x^2}+\frac{\partial^2\theta}{\partial y^2}-\frac{1}{k}\frac{\partial\theta}{\partial t}=0 \qquad (2.4)$$

by applying a standard relaxation technique. The channel dimensions are defined at the beginning of a run. The temperature of all points within the channel are set equal to the lava temperature, with that of the rest of the substrate being set to 0°C. The other boundary condition is that the surface of the substrate which is not part of the channel is maintained at 0°C for the whole of a run.

Erosion is simulated by replacing any point that reaches a yield temperature with a point equal to the lava temperature. This is meant to represent material on the channel boundary being raised to the yield temperature and incorporated into the lava stream. The model assumes that the whole eroded cavity is maintained at the lava temperature when in fact as the lava eroded down into the substrate, unless there was an increase in the eruption rate, the upper part of the walls would no longer be in contact with the lava and would therefore cool. Latent heat effects are simulated by using a higher value for the specific heat capacity, and hence a lower value for the thermal diffusivity, when the temperature is in the solidus - liquidus range.

The results from the runs done by Carr showed that the erosion rate was very sensitive to the difference between the lava temperature and the temperaature at which the substate yields. Carr (1974) concludes that large amounts of thermal erosion is possible assuming long enough eruption durations as he predicts erosion rates of the order of a few meters a year.

2.3.3 Huppert et al. (1984).

Huppert et al. (1984) consider the emplacement of turbulent komatiite flows. They quote an erosion rate of

$$\frac{h(\theta_l - \theta_m)}{\rho[c(\theta_m - \theta_s) + L]} \qquad (2.5)$$

This is the same as the equation used by Hulme (1973), simply expressed in a different way. The same expression for the heat transfer coefficient (Eqn. 2.3) is also used. They use the Hulme model combined with a model for magma ascent

to investigate the sensitivity of the erosion process to different effusion rates, which they find to be relatively small.

2.3.4 Gregg and Greeley (1993).

A recent investigation by Gregg and Greeley (1993) uses the following relation for the erosion rate of the underlying rock:

$$\frac{\left[\frac{k_s(\theta-\theta_s)}{\sqrt{\alpha_s \pi t}}\right]}{\rho_s\left[c_s(\theta_m-\theta_s)+L_s\right]} \tag{2.6}$$

where $k_s, \rho_s, L_s, \theta_m$ are the thermal conductivity, density, latent heat and melting temperature of the substrate respectively. The numerator is a derivative of

$$\frac{\theta-\theta_s}{\theta-\theta_{surf}} = \text{erfc}\frac{x}{2\sqrt{\alpha t}} \tag{2.7}$$

which is the solution to the semi-infinite substrate conduction problem (Section 5.3.1). The numerator represents the rate at which energy enters a semi-infinite solid. The denominator is the amount of energy required to melt one metre of rock. The ratio represents an erosion rate. This equation is based on several simplifying assumptions. A significant one is that no allowance is made for the fact that, once the melting temperature is reached, the temperature remains constant whilst latent heat is supplied. This affects the heat flux into the ground. The rock temperature is now lower than the temperature used in (2.6) and hence the conduction rate is higher. Gregg and Greeley (1993) conclude that thermal erosion will be greater on Earth than on Venus due to the greater temperature difference between the lava and the ground causing a higher heat transfer rate.

Chapter 3
Morphometric Analysis of Canali

3.1 Introduction.

A preliminary global study of the venusian surface by Baker et al (1992) and Bussey and Guest (1992) indicated an unusually high density of channels in a region roughly 30° latitude by 30° longitude to the south east of Aphrodite Terra and to the east of Artemis Chasma. It is defined by the 150 and 180° lines of longitude and the 30 and 60° lines of latitude. An initial study, using SAR photo products, indicated the presence of approximately twelve channels, of the type referred to as canali by Baker, in this region. A map of these channels is shown in Figure 3.1.

Utilising Magellan data in both photographic and digital form, this chapter describes the study undertaken of these channels, including the measurements taken. If a channel extends beyond the boundary of the region being considered, its entire length is still mapped. An analysis of these data is presented in Chapter 4.

3.2 Method.

The research described in this chapter was carried out on a Sun Sparc 1+ and on several different types of Apple Macintosh. On the Sun the primary piece of software used was Gipstool written by Dr. Peter Ford at MIT. Gipstool is an image processing software package which enables both MIDRs and GTDR data to be viewed. On the Macs an image processing package called Image was used.

Figure 3.1 A map showing the positions of the channels studied.

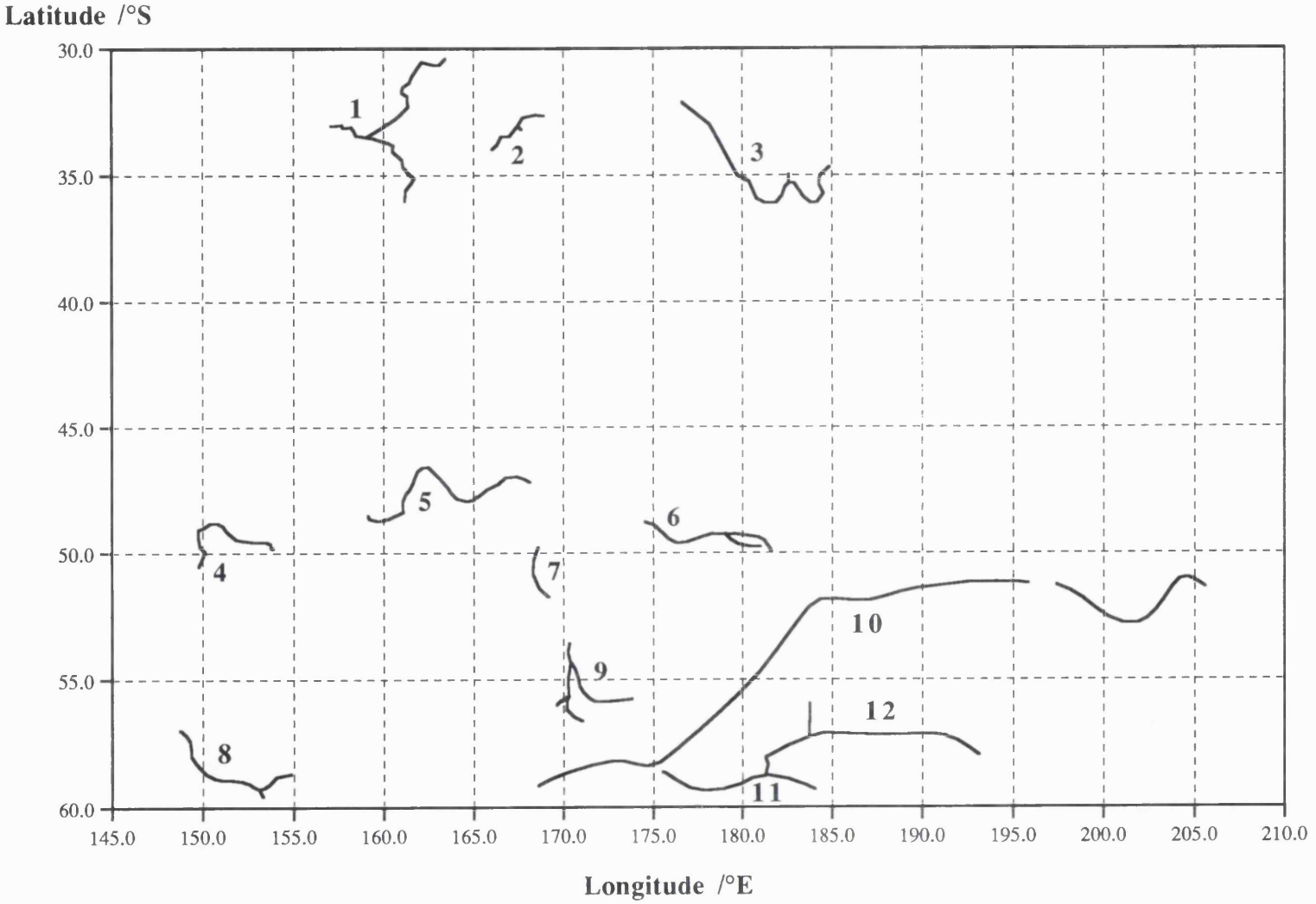
Latitude /°S
30.0
35.0
40.0
45.0
50.0
55.0
60.0
145.0
150.0
155.0
160.0
165.0
170.0
175.0
180.0
185.0
190.0
195.0
200.0
205.0
210.0
Longitude /°E
1
2
3
4
5
6
7
8
9
10
11
12

This is public domain software written by Nih. Gipstool and Image were used in tandem because each has advantages and disadvantages. Image is easier to use for general viewing, whilst Gipstool has certain unique features such as the ability to change the projection of an image. Another advantage of Image is that it has a Macro programming language, similar in syntax to Pascal, which enables quite complex tasks to be carried out quickly and easily.

Several small programs were written to facilitate the taking of measurements off the MIDRs. The simplest and most useful of these is a Macro for Image called 'Grid'. This overlaid on top of a browse image being displayed a grid consisting of 56 numbered boxes, each one 128 pixels squared. Each square shows the region covered by the individual framelets that make up the MIDR. The reason for doing this is to be able to see quickly which framelets correspond to areas of interest. Figure 3.2 shows the result of using Grid on a browse image. A listing for Grid can be found in Appendix A.

During the initial part of this study the only computer available was the Sun, and one problem with Gipstool is that it is not possible to make measurements off the screen of parameters such as channel length, etc. Therefore it became necessary to print out images and take measurements off them. A full description of how this was achieved is given in Appendix B.

The quality of the printouts is sufficiently good to allow measurements to be taken directly off them, using a moving wheel measuring device. Due to the lower resolution of the printouts compared with the digital image, there are some points on the printout where it isn't clear where the channel is which is why it is necessary when making measurements to have the relevant image up on the screen at the same time. Several printouts are shown in Appendix B.

Figure 3.2 Part of a browse image showing the result of running the macro 'Grid'.

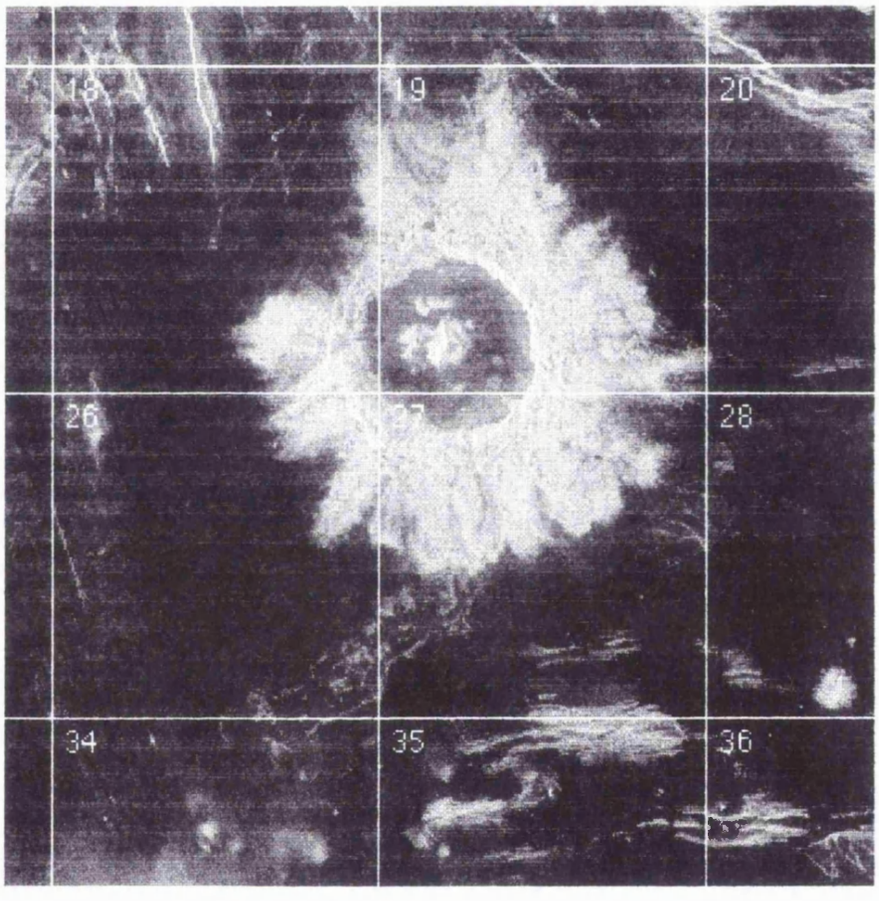
18
19
20
26
28
34
35
36

In order to take measurements off the printouts it is necessary to calculate the scale of the hard copy images. Each printout is 181 mm by 181 mm. Each F-MIDR framelet consists of 1024 pixels by 1024 pixels at a scale of 75 m per pixel. Therefore each framelet covers an area 76.8 x 76.8 km. The scale of the print out is 4.24 km cm^{-1}. Similarly the scale of a C1-MIDR framelet is 12.72 km cm^{-1}.

3.3 Radar Interpretation.

As explained in Chapter 1, interpretation of Magellan data is based on the oblique incident angle of the radar, which results in an association of characteristic signatures with specific geometries for channels running in a north-south direction. It is assumed that a bright radar return indicates the presence of a slope facing the incident radar, whilst a dark return implies one which is facing away. Hence channels with no raised levees are characterised by light and dark returns from the Eastern and Western banks respectively, during a left looking Magellan orbit. This is interpreted as indicating an erosional profile as shown in Figure 3.3. Alternatively, if levees of any magnitude are present, they show in the radar as bright returns from both sides of the channel (Figure 3.4). It is important to note that whilst the presence of levees is clear indication that constructional processes were involved, they in themselves do not necessarily reflect an ending of erosion, as the floor of the channel in Figure 3.4 could be above or below the level of the surrounding ground.

Figure 3.3 A diagram to show how a channel having a dark/light radar return is interpreted as having an erosional profile.

Figure 3.4 A diagram to show how a channel having a light/light return is interpreted as having levees.

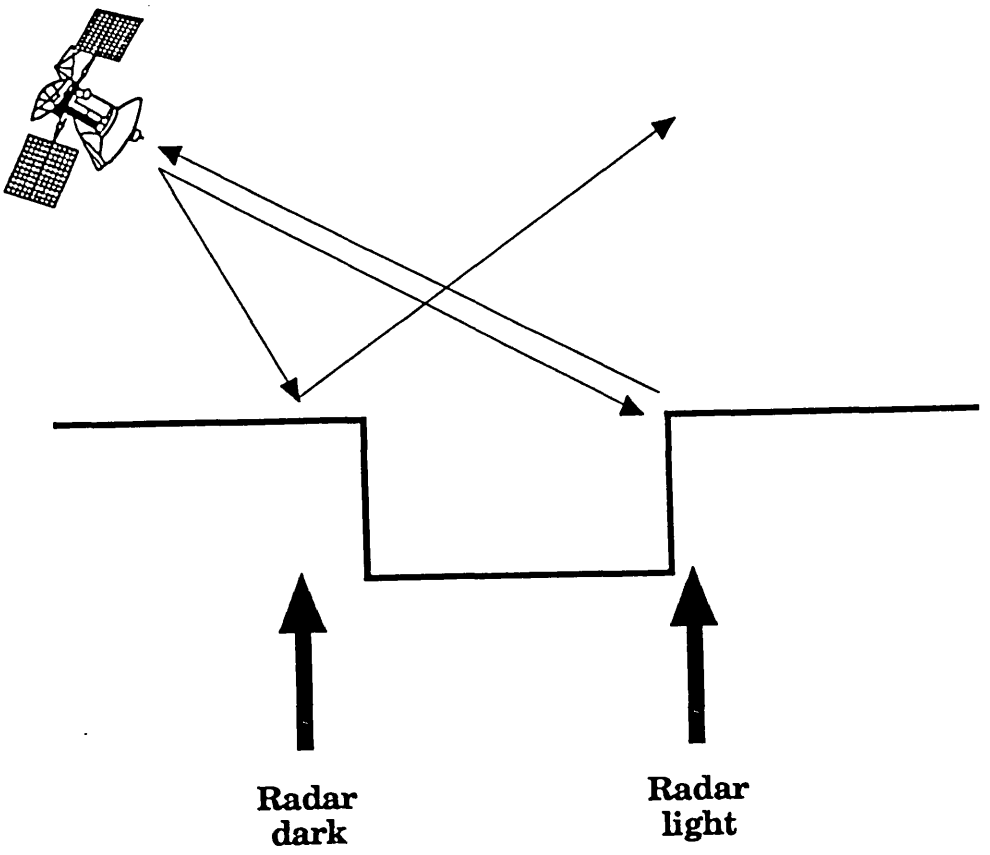
Radar
dark
Radar
light

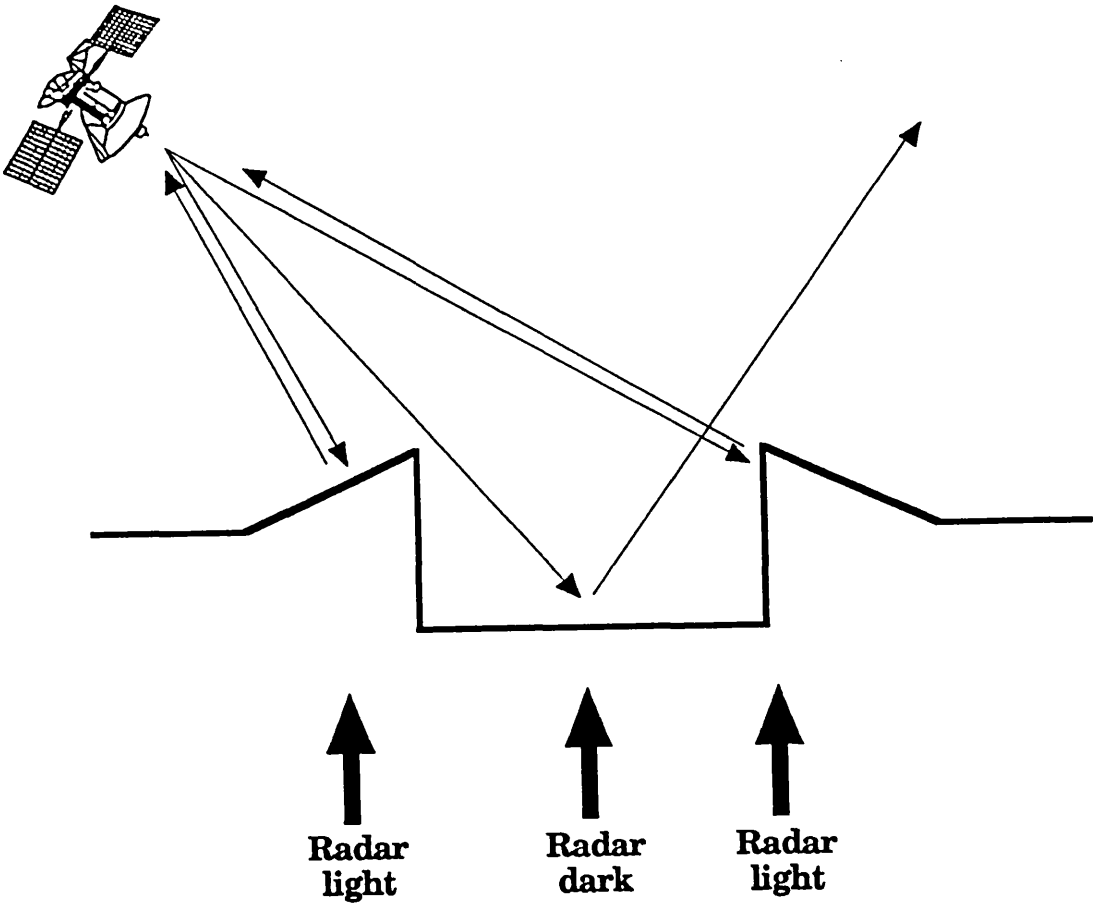
Radar
light
Radar
dark
Radar
light

3.4 Measurements.

Measuring the parameters of the channels in the region chosen for study involved the following procedure.

1. Obtaining which of the MIDR's framelets were relevant.
2. Printing these out, as described in Appendix B.
3. Taking measurements off the hard copy at the same time referring to the digital image of the framelet on a screen.

Where a framelet contained only a small section of straight channel, the measurement was obtained directly from the digital product using the software's measuring tool. When this occurred no measurement is shown in the Distance/cm and Average/cm columns of the tables showing channel measurements. Table 3.1 lists the framelets for all the channels considered.

Channel section lengths taken off the hardcopy were obtained using a rolling wheel measuring device. This allowed lengths to be measured to the nearest 0.5 cm. Each section was measured 3 times in order to try to reduce any errors. This resulted in an error for the average length of a section of $\frac{0.5}{\sqrt{3}}$ cm, corresponding to an error of 1.2 km on a F_MIDR framelet and 3.7 km on a C1_MIDR framelet. Thus the total error associated with a channel depends upon the number of framelets making up its whole length. For example, if the measurements for a particular channel were taken off 2 C1_MIDR framelets and 4 F_MIDR framelets then the error in the value for the length of the whole channel is

$$\sqrt{3.7^2 + 3.7^2 + 1.2^2 + 1.2^2 + 1.2^2 + 1.2^2} \qquad (3.1)$$

or 5.8 km. A treatment of errors associated with measurements can be found in Bevington (1969).

Table 3.1 A list of MIDRs and framelets containing channels.

Channel	MIDR	Framelets	CD
1	C1_30S153	38,46,47	22,91
	F_35S157	5,6,14,15,16,8	76,105
	F_35S163	9,17,18,26,27,34	23,102
	F_30S161	53,45,44,37,38,39	23,109
2	C1_30S171	35,42,43	31,91,99
	F_35S163	16,24,23	23,102
	F_35S170	9,1,2,3	76,102
3	C1_30S171	39,47,48,56	31,91,99
	C1_30S189	50,42,51,43	31,91
4	C1_45S159	43,42	22,92,116
	F_50S147	16,24,23,31,39	76
5	C1_45S159	39,38,37,45,44	22,92,116
6	C1_45S180	43,44,45	69,92,99
	F_50S180	17,26,18,19,20,21,22,28,29,30	76
7	C1_45S159	47,55	22,92,116
8	C1_60S153	20,28,29,21	22,95
9	C1_60S180	2,10,18	33,95
	F_55S171	3,11,12,20,28,29,35,36,37,38,39,43 ,44,45,46	77
10	F_60S164	24	63
	F_60S175	9,10,11,3,12,13,14,6	77,94
	F_55S180	50,42,43,35,36,37,29,30,22,14,15,7	77
	F_50S180	55,56,48	76
	F_50S188	41,42,50,51,43,44,45,46,47,48	76
	C1_45S202	50,51,52,53,54	31,92
	C1_60S208	2,3	34,95
11	C1_60S180	29,28,27,21	33,95
	F_60S185	28,20,19,10,9,17	77,76
	F_60S175	16,24,23,22,21,13	77,94
12	C1_60S180	23,22,21	33,95
	F_60S185	10,2,3	77,76
	F_55S180	54,55,56	77

The detailed measurements from each framelet for each channel are shown below, followed by a description of the channel. F-MIDRs are used in preference to C1-MIDRs. No assumptions are made about the flow direction of the medium which formed the channel. This will be discussed in chapter 4 along with the topography measurements.

3.4.1 Channel 1

Midr/ Framelet	Distance/cm	Average/cm	Distance/km
F_35S157 / 05	20.0, 19.5, 21.0	20.17	85.5
F_35S157 / 06	26.5, 26.0, 26.5	26.33	111.5
F_35S157 / 14	5.0, 4.0, 4.5	4.50	19.0
F_35S157 / 15	42.0, 42.0, 42.0	42.00	178.0
F_35S157 / 16	22.5, 22.5, 22.5	22.50	95.5
F_35S163 / 09	10.0, 10.0, 10.0	10.00	42.5
F_35S163 / 17	8.0, 8.0, 8.0	8.00	34.0
F_35S163 / 18	15.5, 15.5, 15.5	15.50	65.5
F_35S163 / 26	21.0, 20.5, 20.0	20.50	87.0
F_35S163 / 27	3.0, 3.0, 2.5	2.83	12.0
F_35S163 / 34	18.5, 18.5, 18.5	18.50	78.5
F_35S157 / 16	13.0, 13.0, 13.5	13.17	56.0
F_35S157 / 08	8.0, 7.5, 7.5	7.67	32.5
F_35S163 / 01	17.5, 17.5, 17.5	17.5	74.0
F_35S163 / 02	2.0, 1.5, 2.0	1.83	8.0
C1_30S153 / 39	1.5, 1.5. 2.0	1.67	21.0
C1_30S153 / 40	2.5, 2.5, 2.5	2.5	32.0
F_30S161 / 53	8.5, 9.0, 8.5	8.67	36.5
F_30S161 / 45	18.5, 18.0, 18.5	18.17	77.0
F_30S161 / 44	5.5. 5.0, 5.5	5.33	22.5
F_30S161 / 37	14.5, 14.0, 14.0	14.17	60.0
F_30S161 / 38	20.0, 20.0, 20.0	20.0	85.0
F_30S161 / 39	9.0, 8.5, 9.0	8.83	37.5

Table 3.2. Measurements for channel 1.

One end of the channel appears to originate from a graben like feature situated at 157.08°E 33.05°S. For the first 248 km the channel meanders and has an erosional profile. Then at 158.75°E 33.47°S the channel encounters a fault and appears to branch. One branch heads off in a north-east direction (and will be considered later) whilst the other branch continues in a south easterly direction and appears to form a lava tube 21 km long (Figure 3.5). On reappearing the channel again has an erosional profile, although now there is evidence for a certain amount of overflow on the banks of the channel, in the form of slightly lighter radar returns. The channel continues to meander in a predominantly east-west direction for another 185 km to 160.60°E 33.82°S whereupon the channel veers southwards. Over the next 19 km, the channel is bounded by levees but at 160.66°E 34.08°S the channel roofs over once again to form a lava tube, some 61 km in length. At 161.16°E 34.42°S, a leveed channel re-emerges for 24 km whereupon it roofs again, at 161.20°E 34.66°S, for a distance of 47 km. The channel then remains simply a leveed channel for a further 82 km until 161.38°E 35.60°S, where it either roofs again or possibly has failed to drain for 45 km terminating at 161.23°E 36.01°S (Figure 3.6). The total length of the channel is 745.5 ± 6.0 km. The width of the channel stays fairly constant throughout the whole length of the channel, being measured directly off the digital products as 9 to 10 pixels or ~ 700 metres.

The second branch of the channel originates at a fracture at 158.64°E 33.38°S. This channel extends north-eastwards for 159 km until 160.27°E 32.99°S where it appears to have roofed over for a distance of 53 km before reappearing at 160.70°E 32.77°S. The channel then becomes very difficult to identify as it passes through a region of intense fractures/ridges. Where it is possible to make out any detail there is evidence for levees. There is then intermittent evidence for levees and erosion until the channel again roofs over at 162.89°E 30.70°S, for 25 km,

(This page) Figure 3.5 A section of F_35S157 showing the first part of channel 1. The channel has a meandering profile and a dark/light radar return from which an erosional cross-sectional profile is inferred. The figure also shows the channel branching at a fracture. The area covered is approximately 143 km x 255 km. North is to the left.

(Next Page) Figure 3.6 A length of channel 1 consisting of leveed sections and regions where the channel appears to have roofed over. The figure is from F_35S163 and covers an area roughly 180 km x 255 km. North is to the top.

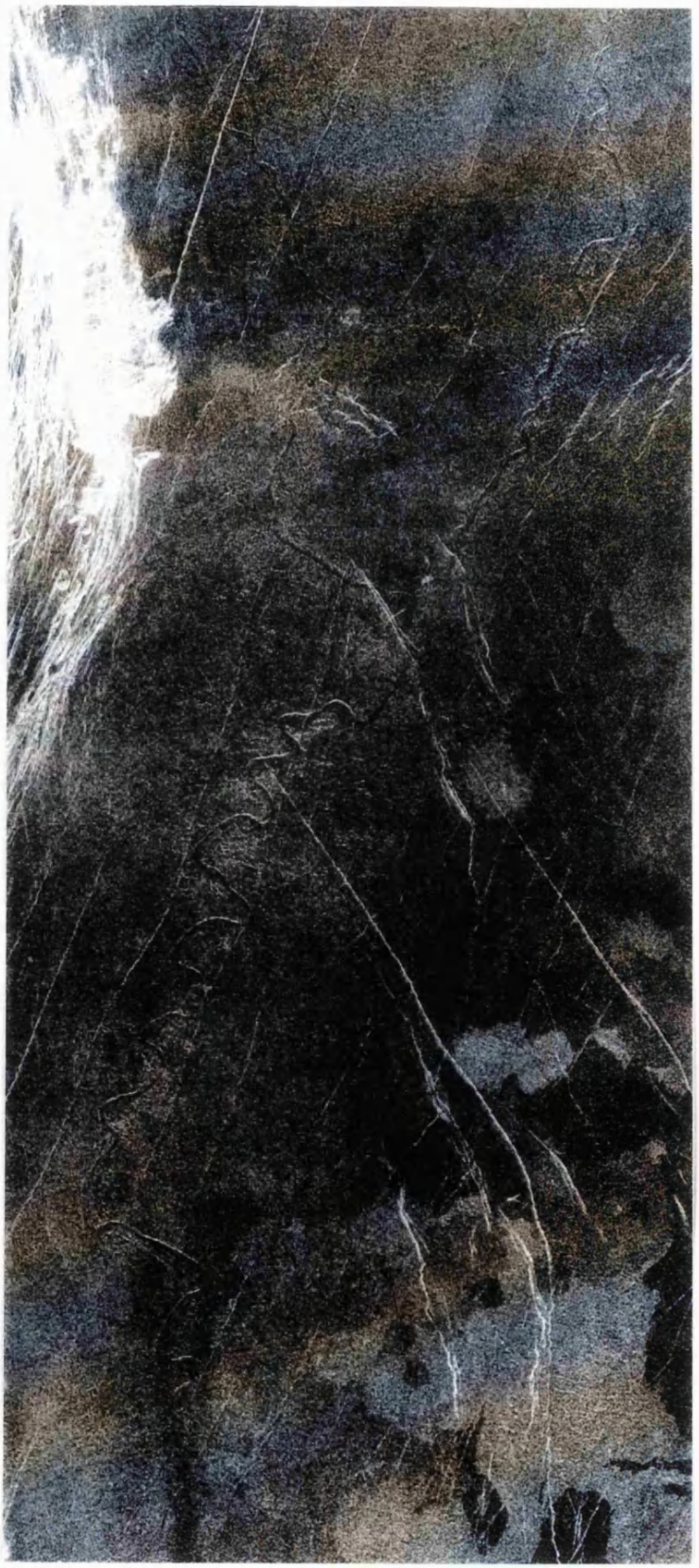

becoming visible again at 163.15°E 30.67°S, for 36 km before ending at 163.44°E 30.45°S. The total length of this branch of channel 1 is 614 km.

3.4.2 Channel 2

Midr/ Framelet	Distance/cm	Average/cm	Distance/km
F_35S163 / 23			5.5
F_35S163 / 24	2.5, 2.5, 2.5	2.5	10.5
F_35S163 / 16	21.5, 21.5, 21.5	21.5	91.0
F_35S170 / 09	14.5, 14.0, 14.0	14.17	60.0
F_35S170 / 01			8.0
F_35S170 / 02	23.5, 22.5, 23.0	23	97.5
F_35S170 / 03	11.5, 11.5, 11.0	11.33	48.0

Table 3.3. Measurements for channel 2.

The SW end of the channel terminates at a fracture. The exact position is unclear but is approximately at 166.03°E 33.99°S. For the initial 5 km of its length the channel is rather indistinct. The channel then runs fairly straight for 64 km, with the evidence for levees becoming progressively more pronounced. At 166.40°E 33.61°S the channel briefly becomes topographically constrained by a fracture. The channel, which takes on an increasingly erosional profile, then meanders for 150 km, (with a possible fork at 108 km) before turning E - W at 167.77°E 32.73°S (Figure 3.7). The channel then proceeds in a E-W orientation for a further 57 km, leading into a meander which appears weakly erosional. For most of this longitudinal traverse, determination of the channel's cross-sectional profile is difficult. At 168.61°E 32.67°S there is evidence to suggest that either the channel has formed a tube or failed to drain free of liquid. It remains like this for some 25 km, terminating at 168.93°E 32.66°S. At this terminus there appears to have been a substantial outflow of liquid from the channel (Figure 3.8). The total length of the channel is 320.5 ± 2.5 km. The SW region of the channel retains a fairly constant width of approximately 1.5 km, but gradually narrows to ~750m in the NE section.

(This page) Figure 3.7 The early reaches of channel 2 showing where it is topographically constrained by a fracture and where it turns sharply east-west. The figure is from F_35S163 and shows an area approximately 128 km square. North is to the top.

(Next Page) Figure 3.8 Part of F_35S170 showing the eastern region of channel 2, including a possible flow from the end of the channel. The area shown covers 143 km x 255 km. North is to the left.

3.4.3 Channel 3

Midr/ Framelet	Distance/cm	Average/cm	Distance/km
C1_30S171 / 39	14.0, 14.0, 14.0	14	152
C1_30S171 / 47	15.5, 15.5, 16.0	15.67	199
C1_30S171 / 48	8.5, 9.0, 8.5	8.67	110
C1_30S171 / 56	14.0, 14.0, 14.0	14	152
C1_30S189 / 50	13.5, 13.5, 13.0	13.33	169
C1_30S189 / 42	4.0, 4.0, 4.0	4	51
C1_30S189 / 51	9.0, 9.0, 9.0	9	114
C1_30S189 / 43	6.5, 7.0, 7.0	6.83	87

Table 3.4. Measurements for channel 3.

One end of the channel originates at a fracture 176.62°E 32.11°S. From here the channel meanders in a south easterly direction for 340 km, and appears to be erosional, although the lower resolution makes this hard to determine in places. The channel appears to have roofed over at 179.81°E 35.01°S for a length of 70 km, but subsequently gives way to a leveed channel. Within the tubed region, radar bright and flow feature structures occur in the regions adjacent to the roofed channel. These may be analogous with overflow occurrences from actual lava flows which have been observed on Earth. The channel continues to be leveed for 67 km but then disappears at 180.95°E 35.87°S for a distance of 70 km. On reappearing the channel turns eastwards before looping back up in a northerly direction. Along this northerly section the channel appears erosional. The channel then loops around 180° and heads off in a south-easterly direction. At the northern tip of the loop, 182.66°E 35.30°S, there is either a fork or a tributary.

The channel runs SE for 112 km. Within this stretch there are signs of overflow on the banks in the form of radar bright patches. Levees are visible

towards the end of this section. The leveed channel then turns eastwards for 27 km before veering northwards for the remaining 175 km. The terminus of the channel is not absolutely clear but appears to be at 184.89°E 34.70°S. As only C1-MIDR coverage is available for this channel, it is not possible to make an accurate assessment of it s width. However the channel does appear to remain at a constant width throughout it s length of 4 to 5 pixels which corresponds to an actual width of about 1 km. The total length of this channel is 1034 ± 10 km.

3.4.4 Channel 4

Midr/ Framelet	Distance/cm	Average/cm	Distance/km
C1_45S159 / 43	8.5, 8.0, 8.0	8.17	104
C1_45S159 / 42	11.0, 10.5, 10.5	10.67	136
F_50S147 / 16	15.0, 15.0, 15.0	15.0	63.5
F_50S147 / 24	6.0, 6.0, 6.0	6.0	25.5
F_50S147 / 23	18.0, 17.5, 17.5	17.67	75.0
F_50S147 / 31	18.5, 18.5, 18.5	18.5	78.5
F_50S147 / 39	4.0, 4.0, 4.0	4.0	17.0

Table 3.5. Measurements for channel 4.

One end of the channel appears to start from a network of fractures at 153.84°E 49.85°S. From here the channel trends north-westwards, and appears to have an erosional profile. There is then a section of tubing. The re-emergence of a channel profile coincides with a directional change in the trend of the channel from east to west. At 151.76°E 49.43°S the channel returns to a north-westward trend and appears erosional. At 150.79°E 48.81°S the channel turns eastwards for 42 km before turning SW at 150.26°E 48.92°S. It appears to form a lava tube at 150.10°E 48.99°S for 15.5 km. On reappearing the channel is indistinct for the remaining 170.5 km of it s length. It ends at 149.77°E 50.52°S, where there is a small outflow of lava (Figure 3.9). The total length of the channel is 499.5 ± 3.0 km.

Figure 3.9 The western end of channel 4 including an outflow of lava from the end of the channel. The figure shows a 128 km x 263 km section of F_50S147. North is to the top of the page.

3.4.5 Channel 5

Midr/ Framelet	Distance/cm	Average/cm	Distance/km
C1_45S159 / 39	15.0, 15.0, 15.0	15.0	190
C1_45S159 / 38	24.0, 23.5, 23.5	23.67	301
C1_45S159 / 37	15.5, 15.0, 15.0	15.17	193
C1_45S159 / 45	11.5, 12.0, 11.5	11.67	148
C1_45S159 / 44			6

Table 3.6. Measurements for channel 5.

Both ends of this channel are not definite, but the western end of the channel seems to begin at approximately 159.15°E 48.48°S. From here it trends south-eastwards for 20 km with what is possibly an erosional profile. The channel then swings east until 161.05°E 48.29°S where it swings through 90° to head northwards, meandering and seeming to be erosional. The channel loops around to head south eastwards with the evidence for erosion being intermittent. The continuation of the channel eastwards is characterised by it becoming increasingly difficult to make out the channel morphology. This could be attributed to a shallowing channel bottom, which in turn could be explained by ponded lava in an undrained channel. The approximate end of the channel is 168.16°E 47.24°S, a total length of 838 ± 7 km. The entire length of this channel is shown in Figure 10.

Figure 3.10 This figure shows the whole of channel 5. North is to the left and the area shown covers 315 km x 788 km of C1_45S159.

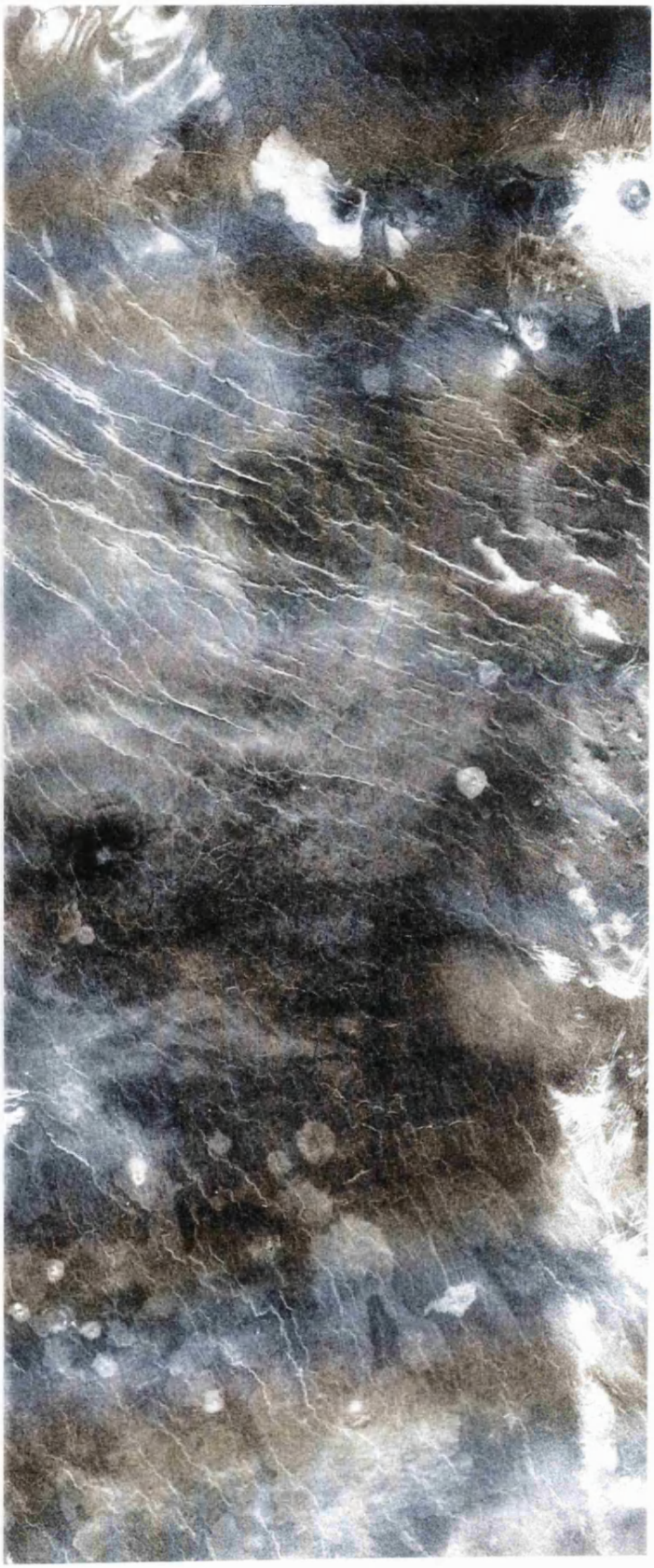

3.4.6 Channel 6

Midr/ Framelet	Distance/cm	Average/cm	Distance/km
C1_45S180 / 43	8.0, 7.5, 7.5	7.67	98
F_50S180 / 17	20.0, 20.0, 20.0	20.00	85.0
F_50S180 / 18	18.0, 18.0, 17.5	17.83	75.5
F_50S180 / 26	1.0, 1.5. 1.5	1.33	5.5
F_50S180 / 19	18.0, 18.0, 18.0	18.00	76.5
F_50S180 / 20	18.0, 18.0, 18.5	18.17	77.0
F_50S180 / 21	19.5, 19.5, 19.0	19.33	82.0
F_50S180 / 22	1.0, 1.0, 1.0	1.00	4.0
F_50S180 / 30	9.0, 9.0, 9.0	9.00	38.0
F_50S180 / 28	5.0, 5.5, 5.5	5.33	22.5
F_50S180 / 29	14.0, 14.0, 14.0	14.00	59.5

Table 3.7. Measurements for channel 6.

The end of this channel is once again indistinct but seems to occur at approximately 174.57°E 48.79°S. The most noticeable feature about this channel is that right from the point at which the channel can first be determined it has very large levees, spanning about two channel widths on either side of the channel. The channel meanders gently and trends in a predominantly east west direction. The channel branches at 179.07°E 49.30°S, with one branch continuing eastwards and the other going off in a south-easterly direction (Figure 3.11). Examination of the former branch reveals an extensive area of overflow close to the branching point, predominantly to the north of the channel. After this region the channel sides become more radar dark for a length of 78 km, which makes the morphology of the channel difficult to make out. A strong channel morphology only becomes re-established over the final 17 km of the channel with the presence of substantial levees. The channel ends at 181.65°E 49.92°S. The second branch

Figure 3.11 A 127 km x 405 km section of F_50S180 showing the eastern ends of channel 6. There is evidence for substantial amounts of overflow along the sides of this channel. North is to the left.

shows levees for the first 15 km after branching but then becomes difficult to make out until near its terminus at 180.98°E 49.77°S, where again levees can be seen. The total length of the channel is 624 ± 5 km.

3.4.7 Channel 7

Midr/ Framelet	Distance/cm	Average/cm	Distance/km
C1_45S159 / 55	11.5, 11.5, 11.5	11.5	146
C1_45S159 / 47	4.5, 5.0, 5.0	4.83	61

Table 3.8. Measurements for channel 7.

There is no distinct end to this channel, but it can be traced as far as 169.22°E 51.74°S. The channel lies in a north-south direction for a distance of 207 ± 5 km to a point which lies at 168.67°E 49.79°S, some 95 km southeast of an impact crater. The channel disappears beyond this point. As there are no obvious sources for the lava which formed this channel, it is likely that this is a section from part of an earlier, larger channel which is no longer visible due to resurfacing of the local area.

3.4.8 Channel 8

Midr/ Framelet	Distance/cm	Average/cm	Distance/km
C1_60S153 / 19			7
C1_60S153 / 20	23.5, 23.5, 23.5	23.5	299
C1_60S153 / 28	3.5, 3.5, 3.5	3.5	45
C1_60S153 / 29	10.0, 10.0, 10.5	10.17	129
C1_60S153 / 21	4.0, 4.0, 4.0	4.0	51

Table 3.9. Measurements for channel 8.

This channel starts at 148.75°E 56.99°S. It appears erosional for the first 348 km to 152.90°E 59.19°S, where the channel branches. The minor branch heads south for 45 km before terminating at 153.38°E 59.55°S, possibly being connected with a nearby lava flow. The northern branch now shows some evidence of levees before becoming indistinct. It can last be made out at 154.85°E 58.71°S. It may also be connected with a nearby lava flow. The entire length of channel 8 is shown in Figure 3.12.

Figure 3.12 A figure showing the entire length of channel 8. The area shown comes from C1_60S153 and covers approximately 360 km x 450 km. North is to the left.

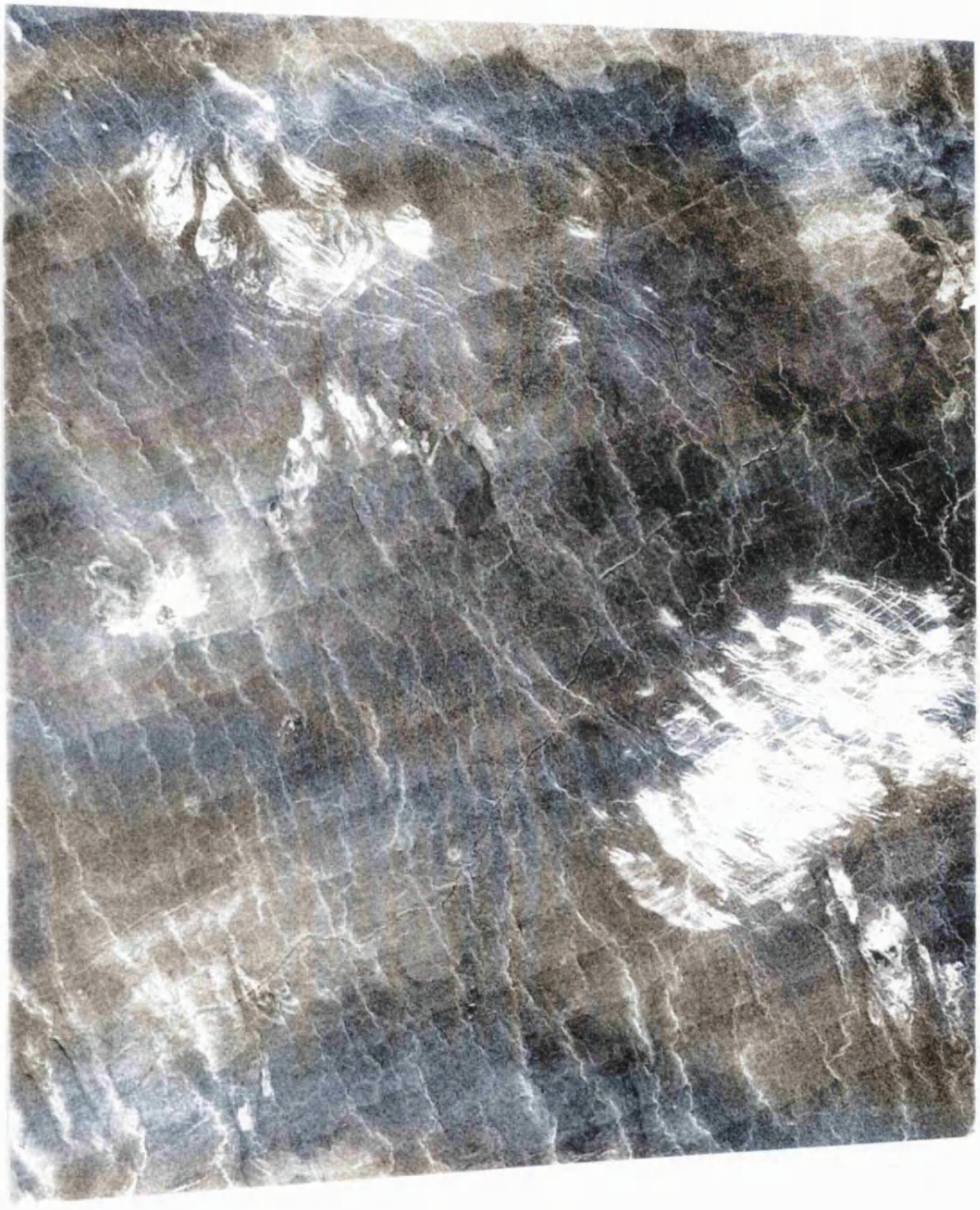

3.4.9 Channel 9

Midr/ Framelet	Distance/cm	Average/cm	Distance/km
F_55S171 / 12	7.5, 7.5, 7.5	7.5	33.0
F_55S171 / 20	26.0, 25.5, 25.5	25.67	113.5
F_55S171 / 28	39.0, 39.5, 39.0	39.17	173.0
F_55S171 / 36	28.5, 28.0, 28.5	28.33	125.0
F_55S171 / 44	12.0, 11.5, 12.0	11.83	52.5
F_55S171 / 45	3.5, 4.0, 4.0	3.83	17.0
F_55S171 / 29	2.5, 2.5, 3.0	2.67	12.0
F_55S171 / 37	24.5, 24.5, 25.0	24.67	109.0
F_55S171 / 38	19.0, 19.0, 19.0	19.0	84.0
F_55S171 / 39	4.5, 4.0, 4.5	4.33	19.0

Table 3.10. Measurements for channel 9.

The channel is first visible at 170.34°E 53.60°S. Initially it is 2 km wide, but soon narrows to 1 km. This section is fairly straight and shows evidence for erosion over the 76 km length to 170.38E 54.35°S. The channel forks at this point. Both branches of the channel appear erosional although the eastern branch is much better defined than the western one. Both branches initially run in a southerly direction, being almost parallel for 93 km. Subsequently the eastern branch turns south-eastwards whilst the other branch continues on a southerly heading until 170.26°E 55.66°S where it forks again. Associated with this branching is an area of overflow. Both branches of the channel show evidence of the existence of levees. The western branch terminates after some 64 km at 169.64°E 56.01°S whilst the eastern branch continues to be leveed for 123 km, before ending at 171.06°E 56.63°S. The original eastern branch shows a strong erosional radar return with a weak evidence for levees as well. Throughout the length of this branch there is intermittent evidence of terracing which would

indicate that the channel was produced by more than one flow event. This branch terminates at 173.83°E 55.78°S. The total length of all three sections combined is 738 ± 4.0 km. The whole of channel 9 is displayed in Figure 3.13.

Figure 3.13 An image from F_55S171 showing all 3 branches of channel 9. The size of the region covered is approximately 360 km x 428 km. North is to the top.

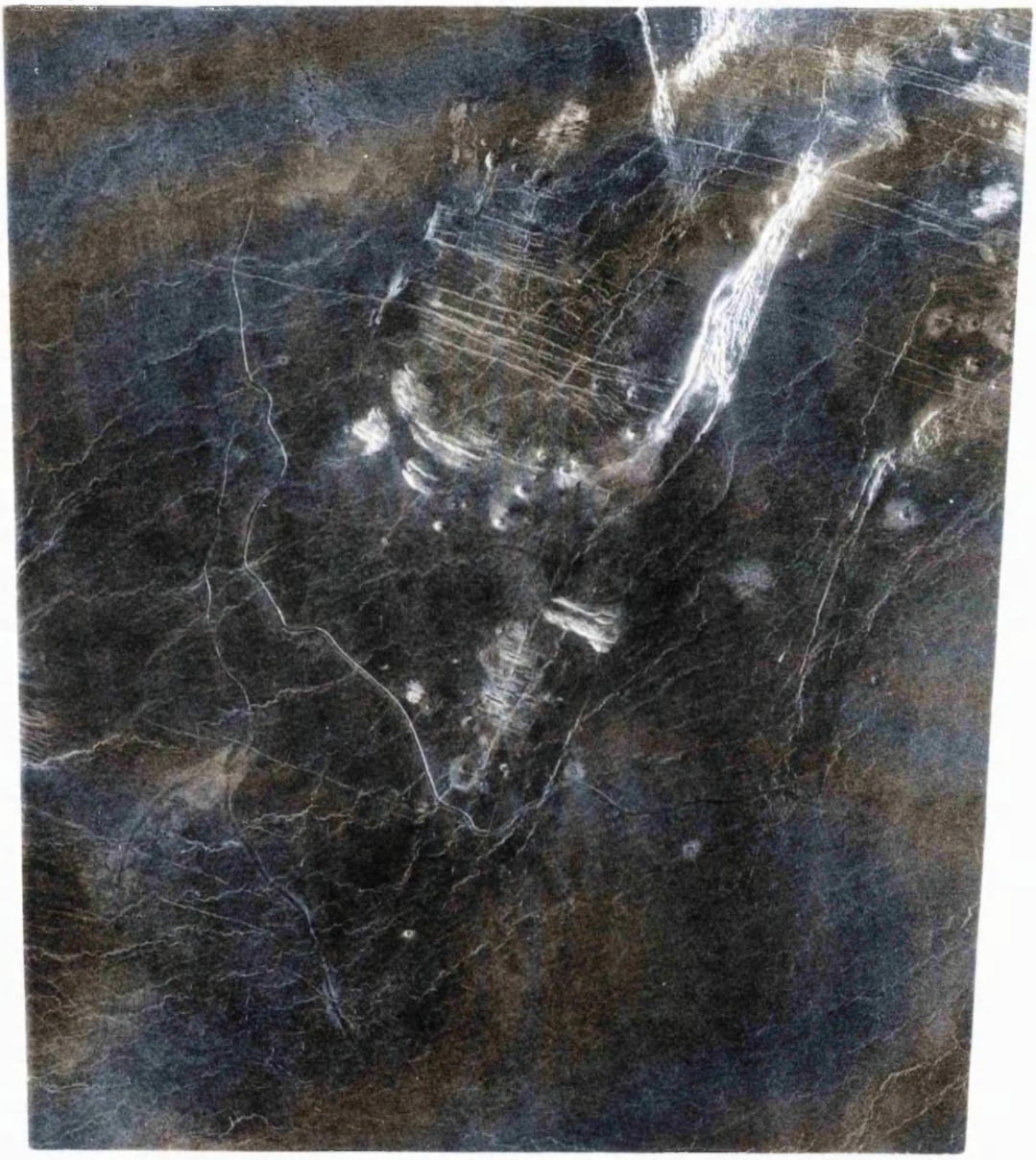

3.4.10 Channel 10

Midr/ Framelet	Distance/cm	Average/cm	Distance/km
F_60S164 / 24	13.5, 13.5, 13.5	13.5	57.0
F_60S175 / 09	19.0, 19.5, 19.5	19.33	82.0
F_60S175 / 10	18.5, 18.5, 18.5	18.5	78.5
F_60S175 / 11	15.0, 15.0, 14.0	14.67	62.0
F_60S175 / 03	3.5, 3.5, 3.5	3.5	15.0
F_60S175 / 12	18.5, 18.5, 19.0	18.67	79.0
F_60S175 / 13	25.0, 25.0, 25.0	25.0	106.0
F_60S175 / 14			4.5
F_60S175 / 06	22.0, 22.0, 22.5	22.17	94.0
F_55S180 / 50	16.5, 16.0, 16.0	16.17	68.5
F_55S180 / 42	13.5, 13.5, 14.0	13.67	58.0
F_55S180 / 43	15.5, 16.0, 15.5	15.67	66.5
F_55S180 / 35	6.0, 6.0, 6.0	6.0	25.5
F_55S180 / 36	22.0, 22.0, 21.5	21.83	92.5
F_55S180 / 37	11.0, 11.0, 11.0	11.0	46.5
F_55S180 / 29	13.5, 13.5, 13.5	13.5	57.0
F_55S180 / 30	14.0, 14.0, 14.0	14.0	59.5
F_55S180 / 22	20.0, 20.0, 20.0	20.0	85.0
F_55S180 / 14	9.5, 9.5, 9.5	9.5	40.5
F_55S180 / 15	13.0, 13.5, 13.0	13.17	56.0
F_55S180 / 07	20.0, 19.5, 19.5	19.67	83.5
F_50S180 / 55	13.0, 13.5, 13.0	13.17	56.0
F_50S180 / 56	8.5, 9.0, 8.5	8.67	36.5
F_50S180 / 48	11.5, 11.5, 11.5	11.5	49.0
F_50S188 / 41	1.5, 2.0, 2.0	1.83	8.0
F_50S188 / 42	12.0, 12.0, 12.0	12.0	51.0

F_50S188 / 50	5.5, 6.0, 5.5	5.67	24.0
F_50S188 / 51	18.5, 18.5, 18.5	18.5	78.5
F_50S188 / 52	3.5, 4.0, 4.0	3.83	16.5
F_50S188 / 44	17.0, 17.0, 17.0	17.0	72.0
F_50S188 / 45	18.5, 18.5, 19.0	18.67	79.0
F_50S188 / 46	18.5, 18.5, 18.5	18.5	78.5
F_50S188 / 47	18.0, 18.5, 18.0	18.17	77.0
F_50S188 / 48	14.0, 14.0, 14.0	14.0	59.5
F_50S188 / 40	5.0, 5.5, 5.0	5.17	22.0
C1_45S202 / 50	8.0, 8.5, 8.5	8.33	106
C1_45S202 / 51	12.5, 12.5, 13.0	12.67	161
C1_45S202 / 52	15.0, 15.5, 15.5	15.33	195
C1_60S208 / 02	5.0, 5.0, 5.0	5.0	64
C1_60S208 / 03	9.5, 9.5, 9.5	9.5	121
C1_45S202 / 53	22.0, 22.0, 22.5	22.17	282
C1_45S202 / 54	2.5, 2.5, 2.5	2.5	32

Table 3.11. Measurements for channel 10.

One end of the channel emerges from a network of fractures at 168.60°E 59.15°S. Initially there is intermittent evidence for levees and erosional characteristics until 172.69°E 58.17°S, whereupon the channel appears solely erosional. The first 414 km of the channel lies in a predominantly east-west orientation, then at 175.32°E 58.61°S the channel turns north-eastwards. Close to this point, and visible on the same framelet, is one end of channel 11 (Figure 3.14). Whilst there is no visible meeting point between the two channels the very close proximity makes a branching a distinct possibility. From here the channel meanders in a north-easterly direction, for 1000 km until 184.22°E 51.73°S. The channel retains its erosional profile and there is occasional evidence for terracing within the channel. It then turns eastwards again. Due to the orientation of the

Figure 3.14 This image shows one end of channel 11, which is only 6 km from part of channel 10. The figure comes from F_60S175 and covers an area 165 km x 240 km. North is to the left.

channel along with a higher amount of background noise, it becomes difficult to make out any channel profile data for quite large portions of the channel, but where it is available the channel appears to be leveed. The channel continues eastwards for 747 km where it disappears at 195.87°E 51.13°S. It reappears at 197.45°E 51.29°S and continues eastwards. As there is only C1_MIDR coverage of this region the channel profile becomes hard to make out in places due to the channel width being of the order of four pixels. However where it is possible to make out any detail, the channel again appears erosional. The channel loops around to the south at 201.01°E 52.96°S before becoming progressively more indistinct, and disappearing at 205.62°E 51.38°S. The total length of the channel is 2985.5 ± 12.0 km.

3.4.11 Channel 11

Midr/ Framelet	Distance/cm	Average/cm	Distance/km
F_60S175 / 13	10.0, 9.5, 9.5	9.67	41.0
F_60S175 / 21	3.5, 3.5, 3.5	3.5	15.0
F_60S175 / 22	21.5, 21.5, 21.5	21.5	91.0
F_60S175 / 23	18.0, 18.5, 18.0	18.17	77.0
F_60S175 / 24	20.0, 20.0, 19.0	19.67	83.5
F_60S185 / 09	12.5, 12.5, 13.0	12.67	53.5
F_60S185 / 10	18.5, 18.5, 19.0	18.67	79.0
F_60S185 / 19	24.0, 24.0, 24.0	24.0	102.0
F_60S185 / 20	2.0, 2.0, 2.0	2.0	8.5

Table 3.12. Measurements for channel 11.

This channel first becomes visible at 175.57°E 58.64°S. At this point it is only 6 km from channel 10 which raises the possibility that they are in fact connected (Figure 3.14). The channel appears erosional for the first 41 km and then the evidence of levees can be observed. Initially the channel lies in a southeast or easterly direction until 179.29°E 59.30°S where it turns north-eastwards. This direction change coincides with the channel again appearing to be erosional. This lasts for only 23 km whereupon faint evidence for levees becomes visible again. At 181.33°E 58.67°S the channel branches, one branch continuing eastwards and the other heading off at a right angle northwards. The northern branch is in fact the beginning of channel 12 which did not appear to join on looking at the images and so will be considered as a separate channel. The eastern branch continues to show indications of levees for a further 79 km but then, partly as a result of increased noise in the images, the channel becomes poorly defined. Alternatively, this may be due to a change in channel morphology, as when the channel can be made out clearly it appears erosional. It

possibly roofs over for the last 42 km of it s length before terminating at 184.04°E 59.33°S. The total length of the channel is 550.5 ± 3.5 km.

3.4.12 Channel 12

Midr/ Framelet	Distance/cm	Average/cm	Distance/km
F_60S185 / 10	13.0, 13.5, 13.5	13.33	56.5
F_60S185 / 02	26.5, 26.5, 26.5	26.5	112.5
F_60S185 / 03	4.5, 4.5, 4.5	4.5	19.0
F_55S180 / 55	26.0, 26.5, 26.0	26.17	111.0
F_55S180 / 47	18.0, 18.0, 18.0	18.0	76.5
F_55S180 / 39	3.5, 3.5, 4.0	3.67	15.5
F_55S180 / 56	19.5, 20.0, 19.5	19.67	83.5
C1_60S180 / 22	15.5, 15.0, 15.0	15.17	193
C1_60S180 / 23	23.5, 23.5, 23.0	23.33	297
C1_60S180 / 24	1.5, 1.5, 2.0	1.67	21

Table 3.13. Measurements for channel 12.

The channel originates as a branch from channel 11 at 181.33°E 58.69°S. The channel heads northwards and initially appears to be leveed. After about 57 km background radar noise makes the channel increasingly difficult to make out. Where detail about the channel profile can be determined the channel appears to have levees. The channel branches at 183.81°E 57.11°S. One branch goes north and the other south east. The northerly branch is 121.5 km long and is possibly leveed. It terminates at 183.82°E 55.92°S where there is an associated small flow feature. The eastern branch is 618 km long. For the majority of it s length only C1_MIDR coverage is available and that combined with the fact that it lies in a predominantly east west orientation means that it is not possible to make out a great deal of detail with regards to the channel profile. There is however periodic evidence for roughness on both banks of the channel. This branch terminates at 193.09°E 58.01°S.

Chapter 4
Determination of Emplacement Direction

4.1 Introduction.

The next step in analysing the channels in the region chosen involves determining in which direction they were emplaced. The most obvious data set to use for this purpose is the GTDR data. However there is the problem that there may have been large scale deformation of the region being considered so that the slopes that are seen now may not be the same as those that were present when the channels were formed. In order to decide on the orientation of formation it is necessary to consider the physical attributes of the channels, such as evidence for erosion or branching of the channel. Clearly it is more probable that a channel bifurcates than that two separate channels merge to form one channel. It is also likely that lava close to its source, where it is hotter, will be more capable of thermally eroding than further away where features associated with the cooling of lava such as levees and tubing may be seen. However an erosional profile is not conclusive evidence that we are near the source as a sudden change in slope may also promote erosion, particularly mechanical erosion.

In the next section the channels will be considered individually in order to determine the direction of their emplacement. The maps of the channels show the interpreted channel profile at a given point. Four different profiles were chosen for indication, erosional, leveed, tubed and indistinct. These are represented by the use of different colours on the maps. Erosional sections are shown in red, leveed in green, roofed in blue and indistinct sections are in magenta. Also on the maps are crosses which show not only where there is a change in channel profile, but also indicate where the planetary radius has been measured

to estimate the current slopes in the region. A table showing the position of these points and the measured planetary radii is included for each channel.

4.2 Determination of Flow Direction.

4.2.1 Channel 1.

A map of channel 1 is displayed in Figure 4.1. and the measured planetary radii at various points on the channel are shown in Table 4.1. The main evidence in determining the direction in which this channel was emplaced comes from the bifurcation at a fracture at 158.75°S 33.47°E. This indicates that the origin of the channel is at 157.08°E 33.05°S. Further evidence for this comes from the fact that the region of channel emanating from this end has an erosional profile and also that, of the three ends of this channel, the western most one has the likeliest feature for a source of the lava, a graben. The altimetry data (Table 4.1) do not facilitate the solving of this problem. The southern of the two channel sections does appear to have a generally west to east slope, but the northern branch of the channel undulates vertically by up to 300 meters and clearly must have been modified since the channel was formed.

4.2.2 Channel 2.

Figure 4.2 shows a map of this channel and the spot heights measured are indicated in Table 4.2. The position of the source of this channel is unclear, but it is possible to infer which ends are more likely to be the origin than others. The eastern end of the channel at 168.93°E 32.66°S seems most likely to be the terminus of the channel. The main evidence for this comes from the fact that there

Figure 4.1. A map of channel 1, using different colours to represent different interpreted cross-sectional profiles.

Table 4.1. A list of spot heights for channel 1.

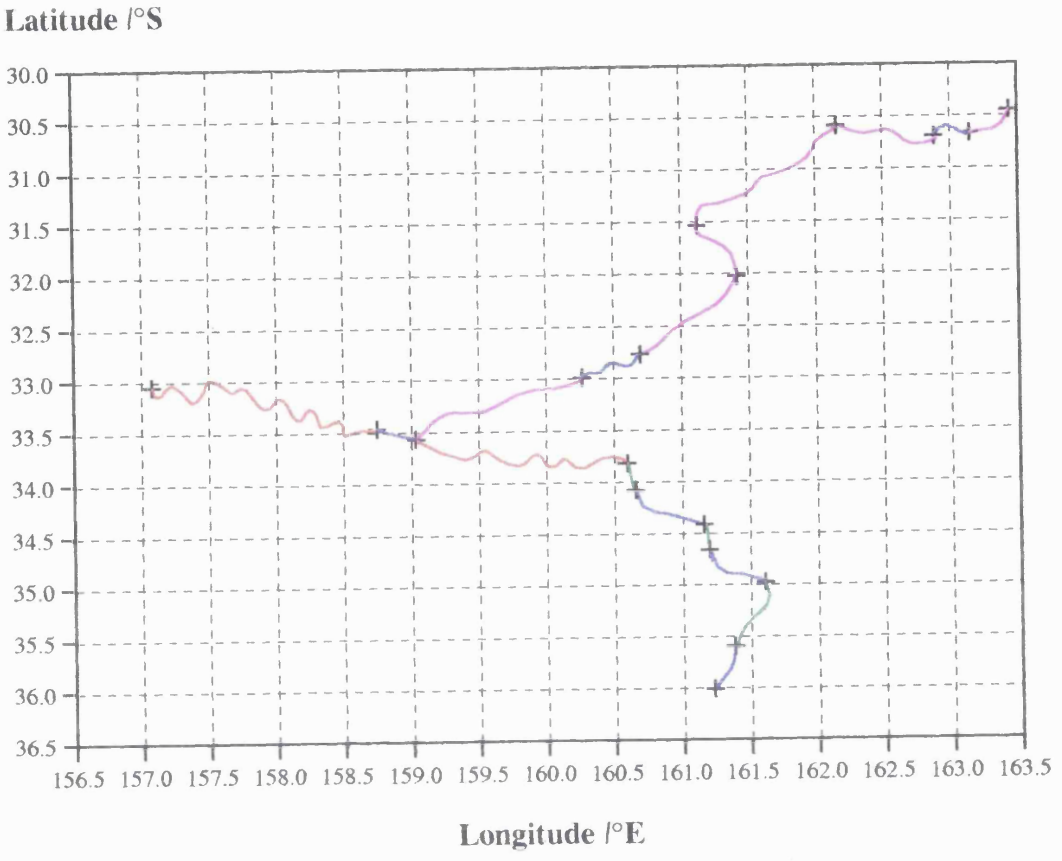

Key:

Erosional --------	Red
Leveed --------	Green
Roofed --------	Blue
Indistinct --------	Magenta

Longitude /°E	Latitude /°S	Radius /m
157.08	33.05	6052067
158.75	33.47	6052164
159.04	33.57	6052213
160.60	33.82	6051822
160.66	34.08	6051822
161.16	34.42	6051773
161.20	34.66	6051773
161.61	34.98	6051627
161.38	35.60	6051578
161.23	36.01	6051529
160.27	32.99	6052359
160.70	32.77	6052164
161.42	32.03	6052115
161.13	32.54	6052457
162.17	30.59	6052261
162.89	30.70	6052164
163.15	30.67	6052115
163.44	30.45	6052115

Figure 4.2. A map of channel 2, using different colours to represent different interpreted cross-sectional profiles.

Table 4.2. A list of spot heights for channel 2.

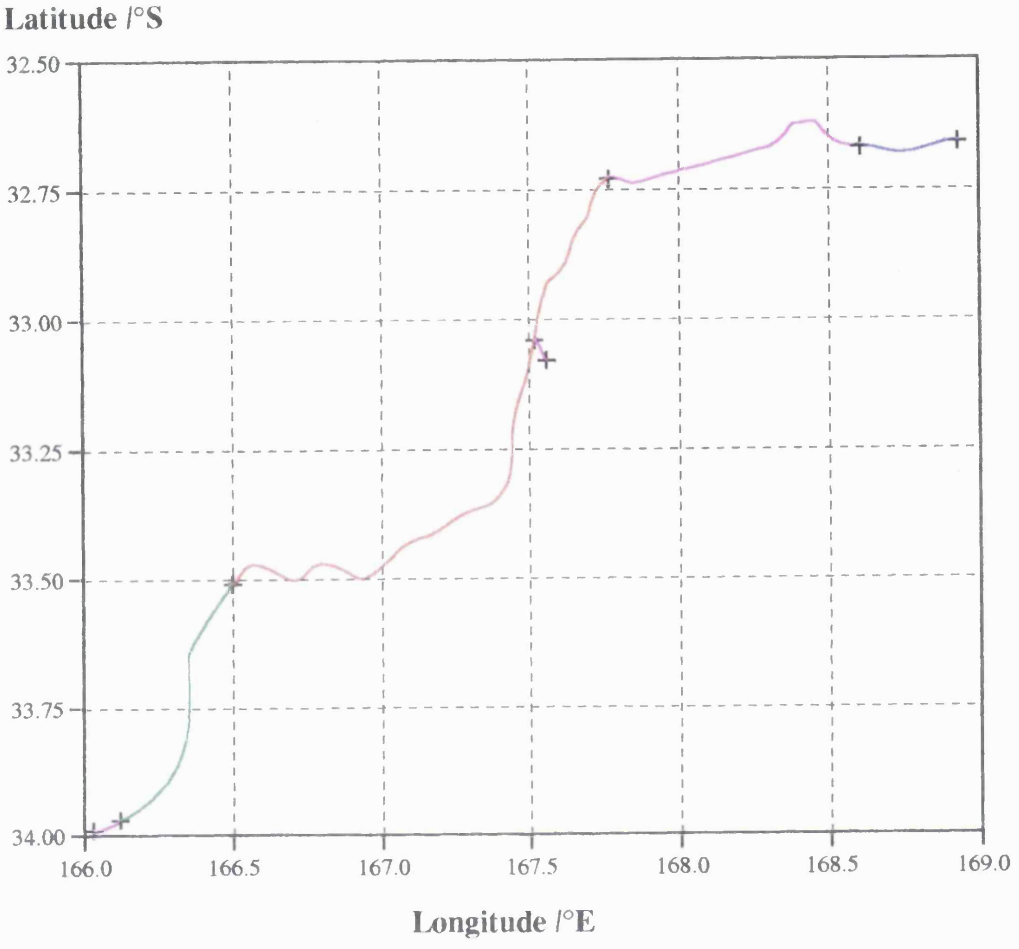

Key:

Erosional -------- Red
Leveed -------- Green
Roofed -------- Blue
Indistinct -------- Magenta

Longitude /°E	Latitude /°S	Radius /m
166.03	33.99	6051334
166.12	33.97	6051334
166.50	33.51	6051480
167.52	33.04	6051578
167.56	33.08	6051578
167.77	32.73	6051578
168.61	32.67	6051431
168.93	32.66	6051383

appears to have been a substantial outpouring of fluid here, which is consistent with lava flowing in an easterly direction in this region. This leaves two possibilities for the source of the channel: the SE end at 166.03°E 33.99°S, and the small tributary/fork at 167.56°E 33.08°S. Evidence for the former is that it appears to originate from a fracture which is a possible source of lava whilst evidence for the latter consists of the fact that it lies on the highest part of the channel and that the section of channel around it is erosional.

4.2.3 Channel 3.

A map of this channel is displayed in Figure 4.3, and a list of planetary radii with associated longitude and latitude is shown in Table 4.3. Due primarily to this channel having only relatively low resolution C1-MIDR coverage there is little evidence to support any of the three possible sources. There is only one definite end to this channel which occurs at a fracture at 176.62°E 32.11°S. The other two termini simply become increasingly indistinct until it is no longer possible to make them out. The altimetry data indicate that the channel now cuts undulating terrain which has therefore probably undergone some form of vertical reorganisation since the channel was emplaced.

4.2.4 Channel 4.

The direction of the flow which formed this channel can be determined by considering the regions surrounding the two ends of this channel. The eastern end at 153.84°E 49.85°S lies within a fracture system which is a possible source of lava whilst at the other end at 149.77°E 50.52°S there appears to have been an out-flowing of lava. This latter piece of evidence indicates that the lava that formed

Figure 4.3. A map of channel 3, using different colours to represent different interpreted cross-sectional profiles.

Table 4.3. A list of spot heights for channel 3.

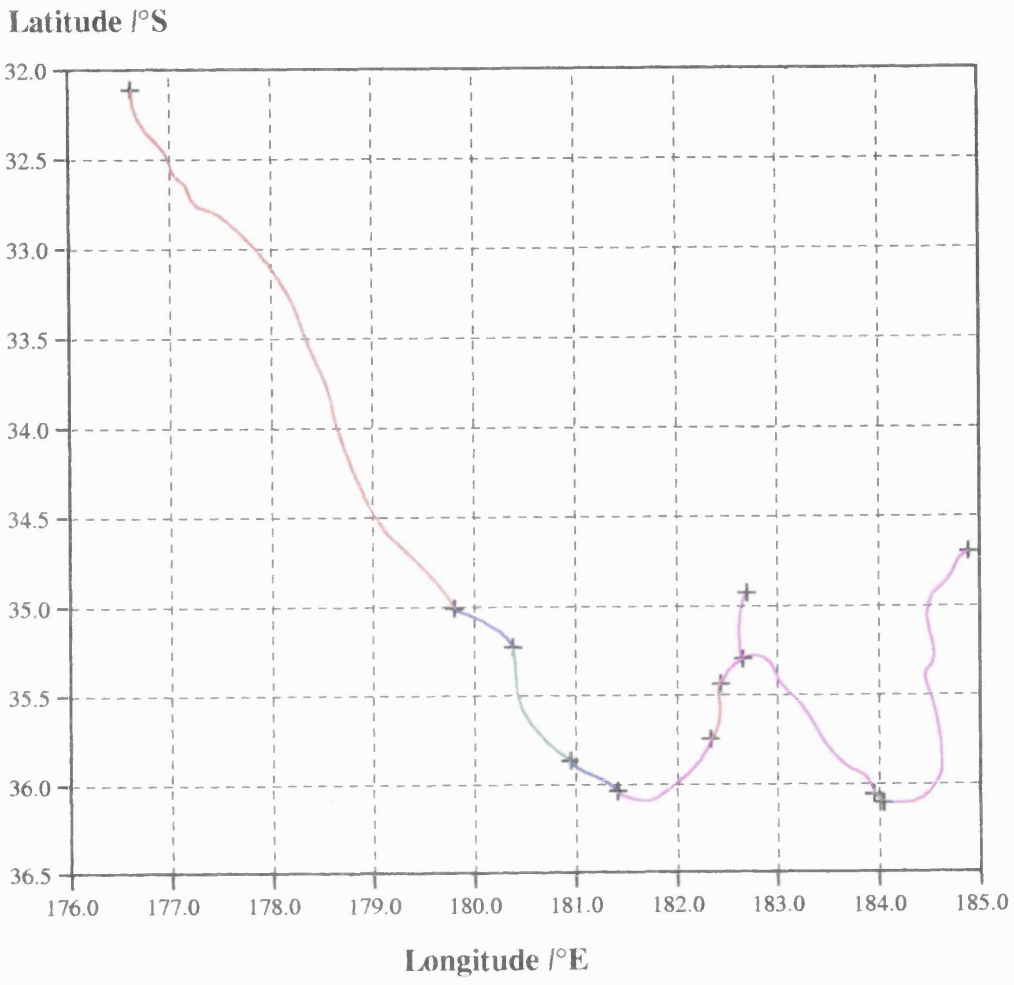

Key:

Erosional -------- Red
Leveed -------- Green
Roofed -------- Blue
Indistinct -------- Magenta

Longitude /°E	Latitude /°S	Radius /m
176.62	32.11	6051578
179.81	35.01	6051529
180.39	35.23	6051676
180.95	35.87	6051676
181.42	36.04	6051627
182.34	35.75	6051676
182.44	35.44	6051676
182.66	35.30	6051774
182.70	34.93	6051774
183.95	36.06	6051871
184.05	36.11	6051871
184.89	34.70	6051578

this channel was erupted from the fracture system and flowed initially eastwards and then in a southerly direction. A map of this channel indicating the different cross-sectional profiles that can be determined is shown in Figure 4.4. Planetary radii at various points on the channel are shown in Table 4.4. These indicate that the channel now undulates, showing that the region on which the channel lies has changed since this channel was emplaced.

4.2.5 Channel 5.

A map of the channel is shown in Figure 4.5, and a list of spot heights is displayed in Table 4.5. Due mainly to the fact that both ends of this channel are not well defined, combined with the availability of only relatively low C1 resolution being available for this area, it is not clear in which direction the channel was formed. The GTDR data do not help solve this problem as they show the channel to now lie on undulating terrain.

4.2.6 Channel 6.

Figure 4.6 shows a map of this channel. The bifurcation of this channel at 179.07°E 49.30°S points to the origin being at its western end. This is supported by the GTDR data which show a general downward easterly trend (Table 4.6). However it is unlikely that the source for the channel is at 174.57°E 48.79°S (the last point at which the channel can be made out), as there is no feature, such as a graben or fracture, so the actual source probably lies further west but is no longer visible due to resurfacing.

Figure 4.4. A map of channel 4, using different colours to represent different interpreted cross-sectional profiles.

Table 4.4. A list of spot heights for channel 4.

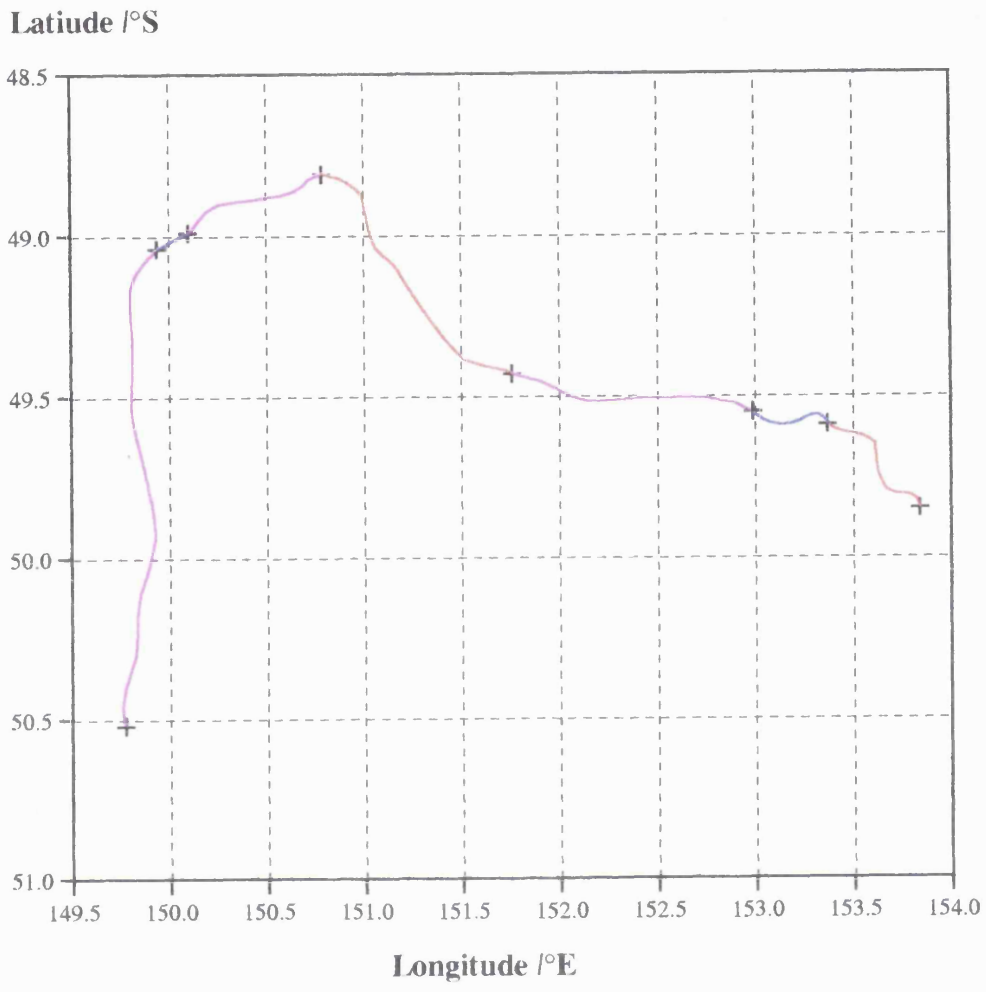

Key:

Erosional -------- Red
Roofed -------- Blue
Indistinct -------- Magenta

Longitude /°E	Latitude /°S	Radius /m
153.84	49.85	6051254
153.37	49.59	6051254
152.99	49.55	6051201
151.76	49.43	6051114
150.79	48.81	6051236
150.10	48.99	6051446
149.94	49.04	6051306
149.77	50.52	6050979

Figure 4.5. A map of channel 5, using different colours to represent different interpreted cross-sectional profiles.

Table 4.5. · A list of spot heights for channel 5.

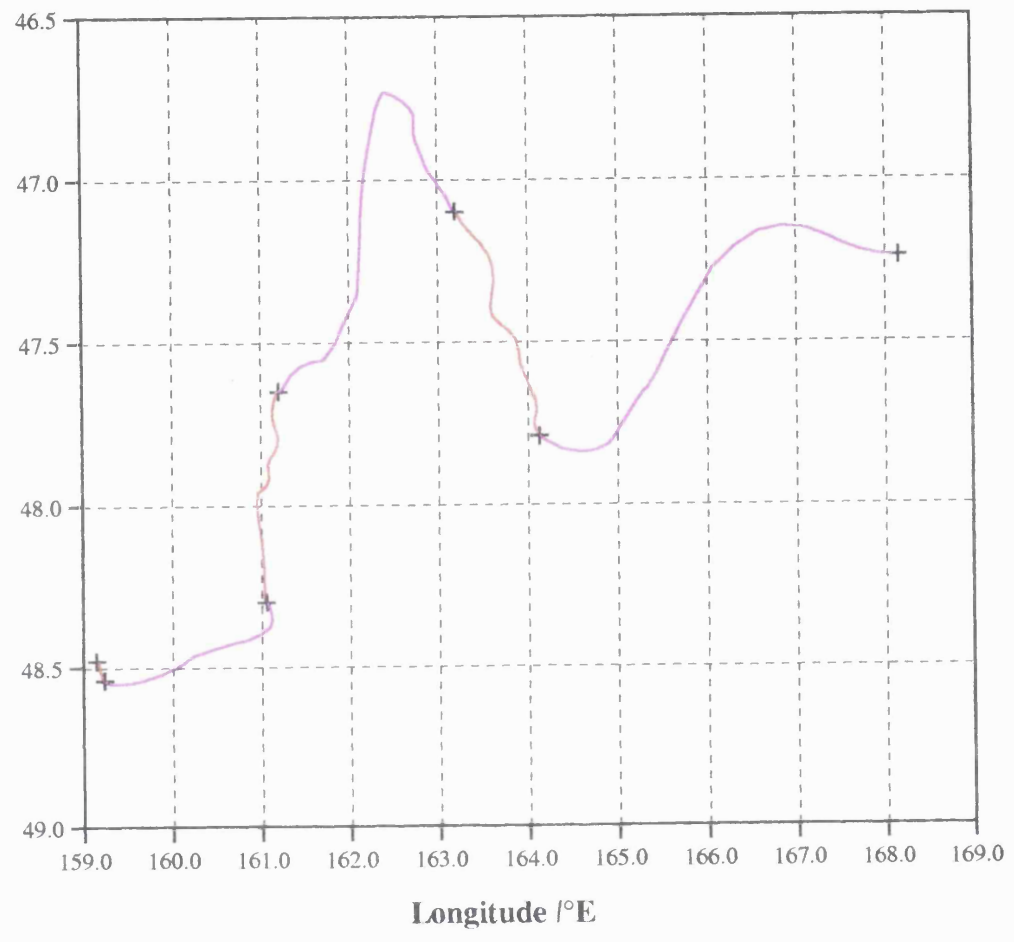

Key:

Erosional -------- Red
Indistinct -------- Magenta

Longitude /°S	Latitude /°E	Radius /m
168.16	47.24	6051515
164.13	47.79	6051271
163.20	47.10	6051271
161.21	47.65	6051341
161.06	48.30	6051375
159.24	48.54	6051463
159.15	48.48	6051445

Figure 4.6. A map of channel 6, using different colours to represent different interpreted cross-sectional profiles.

Table 4.6. A list of spot heights for channel 6.

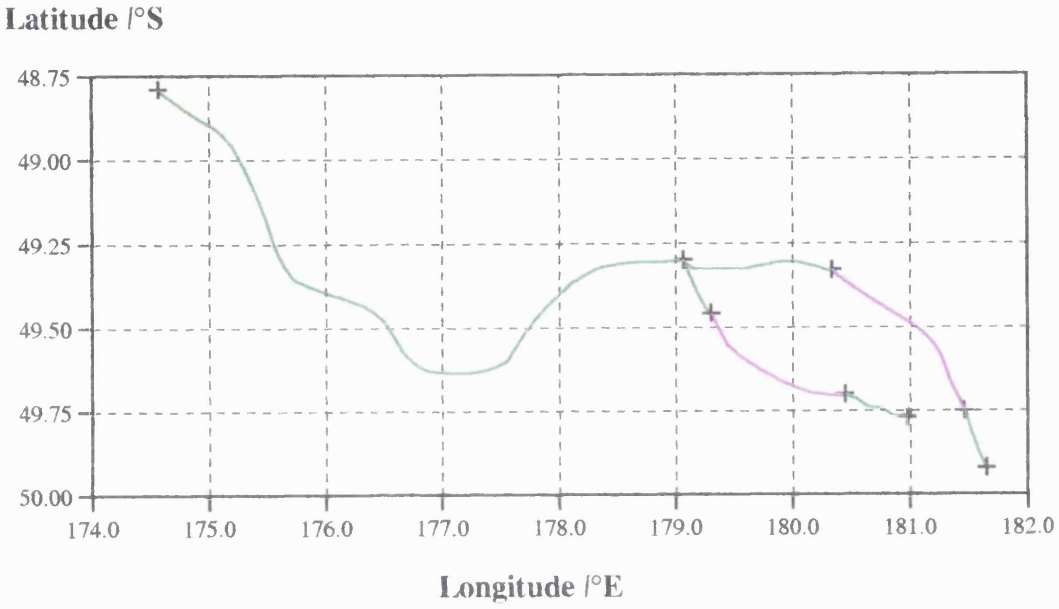

Key:

Leveed -------- Green
Indistinct -------- Magenta

Longitude /°E	Latitude /°S	Radius /m
174.57	48.79	6051568
179.07	49.30	6051445
180.34	49.33	6051341
181.46	49.75	6051079
181.65	49.92	6051009
179.31	49.46	6051445
180.45	49.70	6051323
180.98	49.77	6051166

4.2.7 Channel 7.

There are no distinct ends to this channel so it is likely that we are seeing only part of the original channel. Figure 4.7 shows a map of this channel. Consideration of the GTDR data (Table 4.7) shows a lower planetary radius the further north you go, so possibly the source for this channel lies to the south of the end that can presently be seen.

4.2.8 Channel 8.

The evidence for the origin of this channel is ambiguous. The GTDR data (Table 4.8) indicate that the channel now rests on a slope which is higher at the eastern end of the channel. However, consideration of the map of the channel (Figure 4.8) shows that,as the channel bifurcates, the western end of the channel is more likely to be the source. This is backed up by the fact that both the eastern ends of the channel have possible flow features associated with them, and that the western part of the channel has an erosional profile. The weight of evidence for the western end of the channel being the source is great enough to presume that the profile given by the GTDR data is not the same as was present when the channel was emplaced.

4.2.9 Channel 9

Evidence for the origin of this channel comes from consideration of the map of the channel (Figure 4.9). The channel bifurcates twice, both times pointing towards the source of the channel being at it s northern most extent. This is supported by the fact that the northern region of the channel has an erosional

Figure 4.7. A map of channel 7, using different colours to represent different interpreted cross-sectional profiles.

Table 4.7. A list of spot heights for channel 7.

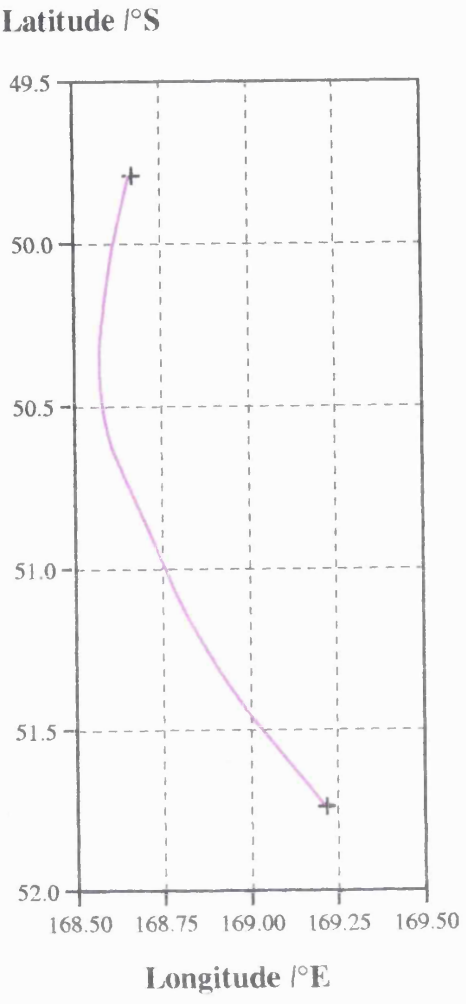

Key:

Indistinct -------- Magenta

Longitude /°E	Latitude /°S	Radius /m
169.22	51.74	6051708
168.67	49.79	6051585
168.55	50.39	6051620

Figure 4.8. A map of channel 8, using different colours to represent different interpreted cross-sectional profiles.

Table 4.8. A list of spot heights for channel 8.

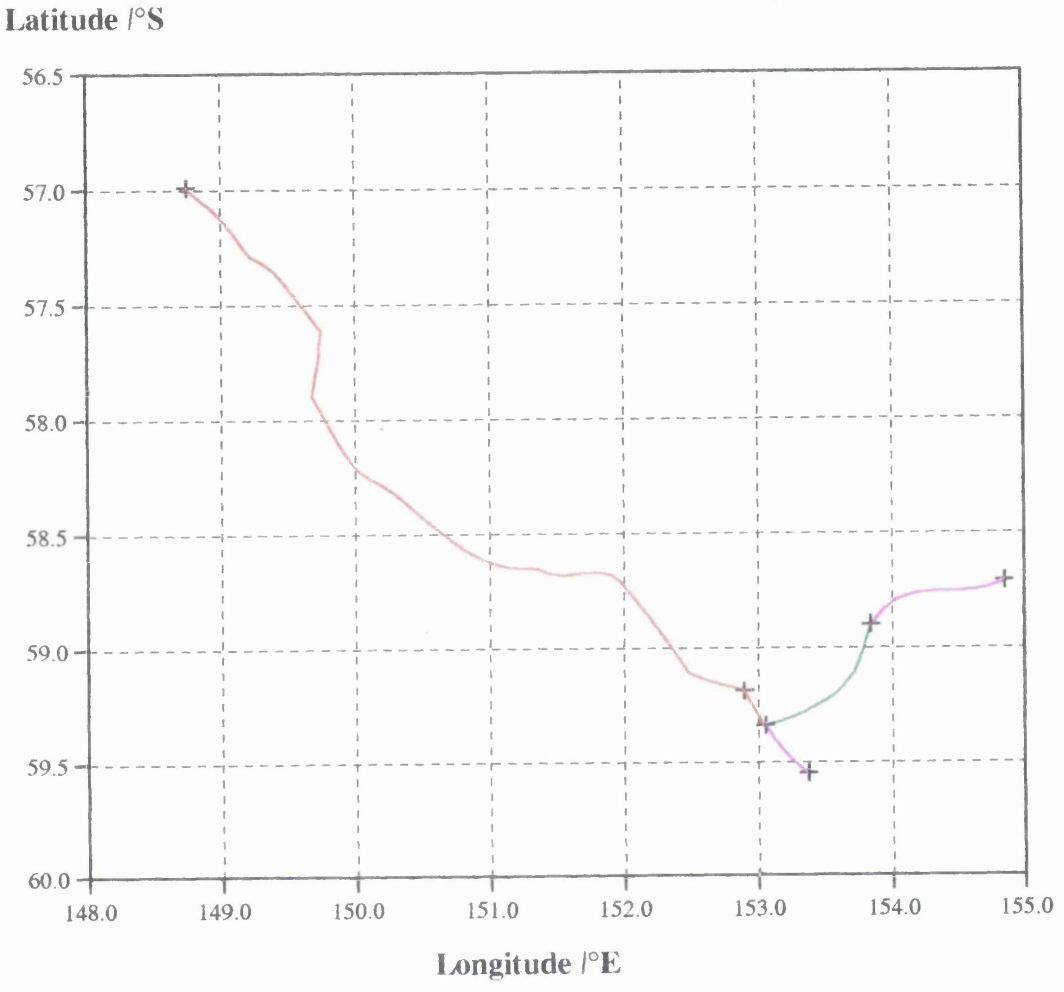

Key:

Erosional -------- Red
Leveed -------- Green
Indistinct -------- Magenta

Longitude /°E	Latitude /°S	Radius /m
148.75	56.99	6050726
152.90	59.19	6050887
153.84	58.90	6051131
154.85	58.71	6051027
153.06	59.34	6050852
153.38	59.55	6050835

Figure 4.9. A map of channel 9, using different colours to represent different interpreted cross-sectional profiles.

Table 4.9. A list of spot heights for channel 9.

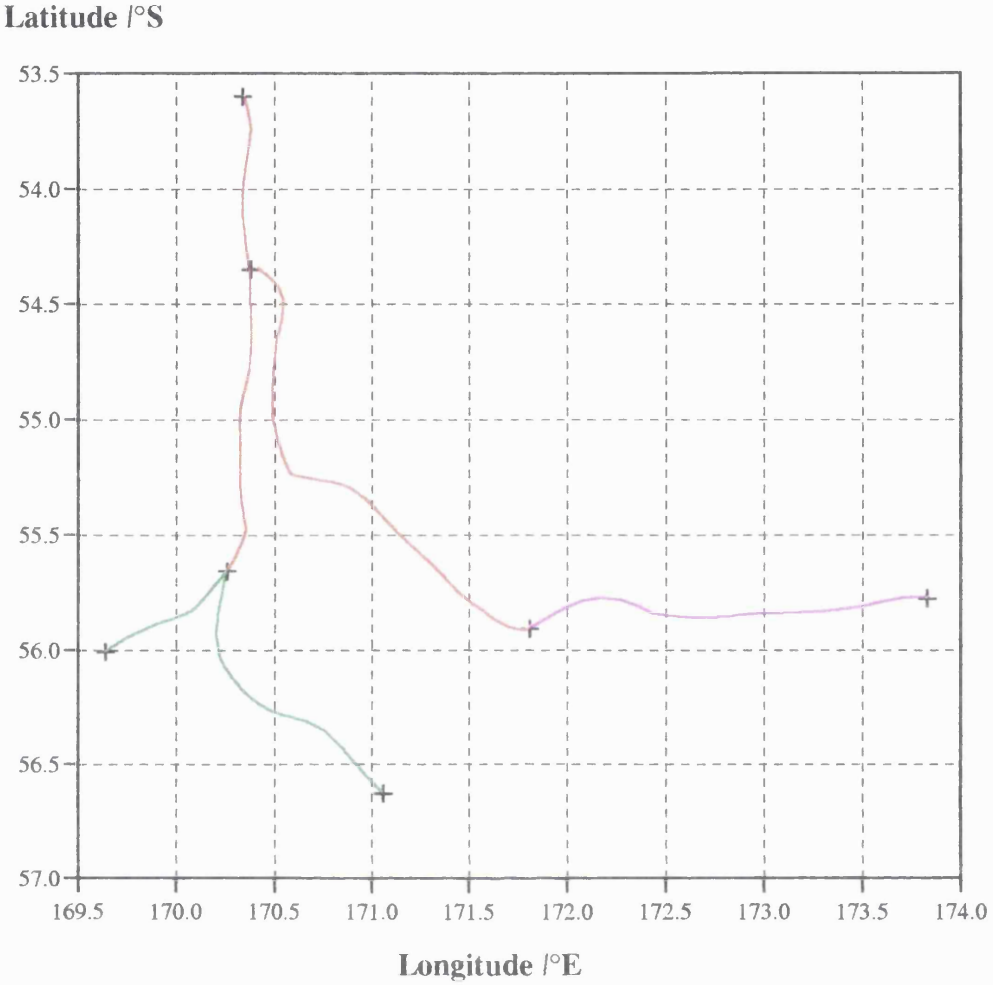

Key:

Erosional -------- Red
Leveed -------- Green
Indistinct -------- Magenta

Longitude /°E	Latitude /°S	Radius /m
170.34	53.60	6051690
170.38	54.35	6051708
171.81	55.91	6051550
173.83	55.78	6051306
170.26	55.66	6051516
169.64	56.01	6051376
171.06	56.63	6051393

profile, which becomes either leveed or indistinct the further away from the northern end of the channel. The episodic terracing evident in the eastern branch of the channel may be interpreted to indicate that this channel system was not formed by one flow event.

4.2.10 Channel 10

There is little indication to support one end of this channel being the source instead of the other. What evidence there is points towards the southwest end of the channel being the source. This is due to the fact that this end lies within a system of fractures which are a possible source of the lava that may have formed this channel. This is in no way conclusive as there is no definite end to the northeast part of the channel, due partly to this region only having the lower resolution C1-MIDR coverage. The GTDR data (Table 4.10) do not facilitate the solving of this problem as they show that the channel currently lies on undulating terrain which is therefore unlikely to represent the vertical orientation of the region when the channel was emplaced. A map of the channel is shown in Figure 4.10.

4.2.11 Channel 11

The main evidence as to the direction in which this channel was emplaced comes from the close proximity of the western end of this channel to channel 10. It is therefore possible that channel 11 is a branch of channel 10. There is little other evidence to support either end of the channel as the source relative to the other, with the GTDR data (Table 4.11) revealing that the channel now undulates vertically along its length. A map of the channel is shown in Figure 4.11.

Figure 4.10. A map of channel 10, using different colours to represent different interpreted cross-sectional profiles.

Table 4.10. A list of spot heights for channel 10.

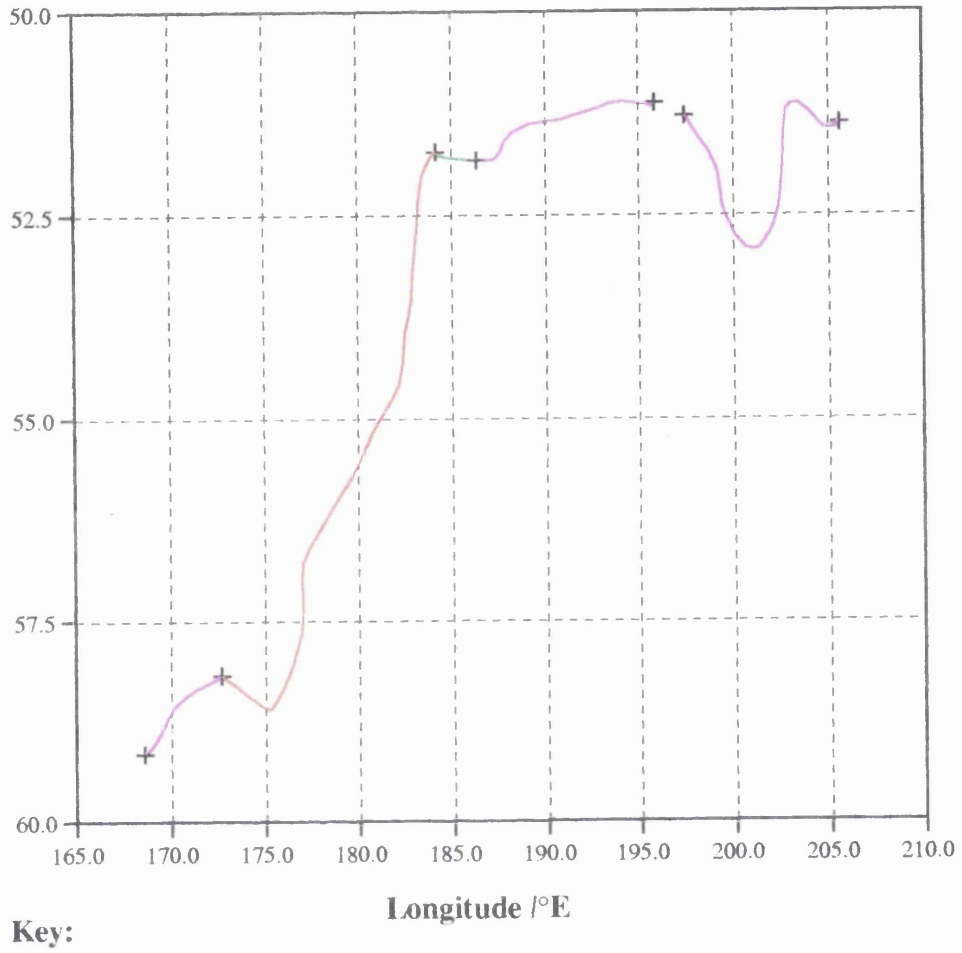

Key:

Erosional -------- Red
Leveed -------- Green
Indistinct -------- Magenta

Longitude /°E	Latitude /°S	Radius /m
168.60	59.15	6051219
172.69	58.17	6051219
184.22	51.73	6050932
186.37	51.83	6051044
195.87	51.13	6050964
197.45	51.29	6051182
205.62	51.38	6051455

Figure 4.11. A map of channel 11, using different colours to represent different interpreted cross-sectional profiles.

Table 4.11. A list of spot heights for channel 11.

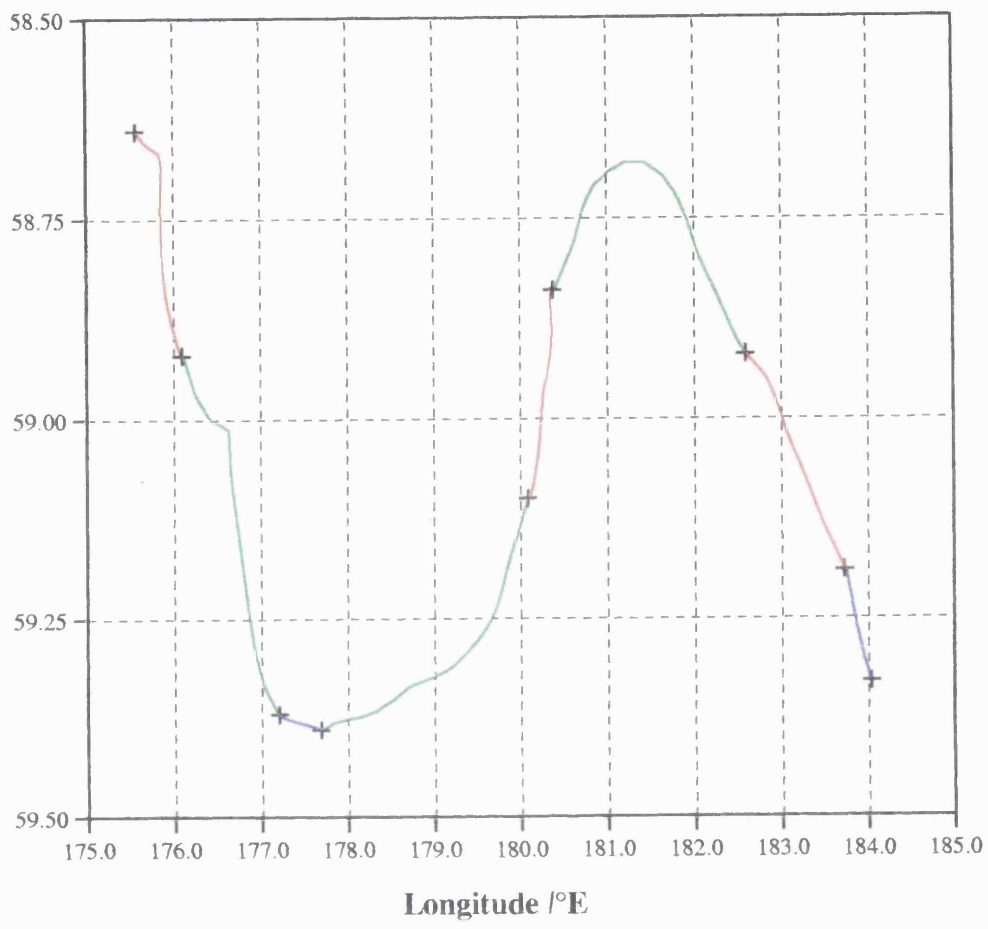

Key:

Erosional -------- Red
Leveed -------- Green
Roofed -------- Blue

Longitude /°E	Latitude /°S	Radius /m
175.57	58.64	6051149
176.10	58.92	6051062
177.21	59.37	6050974
177.69	59.39	6050974
180.09	59.10	6051131
180.38	58.84	6051027
182.60	58.92	6050800
183.73	59.19	6050939
184.04	59.33	6051044

4.2.12 Channel 12

This channel originates from one of the meanders of channel 11. This is more likely than channel 12 being a tributary of channel 11. Evidence for this is the fact that there is a flow feature associated with the end at 183.82°E 55.92°S making this very unlikely to be the source, and that the orientation of the bifurcation is not consistent with a flow originating from the eastern end of the channel. (Figure 4.12). Table 4.12 shows the spot heights at various points along the channel, which indicate that the region on which this channel was emplaced has undergone vertical displacement since the channel was formed.

4.3 Slope Survey

In the previous section, the GTDR data were little help in determining the direction of emplacement for the channels as in the majority of cases they revealed the channel to currently lie on undulating terrain. This section describes a study undertaken to try to calculate the extent of vertical deformation that may have occurred since the channels were formed.

4.3.1 Method.

Of the twelve channels considered, the direction of emplacement for seven of them (channels 1, 4, 6, 8, 9, 11 and 12) can be determined with some confidence. This is done by studying features such as flow fields emanating from ends of the channels, indicating an outpouring of lava, and bifurcations along the channel's length. As shown in the previous section, each

Figure 4.12. A map of channel 12, using different colours to represent different interpreted cross-sectional profiles.

Table 4.12. A list of spot heights for channel 12.

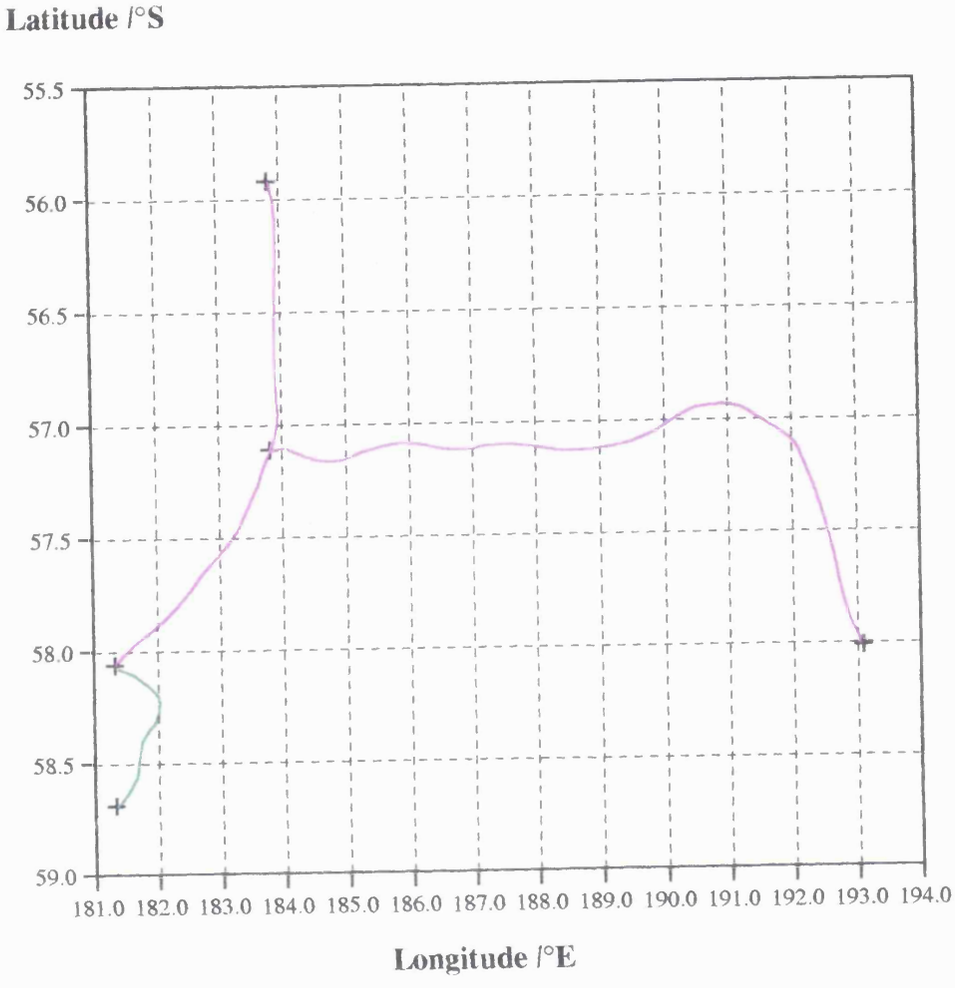

Key:

Leveed -------- Green
Indistinct -------- Magenta

Longitude /°E	Latitude /°S	Radius /m
181.33	58.69	6050852
181.33	58.06	6050974
183.81	57.11	6050870
183.82	55.92	6050852
193.09	58.01	6050957

channel has been broken up into identifiable sections of different types; erosional, leveed, roofed and indistinct.

For each section of the seven channels considered, an average slope was measured using the following technique. The latitude and longitude of each end of a section is measured. The distance between these two points is calculated using spherical trigonometry. Let the two ends of the channel section be points A and B in Figure 4.13. The cosine formula for the spherical triangle *PBA* yields

$$\cos AB = \cos AP \cos BP + \sin AP \sin BP \cos APB \qquad (4.1)$$

where *AB* is the angle subtended by the great circle arc between the two points and the centre of the sphere, *BP* is the colatitude of point B, *AP* is the colatitude of point A, and *BPA* is the difference in longitude between A and B. Once angle *AB* is known, multiplying by the radius gives the length of the arc between A and B. Dividing the difference in planetary radius of the two ends of the channel section by this arc length yields an average slope angle.

4.3.2 Results.

The results for the seven channels are displayed in Tables 4.13 - 4.19. These show the angle subtended at the planetary centre and the associated arc length as well as the slopes for the various sections. The mean planetary radius of 6051 km was used for all calculations of arc length. The results from this study are shown in Figure 4.14 and Table 4.20. The data are plotted as slope angle against type, allowing for easy comparison between kinds of section to be made. A positive slope angle implies a downhill slope relative to the inferred source.

Figure 4.13. Diagram showing the spherical trigonometry associated with calculating the great circle distance between 2 points of known latitude and longitude (Roy & Clarke, p43, 1988).

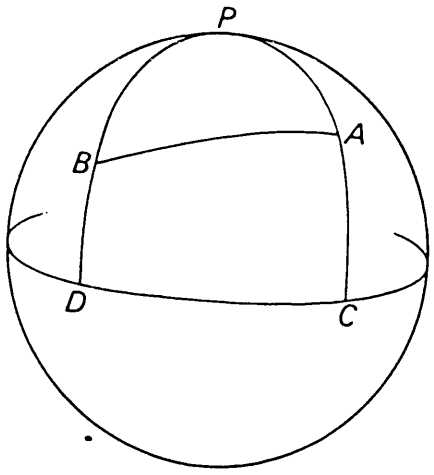
P
A
B
D
C

Table 4.13. Channel section slopes for channel 1.

Start Longitude /°E, Latitude /°S, Planetary Radius /m	Finish Longitude /°E, Latitude /°S, Planetary Radius /m	Type	Angle Subtended at Planetary Centre /°	Length of Arc between the Two Ends of the Section /km	Gradient of Channel Section /°
157.08, 33.05, 6052067	158.75, 33.47, 6052164	Erosional	1.4582	154.00	-0.036
158.75, 33.47, 6052164	159.04, 33.57, 6052213	Roofed	0.2616	27.63	-0.102
159.04, 33.57, 6052213	160.60, 33.82, 6051822	Erosional	1.3218	139.60	0.160
160.60, 33.82, 6051822	160.66, 34.08, 6051822	Leveed	0.2647	27.95	0.000
160.66, 34.08, 6051822	161.16, 34.42, 6051773	Roofed	0.5352	56.52	0.050
161.16, 34.42, 6051773	161.20, 34.66, 6051773	Leveed	0.2423	25.59	0.000
161.20, 34.66, 6051773	161.61, 34.98, 6051627	Roofed	0.4644	49.05	0.171
161.61, 34.98, 6051627	161.38, 35.60, 6051578	Leveed	0.6478	68.41	0.041
161.38, 35.60, 6051578	161.23, 36.01, 6051529	Roofed	0.4277	45.20	0.062
159.04, 33.57, 6052213	160.27, 32.99, 6052359	Indistinct	1.1806	124.68	-0.067
160.27, 32.99, 6052359	160.70, 32.77, 6052164	Roofed	0.4229	44.66	0.250
160.70, 32.77, 6052164	161.42, 32.03, 6052115	Indistinct	0.9577	101.14	0.028
161.42, 32.03, 6052115	161.13, 32.54, 6052457	Indistinct	0.5659	59.76	-0.328
161.13, 32.54, 6052457	162.17, 30.59, 6052261	Indistinct	2.1419	226.21	0.050
162.17, 30.59, 6052261	162.89, 30.70, 6052164	Indistinct	0.6291	66.44	0.084
162.89, 30.70, 6052164	163.15, 30.67, 6052115	Roofed	0.2256	23.83	0.118
163.15, 30.67, 6052115	163.44, 30.45, 6052115	Indistinct	0.3328	35.15	0.000

(Top) Table 4.14. Channel section slopes for channel 4.

(Bottom) Table 4.15. Channel section slopes for channel 6.

Start Longitude /°E, Latitude /°S, Planetary Radius /m	Finish Longitude /°E, Latitude /°S, Planetary Radius /m	Type	Angle Subtended at Planetary Centre /°	Length of Arc between the Two Ends of the Section /km	Gradient of Channel Section /°
153.84, 49.85, 6051254	153.37, 49.59, 6051254	Erosional	0.3999	42.23	0.000
153.37, 49.59, 6051254	152.99, 49.55, 6051201	Roofed	0.2497	26.37	0.115
152.99, 49.55, 6051201	151.76, 49.43, 6051114	Indistinct	0.8079	85.32	0.058
151.76, 49.43, 6051114	150.79, 48.81, 6051236	Erosional	0.8874	93.72	-0.075
150.79, 48.81, 6051236	150.10, 48.99, 6051446	Indistinct	0.4880	51.54	-0.233
150.10, 48.99, 6051446	149.94, 49.04, 6051306	Roofed	0.1162	12.27	0.654
149.94, 49.04, 6050979	149.77, 50.52, 6050979	Indistinct	1.4841	156.74	0.120

Start Longitude /°E, Latitude /°S, Planetary Radius /m	Finish Longitude /°E, Latitude /°S, Planetary Radius /m	Type	Angle Subtended at Planetary Centre /°	Length of Arc between the Two Ends of the Section /km	Gradient of Channel Section /°
174.57, 48.79, 6051568	179.07, 49.30, 6051445	Leveed	2.9929	316.08	0.023
179.07, 49.30, 6051445	152.99, 49.55, 6051201	Leveed	0.8284	87.49	0.068
180.34, 49.33, 6051341	181.46, 49.75, 6051079	Indistinct	0.8394	88.65	0.169
181.46, 49.75, 6051079	181.65, 49.92, 6051009	Leveed	0.2096	22.14	0.181
179.07, 49.30, 6051445	179.31, 49.46, 6051445	Leveed	0.2236	23.61	0.000
179.31, 49.46, 6051445	180.45, 49.70, 6051323	Indistinct	0.7771	82.07	0.085
180.45, 49.70, 6051323	180.98, 49.77, 6051166	Leveed	0.3496	36.92	0.244

(Top) Table 4.16. Channel section slopes for channel 8.

(Bottom) Table 4.17. Channel section slopes for channel 9.

Start Longitude /°E, Latitude /°S, Planetary Radius /m	Finish Longitude /°E, Latitude /°S, Planetary Radius /m	Type	Angle Subtended at Planetary Centre /°	Length of Arc between the Two Ends of the Section /km	Gradient of Channel Section /°
148.75, 56.99, 6050726	152.90, 59.19, 6050887	Erosional	3.1057	327.99	-0.028
152.90, 59.19, 6050887	153.84, 58.90, 6051131	Leveed	0.5638	59.54	-0.235
153.84, 58.90, 6051131	154.85, 58.71, 6051027	Indistinct	0.5566	58.78	0.101
152.90, 59.19, 6050887	153.06, 59.34, 6050852	Erosional	0.1708	18.04	0.111
153.06, 59.34, 6050852	153.38, 59.55, 6050835	Indistinct	0.2656	28.05	0.035

Start Longitude /°E, Latitude /°S, Planetary Radius /m	Finish Longitude /°E, Latitude /°S, Planetary Radius /m	Type	Angle Subtended at Planetary Centre /°	Length of Arc between the Two Ends of the Section /km	Gradient of Channel Section /°
170.34, 53.60, 6051690	170.38, 54.35, 6051708	Erosional	0.7504	79.25	-0.013
170.38, 54.35, 6051708	171.81, 55.91, 6051550	Erosional	1.7612	186.00	0.049
171.81, 55.91, 6051550	173.83, 55.78, 6051306	Indistinct	1.1415	120.45	0.116
170.38, 54.35, 6051708	170.26, 55.66, 6051516	Erosional	1.3118	138.54	0.065
170.26, 55.66, 6051516	169.64, 56.01, 6051376	Leveed	0.6294	66.47	0.121
170.26, 55.66, 6051516	171.06, 56.63, 6051393	Leveed	0.8104	85.59	0.082

(Top) Table 4.18. Channel section slopes for channel 11.

(Bottom) Table 4.19. Channel section slopes for channel 12.

Start Longitude /°E, Latitude /°S, Planetary Radius /m	Finish Longitude /°E, Latitude /°S, Planetary Radius /m	Type	Angle Subtended at Planetary Centre /°	Length of Arc between the Two Ends of the Section /km	Gradient of Channel Section /°
175.57, 58.64, 6051149	176.10, 58.92, 6051062	Erosional	0.3923	41.43	0.120
176.10, 58.92, 6051062	177.21, 59.37, 6050974	Leveed	0.7256	76.63	0.066
177.21, 59.37, 6050974	177.69, 59.39, 6050974	Roofed	0.2453	25.91	0.000
177.69, 59.39, 6050974	180.09, 59.10, 6051131	Leveed	1.2610	133.17	-0.068
180.09, 59.10, 6051131	180.38, 58.84, 6051027	Erosional	0.2999	31.67	0.188
180.38, 58.84, 6051027	182.60, 59.19, 6050800	Leveed	1.1501	121.46	0.107
182.60, 59.19, 6050800	183.73, 59.33, 6050939	Erosional	0.6407	67.66	-0.118
183.73, 59.33, 6050939	184.04, 59.33, 6051044	Roofed	0.2114	22.33	-0.269

Start Longitude /°E, Latitude /°S, Planetary Radius /m	Finish Longitude /°E, Latitude /°S, Planetary Radius /m	Type	Angle Subtended at Planetary Centre /°	Length of Arc between the Two Ends of the Section /km	Gradient of Channel Section /°
181.33, 58.69, 6050852	181.33, 58.06, 6050974	Leveed	0.6300	66.53	-0.105
181.33, 58.06, 6050974	183.81, 57.11, 6050870	Indistinct	1.6338	172.55	0.035
183.81, 57.11, 6050870	183.82, 55.92, 6050852	Indistinct	1.1900	125.68	0.008
183.81, 57.11, 6050870	193.09, 58.01, 6050957	Indistinct	5.0544	533.79	-0.009

Figure 4.14. Results from the measurements of the present day slopes of the different type of sections of the channels. Positive slope angles reflect 'normal' downhill slopes.

Table 4.20. An analysis of the different types of channel section seen, including the direction of the present day slope.

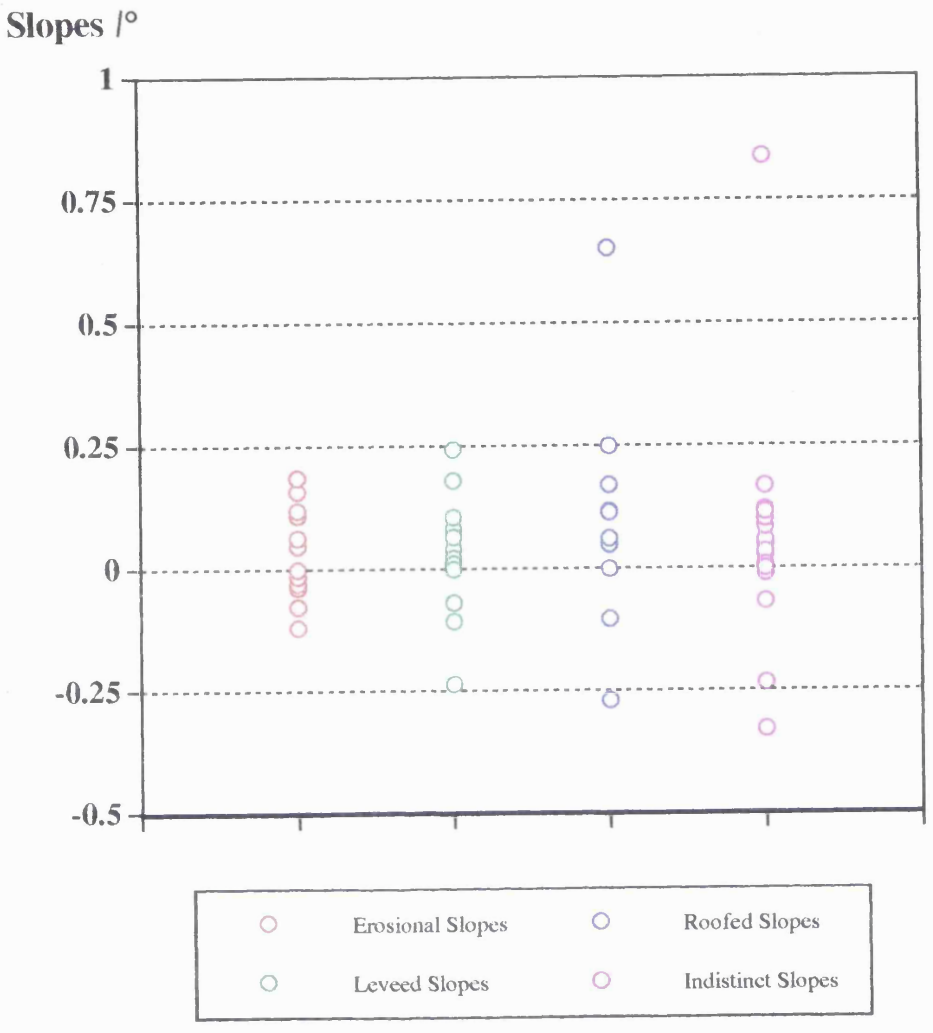

Slope Angle	No. of Erosional Sections	No. of Leveed Sections	No. of Roofed Sections	No. of Indistinct Sections	Total No. of Sections
Positive	6	9	7	11	33
Negative	5	3	2	4	14
Zero	2	3	1	1	7

4.3.3 Conclusion.

There are several conclusions that can be drawn from consideration of Figure 4.14. An estimate can be made as to the amount of vertical movement that the region in which the channels lie has undergone. In Figure 4.14 negative gradients are represented by positive angles for slope on the y axis. It is reasonable to assume that when the channels were emplaced, the vast majority of slope angles were positive. (The possible exception being slopes on which the lava was eroding and here it is necessary for the erosion rate to be so high that the lava was able to carve its own channel through gently upward sloping terrain. This is likely to be the exception rather than the rule.) Assuming that the orientation of any vertical deformation is random, then large scale changes would not affect the mean slope, as the gradients of the channel sections will have been increased or decreased to the same extent. We would expect the deformation to widen the range of slope angles, producing some which are relatively large, (having increased the incline of a section), and also some negative slope angles where the channel section now lies in an opposite direction to the one when it was emplaced. Analysis of the data (Table 4.20 & Figure 4.14) indicates that there has been some movement in this region as 13% of the slope angles are negative. Also there are some slope angles which are much greater then the average. There does not appear to be any relation between the value of the slope angle and the type of section, for the three distinguishable types of section. This is somewhat surprising as one would possibly expect the erosional sections to lie on steeper terrain, which promotes mechanical erosion, than the other types of section.

4.4 Conclusions.

The study of the canali has shown that it is not uncommon for them to have an erosional profile at some point along their length. 75% of the channels considered in the study contain an erosional section. Also of the seven channels for which it is possible to determine the direction of emplacement, five have an erosional section as the first section of their length. Assuming that these channels were formed by lava it is likely that thermal processes will have played an important role in these erosional sections. As thermal erosion by lava is uncommon on Earth, I decided to start work on a model for thermal erosion close to a lava source, to see under what conditions lava is capable of eroding and in particular whether lava is more likely to erode on Venus than on Earth. A description of this model and the results obtained with it can be found in chapters 5 & 6.

Chapter 5
A Model for Thermal Erosion by Lava

This chapter describes the development of a one dimensional model for thermal erosion by lava. Several non-erosional models were produced before the final erosional one; these are also discussed. The chapter presents the theory behind solving the heat conduction equation using the principle of finite differences.

5.1 Heat Conduction.

If a temperature gradient exists within a body then heat will flow to cancel out the heat gradient present. This is the principle of heat conduction. The heat flow per unit area within the body is proportional to the temperature gradient. The constant of proportionality is called the thermal conductivity of the body. This process is expressed mathematically by Fourier's law (e.g. Holman, 1989).

$$\dot{Q} = -kA\frac{d\theta}{dx} \tag{5.1}$$

where $\dot{Q}$ is the rate of heat flow, k is the thermal conductivity, A is the cross-sectional area and $\frac{d\theta}{dx}$ is the temperature gradient. The negative sign ensures that the second law of thermodynamics is not violated (Adkins, 1983). i.e. heat flows from warmer areas to cooler areas.

The next step is to formulate the differential equations governing the heat transfer process. Consider Figure 5.1. Let the temperature at the centre of the box be θ. The temperature at the left hand face is $\theta - \frac{1}{2}\frac{\partial\theta}{\partial x}dx$.

Figure 5.1. An elemental volume representing one dimensional heat flow by conduction.

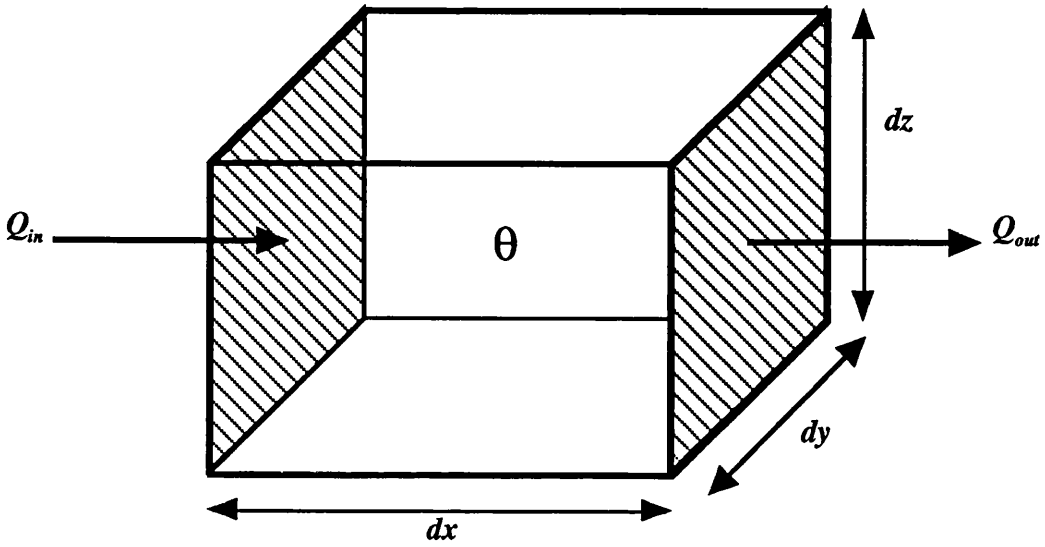
Q_{in}
θ
Q_{out}
dz
dy
dx

Therefore the amount of heat flowing into the left hand face in a time dt is

$$-k\frac{\partial}{\partial x}\left(\theta-\tfrac{1}{2}\frac{\partial\theta}{\partial x}dx\right)dy\,dz\,dt \tag{5.2}$$

Similarly the heat flowing out of the right hand face is

$$-k\frac{\partial}{\partial x}\left(\theta+\tfrac{1}{2}\frac{\partial\theta}{\partial x}dx\right)dy\,dz\,dt \tag{5.3}$$

The net heat gain of the element is

$$k\frac{\partial^2\theta}{\partial x^2}dx\,dy\,dz\,dt \tag{5.4}$$

As there are no internal sources of energy this influx of heat results in a change of temperature equal to $\frac{\partial\theta}{\partial t}dt$. The energy required to obtain this temperature change is

$$\frac{\partial\theta}{\partial t}dt\;c\rho\,dx\,dy\,dz \tag{5.5}$$

where c is the specific heat capacity and ρ is the density. Equating 5.4 and 5.5 yields the partial differential equation for heat conduction.

$$\frac{\partial\theta}{\partial t}=\alpha\frac{\partial^2\theta}{\partial x^2} \tag{5.6}$$

where $\alpha=\frac{k}{\rho c}$. α is called the thermal diffusivity.

5.2 Finite Difference Formulations.

5.2.1 Introduction.

The purpose of finite difference formulations is to express the differentials of dependent variables in a partial differential equation in an approximate form which then allows the equation to be solved numerically, possibly with the aid of a computer. The first step involves calculating the approximate expressions for the partial differentials. One method for doing this involves a Taylor series expansion.

5.2.2 Taylor Series Expansion.

Proof for the Taylor series can be found in Heading (1970). Given an analytical function $f(x)$, $f(x+\Delta x)$ can be expanded in a Taylor series about x as

$$f(x+\Delta x) = f(x) + (\Delta x)\frac{\partial f}{\partial x} + \frac{(\Delta x)^2}{2!}\frac{\partial^2 f}{\partial x^2} + \frac{(\Delta x)^3}{3!}\frac{\partial^3 f}{\partial x^3} + \ldots$$
$$f(x+\Delta x) = f(x) + \sum_{n=1}^{\infty}\frac{(\Delta x)^n}{n!}\frac{\partial^n f}{\partial x^n} \qquad (5.7)$$

Solving for $\frac{\partial f}{\partial x}$,

$$\frac{\partial f}{\partial x} = \frac{f(x+\Delta x) - f(x)}{\Delta x} - \frac{\Delta x}{2!}\frac{\partial^2 f}{\partial x^2} - \frac{(\Delta x)^2}{3!}\frac{\partial^3 f}{\partial x^3} + \ldots \qquad (5.8)$$

Representing the sum of all the terms with factors of Δx and higher as $O(\Delta x)$ yields

$$\frac{\partial f}{\partial x} = \frac{f(x+\Delta x) - f(x)}{\Delta x} + O(\Delta x) \tag{5.9}$$

which is an approximation for the first partial derivative of f with respect to x. This is shown graphically in Figure 5.2. Equation 5.9 calculates the straight line gradient between points C and B. If a set of discrete points is considered and f_i is defined as the value for $f(x)$ at the ith point, then Equation 5.9 may be rewritten as

$$\left.\frac{\partial f}{\partial x}\right|_i = \frac{f_{i+1} - f_i}{\Delta x} + O(\Delta x) \tag{5.10}$$

This equation is known as the first forward difference approximation of $\frac{\partial f}{\partial x}$ of order (Δx). Clearly as the step size is reduced the error term becomes smaller and the approximation more accurate.

Now consider a similar expansion, namely that of $f(x-\Delta x)$ about x.

$$\begin{aligned} f(x-\Delta x) &= f(x) - (\Delta x)\frac{\partial f}{\partial x} + \frac{(\Delta x)^2}{2!}\frac{\partial^2 f}{\partial x^2} - \frac{(\Delta x)^3}{3!}\frac{\partial^3 f}{\partial x^3} + \ldots \\ f(x-\Delta x) &= f(x) + \sum_{n=1}^{\infty}\left[\pm\frac{(\Delta x)^n}{n!}\right]\frac{\partial^n f}{\partial x^n} \quad \begin{cases} + \text{ for even } n \\ - \text{ for odd } n \end{cases} \end{aligned} \tag{5.11}$$

Solving for $\frac{\partial f}{\partial x}$,

$$\frac{\partial f}{\partial x} = \frac{f(x) - f(x-\Delta x)}{\Delta x} + O(\Delta x) \tag{5.12}$$

or

$$\left.\frac{\partial f}{\partial x}\right|_i = \frac{f_i - f_{i-1}}{\Delta x} + O(\Delta x) \tag{5.13}$$

Figure 5.2. A diagrammatic representation of the first forward difference approximation of $\frac{\partial f}{\partial x}$ of order (Δx).

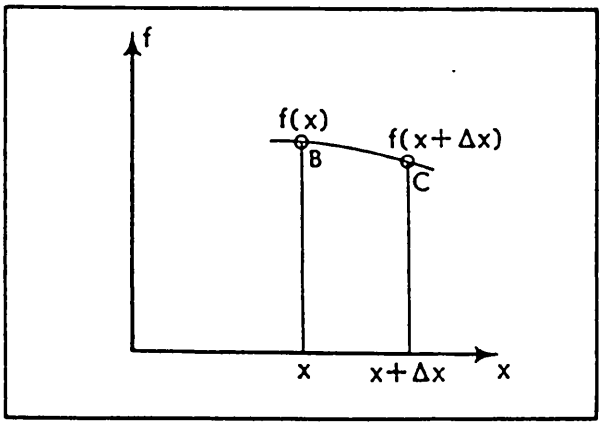
f
f(x)
B
f(x+Δx)
C
x
x+Δx
x

which represents the straight line gradient between points A and B in Figure 5.3. Equation 5.13 is known as the first backward difference approximation of $\frac{\partial f}{\partial x}$ of order (Δx).

Determining expressions for higher order derivatives is a simple process. Consider Equations 5.7 and 5.11, repeated below,

$$f(x+\Delta x)=f(x)+(\Delta x)\frac{\partial f}{\partial x}+\frac{(\Delta x)^2}{2!}\frac{\partial^2 f}{\partial x^2}+\frac{(\Delta x)^3}{3!}\frac{\partial^3 f}{\partial x^3}+\ldots \tag{5.14}$$

and

$$f(x-\Delta x)=f(x)-(\Delta x)\frac{\partial f}{\partial x}+\frac{(\Delta x)^2}{2!}\frac{\partial^2 f}{\partial x^2}-\frac{(\Delta x)^3}{3!}\frac{\partial^3 f}{\partial x^3}+\ldots \tag{5.15}$$

Adding 5.14 and 5.15 and then solving for $\frac{\partial^2 f}{\partial x^2}$ yields,

$$\frac{\partial^2 f}{\partial x^2}=\frac{f(x+\Delta x)-2f(x)+f(x-\Delta x)}{(\Delta x)^2}+O(\Delta x)^2 \tag{5.16}$$

or

$$\left.\frac{\partial^2 f}{\partial x^2}\right|_i=\frac{f_{i+1}-2f_i+f_{i-1}}{(\Delta x)^2}+O(\Delta x)^2 \tag{5.17}$$

Figure 5.3. A diagrammatic representation of the first backward difference approximation of $\frac{\partial f}{\partial x}$ of order (Δx).

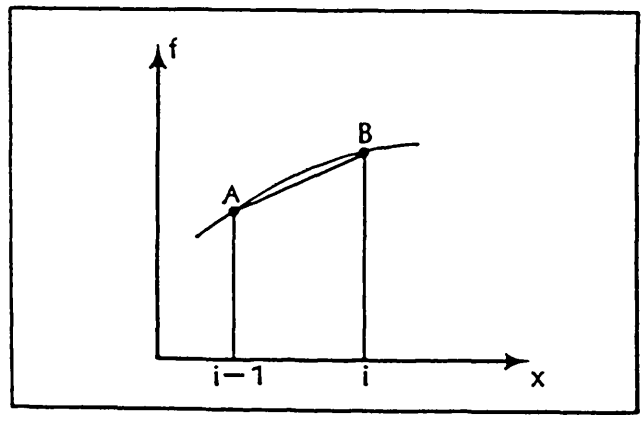
f
B
A
i−1
i
x

5.3 Non Erosional Models.

5.3.1 The Problem.

The first system considered was that of a semi infinite region of substrate, defined by the equation $x > 0$. Initially this region is all at a temperature θ_s. At time $t = 0$, the surface $x = 0$ is raised to, and maintained at, a temperature θ_{surf}. Energy enters the substrate which consequently heats up. Calculation of temperature profiles at later times is required. The reason for choosing to solve this problem is that it has an exact analytical solution, which can be used to check the accuracy of further solutions obtained using numerical modelling.

The analytical solution is

$$\frac{\theta - \theta_s}{\theta - \theta_{surf}} = \text{erfc}\,\frac{x}{2\sqrt{\alpha t}} \qquad (5.18)$$

where α is the thermal diffusivity of the substrate (Turcotte, and Schubert, 1982). In order to be able to obtain temperature profiles for different values of the parameters, a computer program called erfc.c was written that outputs the temperature profiles after chosen amounts of time for different values of substrate temperature, surface temperature and thermal diffusivity. A listing is shown in Appendix C1. Figure 5.4 shows the results corresponding to an initial substrate temperature of 300 K, a surface temperature of 1500 K, and a thermal diffusivity of 5.07×10^{-7} m^2 s^{-1}. Temperature profiles for 1, 2, 3, 4, 5 and 10 hours are shown.

Figure 5.4. The graph shows temperature profiles within the substrate for an initial substrate temperature of 300 K, a surface temperature of 1500 K, and a thermal diffusivity of 5.07 $\overset{\text{x } 10^{-7}}{\wedge}$ m^2 s^{-1}. The profiles were produced using the program erfc.c (Appendix C1), and represent the analytical solution to the heat conduction problem.

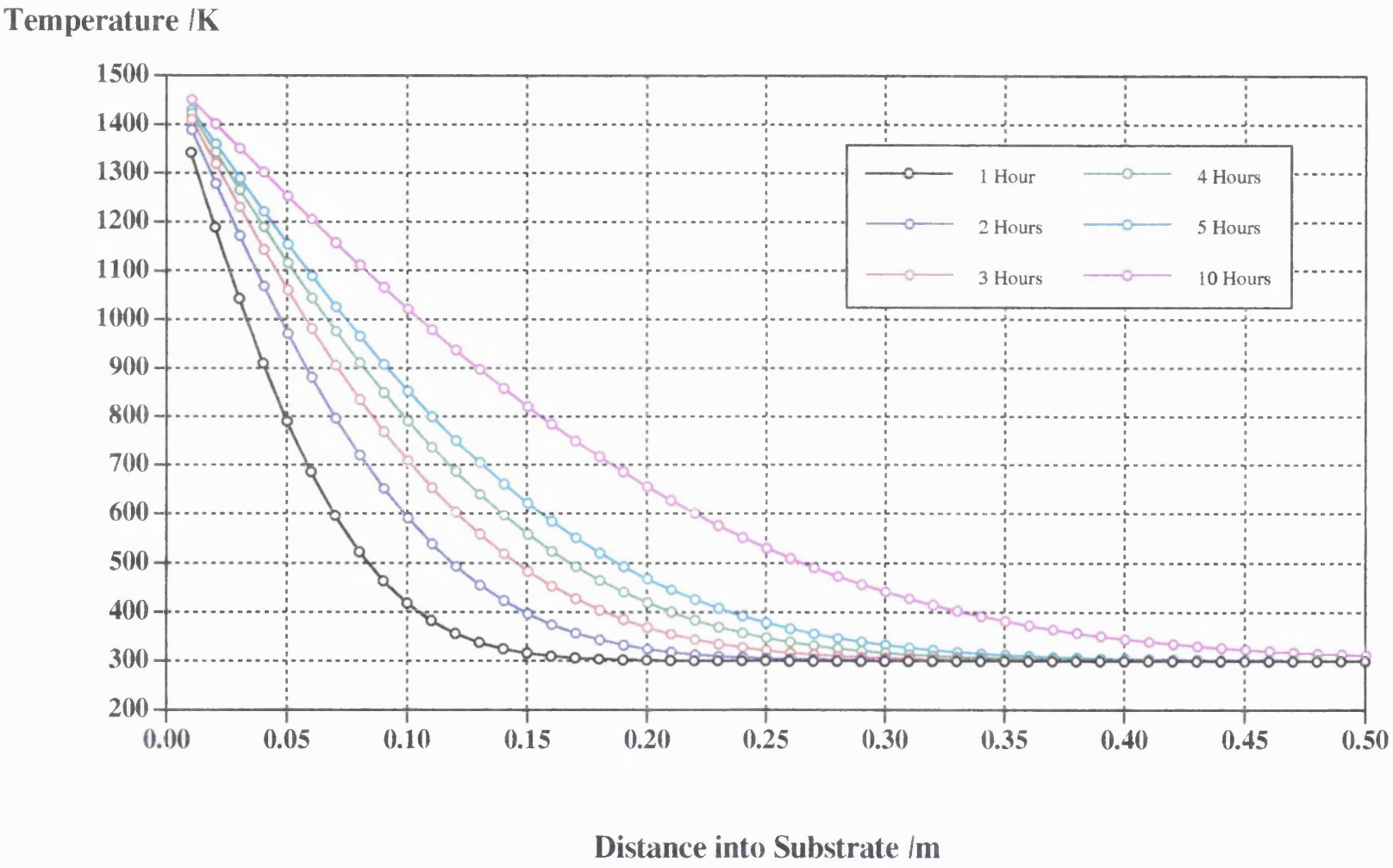
Temperature /K
1500
1400
1300
1200
1100
1000
900
800
700
600
500
400
300
200
0.00
0.05
0.10
0.15
0.20
0.25
0.30
0.35
0.40
0.45
0.50
1 Hour
2 Hours
3 Hours
4 Hours
5 Hours
10 Hours
Distance into Substrate /m

5.3.2 The First Model.

The first numerical model is based on the principle of finite differences. The substrate is broken down into a set of discrete points, all a distance Δx apart (Figure 5.5), each one representing a plane parallel to the surface of the substrate. Using finite differences, the differential equations dictating the temperature within the substrate with time can be expressed in a form where they are simply a function of the temperatures at the discrete points within the substrate. Since the temperatures at these planes will vary with time, it is necessary to calculate temperatures at specific times, the interval between these times, or time step (Δt), being constant. Thus the time at the nth plane after the pth time step is expressed as $\theta_{n,p}$. What is required is an expression for the temperature at the nth plane, after a time step, as a function of the temperatures of neighbouring planes before the time step. i.e. the calculation of $\theta_{n,p+1}$ as a function of $\theta_{n-1,p}$ and $\theta_{n+1,p}$ etc.. .

The equation to be solved is the heat conduction equation

$$\frac{\partial \theta}{\partial t} = \alpha \frac{\partial^2 \theta}{\partial x^2} \tag{5.19}$$

From section 5.2 the two partial differentials can be replaced by expressions containing the temperatures at the points in the finite difference lattice.

$$\left.\frac{\partial \theta}{\partial t}\right|_{n,p} = \frac{\theta_{n,p+1} - \theta_{n,p}}{\Delta t} \tag{5.20}$$

and

$$\left.\frac{\partial^2 \theta}{\partial x^2}\right|_{n,p} = \frac{\theta_{n+1,p} + \theta_{n-1,p} - 2\theta_{n,p}}{\Delta x^2} \tag{5.21}$$

Figure 5.5. Finite difference modelling works by breaking the substrate up into a discrete set of points, each point representing a plane parallel to the surface of the substrate.

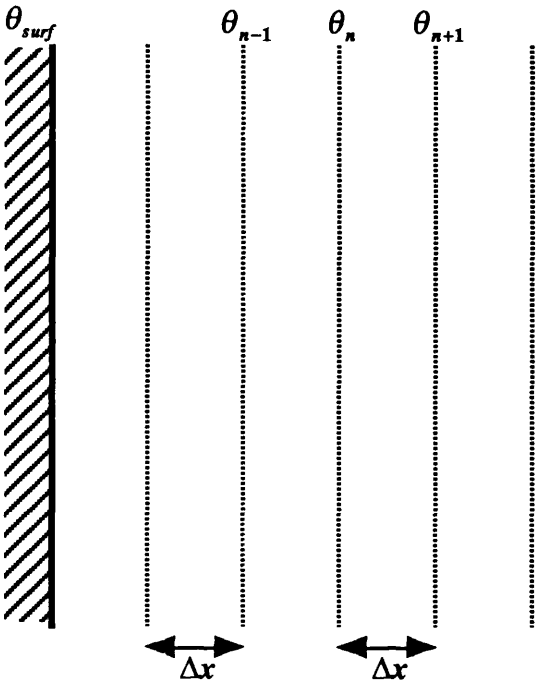
θ_{surf}
θ_{n-1}
θ_n
θ_{n+1}
Δx
Δx

Substituting these into 5.19 gives

$$\theta_{n,p+1} = \theta_{n,p} + \frac{\alpha \Delta t}{\Delta x^2}\left(\theta_{n+1,p} + \theta_{n-1,p} - 2\theta_{n,p}\right) \qquad (5.22)$$

Whilst it is possible to calculate a simple model by hand, this is not feasible when the number of points in the finite difference lattice becomes large. This method of numerical modelling does however lend itself to the use of computers when large systems are being considered. To this end a computer program implementation of this model, called fd.c, was written, and a full listing is shown in Appendix C2.

When run, the program produces the temperature profile within the substrate after one hour. This takes the form of two tab delimited columns of results, the first column showing the distance into the substrate and the second column the appropriate temperature. The results are shown in Figure 5.6, along with the results from the analytical solution. It can be seen that the results match well.

5.3.3 The Second Model.

The second numerical model consists of a slight modification of the previous model. It uses energy as its main modelling parameter as opposed to temperature. The model calculates the net energy transfer by conduction between all the cells in the model. The reason for this is that energy is a conserved quantity, and thus when melting of the substrate is to be modelled it is the logical choice of parameter. Therefore this model is an intermediate step between the first model and the final erosional model.

Figure 5.6. The results from fd.c (Appendix C2) which solved the semi-infinite substrate problem using numerical techniques. The one hour profile is shown together with the results from the analytical solution.

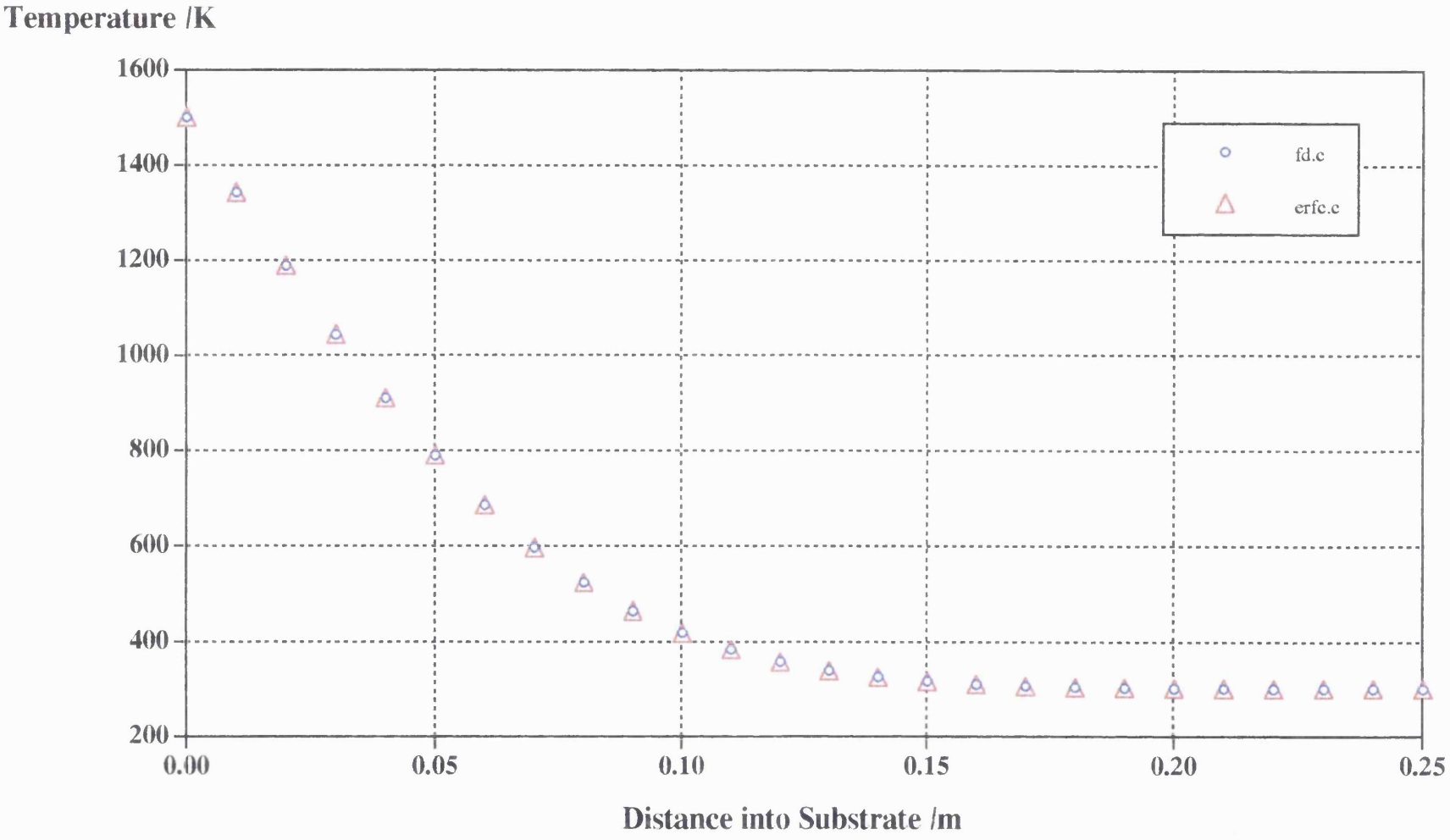
Temperature /K
1600
1400
1200
1000
800
600
400
200
0.00
0.05
0.10
0.15
0.20
0.25
Distance into Substrate /m
fd.c
erfc.c

This model consists of a one dimensional array of cells, each cell representing a small element of substrate. It is assumed that within a cell the energy density is homogeneous. All cells are of a constant thickness Δx. Initially all the cells are at the same temperature, θ_s. At a time $t = 0$, the upper cell is held constant at some temperature, θ_{surf}, higher than the initial substrate temperature. As time increases, energy is conducted down through the cells, increasing their temperature. Within each time step the net energy flow into or out of all cells is calculated using the temperatures of the cells at the beginning of the time step. At the end of each time step all the cell temperatures are updated, and the process begins again for the next time step.

As Δx is the thickness of the cell, the energy required per unit cross-sectional area to raise the temperature of a cell by one Kelvin is

$$\rho c \Delta x \tag{5.23}$$

where ρ and c are the density and specific heat capacity of the substrate respectively. Thus the uppermost cell in the model is given an initial energy of

$$\rho c \Delta x \, \theta_{surf} \tag{5.24}$$

and the rest of the cells have an initial energy of

$$\rho c \Delta x \, \theta_s \tag{5.25}$$

In order to illustrate how the net energy gain by one cell during a particular time step is calculated, consider Figure 5.7. This shows three cells, with energies E_1, E_2, E_3. The respective temperatures θ_1, θ_2, θ_3 are given by the equation

$$\theta_n = \frac{E_n}{\rho c \Delta x} \tag{5.26}$$

Figure 5.7. A diagram depicting three cells within the finite difference lattice with energies E_1, E_2 and E_3 respectively.

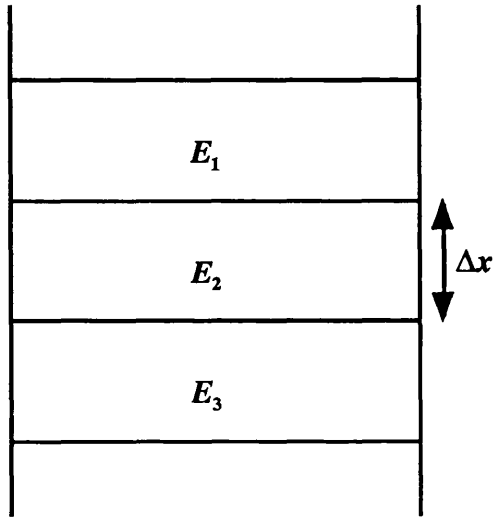
E_1
E_2
E_3
Δx

Thus the rate of heat flow by conduction from cell 2 to cell 1 is

$$-k\frac{\theta_1-\theta_2}{\Delta x}=-k\frac{E_1-E_2}{\rho c(\Delta x)^2} \tag{5.27}$$

Similarly the heat flow from cell 3 to cell 2 is

$$-k\frac{E_2-E_3}{\rho c(\Delta x)^2} \tag{5.28}$$

Therefore the net heat flow rate into cell 2 is 5.28 - 5.27, i.e.

$$k\frac{(E_1+E_3-2E_2)}{\rho c(\Delta x)^2} \tag{5.29}$$

Thus the net gain by cell n during one time step of duration Δt is

$$k\frac{(E_{n+1}+E_{n-1}-2E_n)}{\rho c(\Delta x)^2}\Delta t \tag{5.30}$$

and the temperature increase of the cell is

$$\Delta\theta=k\frac{(E_{n+1}+E_{n-1}-2E_n)}{\rho^2 c^2(\Delta x)^3}\Delta t \tag{5.31}$$

The validity of this equation can be tested by dimensional analysis as follows,

$$\left.\begin{aligned}&[k]=Jms^{-1}K^{-1},\quad [\rho]=kgm^{-1},\quad [c]=Jkg^{-1}K^{-1}\\&\Rightarrow[\Delta\theta]=\frac{Jms^{-1}K^{-1}\quad J\quad s}{kg^2m^{-2}\quad J^2kg^{-2}K^{-2}\quad m^3}\\&\Rightarrow[\Delta\theta]=\frac{J^2mK^{-1}}{J^2mK^{-2}}\\&\Rightarrow[\Delta\theta]=K\end{aligned}\right\} \tag{5.32}$$

This shows that it has the dimension of temperature as expected.

During each time step checks are made as to how far into the substrate energy has permeated. If the bottom-most cell in the model has an influx of energy, then another cell is added below it with an energy given by Equation 5.25, to ensure that the lower boundary condition $\theta(x \rightarrow \infty) = \theta_s$ is not violated. The computer program for this model is called heating.c and a full listing is in Appendix C3. Figure 5.8 shows the results from heating.c together with the corresponding analytical solution. It can be seen that the results match well. The computer implementation of the model allows for several temperature profiles to be calculated simultaneously. The output consists of several tab delimited columns, each column representing the temperature profile within the substrate at a time decided by the variables at the beginning of the code.

5.3.4 Tests.

One important test of any finite difference model is that its results are independent of Δx, the cell size used, i.e. the model should give the same temperature for a point in the substrate after a given time. If the model is run for a second time with a Δx half of that for the initial run then the same temperature should be calculated at the 10th and 20th lattice point respectively. In order to test this model several runs were performed using Δxs of 0.005, 0.01, 0.02 and 0.05 m. The 1 hour profiles are shown in Figure 5.9. They indicate that the heating model is Δx stable. One important feature to note from the graph is how the points representing a Δx of 0.05 m vary slightly from the curve produced by the other points. Equation 5.16 shows that the finite difference approximation for the heat conduction equation has an associated error of $O(\Delta x)^2$, due to the terms in

Figure 5.8. The results from heating.c (Appendix C3) which uses energy as the modelling parameter. The appropriate analytical solutions are also shown.

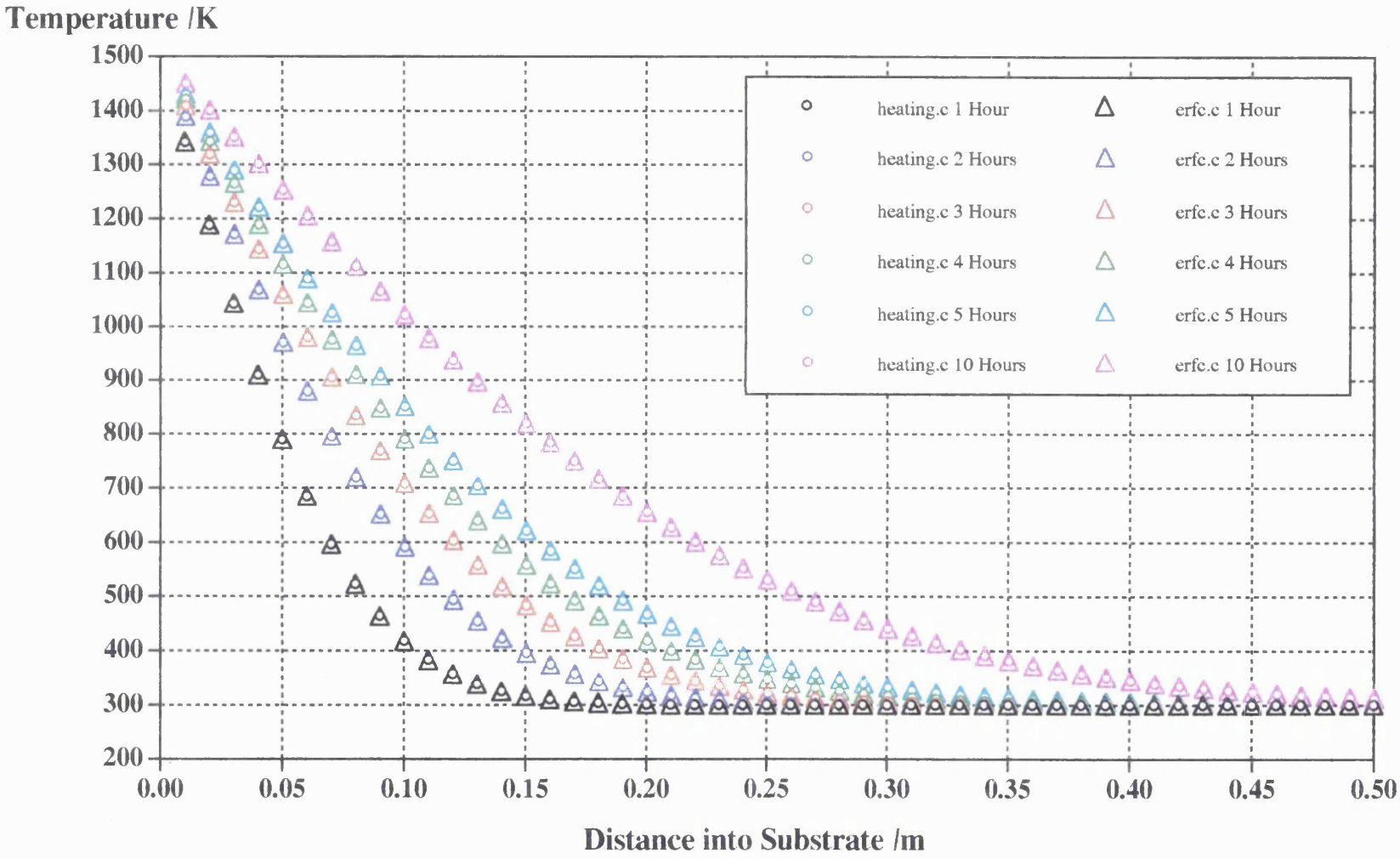
Temperature /K
1500
1400
1300
1200
1100
1000
900
800
700
600
500
400
300
200
0.00
0.05
0.10
0.15
0.20
0.25
0.30
0.35
0.40
0.45
0.50
Distance into Substrate /m
heating.c 1 Hour
heating.c 2 Hours
heating.c 3 Hours
heating.c 4 Hours
heating.c 5 Hours
heating.c 10 Hours
erfc.c 1 Hour
erfc.c 2 Hours
erfc.c 3 Hours
erfc.c 4 Hours
erfc.c 5 Hours
erfc.c 10 Hours

Figure 5.9. heating.c was run several times using different values for Δx. The results show that the program is stable with respect to the size of Δx.

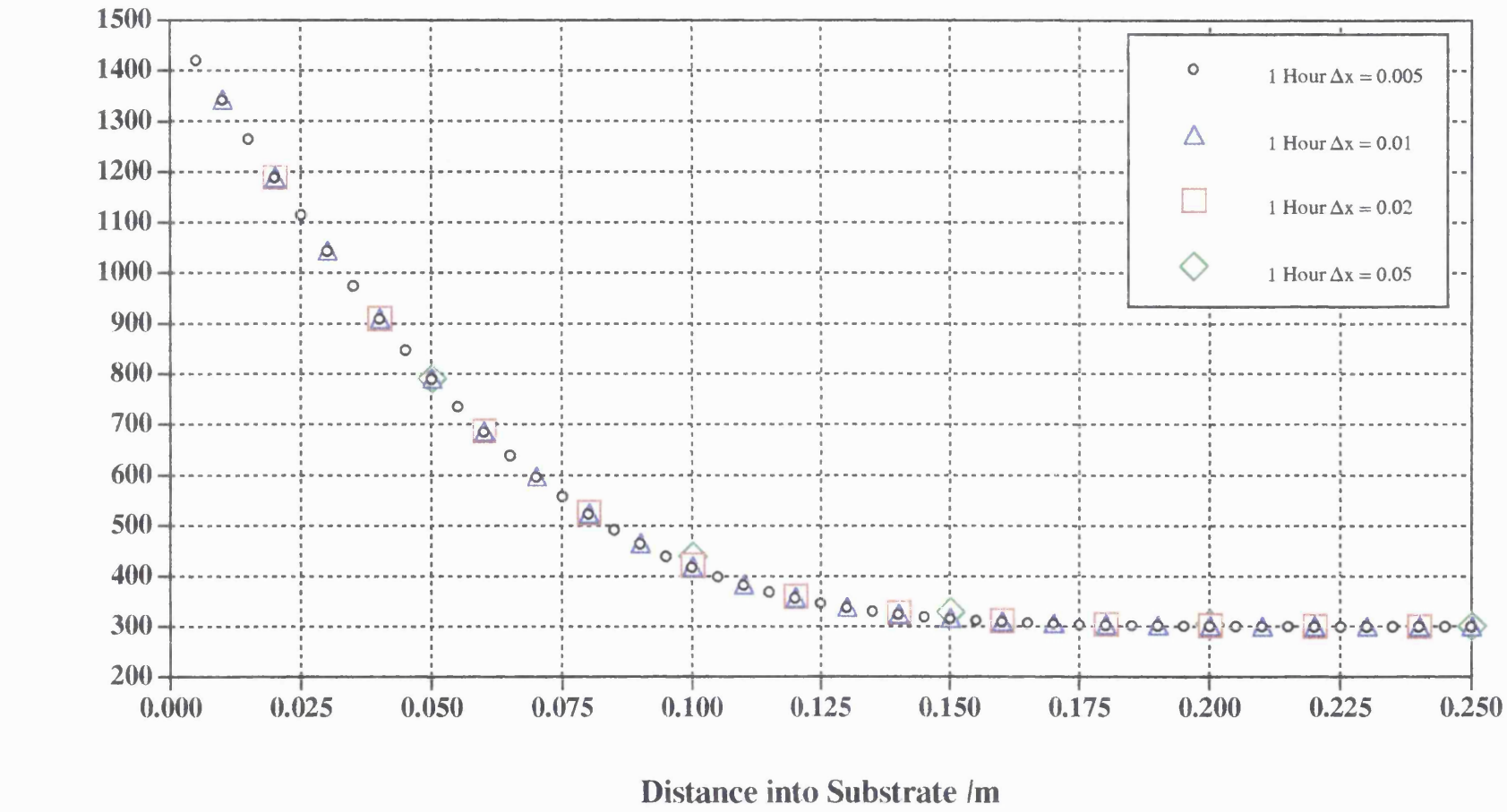
Temperature /K
1500
1400
1300
1200
1100
1000
900
800
700
600
500
400
300
200
0.000
0.025
0.050
0.075
0.100
0.125
0.150
0.175
0.200
0.225
0.250
Distance into Substrate /m
1 Hour Δx = 0.005
1 Hour Δx = 0.01
1 Hour Δx = 0.02
1 Hour Δx = 0.05

Equation 5.15 which are not used. Figure 5.9 shows that this error is not significant until Δx is in the region of 0.05.

Any finite difference model will breakdown if the time step chosen is too large (Rogers and Mayhew, 1980). The limiting criterion of the relevant parameters is that

$$\frac{\alpha \Delta t}{\Delta x^2} \leq \frac{1}{2} \tag{5.33}$$

Using a Δx of 0.01 m and a thermal diffusivity of 5.07 x 10^{-7} yields a maximum time step of 98 seconds. A further criterion used in the modelling is that the amount of energy transferred between any two cells during one time step must not exceed 1 to 2% of the total cell energy. The maximum exchange of energy occurs at the beginning of the solution and is between the top two cells in the model as this is where the greatest temperature difference exists. As time progresses the maximum temperature difference between two cells in the model becomes smaller and therefore the maximum permissible time step increases. It is therefore possible to run the model with a dynamic time step that is always the maximum allowed for the system at the time.

5.4 The Erosion Model.

As some of the channels revealed by Magellan appeared to possibly have an erosional profile it was decided to investigate the process of thermal erosion of a substrate by a lava. The main problem with trying to solve a system involving the melting of a substrate is latent heat. This is the energy required to break the molecular bonds within a solid letting it change phase from a solid to a liquid. The presence of latent heat means that an analytical solution of the problem does

not exist. One way of trying to simulate the process is to use mathematical modelling.

Once melting of the substrate occurs, the error function solution to the heat conduction equation (5.18) can no longer be used to give a value for the heat flux into the substrate. The model, on the other hand, by allowing for how latent heat affects heat flow, can be used to investigate the erosion process.

The model is based on the second heating model. It too considers an array of cells and calculates the energy transfer by conduction between them. A diagrammatic representation of the model is shown in Figure 5.10. The model simulates lava flowing over a substrate by using the uppermost cell to represent the lava and the rest of the cells to represent the substrate. The problem being modelled is simplified by assuming that the region being considered is close to the source of the lava so that the lava will not have had time to cool appreciably. Thus the boundary condition at the top of the model is simply that the lava in contact with the top layer of substrate is at a constant temperature. This is simulated within the model by keeping the uppermost cell, corresponding to a position just inside the lava, at a constant energy density, equivalent to the lava temperature required. The interface between the liquid lava and the solid substrate is represented by a liquid substrate boundary layer of constant thickness. The thickness of this layer will depend on the flow characteristics of the lava above it. The lower boundary condition to be modelled is that as distance into the substrate increases the temperature tends towards the initial substrate temperature. The lower boundary in the model is kept at the initial substrate temperature by dynamically adding new cells as required.

Modelling of the melting of the substrate is achieved as follows. As energy enters a cell representing an element of solid substrate its temperature

Figure 5.10. The diagram shows the structure of the erosional model which is implemented using erosion.c (Appendix C4).

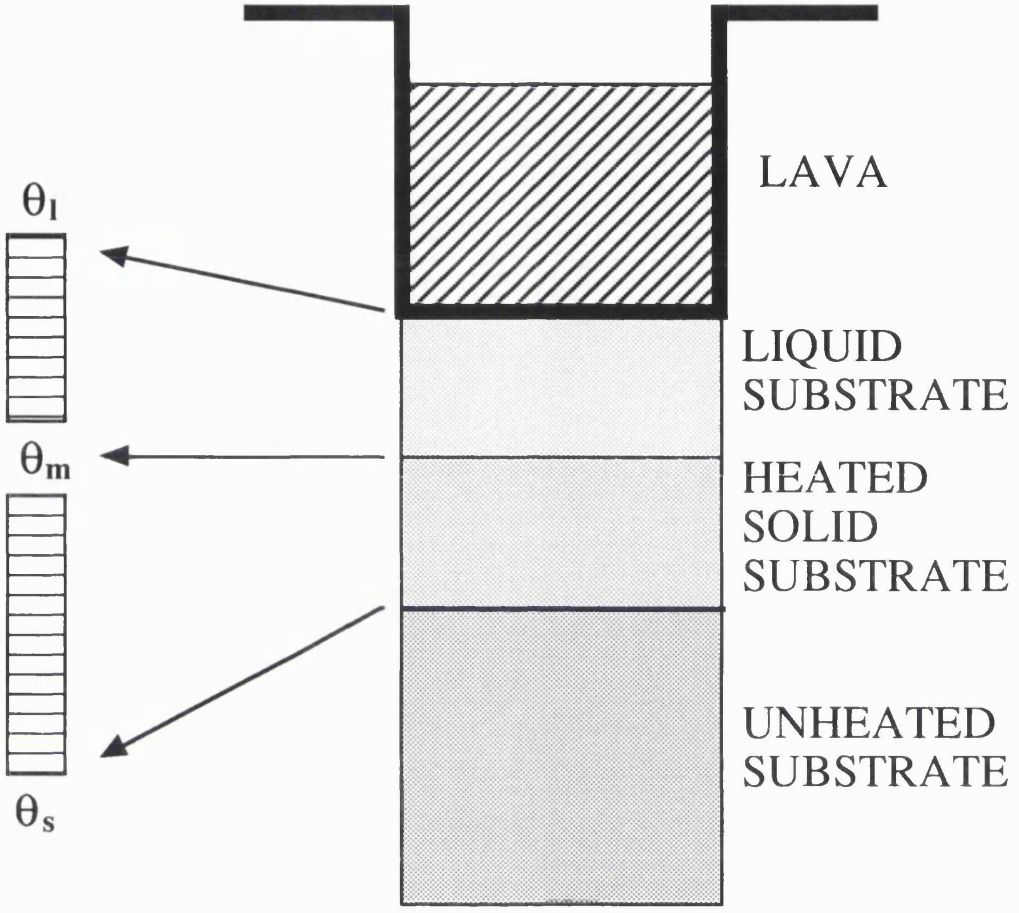
LAVA
θ_l
LIQUID
SUBSTRATE
θ_m
HEATED
SOLID
SUBSTRATE
UNHEATED
SUBSTRATE
θ_s

increases until it reaches the melting temperature. At this point the temperature of the cell is kept constant even though energy continues to enter the cell. When the amount of energy that has entered the cell since it reached melting temperature is equal to the latent heat of the cell, the cell is then assumed to have entered the liquid phase. As cells of the solid substrate are melted, and become part of the liquid substrate boundary layer, the uppermost cell of the boundary layer is removed and replaced by lava. This is done to make sure that the liquid boundary layer remains a constant thickness. The use of an exact melting temperature for the substrate is an approximation as the substrate actually has a melting range defined by its solidus and liquidus temperatures.
*

As it is a steady erosion rate that is being calculated, an initial temperature profile is put into the substrate in order to speed up the settling down of the model. Clearly the error function solution to the heating problem will be a good approximation to the equilibrium profile and therefore that is used; the time for the profile is chosen so that the number of cells with a temperature between the lava and melt temperature is equal to the number of cells required to produce the desired thickness of liquid substrate boundary layer.

The computer program implementation of the model, called erosion.c, is shown in Appendix C4. A full description of the experiments undertaken using the model is discussed in chapter 6. An explanation of what happens during one run of the model is shown below.

Initially the parameters to be used for the run are defined. These include factors such as the thermal and physical properties of the lava and substrate (density, thermal conductivity, initial temperature, melting temperature of the substrate and latent heat.), factors related to the mathematical running of the model (cell size, time step, boundary layer thickness and the initial temperature

* As the model is one dimensional it does not consider the fluid dynamics of the lava flow.

profile to be set up within the substrate) and the times at which temperature profiles within the substrate are required. All of these remain constant during one run of the model. Next, variables which are a function of the parameters just defined are calculated.

The first of these is called e_rock and is defined as the amount of energy required to raise the temperature of a cell by one Kelvin.

$$\text{e\_rock} = \Delta x \times \rho \times c \tag{5.34}$$

The latent heat of an element of solid substrate is defined by qt_rock, where

$$\text{qt\_rock} = \Delta x \times \rho \times L \tag{5.35}$$

The amount of internal energy that a cell has if it has just reached its melting temperature is stored in the variable rocksolid, where

$$\text{rocksolid} = \theta_m \times \text{e\_rock} \tag{5.36}$$

Similarly the internal energy required for a cell to enter the liquid phase is given by rockliquid;

$$\text{rockliquid} = (\theta_m \times \text{e\_rock}) + \text{qt\_rock} \tag{5.37}$$

Once a cell is assumed to have been removed and replaced by lava it is given an energy density equivalent to the lava temperature. This variable is called lavaenergy and is defined by

$$\text{lavaenergy} = (\theta_l \times \text{e\_rock}) + \text{qt\_rock} \tag{5.38}$$

Next the thermal diffusivity of the substrate is calculated.

$$\alpha = \frac{k}{\rho c} \tag{5.39}$$

The number of cells in the liquid substrate boundary layer is calculated by dividing the desired boundary layer thickness by the cell size. This result is stored in the variable bl_cell_no

$$\text{bl\_cell\_no} = \frac{\Delta B}{\Delta x} \tag{5.40}$$

where ΔB is the boundary layer thickness.

Having determined all the variables to be used during the run, the next step is to calculate the initial temperature for the cells. The start-up temperature profile is produced using an adaptation of the erfc.c program (Appendix C1). The time used for the temperature profile is chosen so that the number of cells with temperatures greater than the melt temperature of the substrate but lower than the lava temperature is the same number as is necessary to produce the required thickness of liquid substrate boundary layer.

Within each time step the model calculates the transfer, by conduction, of energy between all the cells and also makes a number of tests. The first of these consists of checking whether the lowest cell in the model has increased in temperature above the initial substrate temperature. If this is positive then another cell is added below it with an energy density equivalent to the initial substrate temperature. There is also a test to check whether or not the uppermost cell of the solid substrate has entered the liquid phase. If this is so, then the cell representing the top of the liquid boundary layer is given an energy density corresponding to

the lava temperature in order to simulate it being replaced by the lava. Also the time at which the cell was "eroded" is noted as well as the number of time steps that has passed since the previous cell was removed. The last test consists of checking whether the length of time simulated is equal to one of the times for which a temperature profile is required. If that is the case then the current temperature profile is stored in the next column of the results.

The results from the run are stored in a tab delimited array. The first column contains the distance into the substrate that the data in the other columns correspond to. The second column contains the time step during which the cell entered the liquid phase and the third column the number of timesteps that have elapsed since the previous cell was removed. The initial temperature profile is stored in the fourth column. Subsequent columns contain temperature profiles within the substrate, with each row representing temperatures at the same depth in the substrate and each column representing the temperatures within the substrate at a given time. The first and fourth columns are calculated just before the main body of the program.

Finally, after the designated amount of time has been simulated, the results are printed out.

This section has explained the theory behind a model for thermal erosion by lava. A series of experiments conducted using this model to investigate the erosion process are described in the next chapter.

Chapter 6
Parametric Study of Thermal Erosion

6.1 Introduction.

This chapter contains the results from the experiments undertaken to look at thermal erosion by lava using the model discussed in the previous chapter. In order to obtain as comprehensive a series of results as possible, several sets of numerical experiments were performed. Each set evaluates the sensitivity of the erosion rate to a particular parameter, by changing the value of the parameter by small amounts between each run.

One of the main problems in modelling the erosion process is that there are no exact values for properties such as density and thermal conductivity for liquid lavas. Instead approximate values obtained from experiments on cooled lava samples are used. However these may be very different from the actual values associated with a fluid lava, where factors such as vesicularity may continuously change parameters such as density, and hence the heat flow. The results shown here indicate how the thermal properties of the lava and the substrate influence the amount of erosion that occurs.

Before considering the results of all the experiments undertaken, we shall look at one particular run in detail in order to illustrate how the experiments were implemented. The run in question used a lava temperature of 1500 K, a melting temperature of 800 K and an initial substrate temperature of 300 K. A full list of the parameters used can be found in Table 6.1. It was assumed that all the latent heat of a solid cell had to be provided before that cell entered the liquid phase. Initially a suitable start-up time had to be chosen to ensure that the correct

Table 6.1. A list of the parameters used in the example run of the erosional model.

Parameter	Value
Lava Temperature	1500 K
Initial Substrate Temperature	300 K
Melting Temperature	800 K
Substrate Density	2700 kg m^{-3}
Solid Substrate Thermal Conductivity	1 J s^{-1} m^{-1} K^{-1}
Liquid Substrate Thermal Conductivity	1 J s^{-1} m^{-1} K^{-1}
Lava Thermal Conductivity	1 J s^{-1} m^{-1} K^{-1}
Substrate Specific Heat Capacity	730 J kg^{-1} K^{-1}
Substrate Latent Heat	5.0×10^5 J kg^{-1}
Cell Size	1 cm
Time Step	6 s
Boundary Layer Thickness	10 cm
Start-Up Time	4.5 hours

temperature profile within the substrate was generated for the required liquid boundary layer thickness. Figure 6.1 and Table 6.2 show the initial temperature profile used for this run. The time used is 4.5 hours and it can be seen that there are 10 cells with temperatures greater than the melt temperature and less than the lava temperature, corresponding to a boundary layer thickness of 10 cm, as required.

The results from the model are plotted in Figure 6.2, where temperature is depicted against vertical distance into the rock. As the lava flows over the substrate, we observe the formation of a thermal interface of solid substrate between the liquid substrate and the unheated ground rock. Across this interface the temperature drops from melt temperature at the top to the initial substrate temperature at its base. As the experiment progresses, the thermal interface moves downward at a constant rate, the erosion rate. It can be seen that after an initial relaxation period, the erosion rate becomes constant. This is reflected in the diagram by the fact that the lines all have the same profile, and that they are equally spaced. A complete set of results output from the run can be found in Appendix D.

For a particular run, as the time simulated increases, the number of time steps elapsing between cells being removed tends towards a constant value as the erosion rate becomes steady. A plot of this parameter against cell number is shown in Figure 6.3. Once a value has been obtained it is simply a question of multiplying by the magnitude of the time step to get the time taken in seconds to remove one cell of substrate, and it is then straightforward to calculate the erosion rate with the units cm day^{-1}. In our example, once a steady state is reached, cells are removed at the rate of one every 770.5 time steps. This corresponds to an erosion rate of 18.69 cm day^{-1}.

Figure 6.1. A graph showing the initial temperature profile set up within the substrate at the beginning of the run.

Table 6.2. The data for the initial substrate temperature profile.

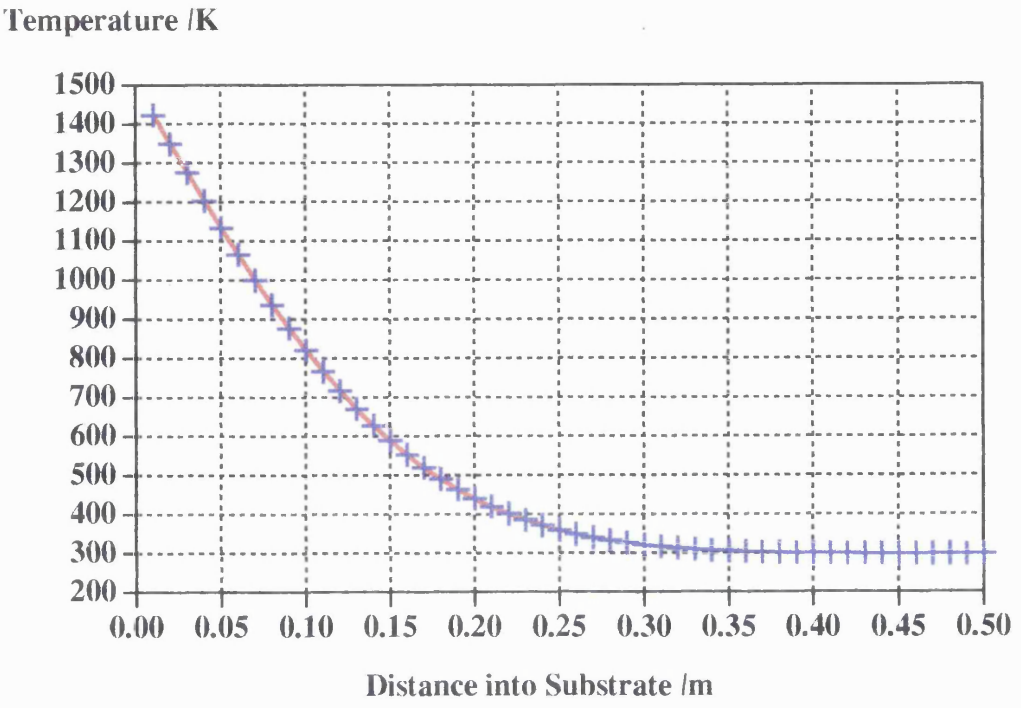

Distance /m	Initial Temperature /K	Distance /m	Initial Temperature /K
0.01	1425	0.26	351
0.02	1351	0.27	342
0.03	1278	0.28	335
0.04	1206	0.29	328
0.05	1136	0.30	323
0.06	1068	0.31	319
0.07	1002	0.32	315
0.08	939	0.33	312
0.09	879	0.34	310
0.10	822	0.35	308
0.11	769	0.36	306
0.12	719	0.37	305
0.13	673	0.38	304
0.14	630	0.39	303
0.15	590	0.40	302
0.16	554	0.41	302
0.17	522	0.42	301
0.18	492	0.43	301
0.19	466	0.44	301
0.20	443	0.45	301
0.21	422	0.46	300
0.22	403	0.47	300
0.23	387	0.48	300
0.24	373	0.49	300
0.25	361	0.50	300

Figure 6.2. Temperature profiles within the substrate. As the experiment progresses the profile stays the same shape indicating that an equilibrium has been reached. In this run a lava temperature of 1500 K was used together with a melting temperature of 800 K and an initial substrate temperature of 300 K.

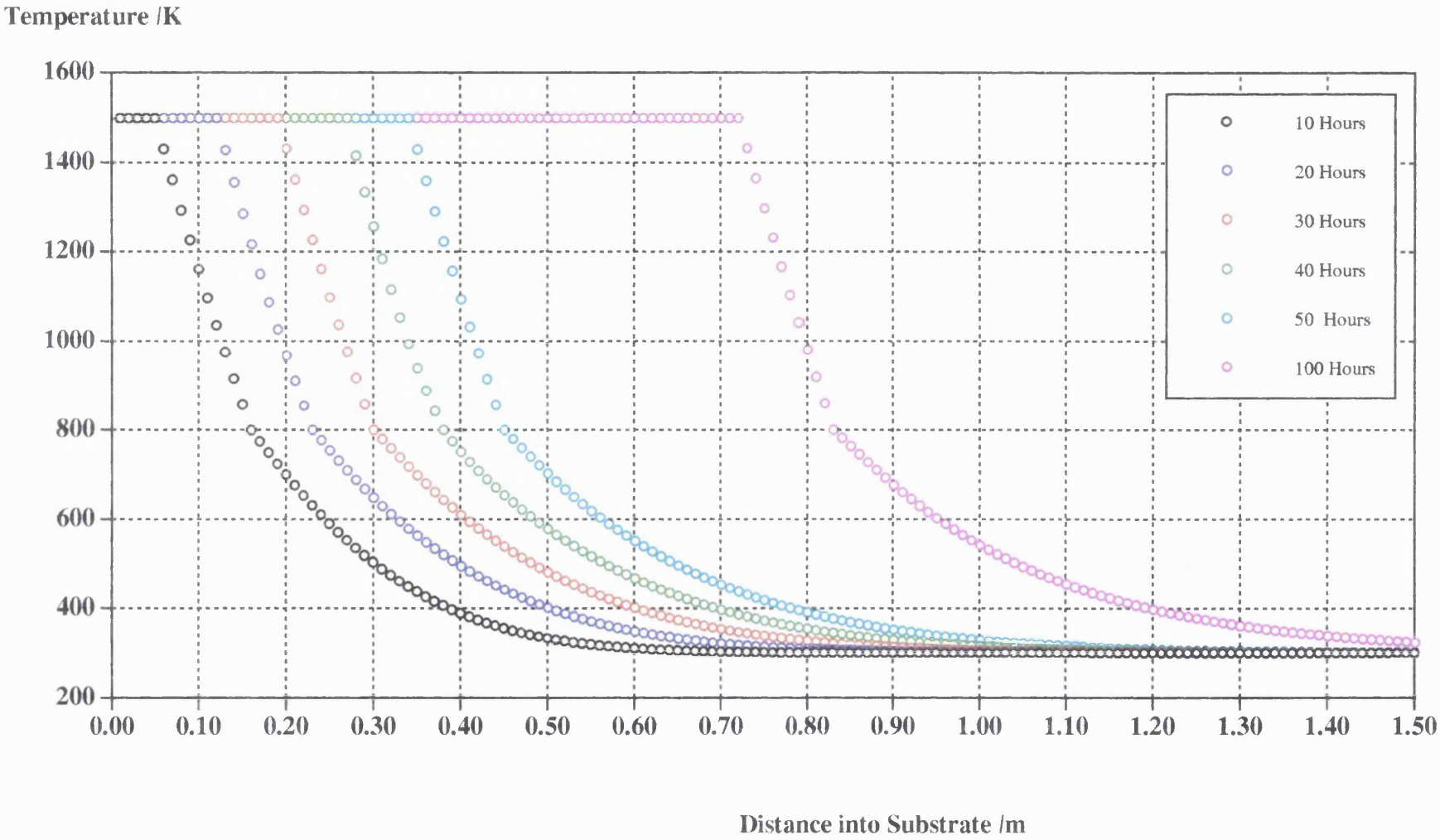
Temperature /K
1600
1400
1200
1000
800
600
400
200
0.00
0.10
0.20
0.30
0.40
0.50
0.60
0.70
0.80
0.90
1.00
1.10
1.20
1.30
1.40
1.50
10 Hours
20 Hours
30 Hours
40 Hours
50 Hours
100 Hours
Distance into Substrate /m

Figure 6.3. The number of time steps required to melt each cell of solid substrate. This tended to a value of 770.5, corresponding to an erosion rate of 18.69 cm day^{-1}.

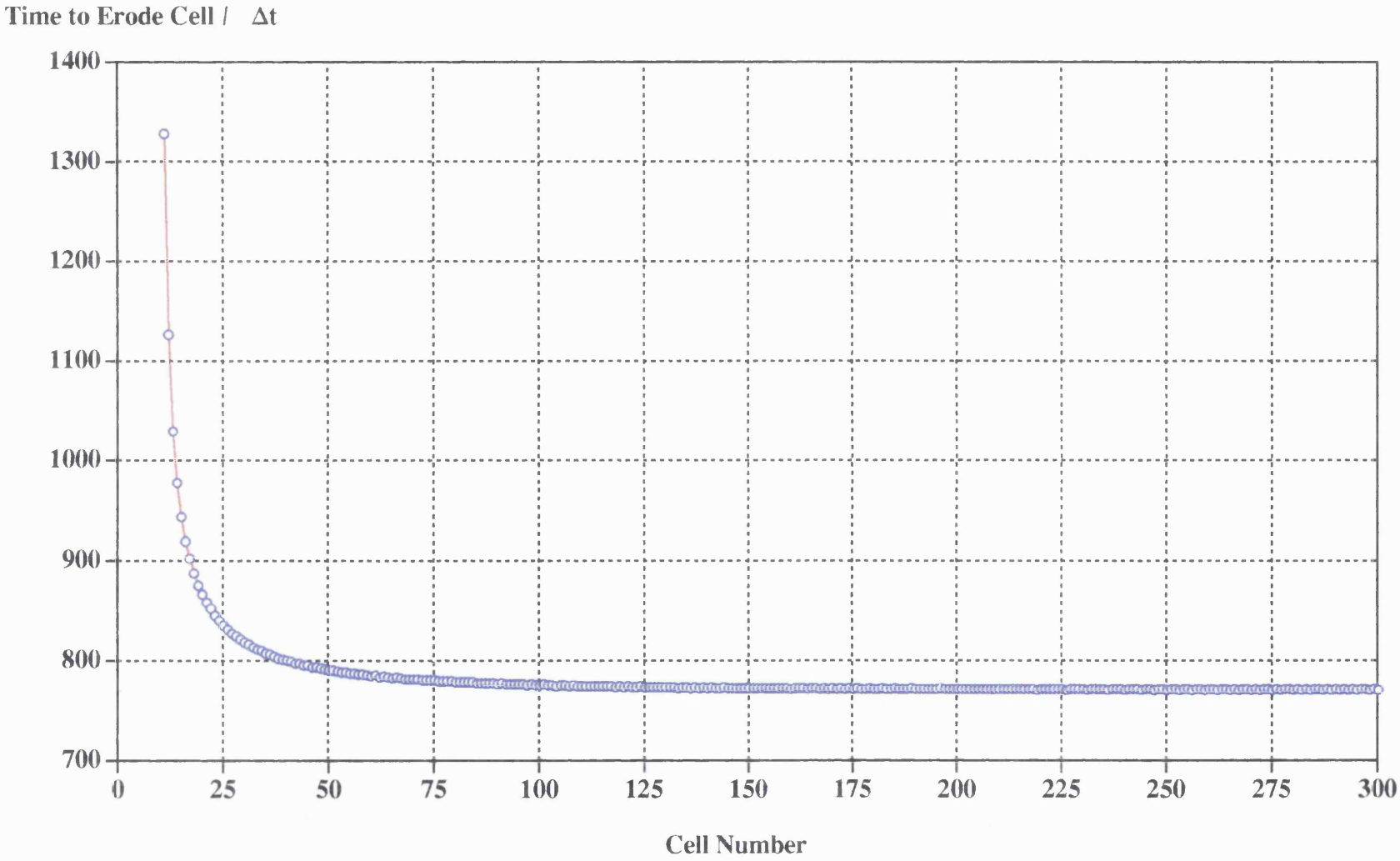
Time to Erode Cell / Δt
1400
1300
1200
1100
1000
900
800
700
0
25
50
75
100
125
150
175
200
225
250
275
300
Cell Number

Another factor which can be considered is how quickly the system settles down to the final erosion rate. An approximate figure which is useful primarily for a comparative study can be calculated by determining the time it takes the system to get within 10% of the final erosion rate. This is done by combining the start up time of 4.5 hours with the time taken for the model to predict an erosion rate equal to 90% of the final erosion rate, i.e. 16.82 cm day^{-1}. This corresponds to the removal of a cell every 856 time steps. Consideration of the results in Appendix D shows that the 21st cell was removed during the 10710th time step of the run and 858 time steps after the previous cell. The 22nd cell was removed during the 11562nd time step of the run and 852 time steps after the 21st cell. Assuming a linear change in erosion rate between the two, extrapolation shows that the required erosion rate of one cell every 856 time steps occurred during the 10994th time step, or 18.32 hours into the run. Therefore the total time taken for the system to reach to within 10% of the final erosion rate is 22.82 hours.

6.2 The Experiments.

6.2.1 Consideration of Different Temperatures and Latent Heat.

The first sets of experiments investigate the sensitivity of the erosion process to lava temperature, initial substrate temperature, melting temperature and percentage of latent heat that has to be supplied before the substrate enters the liquid phase. A list of the variables used is shown in Table 6.3. No assumptions are made on the composition of actual lavas or substrates; the purpose of these experiments is simply to investigate the sensitivity of the erosion process with respect to the different parameters.

Table 6.3. A list of the variables used in the experiments conducted to look at the sensitivity of the erosion rate to lava temperature, melting temperature, initial substrate temperature and latent heat.

Set	θ_l /K	θ_s /K	θ_m /K	% Latent Heat	Boundary Layer /cm
1	900 - 1900	300	800	100	10
2	1500	300	700 - 1400	100	10
3	1500	300 - 900	1000	100	10
4	1500	300	1000	0 - 100	10

The first set of experiments considers how the erosion rate is affected by the lava temperature. The melting and initial substrate temperatures were kept constant while a range of lava temperatures were implemented. This represents variations in the composition of the lava being erupted. For each run a different start-up time must be used within the program to generate the correct initial temperature profile for the required liquid boundary layer thickness. A complete list of the start-up times used is shown in Table 6.4. The calculated erosion rates are shown in Figure 6.4 and Table 6.5. The times taken for the erosion rate to get to within 10% of the steady state value for the different runs are listed in Table 6.5, and plots of this time versus lava temperature and erosion rate are shown in Figures 6.5 & 6.6 respectively.

In order to represent differences in composition of the substrate, only the melting temperature was changed during the second set of experiments. A list of the start-up times is shown in Table 6.6. The erosion rates determined are shown in Figure 6.7 and Table 6.7. Table 6.7 also contains the times taken for the erosion rate to settle down to within 10% of the steady state value. Graphs depicting this time versus melting temperature and erosion rate are shown in Figures 6.8 & 6.9 respectively.

In the third set of experiments run, the initial substrate temperature was the only parameter to be varied. This was done to simulate the eruption process occurring on different planetary bodies. The start-up times used are in Table 6.8 and the predicted erosion rates are illustrated in Figure 6.10 and Table 6.9. The times taken for the erosion rate reach 90% of the steady state value for the different runs are listed in Table 6.9, and plots of this time versus initial substrate temperature and erosion rate are shown in Figures 6.11 & 6.12 respectively.

Table 6.4. A list of the start-up times used to generate the correct initial temperature profile for the experiments considering the effect of lava temperature on the erosion rate.

Lava Temperature /K	Startup Time /Hours
900	62.0
1000	21.0
1100	11.5
1200	8.5
1300	6.5
1400	5.5
1500	4.5
1600	4.0
1700	3.5
1800	3.0
1900	3.0

Figure 6.4. Relation between lava temperature and erosion rate. Lava temperatures in the range 900 - 1900 K were considered using an initial substrate temperature of 300 K and a melting temperature of 800 K.

Table 6.5. Results from the runs performed where lava temperature was the parameter varied. The table shows the calculated erosion rates as well as the time taken for the erosion rate to get within 10% of its steady state value.

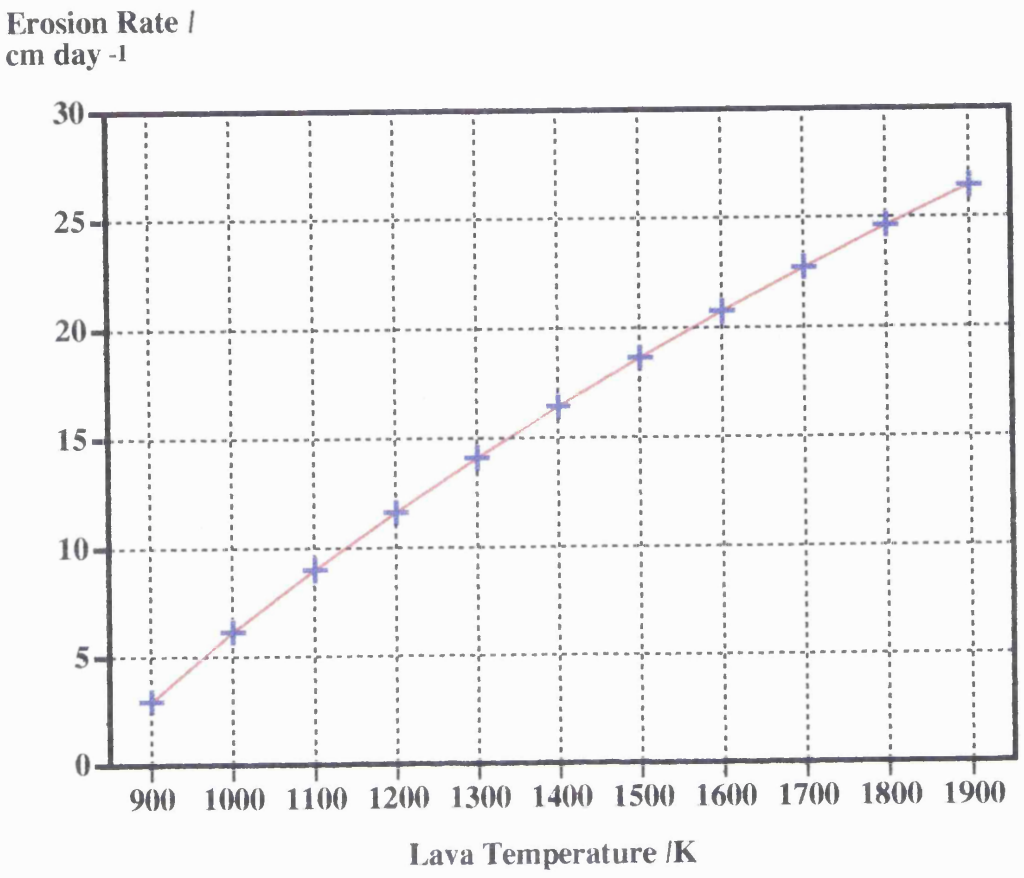

Lava Temperature /K	Erosion Rate /cm day^{-1}	Time to Equilibrium /Hours
900	3.00	513.08
1000	6.20	199.33
1100	9.05	99.64
1200	11.66	58.50
1300	14.15	40.09
1400	16.48	29.37
1500	18.69	22.82
1600	20.79	18.36
1700	22.78	15.13
1800	24.68	12.92
1900	26.49	11.09

Figure 6.5. A plot of time taken to reach equilibrium against lava temperature.

Figure 6.6. A plot of the time taken for the erosion rate to get within 10% of its steady state value versus erosion rate.

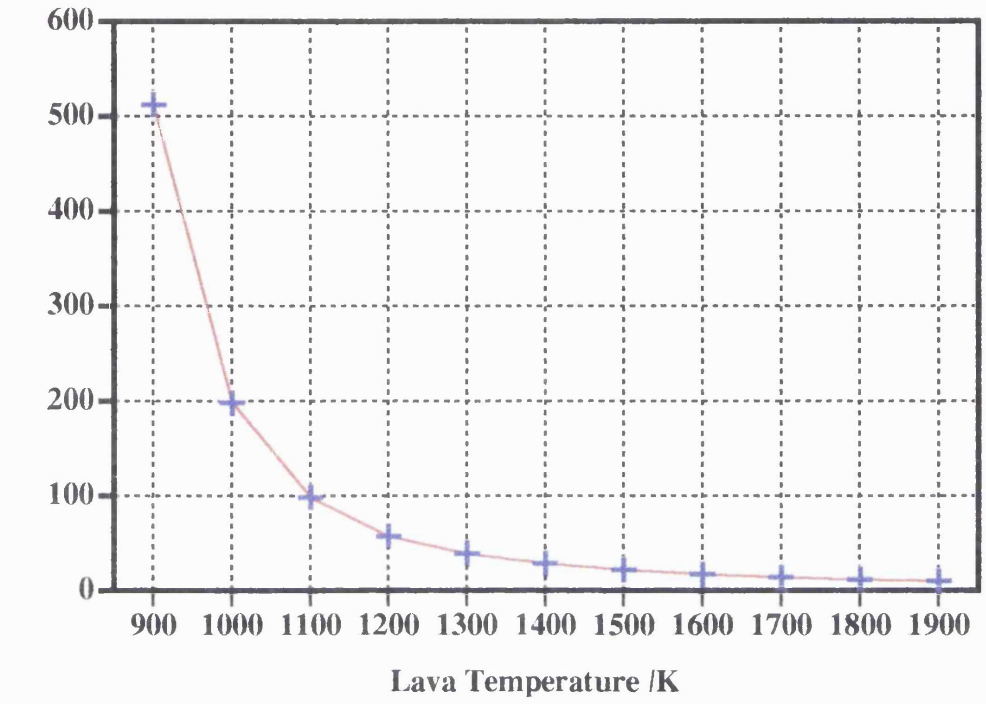
Time to
Equilibrium /hrs
600
500
400
300
200
100
0
900 1000 1100 1200 1300 1400 1500 1600 1700 1800 1900
Lava Temperature /K

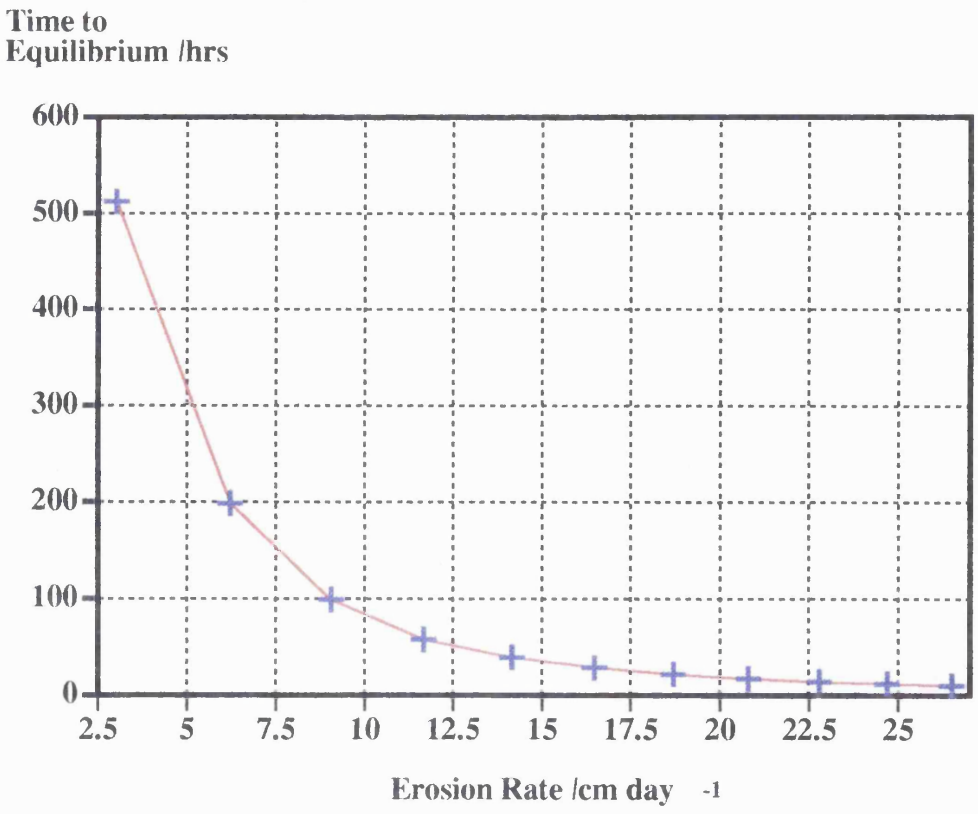
Time to
Equilibrium /hrs
600
500
400
300
200
100
0
2.5 5 7.5 10 12.5 15 17.5 20 22.5 25
Erosion Rate /cm day -1

Table 6.6. A list of the start-up times used to generate the correct initial temperature profile for the experiments considering the effect of the melting temperature of the substrate on the erosion rate.

Melt Temperature /K	Startup Time /Hours
700	3.25
800	4.50
900	6.50
1000	10.00
1100	16.00
1200	30.00
1300	69.00
1400	280.00

Figure 6.7. Relation between melting temperature and erosion rate. Melting temperatures in the range 700 - 1400 K were considered using a lava temperature of 1500 K and an initial substrate temperature of 300 K.

Table 6.7. Results from the runs performed where the melting temperature of the substrate was the parameter varied. The table shows the calculated erosion rates as well as the time taken for the erosion rate to get within 10% of its steady state value.

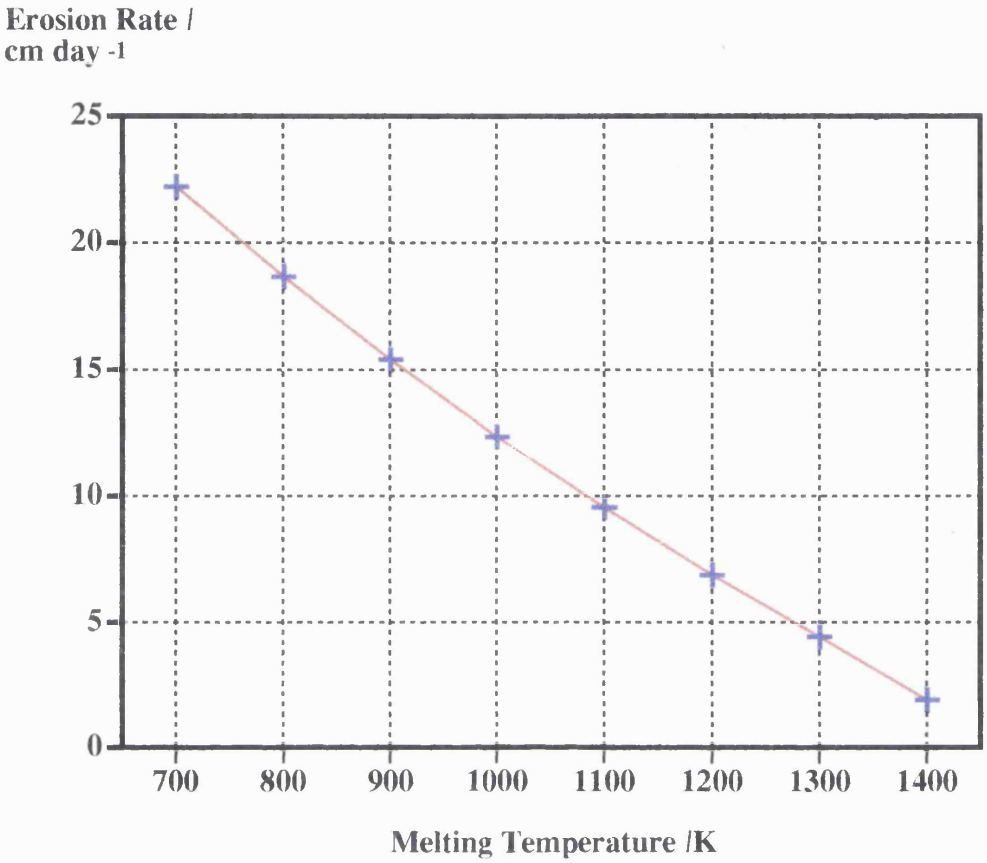

Melt Temperature /K	Erosion Rate /cm day^{-1}	Time to Equilibrium /Hours
700	22.25	14.06
800	18.69	22.82
900	15.42	36.52
1000	12.38	60.51
1100	9.58	107.44
1200	6.91	206.17
1300	4.45	516.73
1400	1.93	1491.62

Figure 6.8. A plot of time taken to reach equilibrium versus the melting temperature of the substrate.

Figure 6.9. A plot of the time taken for the erosion rate to get within 10% of its steady state value versus erosion rate.

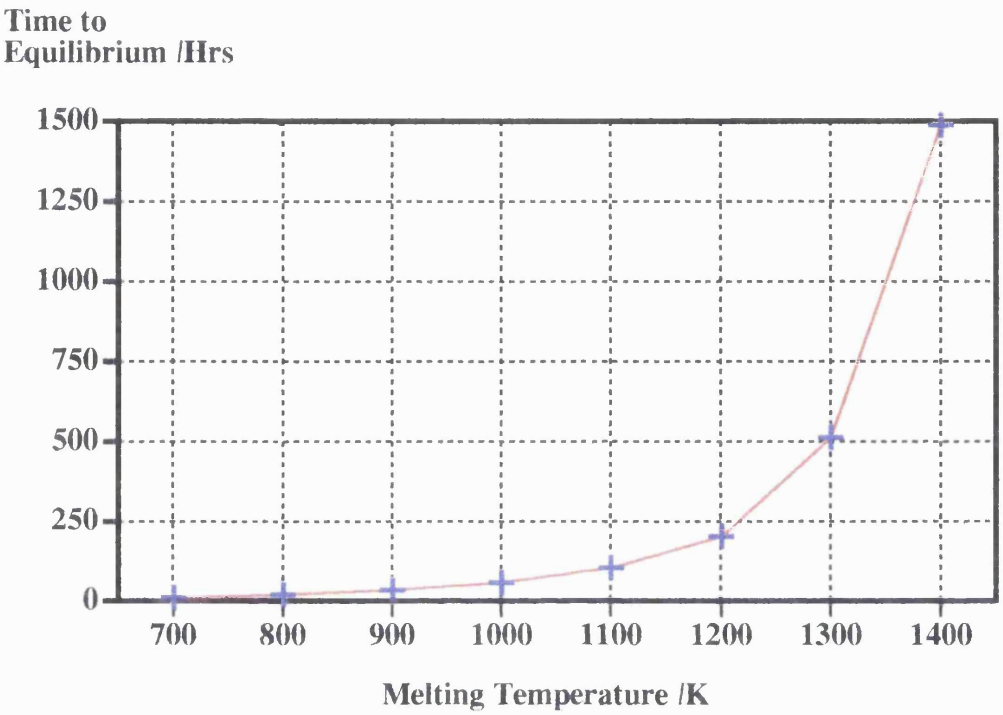
Time to
Equilibrium /Hrs
1500
1250
1000
750
500
250
0
700
800
900
1000
1100
1200
1300
1400
Melting Temperature /K

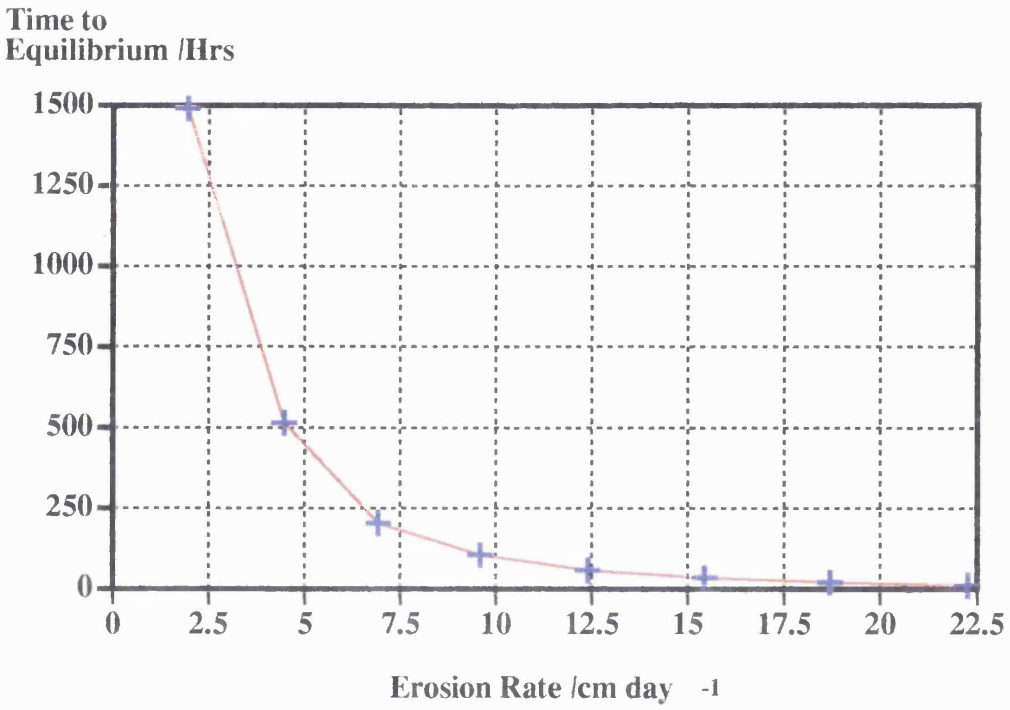
Time to
Equilibrium /Hrs
1500
1250
1000
750
500
250
0
0
2.5
5
7.5
10
12.5
15
17.5
20
22.5
Erosion Rate /cm day -1

Table 6.8. A list of the start-up times used to generate the correct initial temperature profile for the experiments considering the effect of the initial substrate temperature on the erosion rate.

Initial Substrate Temperature /K	Startup Time /Hours
300	10.0
400	8.0
500	7.0
600	5.0
700	4.0
800	2.5
900	1.5

Figure 6.10. Relation between initial substrate temperature and erosion rate. A lava temperature of 1500 K was used together with a melting temperature of 1000 K. The range of substrate temperatures considered was 300 - 900 K.

Table 6.9. Results from the runs performed where the initial substrate temperature was the parameter varied. The table shows the calculated erosion rates as well as the time taken for the erosion rate to get within 10% of its steady state value.

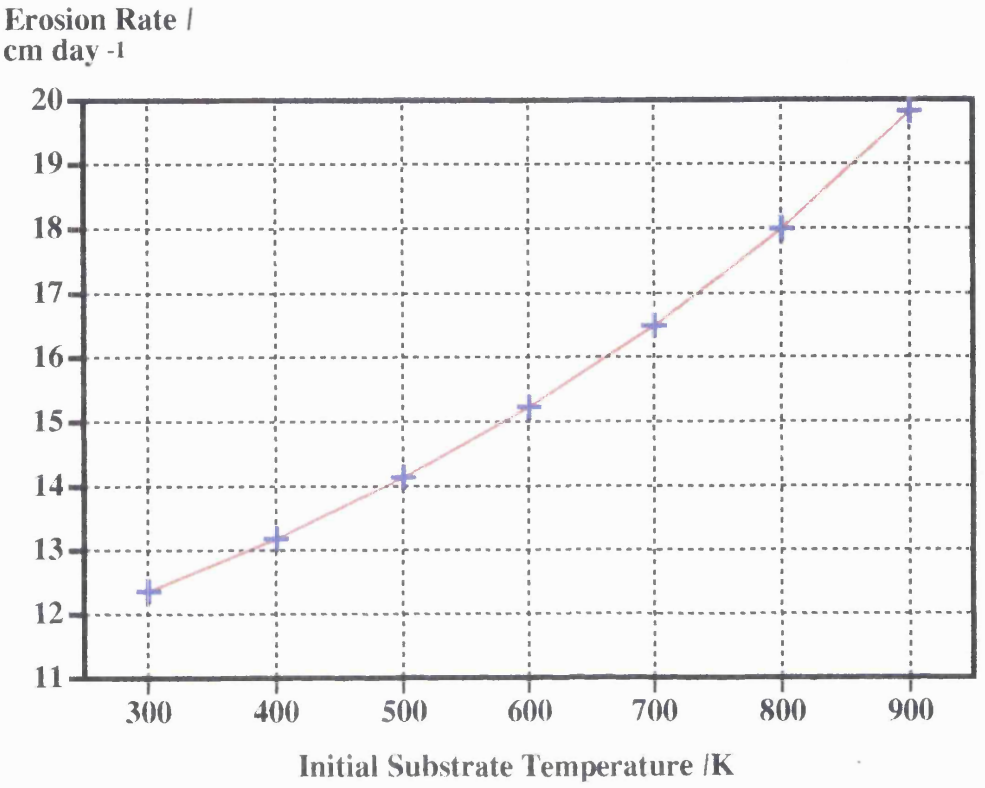

Initial Substrate Temperature /K	Erosion Rate /cm day^{-1}	Time to Equilibrium /Hours
300	12.38	60.51
400	13.20	49.85
500	14.15	40.36
600	15.24	30.54
700	16.51	21.71
800	18.01	13.42
900	19.83	5.91

Figure 6.11. A plot of time taken to reach equilibrium against initial substrate temperature.

Figure 6.12. A plot of the time taken for the erosion rate to get within 10% of its steady state value versus erosion rate.

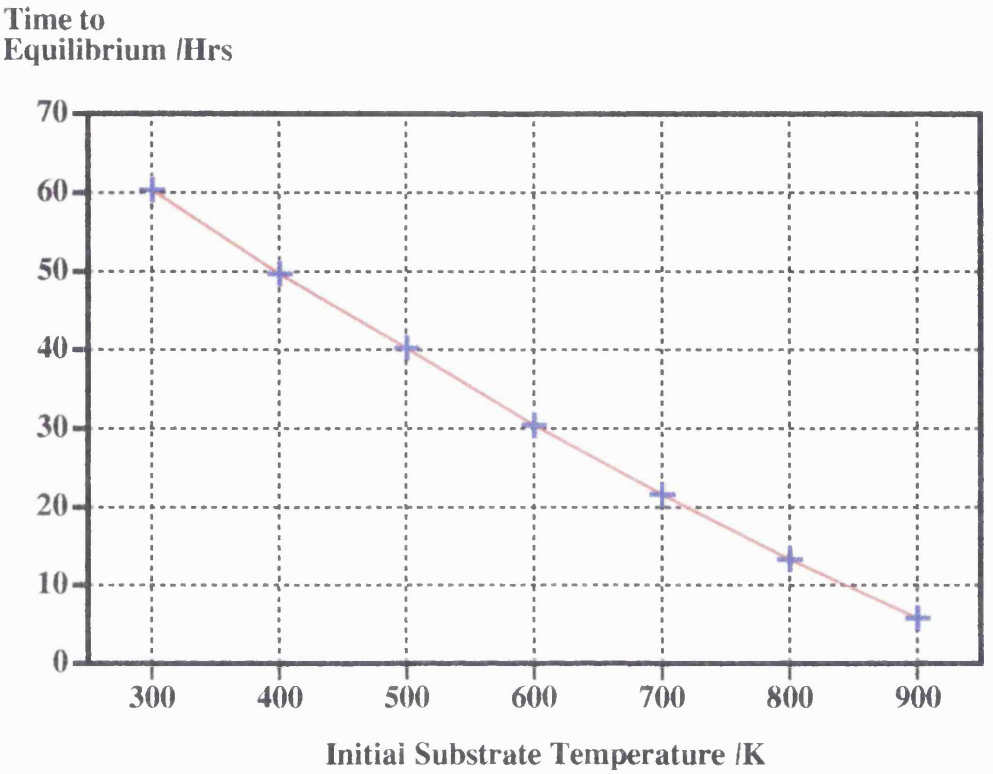
Time to
Equilibrium /Hrs
70
60
50
40
30
20
10
0
300
400
500
600
700
800
900
Initial Substrate Temperature /K

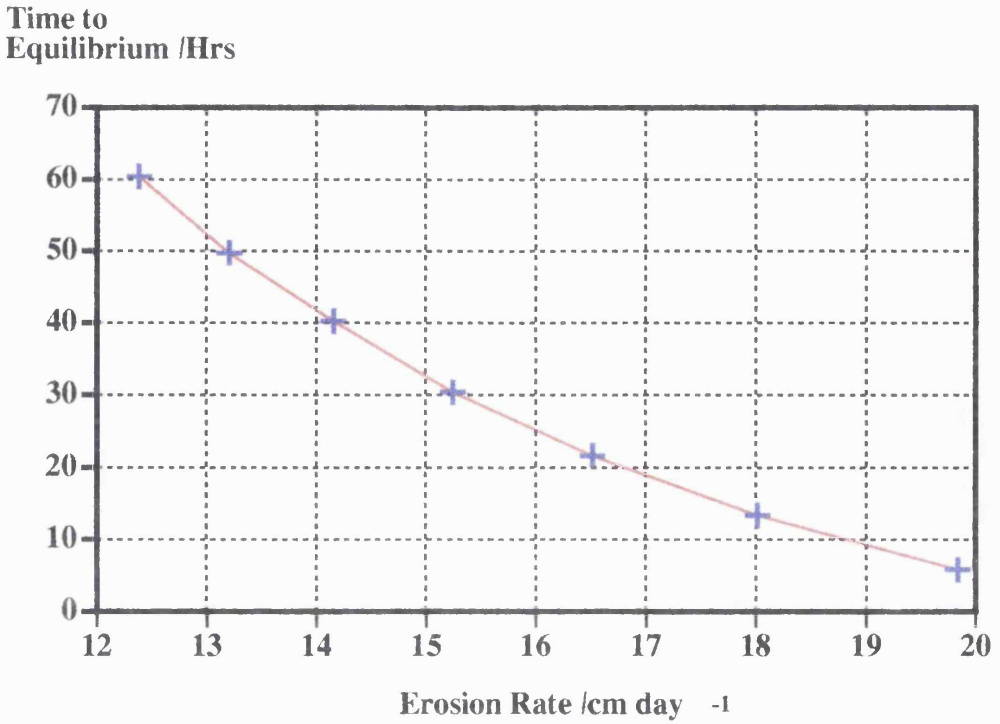
Time to
Equilibrium /Hrs
70
60
50
40
30
20
10
0
12
13
14
15
16
17
18
19
20
Erosion Rate /cm day -1

The fraction of latent heat that must be supplied before the substrate is removed is a key factor in the modelling of the erosion process. The fourth set of experiments investigated this by keeping all thermal parameters constant and changing the percentage of latent heat required to melt the substrate. This set of experiments can be used to consider how the presence of mechanical processes may affect the erosion rate. If mechanical abrasive forces are present then substrate may be scraped away before it is wholly liquid, i.e. when the substrate becomes partly fluid, this fluid acts as a lubricant for the stripping away of the remaining solid substrate. Thus by changing the percentage of latent heat of a cell that must be supplied before it is assumed to be removed this can be investigated. The start-up time used for this set of experiments was 10 hours. How the erosion rate varied throughout the experiments is shown in Figure 6.13 and Table 6.10. The time taken for the erosion rate to get within 10% of its final value is shown in Table 6.10 and plots of this time against the percentage of latent heat used and the erosion rate predicted are shown in Figures 6.14 & 6.15 respectively.

The results in section 6.2.1 show that the erosion rate is more sensitive to the lava and melt temperatures than the initial substrate temperature. For both the former parameters the erosion rate varies by approximately an order of magnitude when the temperature is changed by a factor of two, whilst when the initial substrate temperature is tripled the erosion rate only increases by less than a factor of two.

Another useful result is the importance of latent heat. Comparing the erosion rate from 100% latent heat (pure thermal erosion) to that from 0% latent heat, we see that the erosion rate varies by a factor of two, so clearly how powerful the mechanical erosion processes are is an important factor of the erosion process.

Figure 6.13. Relation between erosion rate and the percentage of the latent heat required to melt the substrate. A lava temperature of 1500 K was used together with a melting temperature of 1000 K and an initial substrate temperature of 300 K.

Table 6.10. Results from the runs performed where the amount of latent heat required to melt the substrate was the parameter varied. The table shows the calculated erosion rates as well as the time taken for the erosion rate to get within 10% of its steady state value.

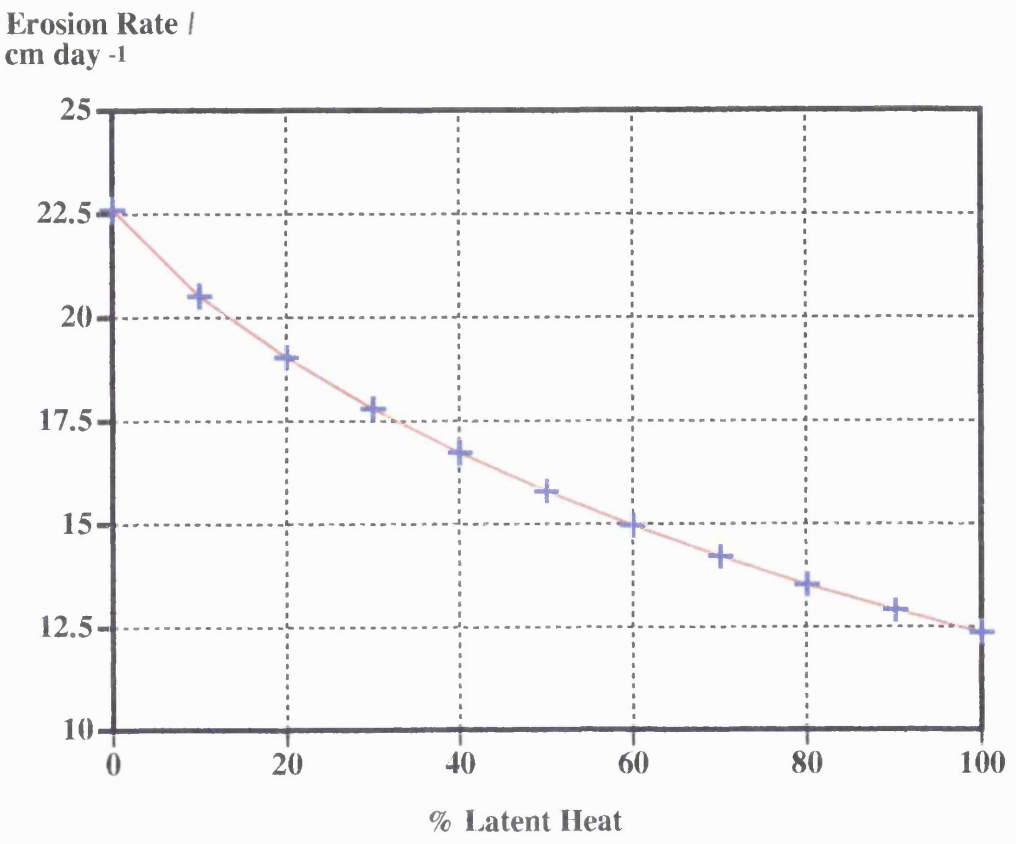

% Latent Heat	Erosion Rate /cm day^{-1}	Time to Equilibrium /Hours
00	22.62	27.23
10	20.54	31.52
20	19.06	35.12
30	17.82	38.47
40	16.75	41.90
50	15.81	45.15
60	14.98	48.35
70	14.23	51.69
80	13.55	54.27
90	12.93	57.18
100	12.38	60.50

Figure 6.14. A plot of time taken to reach equilibrium against percentage of latent heat required to melt the substrate.

Figure 6.15. A plot of the time taken for the erosion rate to get within 10% of its steady state value versus erosion rate.

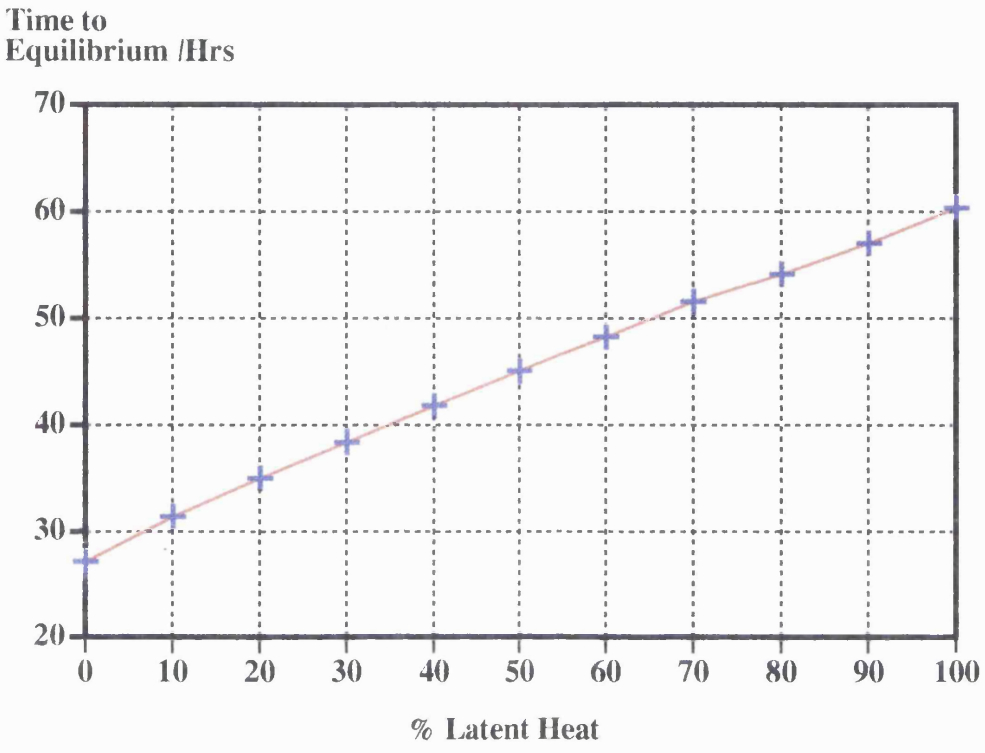
Time to
Equilibrium /Hrs
70
60
50
40
30
20
0
10
20
30
40
50
60
70
80
90
100
% Latent Heat

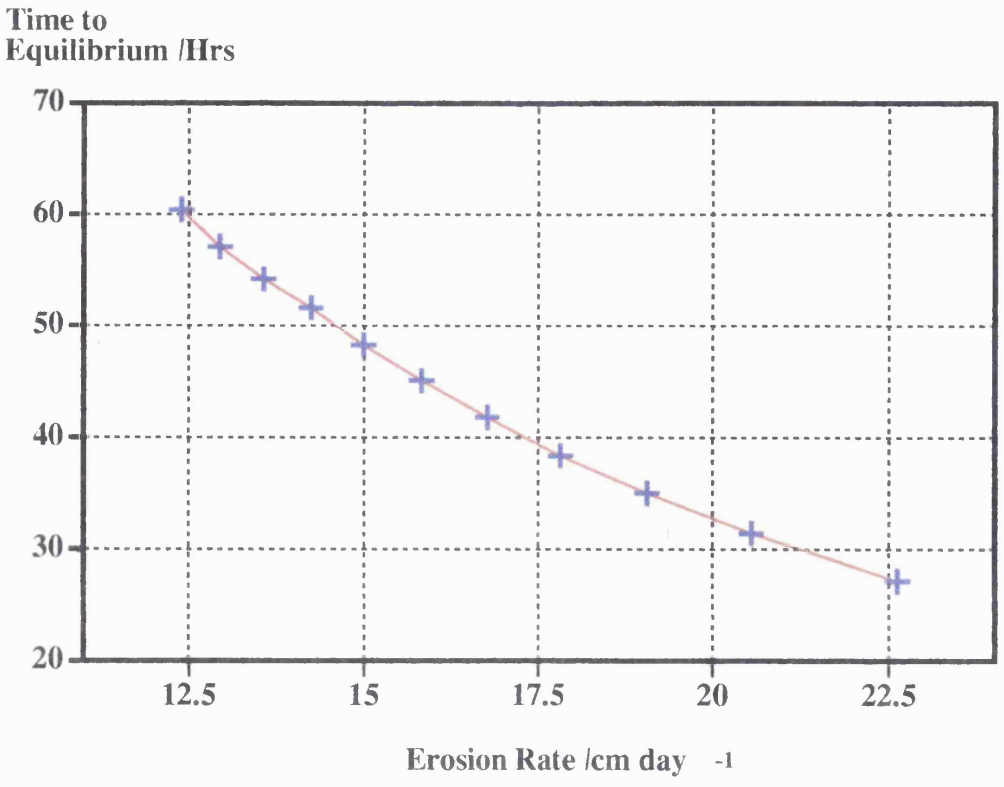
Time to
Equilibrium /Hrs
70
60
50
40
30
20
12.5
15
17.5
20
22.5
Erosion Rate /cm day -1

Consideration of the time to equilibrium factor indicates that the higher the final erosion rate, the sooner the rate is reached. This is possibly opposite to what one would expect. The graphs of equilibrium time against initial substrate temperature and percentage latent heat are interesting as they both have an almost linear profile whilst those for lava and melting temperature are far from linear.

6.2.2 The Liquid Substrate Boundary Layer.

The experiments discussed in this section look at the importance of the liquid substrate boundary layer used in the model to the erosion process. In order to analyse this quantitatively a set of experiments was carried out using different thicknesses of boundary layer in the range 2.5 to 20 centimetres. The thermal parameters were fixed for all the runs. These consisted of a lava temperature of 1500 K, a melting temperature of 1000 K and an initial substrate temperature of 300 K. A list of the non fixed parameters used during the runs is shown in Table 6.11. For each run the cell size was chosen to ensure that the number of cells in the boundary layer remained constant.

The results are shown in Figure 6.16 and Table 6.12. As the liquid boundary layer thickness is reduced the erosion rate behaves asymptotically. The temperature gradient across the boundary layer becomes steeper the narrower the boundary layer, and this leads to an increased erosion rate. Plots of time to reach equilibrium versus boundary layer thickness and erosion rate are shown in Figures 6.17 and 6.18. They show that the thinner the boundary layer, the quicker the system reaches equilibrium.

There are no measured values for the actual thickness of any liquid substrate layer that may be present during a flow, and the values used were chosen

Table 6.11. A list of the modelling parameters used for the experiments undertaken to consider the importance of the size of the liquid substrate boundary layer to the erosion rate.

Boundary Layer Thickness / m	Δx / m	Δt / s	Startup Time / hours
0.2	0.02	24.0	40
0.15	0.015	12.0	22.5
0.1	0.01	6.0	10
0.075	0.075	3.0	5.5
0.05	0.005	1.5	2.5
0.025	0.0025	0.25	0.7

Figure 6.16. Dependence of erosion rate on liquid boundary layer thickness. A lava temperature of 1500 K was used together with a melting temperature of 1000 K and an initial substrate temperature of 300 K.

Table 6.12. Results from the runs performed where the thickness of the liquid substrate boundary layer was the parameter varied. The table shows the calculated erosion rates as well as the time taken for the erosion rate to get within 10% of its steady state value.

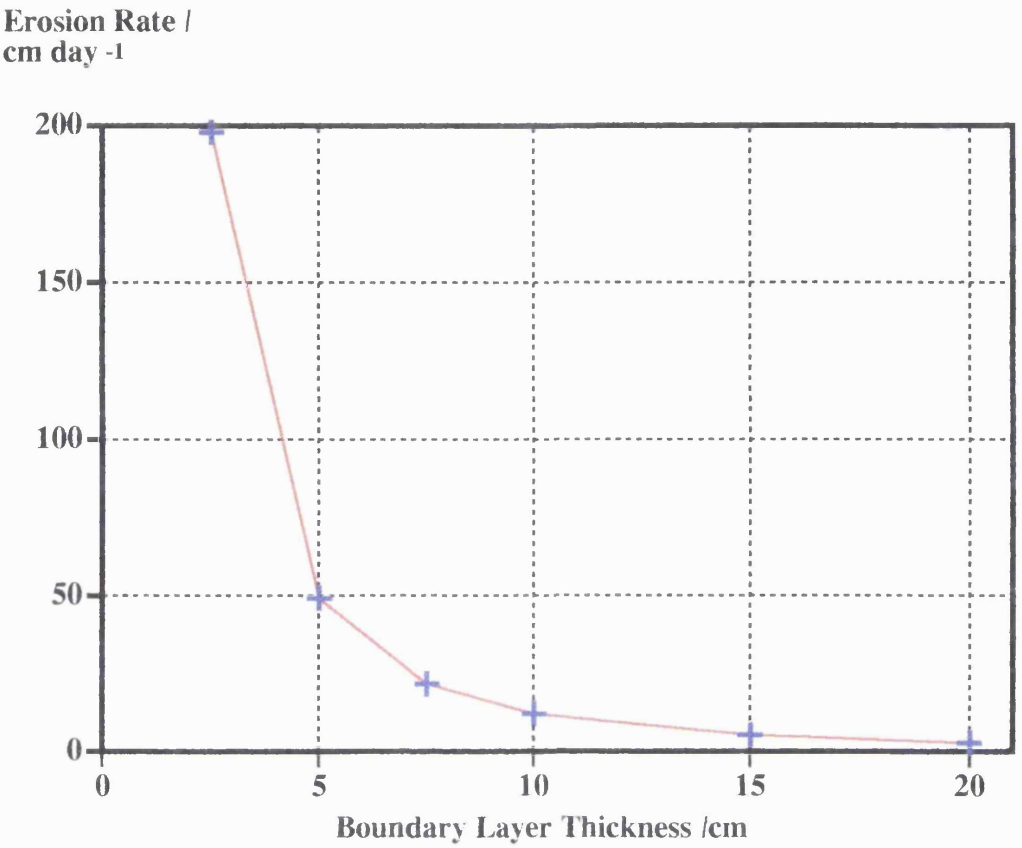

Boundary Layer Thickness / cm	Erosion Rate / cm day^{-1}	Time to Equilibrium / Hours
20	3.09	237.10
15	5.51	136.74
10	12.38	60.51
7.5	22.04	33.33
5	49.57	13.20
2.5	198.32	3.84

Figure 6.17. A plot of time taken to reach equilibrium against liquid substrate boundary layer thickness.

Figure 6.18. A plot of the time taken for the erosion rate to get within 10% of its steady state value versus erosion rate.

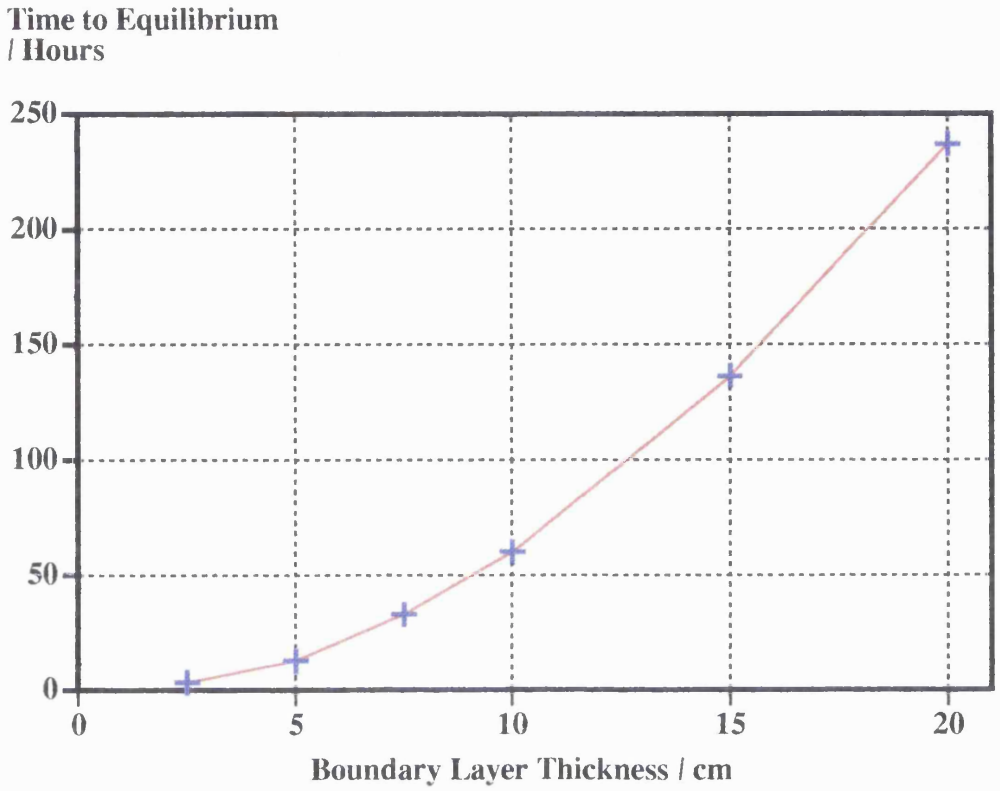
Time to Equilibrium
/ Hours
250
200
150
100
50
0
0
5
10
15
20
Boundary Layer Thickness / cm

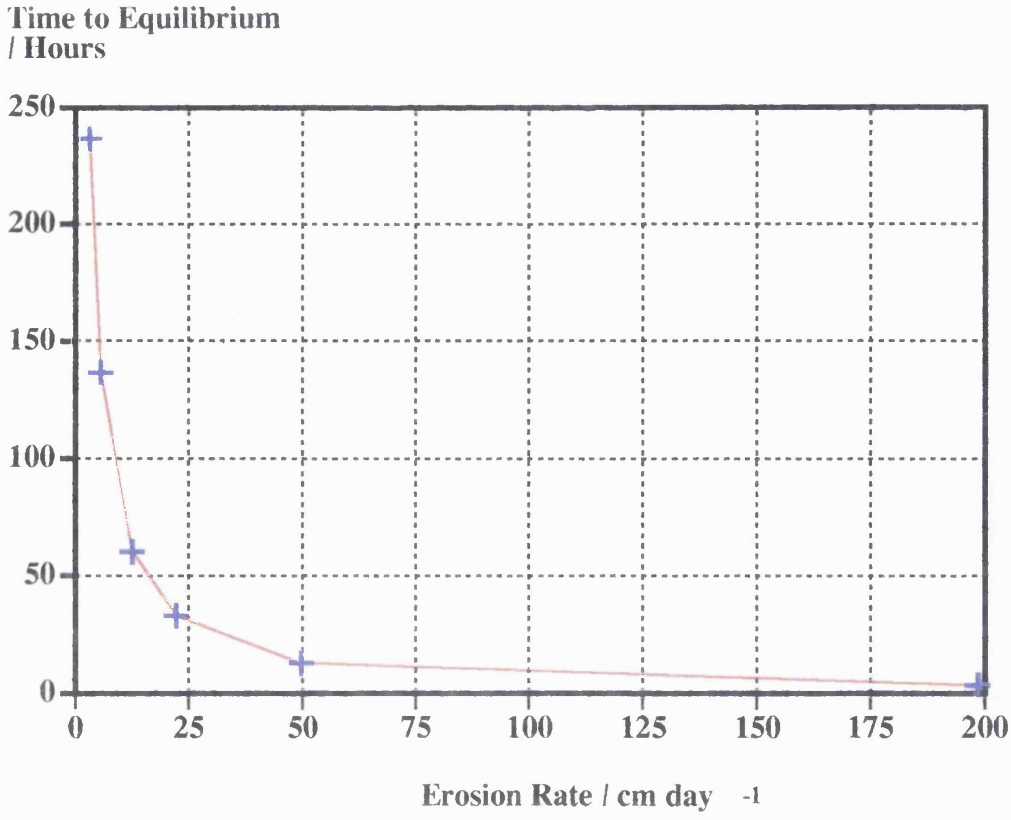
Time to Equilibrium
/ Hours
250
200
150
100
50
0
0
25
50
75
100
125
150
175
200
Erosion Rate / cm day -1

simply to investigate how sensitive the model is to the size of this boundary layer. This approach was deliberately chosen in view of the lack of data concerning the properties of the layer. In a real flow mechanical erosion will have a role in dictating the size of the boundary layer by scraping away the upper surface. Clearly the nature of the flow will affect this scraping with a turbulent lava flow being more affective at eroding the boundary layer.

6.2.3 Thermal Conductivity.

The sensitivity of the erosion rate to the thermal conductivity is investigated by the experiments discussed in this section. This was achieved by fixing the thermal conductivity of the lava, and varying the values for the thermal conductivities of the liquid substrate boundary layer and the solid substrate. The thermal parameters were kept constant for all of the runs, consisting of a lava temperature of 1500 K, a melting temperature of 1000 K and an initial substrate temperature of 300 K. The time step size and the start-up time used are both a function of the solid substrate thermal conductivity. The values used are shown in Table 6.13.

A lava thermal conductivity of 1.0 J s^{-1} m^{-1} K^{-1} was used and the substrate conductivities varied from 0.01 to 10.0 J s^{-1} m^{-1} K^{-1}. This allowed a wide range of ratios between the three thermal conductivities to be considered. The results are shown in Table 6.14 and Figures 6.19 & 6.20. Figure 6.19 shows the results from one particular set of experiments in which the boundary layer thermal conductivity was fixed at 10.0 and the value of the thermal conductivity for the solid substrate was varied from 0.01 to 10.0. It shows that as the thermal conductivity of the solid substrate is reduced the erosion rate increases. This is due to more of the heat being used to melt the top layer of the substrate rather than

Table 6.13. A list of the modelling parameters used for the experiments where thermal conductivity is the parameter varied.

Table 6.14. Results from the runs performed where the thermal conductivity of the liquid substrate boundary layer and the solid substrate was the parameter varied. The table shows the calculated erosion rates as well as whether the erosion rate decreased or increased en route to its steady state value.

Thermal Conductivity of the Solid Substrate	Startup Time / Hours	Δt / s
0.01	450	6
0.05	90	6
0.1	45	6
0.5	9	6
1.0	4.5	6
5.0	0.9	0.6
10.0	0.45	0.6

Thermal Conductivity of the Liquid Substrate	Thermal Conductivity of the Solid Substrate	Erosion Rate / cm day^{-1}	Direction the Erosion Rate varied en route to Equilibrium Value
0.1	0.01	2.06	Decreased
0.1	0.05	2.04	Increased
0.1	0.1	2.02	Increased
0.1	0.5	1.86	Increased
0.1	1.0	1.68	Increased
0.1	5.0	0	n/a
0.1	10.0	0	n/a
0.5	0.01	10.04	Decreased
0.5	0.05	9.90	Decreased
0.5	0.1	9.85	Decreased
0.5	0.5	9.79	Increased
0.5	1.0	9.73	Increased
0.5	5.0	9.71	Increased
0.5	10.0	9.69	Increased
1.0	0.01	19.22	Decreased
1.0	0.05	18.99	Decreased
1.0	0.1	18.88	Decreased
1.0	0.5	18.70	Increased
1.0	1.0	18.69	Increased
1.0	5.0	18.48	Increased
1.0	10.0	18.32	Increased
5.0	0.01	71.36	Decreased
5.0	0.05	71.08	Decreased
5.0	0.1	70.82	Decreased
5.0	0.5	70.07	Decreased
5.0	1.0	69.86	Decreased
5.0	5.0	69.63	Increased
5.0	10.0	69.53	Increased
10.0	0.01	109.48	Decreased
10.0	0.05	109.26	Decreased
10.0	0.1	109.01	Decreased
10.0	0.5	108.14	Decreased
10.0	1.0	107.82	Decreased
10.0	5.0	107.33	Increased
10.0	10.0	107.21	Increased

Figure 6.19. Results from one particular set of experiments where the thermal conductivity of the liquid substrate boundary layer was fixed at 10.0 and the value of the thermal conductivity for the solid substrate was varied from 0.01 to 10.0 J s^{-1} m^{-1} K^{-1}.

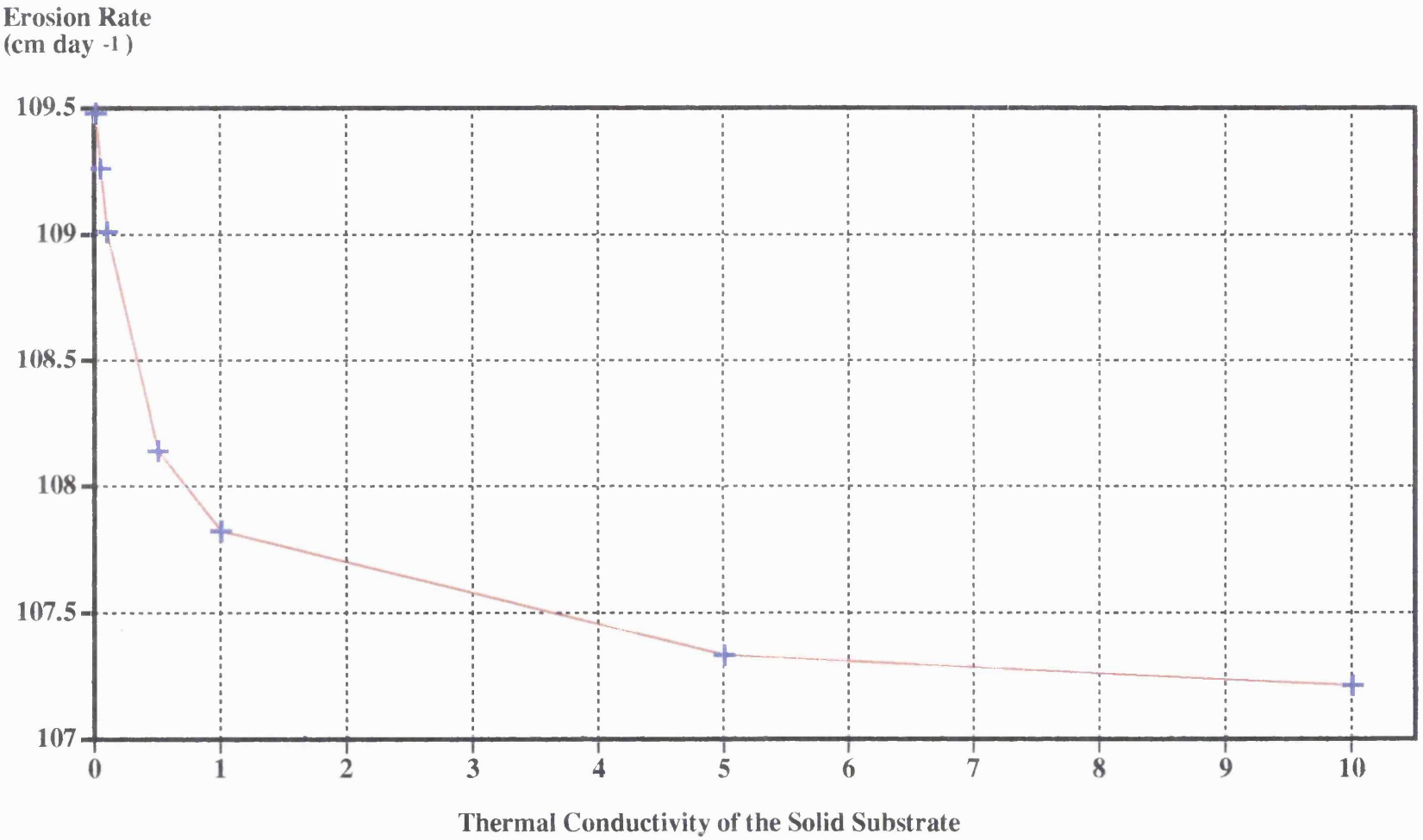
Erosion Rate
(cm day -1)
109.5
109
108.5
108
107.5
107
0
1
2
3
4
5
6
7
8
9
10
Thermal Conductivity of the Solid Substrate

Figure 6.20. Results from all the conductivity experiments carried out. Each line on the graph represents one series of runs in which the liquid substrate boundary layer thermal conductivity was kept constant. There are lines for 0.1, 0.5, 1.0, 5.0 and 10.0 $J\ s^{-1}\ m^{-1}\ K^{-1}$.

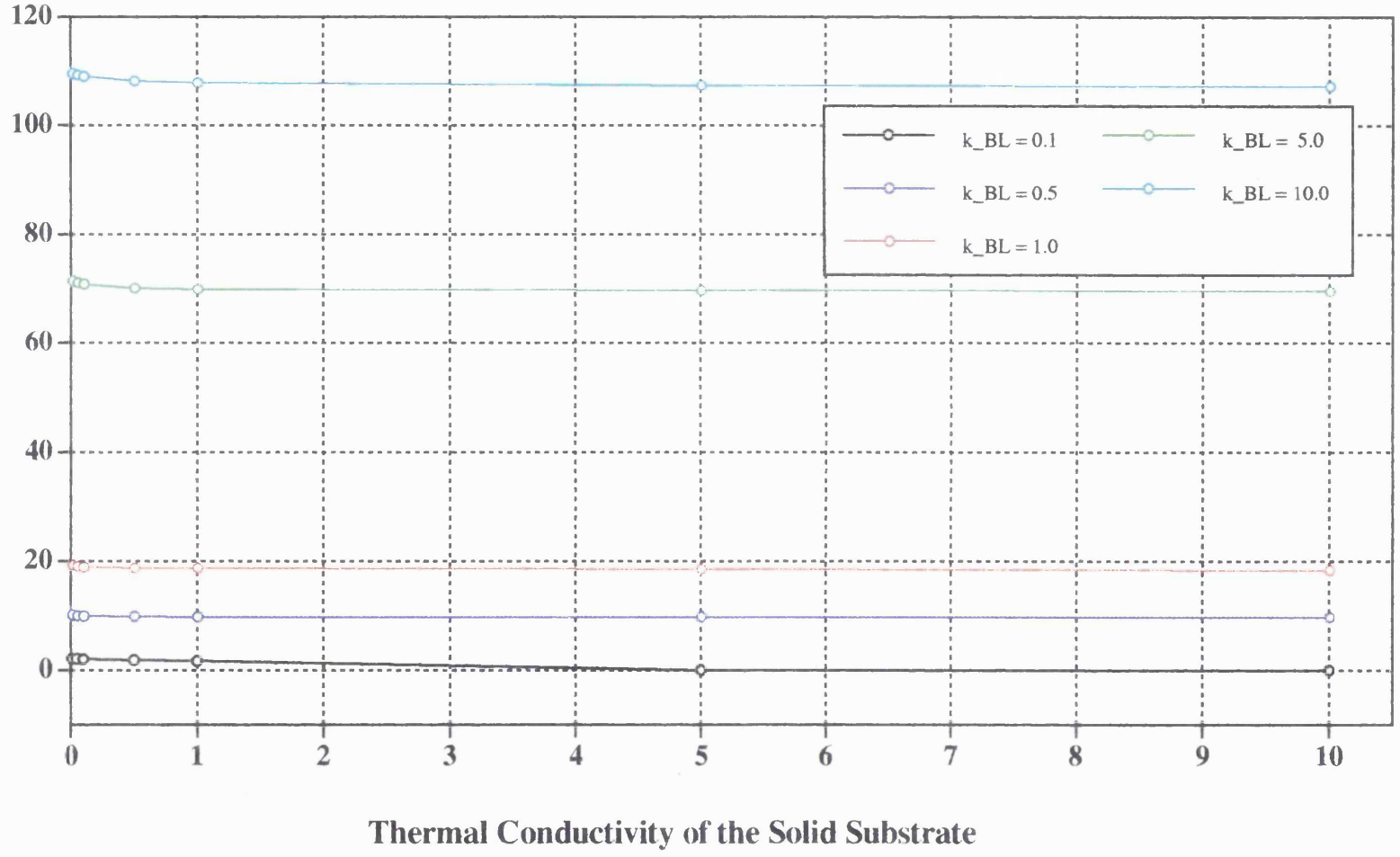
Erosion Rate /
cm day -1
120
100
80
60
40
20
0
0
1
2
3
4
5
6
7
8
9
10
k_BL = 0.1
k_BL = 0.5
k_BL = 1.0
k_BL = 5.0
k_BL = 10.0
Thermal Conductivity of the Solid Substrate

heating the lower substrate as the low conductivity inhibits the heat from being conducted down into the substrate. Figure 6.20 shows the results from all the conductivity experiments carried out. Each line on the graph represents one series of runs in which the liquid substrate boundary layer thermal conductivity was kept constant. There are lines for 0.1, 0.5, 1.0, 5.0 and 10.0 J s^{-1} m^{-1} K^{-1}. The graph shows that the erosion rate increases as the thermal conductivity of the liquid substrate boundary layer is increased. Also, whilst for each line the erosion rate increases as the solid substrate conductivity decreases this is a minor effect when compared to changing the conductivity for the liquid substrate.

Another piece of information shown in Table 6.14 is whether the erosion rate increased or decreased en route to the final equilibrium value. It can be seen that for a set of runs this was a function of the solid substrate thermal conductivity. For low values of the conductivity the erosion rate starts off relatively high and decreases towards the final value. As the conductivity increases this effect becomes less pronounced until the opposite occurs, i.e. the erosion rate starts off low and increases to the equilibrium value. The results show that this switch in direction occurs approximately when the conductivities of the liquid and solid substrates become equal.

6.3 Discussion.

Initial results from the model indicate that higher thermal erosion rates are possible close to the lava source on Venus compared to Earth. If all other factors are the same, the higher initial substrate temperature on Venus leads to an increased rate of erosion. Consideration of Figure 6.10 shows that the higher initial substrate temperature leads to a venusian erosion rate that is approximately 1.5 times greater than the terrestrial rate, all other factors being equal.

The model also shows the sensitivity of the erosion process to other factors in the range expected of typical lavas. Figure 6.4 shows that when the lava temperature is doubled, the erosion rate increases by approximately a factor of 8. Similarly when the melting temperature is doubled, the erosion rate decreases by an order of magnitude (Figure 6.7). The importance of mechanical erosion is considered by changing the amount of latent heat that must be supplied before the substrate is eroded. Figure 6.13 shows that varying the amount of latent heat between 0 and 100% changes the erosion rate by approximately a factor of 2.

It is also important to consider how long it takes before the lava begins to erode, i.e. the warm-up time. A discussion on this topic, not including latent heat effects, can be found in Hulme (1982). In our model, which does allow for latent heat, the time taken for the erosion rate to reach within 10% of the steady state erosion rate was taken. This varied considerably, from a few hours if the steady state erosion rate was high, to several days if it was low. It is interesting to note however that in the run of the model where the difference between the initial substrate and melting temperatures was small, ~ 100 K, the time taken for the erosion rate to reach within 10% of its final value was only about 6 hours.

Of key significance to the erosion rate is the liquid boundary layer, and what factors affect its thickness. These are liable to include the flow characteristics of the lava as well as the physical properties of the substrate. Figure 6.16 indicates that if the size of the liquid boundary layer is reduced from 20 to 2.5 cm, the erosion rate increases by almost two orders of magnitude. The erosion rate is much more sensitive to the thermal conductivity of the liquid substrate boundary layer than to the thermal conductivity of the solid substrate. Figure 6.20 shows that the highest erosion rates occur when there are high liquid substrate and low solid substrate thermal conductivities.

The work presented in this chapter represents the results from a simple model of lava erosion. However, despite its simplicity it is possible to make useful conclusions from the results. On Earth it is rare for basalts to erode their substrate and if erosion does occur, the erosion rate is usually very small. The model shows that if basalts were to erode on Venus, the erosion rate would be approximately 1.5 times the terrestrial value and still quite small. It is therefore unlikely that basalts of the type found on Earth produced the erosional channels we see on Venus; a more exotic lava is probably responsible for their origin.

The model predicts that several conditions can produce high erosion rates close to the source. How the calculated erosion rate varies with both lava temperature and melting temperature indicates that the difference between these two temperatures is an important factor in the ability of a lava to erode. The model indicates that larger differences between the lava temperature and the melting temperature of the substrate produce higher calculated erosion rates. This means that lavas such as komatiite, which can have eruption temperatures of the order of 1850 K, being erupted onto a basaltic substrate, may be able to sustain relatively high erosion rates close to the source. A particular attractive substrate into which the channels have eroded is carbonatite. This is because the melting

temperature of carbonatite is just above the ambient venusian temperature. The model indicates that if the difference between the melting and initial substrate temperatures is small, then erosion can occur after only a few hours. This means that any erupted lava flowing over a carbonatite substrate would erode into that substrate even for fairly short eruption durations. The fact that the melting temperature of carbonatite is so close to the ambient venusian temperature also means that any carbonatite lava extruded onto the venusian surface would remain fluid for a long period of time, something that is necessary to produce channels of the length seen.

Thus the model shows that, given the right conditions, near the source of the lava, it is possible not only to get a significant erosion rate but also to get it quite quickly, so that even for fairly short eruption duration, thermal erosion is going to play a role in the development of the channel morphology. It is clear that if erosion rates of the order of a metre a day occur, combined with a warm-up time of only a few hours, then thermal erosion is going to have major consequences on the final channel shape even for fairly short duration eruptions.

The model for lava erosion close to the source developed in chapter 5 represents a step in the production of a mathematical model to predict the emplacement of an entire lava flow field. Modelling of more realistic boundary conditions requires the production of a two dimensional model. This model will allow various velocity profiles to be used to see how channel morphology is affected by the velocity gradient within the lava, as well as looking at crust formation and the cooling of the flow.

Chapter 7
Final Comments

7.1 Conclusions.

The scientific conclusions that can be drawn from this thesis come in two parts. The first conclusions come from the work described in chapters 3 & 4. This consisted of image analysis of a number of canali type channels. A summary of the results of this study follows.

- The canali have a mixture of features that can be interpreted to mean that they consist of erosional, leveed and roofed sections, although not all canali show all the different types of section.

- Canali often appear to have erosional characteristics close to their source.

- The canali that were studied were emplaced in a region which had very shallow slopes and appears to have undergone vertical deformation since they were formed.

The second set of conclusions comes from a series of numerical experiments carried out to consider the sensitivity of the erosion process to different parameters. A precis of the detailed conclusions which can be found in section 6.3 is shown below.

- Although the higher ambient temperature on Venus means that thermal erosion is more likely to occur there than on Earth, the model predicts that the effect of the higher initial substrate temperature results in a calculated

venusian erosion rate, all other factors being equal, only 1.5 times greater than the equivalent terrestrial erosion rate. This means that it is unlikely that the channels were formed by terrestrial basalts and points to a more exotic lava being responsible for their origin.

- The erosion rate determined by the model is more sensitive to the lava and melting temperatures, than to the initial substrate temperature.

- In the model, changing the amount of latent heat required to melt the substrate, from 0 to 100 %, alters the estimated erosion rate by a factor of 2.

- The thickness and thermal conductivity of the liquid substrate boundary layer are critical to the calculated erosion rate.

7.2 Future Work.

There are several ways in which the research presented in this thesis could be taken further. At the moment, the erosional model is one dimensional. It is hoped to eventually develop a model to predict the emplacement of an entire flow field. This will be a gradual task resulting in the production of a number of intermediate models, each slightly more advanced than the last.

It is also hoped to study channels on other planets, particularly the moon. The Clementine mission has recently completed a global multi-spectral high resolution map of the moon. These new mineralogy data can be used to obtain previously unknown information about the sinuous rilles. Figure 7.1 shows a false colour mosaic of the Aristarchus plateau region of the moon including the sinuous rille called Schröter's Valley. The colours in this image represent different

Figure 7.1. A multi-spectral image of the Aristarchus plateau region of the moon. Different colours in this image represent different rock types. The blue areas are fresh highland material, pyroclastic deposits are shown in dark red, yellow regions are outcrops of fresh basalt and mare lava flows show up as reddish-purples.

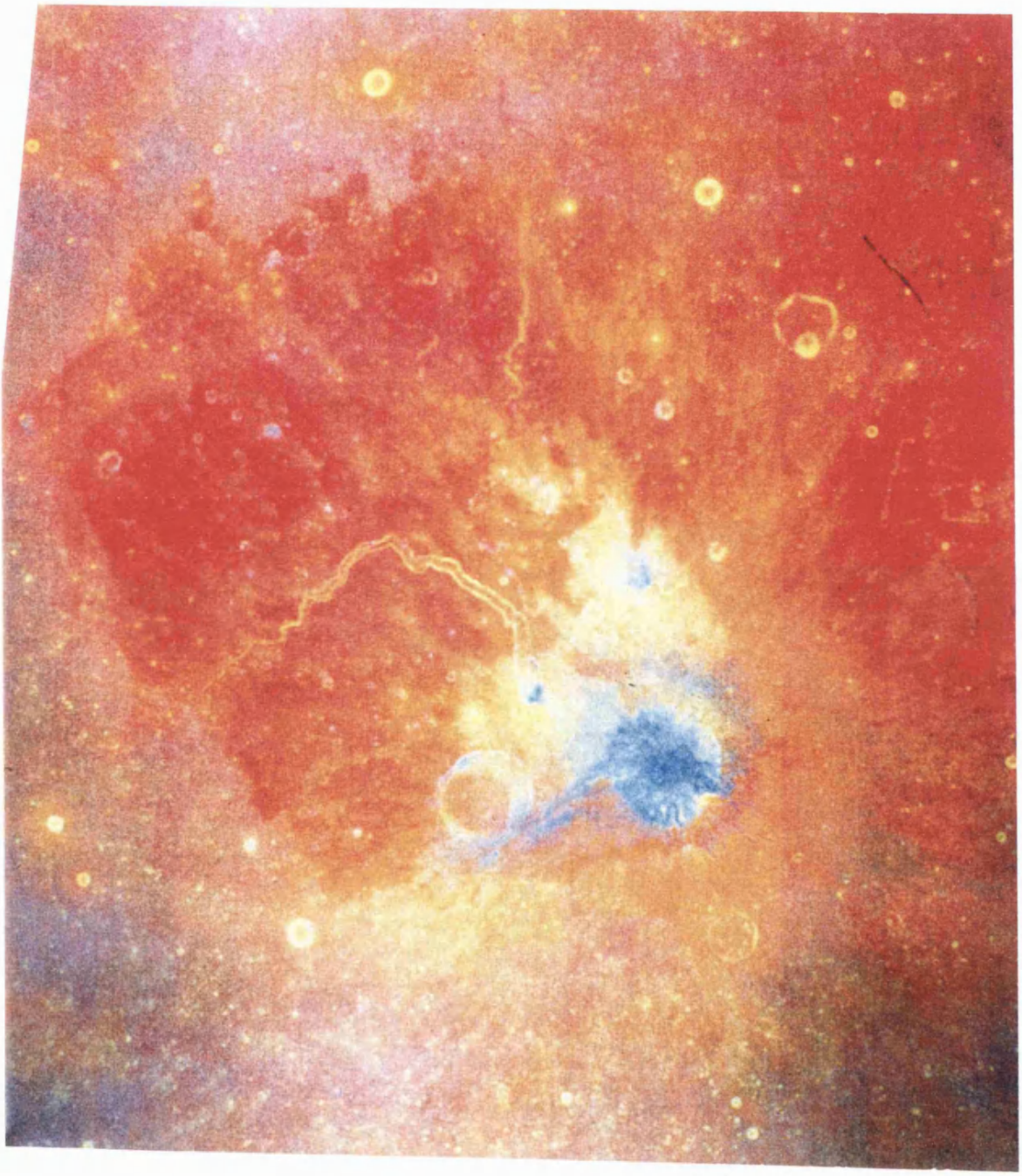

rock types. The blue areas are fresh highland material, pyroclastic deposits are shown in dark red, yellow regions are outcrops of fresh basalt and mare lava flows show up as reddish-purples. The image clearly shows that the Clementine data are of a high enough resolution to determine the mineralogy within a rille. This ability to identify the composition of the different rock units making up a rille will enable one to ascertain how the rille was formed. An inference of the stratigraphic relationship between the rille floor, rille walls and the surrounding terrain should indicate whether the rille formed predominantly by construction or erosion.

I have looked at how various physical parameters affect the ability of a lava to erode. Since the compositions of lavas on Venus are not known, the data that I have supplied allows for the possibility of testing whether any specific composition of lava (predicted by petrogenetic models of the venusian interior) would be able to erode and produce features such as canali.

Of the three previously suggested compositions, carbonatite, sulphur and komatiite, an obvious combination would be komatiite lava eroding into a carbonatite substrate. This combination has all the prerequisites predicted by the model for a high erosion rate, because there is a large difference between the eruption and melting temperatures, and a small difference between the melting and initial substrate temperatures.

On the other hand, the canali could have been formed by a lava-substrate combination that produces a small erosion rate, if the eruption duration was suitably long. One method of estimating eruption duration would be to use a flow model for a lava to calculate an emplacement velocity. These data, combined with the channel length, could provide a rough time of emplacement for the channel. If it were possible to measure the depth of a channel close to its source, then this could be used with the eruption duration to calculate the erosion rate required to produce the channel. Once this information becomes available from future missions it will be possible to use the model described in this thesis to predict the lava-substrate combination that formed the channel.

Appendix A

The following listing is for the macro called Grid for the image processing package Image for the Apple Macintosh. When initiated this macro overlays onto a Magellan browse image 56 numbered squares, each square showing the area covered in full resolution by the framelet with the same number as the square.

Grid

```
Macro 'Grid [G]';
var a,b,i,j,m,n,s:integer;
begin
        a:=0;
        b:=128;
        for i:= 1 to 6 do begin
                MoveTo (0,b);
                LineTo (1023,b);
                MoveTo (b,0);
                LineTo (b,895);
                b:= b+128;
        end;
        MoveTo (b,0);
        LineTo (b,895);

        for j:= 1 to 7 do begin
                n:= ((128*(j-1))+10);
                for i:= 1 to 8 do begin
                        m:= ((128*(i-1))+5);
                        MoveTo (m,n);
                        s:= (((j-1)*8)+i);
                        DrawNumber(s);
                end;
        end;
end;
```

Appendix B

This appendix describes how printouts of the channels were obtained in order to make measurements of the channels. This was not a straightforward task as the only printer available was an ordinary laser printer, the quality of which was far from photographic. Another problem was that the resolution of the laser printer was such that the framelets (1024 x 1024) needed to be scaled in order to be printed. The images are in a format called 'vicar' and the first task required the associated vicar image header to be removed. Next a raster header is placed on the image, and this is then converted to a different image format called 'hips'. Next the image is reduced in size from 1024 x 1024 to 512 x 512. The image format is now changed from hips to gips so that the image can be viewed in 'Gipstool' and a suitable contrast stretch chosen. The gips header is now removed and the remaining raw data is stretched. The now stretched image has a raster header attached and is then converted into a postscript file enabling it to be printed.

A summary of these steps is shown below.

1) The vicar image header is removed.
2) A new raster header is put on and this is then converted to a hips header.
3) The image is reduced from a 1024 x 1024 to 512 x 512.
4) The image format is changed from hips to gips.
5) The image is viewed and a contrast stretch chosen.
6) The header is removed, and the raw data is then stretched.
7) The new stretched image has a raster header attached which is then converted to a postscript file.
8) The final image is printed.

1 - 3 are achieved using the alias reduce.

4 - 5 are achieved using the alias gipsh.

6 - 8 are achieved using the alias lprsh.

The three aliases are shown below.

```
reduce          'tail +2049c !:1 > ~/VOLATILE/tmp ; pushd ~/VOLATILE ; ls ;
makehead -w 1024 -h 1024 -f tmp ; raships < tmp.h > tmp.hip ; ~/bin/shrink <
tmp.hip > tmp.sh ; mv tmp.sh !:2 ; \rm tmp tmp.h tmp.hip ; popd'

gipsh   'hipsras !* | ihfrompix -o tmp.sh.gip ; gipstool tmp.sh.gip'

lprsh   'tail +153c !:3 > tmp.sh.d ; linstretch -m !:1 !:2 -o tmp.sh.st tmp.sh.d ;
makehead -w 512 -h 512 -f tmp.sh.st ; raships < tmp.sh.st.h | pships | lpr ; \rm
tmp.sh.d tmp.sh.st tmp.sh.st.h'
```

When Image became available it was possible to automate this process even more as Image has 'Scale' and 'Enhance Contrast' commands. Some example printouts are displayed in the following pages.

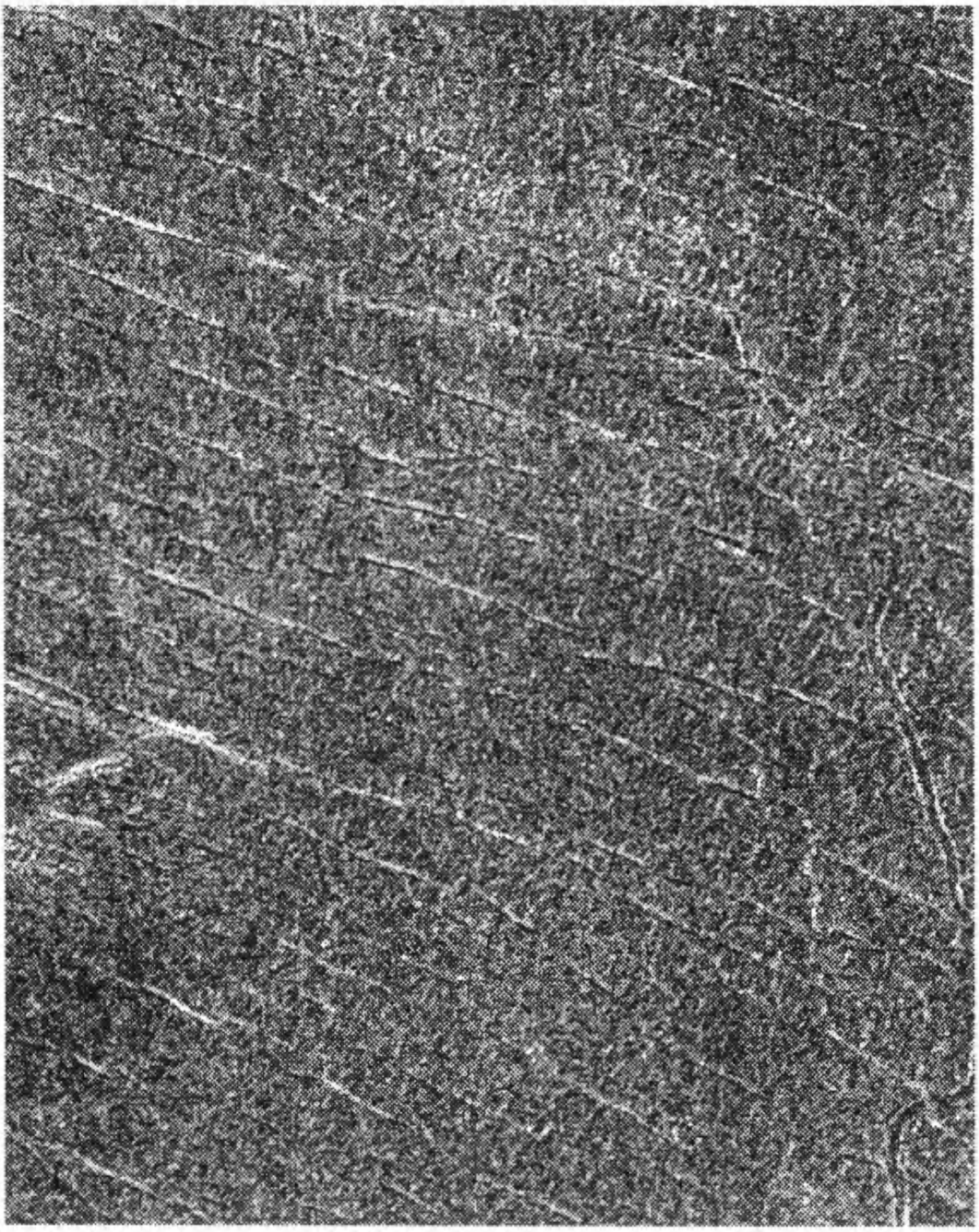

Appendix C1

When run, the program erfc.c outputs temperature profile solutions to the semi-infinite conduction problem.

erfc.c

```
#include <stdio.h>
#include <math.h>
#define SURFACE 1873.0          /* Surface Temperature */
#define INITIAL 273.0           /* Initial Temperature */
#define DENSITY 2700.0          /* Density */
#define CP 730.0                /* Specific Heat */
#define K 1.0                   /* Thermal Conductivity */
#define DX 0.01

main ()         {
                int x,y,p,n;
                double time[10],temperature[10][501],results[10][501],a;

                a = K / (CP * DENSITY);

                time[0] = 1;
                time[1] = 2;
                time[2] = 3;
                time[3] = 4;
                time[4] = 5;
                time[5] = 10;

                for (n = 0; n < 501; n++)
                        results[0][n] = (n * DX);

                for (p = 0; p < 6; p++)
                        {
                        for (n = 1; n < 501; n++)
                                results[p+1][n] = ((SURFACE - INITIAL) * erfc((n
* DX) / (2 * pow((a * (time[p] * 3600.0)),0.5)))) + INITIAL;
                        }


                for (y = 1; y < 501; y++)
                        {
                        printf ("%.4f\t",results[0][y]);
                        for (x = 1; x < 7; x++)
                                printf ("%.2f\t",results[x][y]);
                                printf ("\n");
                        }
                }
```

Appendix C2

fd.c uses finite differences to solve the semi-infinite conduction problem.

fd.c

```
#include <stdio.h>
#define SURFACE 1500        /* Lava Temperature */
#define SUBSTRATE 300       /* Rock Temperature */
#define DENSITY 2700.0      /* Density of the Rock */
#define K 1.0               /* Thermal conductivity of the Rock */
#define CP 730.0            /* Specific Heat of the Rock */
#define DX 0.01             /* Delta x */
#define DT 0.5              /* Delta t */

main ()     {
            int p,n;
            double temp[7301][2],a;


             /* Set initial values */


            temp[0][0] = SURFACE;
            temp[0][1] = SURFACE;

            for (n = 1; n < 7301; n++)
                  temp[n][0] = SUBSTRATE;

             a = K / (CP * DENSITY);



             /* Main body of the program */

            for (p = 1; p < ((3600 / DT) + 1); p++)
                  {
                  for (n = 1; n < 7301; n++)
                        temp[n][1] = temp[n][0] + ((a * DT) / (DX * DX)) *
(temp[n-1][0] + temp[n+1][0] - (2 * temp[n][0]));


                  for (n = 1; n < 7301; n++)
                        temp[n][0] = temp[n][1];
                  }



            /* Print the results */
```

```
for (n = 0; n < 101; n++)
        printf ("%.2f\t%.2f\n",(n * DX),temp[n][1]);

}
```

Appendix C3

heating.c solves the semi-infinite conduction problem by modelling the transfer of energy within the substrate.

heating.c

```
#include <stdio.h>
#define SURFACE 1500            /* Surface temperature */
#define SUBSTRATE 300           /* Substrate Temperature */
#define DENSITY 2700.0          /* Density of the Rock */
#define K 1.0                   /* Thermal conductivity of the Rock */
#define CP 730.0                /* Specific Heat of the Rock */
#define DX 0.01                 /* Delta x */
#define DT 6.0                  /* Delta t */
#define TIME_ONE 1.0            /* Time of first output in Hours */
#define TIME_TWO 2.0
#define TIME_THREE 5.0
#define TIME_FOUR 10.0
#define TIME_FIVE 20.0
#define TIME_SIX 25.0

double e_substrate;

main ()         {
                int p,n,x,y,col = 0,cold = 10;
                double energy[18000][2], results[10][18000], qcond, ducond,
upper, lower, temperature, belowtemperature;
                extern double e_substrate;
                double substratetemperature();


        /* Set initial values */


                e_substrate = DX * DENSITY * CP;

                for (n = 1; n <= cold; n++)
                        energy[n][0] = (SUBSTRATE * e_substrate);


                for (n = 0; n < 1001; n++)
                        results[col][n] = (n * DX);
                col += 1;



                /* Main body of the program */
```

```
        for (p = 1; p < ((TIME_SIX * 3600 / DT) + 1); p++)
                {
                temperature = substratetemperature(energy[1][0]);
                upper = -(K / DX) * (temperature - SURFACE);

                for (n = 1; n < cold; n++)
                        {
                        temperature = substratetemperature(energy[n][0 ]);
                        belowtemperature = substratetemperature(energ
y[n+ 1][0]);
                        lower = -(K / DX) * (belowtemperature -
temperature);
                        qcond = upper - lower;
                        ducond = qcond * DT;
                        energy[n][1] = energy[n][0] + ducond;
                        upper = lower;
                        }

                energy[cold][1] = energy[cold][0];

                for (n = 1; n <= cold; n++)
                        energy[n][0] = energy[n][1];

                if (rocktemperature(energy[cold-1][1]) > SUBSTRATE)
                        {
                        cold += 1;
                        energy[cold][0] = (SUBSTRATE * e_rock);
                        }


                if (p == (TIME_ONE * 3600 / DT) || p == (TIME_TWO *
3600 / DT) || p == (TIME_THREE * 3600 / DT) || p == (TIME_FOUR * 3600 /
DT) || p == (TIME_FIVE * 3600 / DT))
                        {
                        for (n = 1; n <= cold; n++)
                                results[col][n] = substratetemperature(ene
rgy[ n][1]);
                        col += 1;
                        }


                }


        for (y = 1; y < 101; y++)
                {
                for (x = 0; x < col; x++)
                        printf ("%.3f\t",results[x][y]);
                        printf ("\n");
                }
        }

double substratetemperature(joule)
        double joule;
```

```
{
extern double e_substrate;
return (joule / e_substrate);
}
```

Appendix C4

A complete listing of the erosional model erosion.c is shown below, followed by an expanded listing containing comments explaining what different sections of the code does.

erosion.c

```
#include <stdio.h>
#include <math.h>
#define LAVA 1500.0              /* Lava Temperature */
#define ROCK 300.0               /* Rock Temperature */
#define MELT 800.0               /* Melting Temperature */
#define DENSITY_ROCK 2700.0      /* Density of the Rock */
#define DENSITY_LAVA 2800.0      /* Density of the Lava */
#define K_ROCK 1.0               /* Thermal Conductivity of the Rock */
#define K_BL 1.0                 /* Thermal Conductivity of Boundary Layer */
#define K_LAVA 1.0               /* Thermal Conductivity of the Lava */
#define CP_ROCK 730.0            /* Specific Heat of the Rock */
#define CP_LAVA 730.0            /* Specific Heat of the Lava */
#define LATENT_ROCK 5.0e5        /* Latent Heat of the Rock */
#define LATENT_LAVA 5.0e5        /* Latent Heat of the Lava */
#define DX 0.01                  /* Delta x */
#define DT 6.0                   /* Delta t */
#define BL_DEPTH 0.1             /* Boundary Layer thickness in Meters */
#define TIME_ONE 10.0            /* Time of First Output in Hours */
#define TIME_TWO 20.0            /* Time of Second Output in Hours */
#define TIME_THREE 30.0          /* Time of Third Output in Hours */
#define TIME_FOUR 40.0           /* Time of Fourth Output in Hours */
#define TIME_FIVE 50.0           /* Time of Fifth Output in Hours */
#define TIME_SIX 100.0           /* Time of Sixth Output in Hours */
#define SETUP 4.5                        /* Initial Time for Temperature Profile */

double e_rock,qt_rock,rocksolid,rockliquid,bl_cell_no;
int flag = 0,hot = 1,melted[1000];

main ()          {
                 int p,n,x,y,col = 0,cold = 70,last = 0,diff;
                 double energy[18000][2], results[10][18000], initialtemp[101], lavaenergy,
qcond, ducond, upper, lower, temperature, belowtemperature, a;
                 extern double e_rock,qt_rock,bl_cell_no;
                 extern int flag,hot,melted[1000];
                 double rocktemperature();


                                  /* Set initial values */


                 e_rock = DX * DENSITY_ROCK * CP_ROCK;

                 qt_rock = DX * DENSITY_ROCK * LATENT_ROCK;

                 rocksolid = MELT * e_rock;
                 rockliquid = (MELT * e_rock) + qt_rock;
```

```
lavaenergy = (LAVA * e_rock) + qt_rock;

a = K_ROCK / (CP_ROCK * DENSITY_ROCK);

bl_cell_no = BL_DEPTH / DX;

for (n = 1; n < 101; n++)
        if (n <= bl_cell_no)
                melted[n] =1;
        else
                melted[n] = 0;

for (n = 1; n < 101; n++)
        {
        initialtemp[n] = ((LAVA - ROCK) * erfc((n * DX) / (2 * pow((a *
(SETUP * 3600)),0.5)))) + ROCK;
        energy[n][0] = initialtemp[n] * e_rock;
        if (initialtemp[n] > MELT)
                energy[n][0] = energy[n][0] + qt_rock;
        }


for (n = 0; n < 1001; n++)
        results[col][n] = (n * DX);
col += 3;

for (n = 1; n < 101; n++)
        results[col][n] = rocktemperature(energy[n][0],n);
col += 1;



                        /* Main body of the program */



for (p = 1; p < ((TIME_SIX * 3600 / DT) + 1); p++)
        {
        temperature = rocktemperature(energy[hot][0],hot);
        upper = -(K_LAVA / DX) * (temperature - LAVA);

        for (n = hot; n < cold; n++)
                {
                temperature = rocktemperature(energy[n][0],n);
                belowtemperature = rocktemperature(energy[n+ 1][0],n);
                if (n<hot + bl_cell_no)
                        lower = -(K_BL / DX) * (belowtemperature -
temperature);
                else
                        lower = -(K_ROCK / DX) * (belowtemperature -
temperature);
                qcond = upper - lower;
                ducond = qcond * DT;
                energy[n][1] = energy[n][0] + ducond;
                upper = lower;
                }

        energy[cold][1] = energy[cold][0];

        for (n = hot; n <= cold; n++)
                energy[n][0] = energy[n][1];
```

```
                        if (rocktemperature(energy[cold-1][1],(cold-1)) > ROCK)
                                {
                                cold += 1;
                                energy[cold][0] = (ROCK * e_rock);
                                }

                        if (flag == 1)
                                {
                                energy[hot][0] = lavaenergy;
                                energy[hot][1] = lavaenergy;
                                results[1][hot+bl_cell_no] = p;
                                diff = p - last;
                                results[2][hot+bl_cell_no] = diff;
                                last = p;
                                hot += 1;
                                flag = 0;
                                }


                        if (p == (TIME_ONE * 3600 / DT) || p == (TIME_TWO * 3600 / DT) ||
p == (TIME_THREE * 3600 / DT) || p == (TIME_FOUR * 3600 / DT) || p == (TIME_F IVE *
3600 / DT) || p == (TIME_SIX * 3600 / DT))
                                {
                                for (n = 1; n <= cold; n++)
                                        results[col][n] = rocktemperature(energy[ n][1],n);
                                col += 1;
                                }


                        }


                for (y = 1; y < 501; y++)
                        {
                        printf ("%.3f\t",results[0][y]);
                        for (x = 1; x < col; x++)
                                printf ("%.2f\t",results[x][y]);
                                printf ("\n");
                        }
                }

double rocktemperature(joule,cell)
        double joule;
        int cell;
        {
        extern double e_rock,rocksolid,rockliquid;
        extern int flag;

        if (joule >= rockliquid)
                {
                if (melted[cell] == 0 && cell > hot + bl_cell_no - 1)
                        {
                        melted[cell] = 1;
                        flag = 1;
                        }
                return((joule - qt_rock) / e_rock);
                }
        if (joule > rocksolid && joule < rockliquid)
                return(MELT);
        if (joule <= rocksolid)
                return (joule / e_rock);
```

```
}
```

Tells the compiler to include the standard input/output and maths libraries.

```
#include <stdio.h>
#include <math.h>
```

Defines the thermal properties of the lava and the substrate.

```
#define LAVA 1873.0              /* Lava Temperature */
#define ROCK 273.0               /* Rock Temperature */
#define MELT 1473.0              /* Melting Temperature */
#define DENSITY_ROCK 2700.0      /* Density of the Rock */
#define DENSITY_LAVA 2800.0      /* Density of the Lava */
#define K_ROCK 1.0               /* Thermal Conductivity of the Rock */
#define K_BL 1.0                 /* Thermal Conductivity of Boundary Layer */
#define K_LAVA 1.0               /* Thermal Conductivity of the Lava */
#define CP_ROCK 730.0            /* Specific Heat of the Rock */
#define CP_LAVA 730.0            /* Specific Heat of the Lava */
#define LATENT_ROCK 5.0e5        /* Latent Heat of the Rock */
#define LATENT_LAVA 5.0e5        /* Latent Heat of the Lava */
```

Defines the cell size in metres, the timestep in seconds, and the liquid boundary layer in metres.

```
#define DX 0.01                  /* Delta x */
#define DT 6.0                   /* Delta t */
#define BL_DEPTH 0.1             /* Boundary Layer thickness in Meters */
```

Defines the times at which the program will output a temperaure profile.

```
#define TIME_ONE 10.0            /* Time of First Output in Hours */
#define TIME_TWO 20.0            /* Time of Second Output in Hours */
#define TIME_THREE 30.0          /* Time of Third Output in Hours */
#define TIME_FOUR 40.0           /* Time of Fourth Output in Hours */
#define TIME_FIVE 50.0           /* Time of Fifth Output in Hours */
#define TIME_SIX 100.0           /* Time of Sixth Output in Hours */
```

Defines the time to be used for the inital temperature profile within the substrate.

```
#define SETUP 4.5                /* Initial Time for Temperature Profile */
```

Declaration of global variables.

```
double e_rock,qt_rock,rocksolid,rockliquid,bl_cell_no;
int flag = 0,hot = 1,melted[1000];
```

Declaration of local variables for function main.

```
main () {
        int p,n,x,y,col = 0,cold = 70,last = 0,diff;
        double energy[18000][2],results[10][18000],initialtemp[101],lavaenergy,qcond,
ducond,upper,lower,temperature,belowtemperature,a;
        extern double e_rock,qt_rock,bl_cell_no;
        extern int flag,hot,melted[1000];
        double rocktemperature(),lavatemperature();


                                /* Set initial values */
```

Calculation of local thermal variables.

```
e_rock = DX * DENSITY_ROCK * CP_ROCK;

qt_rock = DX * DENSITY_ROCK * LATENT_ROCK;

rocksolid = MELT * e_rock;
rockliquid = (MELT * e_rock) + qt_rock;


lavaenergy = (LAVA * e_rock) + qt_rock;
```

Calculation of thermal diffusivity.

```
a = K_ROCK / (CP_ROCK * DENSITY_ROCK);
```

Calculation of number of cells in the liquid boundary layer.

```
bl_cell_no = BL_DEPTH / DX;
```

Sets the flag 'melted' to one for the liquid boundary layer and zero for the next 90 cells.

```
for (n = 1; n < 101; n++)
        if (n <= bl_cell_no)
                melted[n] = 1;
        else
                melted[n] = 0;
```

Sets up the initial temperarure profile within the substrate.

```
for (n = 1; n < 101; n++)
        {
        initialtemp[n] = ((LAVA - ROCK) * erfc((n * DX) / (2 * pow((a * (SETUP *
3600)),0.5)))) + ROCK;
        energy[n][0] = initialtemp[n] * e_rock;
        if (initialtemp[n] > MELT)
                energy[n][0] = energy[n][0] + qt_rock;
        }
```

Puts depth into substrate as the first column of the results.

```
for (n = 0; n < 1001; n++)
        results[col][n] = (n * DX);
col += 3;
```

Puts initial subtrate temperature as the fourth column of the results.

```
for (n = 1; n < 101; n++)
        results[col][n] = rocktemperature(energy[n][0],n);
col += 1;
```

/* Main body of the program */

Beginning of main loop.

```
for (p = 1; p < ((TIME_SIX * 3600 / DT) + 1); p++)
```

Calculation of heat flow into the top of the liquid boundary layer.

```
{
temperature = rocktemperature(energy[hot][0],hot);
upper = -(K_LAVA / DX) * (temperature - LAVA);
```

Calculation of heat flow within the liquid boundary layer and the solid substrate.

```
for (n = hot; n < cold; n++)
        {
        temperature = rocktemperature(energy[n][0],n);
        belowtemperature = rocktemperature(energy[n+1][0],n) ;
        if (n<hot + bl_cell_no)
                lower = -(K_BL / DX) * (belowtemperature - temperature);
        else
                lower = -(K_ROCK / DX) * (belowtemperature - temperature);
        qcond = upper - lower;
        ducond = qcond * DT;
        energy[n][1] = energy[n][0] + ducond;
        upper = lower;
        }

energy[cold][1] = energy[cold][0];

for (n = hot; n <= cold; n++)
        energy[n][0] = energy[n][1];
```

Checks to see if heat has reached the lowest cell in the solid substrate, and if so, add another cell to the model.

```
if (rocktemperature(energy[cold-1][1],(cold-1)) > ROCK)
        {
        cold += 1;
        energy[cold][0] = (ROCK * e_rock);
        }
```

Checks to see if the uppermost cell of the liquid boundary layer has melted, and if so, amalgamates it into the lava.

```
if (flag == 1)
        {
        energy[hot][0] = lavaenergy;
        energy[hot][1] = lavaenergy;
        results[1][hot+bl_cell_no] = p;
        diff = p - last;
        results[2][hot+bl_cell_no] = diff;
        last = p;
        hot += 1;
        flag = 0;
        }
```

Checks to see if the elapsed simulated time is equal to one of the output times, and if so, outputs the current temperature profile as the next column of the results.

```
        if (p == (TIME_ONE * 3600 / DT) || p == (TIME_TWO * 3600 / DT) || p ==
(TIME_THREE * 3600 / DT) || p == (TIME_FOUR * 3600 / DT) || p == (TIME_F IVE * 3600 /
DT) || p == (TIME_SIX * 3600 / DT))
                {
                for (n = 1; n <= cold; n++)
                        results[col][n] = rocktemperature(energy[n][1],n );
                col += 1;
                }
```

```
        }
```

Outputs the results.

```
    for (y = 1; y < 501; y++)
        {
        printf ("%.3f\t",results[0][y]);
        for (x = 1; x < col; x++)
            printf ("%.2f\t",results[x][y]);
            printf ("\n");
        }
    }
```

Function which returns the temperature of a cell.

```
double rocktemperature(joule,cell)
    double joule;
    int cell;
    {
    extern double e_rock,rocksolid,rockliquid;
    extern int flag;

    if (joule >= rockliquid)
        {
        if (melted[cell] == 0 && cell > hot + bl_cell_no - 1)
            {
            melted[cell] = 1;
            flag = 1;
            }
        return((joule - qt_rock) / e_rock);
        }
    if (joule > rocksolid && joule < rockliquid)
        return(MELT);
    if (joule <= rocksolid)
        return (joule / e_rock);
    }
```

Appendix D

This appendix contains the results from one run of the erosional model described in section 5.4. For a description of the parameters used in this run, see section 6.1.

0.010	0	0	1425.40	1500.00	1500.00	1500.00	1500.00	1500.00	1500.00
0.020	0	0	1351.25	1500.00	1500.00	1500.00	1500.00	1500.00	1500.00
0.030	0	0	1277.99	1500.00	1500.00	1500.00	1500.00	1500.00	1500.00
0.040	0	0	1206.06	1500.00	1500.00	1500.00	1500.00	1500.00	1500.00
0.050	0	0	1135.86	1500.00	1500.00	1500.00	1500.00	1500.00	1500.00
0.060	0	0	1067.76	1430.47	1500.00	1500.00	1500.00	1500.00	1500.00
0.070	0	0	1002.10	1361.42	1500.00	1500.00	1500.00	1500.00	1500.00
0.080	0	0	939.18	1293.29	1500.00	1500.00	1500.00	1500.00	1500.00
0.090	0	0	879.24	1226.43	1500.00	1500.00	1500.00	1500.00	1500.00
0.100	0	0	822.50	1161.11	1500.00	1500.00	1500.00	1500.00	1500.00
0.110	1328	1328	769.10	1097.46	1500.00	1500.00	1500.00	1500.00	1500.00
0.120	2454	1126	719.16	1035.50	1500.00	1500.00	1500.00	1500.00	1500.00
0.130	3483	1029	672.73	975.08	1427.49	1500.00	1500.00	1500.00	1500.00
0.140	4460	977	629.83	915.94	1355.70	1500.00	1500.00	1500.00	1500.00
0.150	5403	943	590.43	857.73	1285.29	1500.00	1500.00	1500.00	1500.00
0.160	6322	919	554.47	800.00	1216.80	1500.00	1500.00	1500.00	1500.00
0.170	7224	902	521.84	774.44	1150.62	1500.00	1500.00	1500.00	1500.00
0.180	8111	887	492.41	749.09	1086.98	1500.00	1500.00	1500.00	1500.00
0.190	8986	875	466.03	724.13	1025.86	1500.00	1500.00	1500.00	1500.00
0.200	9852	866	442.54	699.74	967.06	1430.58	1500.00	1500.00	1500.00
0.210	10710	858	421.73	676.05	910.21	1361.63	1500.00	1500.00	1500.00
0.220	11562	852	403.42	653.16	854.74	1293.57	1500.00	1500.00	1500.00
0.230	12407	845	387.39	631.17	800.00	1226.78	1500.00	1500.00	1500.00
0.240	13247	840	373.46	610.10	776.65	1161.49	1500.00	1500.00	1500.00
0.250	14082	835	361.43	589.99	753.53	1097.86	1500.00	1500.00	1500.00
0.260	14913	831	351.09	570.83	730.87	1035.87	1500.00	1500.00	1500.00
0.270	15740	827	342.26	552.60	708.84	975.39	1500.00	1500.00	1500.00
0.280	16564	824	334.77	535.29	687.56	916.17	1415.68	1500.00	1500.00
0.290	17385	821	328.45	518.87	667.13	857.85	1333.90	1500.00	1500.00
0.300	18203	818	323.15	503.32	647.57	800.00	1256.41	1500.00	1500.00
0.310	19019	816	318.73	488.60	628.88	778.94	1183.82	1500.00	1500.00
0.320	19832	813	315.08	474.68	611.05	758.04	1115.97	1500.00	1500.00
0.330	20643	811	312.07	461.55	594.04	737.42	1052.44	1500.00	1500.00
0.340	21453	810	309.61	449.18	577.80	717.23	993.12	1500.00	1500.00
0.350	22260	807	307.60	437.54	562.30	697.57	938.29	1429.33	1500.00
0.360	23066	806	305.98	426.61	547.50	678.51	888.25	1359.24	1500.00
0.370	23870	804	304.68	416.36	533.37	660.12	842.71	1290.23	1500.00
0.380	24672	802	303.65	406.77	519.88	642.43	800.00	1222.76	1500.00
0.390	25473	801	302.82	397.81	507.02	625.45	774.30	1157.12	1500.00
0.400	26273	800	302.17	389.46	494.76	609.18	750.01	1093.48	1500.00
0.410	27072	799	301.66	381.69	483.08	593.60	727.76	1031.85	1500.00
0.420	27869	797	301.26	374.46	471.97	578.71	707.41	972.05	1500.00
0.430	28666	797	300.96	367.77	461.40	564.46	688.51	913.78	1500.00
0.440	29461	795	300.72	361.57	451.35	550.84	670.64	856.61	1500.00
0.450	30256	795	300.54	355.84	441.82	537.82	653.57	800.00	1500.00
0.460	31049	793	300.40	350.57	432.78	525.38	637.17	779.74	1500.00
0.470	31842	793	300.30	345.71	424.21	513.49	621.38	759.65	1500.00
0.480	32634	792	300.22	341.25	416.10	502.13	606.20	739.88	1500.00
0.490	33425	791	300.16	337.16	408.43	491.28	591.61	720.55	1500.00
0.500	34215	790	300.12	333.42	401.18	480.92	577.61	701.78	1500.00
0.510	35005	790	300.08	330.00	394.33	471.04	564.19	683.64	1500.00
0.520	35794	789	300.06	326.88	387.87	461.61	551.33	666.18	1500.00
0.530	36582	788	300.04	324.05	381.77	452.63	539.01	649.42	1500.00
0.540	37370	788	300.03	321.48	376.04	444.07	527.23	633.36	1500.00
0.550	38157	787	300.02	319.15	370.64	435.92	515.95	617.99	1500.00

0.560	38944	787	300.02	317.04	365.57	428.16	505.17	603.28	1500.00
0.570	39730	786	300.01	315.13	360.81	420.78	494.85	589.21	1500.00
0.580	40516	786	300.01	313.42	356.34	413.76	485.00	575.75	1500.00
0.590	41301	785	300.01	311.88	352.15	407.09	475.58	562.86	1500.00
0.600	42085	784	300.00	310.50	348.23	400.75	466.58	550.52	1500.00
0.610	42870	785	300.00	309.26	344.56	394.74	457.99	538.71	1500.00
0.620	43653	783	300.00	308.15	341.13	389.04	449.78	527.40	1500.00
0.630	44437	784	300.00	307.16	337.93	383.63	441.95	516.57	1500.00
0.640	45220	783	300.00	306.28	334.95	378.50	434.48	506.21	1500.00
0.650	46002	782	300.00	305.50	332.17	373.65	427.35	496.29	1500.00
0.660	46785	783	300.00	304.81	329.58	369.05	420.55	486.81	1500.00
0.670	47567	782	300.00	304.20	327.18	364.70	414.07	477.73	1500.00
0.680	48348	781	300.00	303.66	324.95	360.59	407.90	469.05	1500.00
0.690	49129	781	300.00	303.18	322.87	356.71	402.02	460.75	1500.00
0.700	49910	781	300.00	302.76	320.95	353.04	396.43	452.81	1500.00
0.710	50691	781	300.00	302.39	319.17	349.59	391.10	445.23	1500.00
0.720	51471	780	300.00	302.07	317.53	346.32	386.03	437.98	1500.00
0.730	52251	780	300.00	301.78	316.01	343.25	381.21	431.06	1500.00
0.740	53031	780	300.00	301.54	314.61	340.35	376.63	424.45	1500.00
0.750	53811	780	300.00	301.32	313.32	337.63	372.27	418.14	1500.00
0.760	54590	779	300.00	301.13	312.13	335.06	368.14	412.12	1500.00
0.770	55369	779	300.00	300.97	311.03	332.65	364.21	406.37	1500.00
0.780	56148	779	300.00	300.83	310.02	330.39	360.48	400.88	1500.00
0.790	56927	779	300.00	300.71	309.10	328.26	356.95	395.65	1500.00
0.800	57705	778	300.00	300.60	308.25	326.27	353.59	390.67	1500.00
0.810	58483	778	300.00	300.51	307.48	324.40	350.42	385.91	1500.00
0.820	59261	778	300.00	300.44	306.77	322.65	347.41	381.38	1500.00
0.830	60039	778	300.00	300.37	306.12	321.01	344.56	377.07	1500.00
0.840	60817	778	300.00	300.31	305.53	319.48	341.86	372.96	1500.00
0.850	61594	777	300.00	300.26	304.99	318.05	339.30	369.04	1500.00
0.860	62371	777	300.00	300.22	304.50	316.71	336.89	365.32	1500.00
0.870	63148	777	300.00	300.19	304.05	315.46	334.61	361.77	1500.00
0.880	63925	777	300.00	300.16	303.64	314.29	332.45	358.40	1500.00
0.890	64702	777	300.00	300.13	303.27	313.21	330.42	355.19	1500.00
0.900	65478	776	300.00	300.11	302.94	312.19	328.49	352.15	1500.00
0.910	66255	777	300.00	300.09	302.63	311.25	326.68	349.25	1500.00
0.920	67031	776	300.00	300.08	302.36	310.37	324.97	346.50	1500.00
0.930	67807	776	300.00	300.06	302.11	309.56	323.36	343.88	1500.00
0.940	68583	776	300.00	300.05	301.89	308.80	321.84	341.40	1500.00
0.950	69359	776	300.00	300.04	301.69	308.10	320.41	339.05	1500.00
0.960	70135	776	300.00	300.04	301.50	307.45	319.07	336.81	1500.00
0.970	70910	775	300.00	300.03	301.34	306.84	317.80	334.70	1500.00
0.980	71686	776	300.00	300.02	301.19	306.28	316.61	332.69	1500.00
0.990	72461	775	300.00	300.02	301.06	305.77	315.50	330.79	1500.00
1.000	73236	775	300.00	300.02	300.94	305.29	314.45	328.98	1500.00
1.010	74012	776	0.00	300.01	300.84	304.84	313.46	327.27	1500.00
1.020	74787	775	0.00	300.01	300.74	304.44	312.54	325.66	1500.00
1.030	75562	775	0.00	300.01	300.66	304.06	311.67	324.13	1500.00
1.040	76336	774	0.00	300.01	300.58	303.71	310.86	322.68	1500.00
1.050	77111	775	0.00	300.01	300.51	303.39	310.10	321.31	1500.00
1.060	77886	775	0.00	300.01	300.45	303.10	309.38	320.02	1500.00
1.070	78660	774	0.00	300.00	300.40	302.82	308.72	318.80	1500.00
1.080	79435	775	0.00	300.00	300.35	302.58	308.09	317.64	1500.00
1.090	80209	774	0.00	300.00	300.31	302.35	307.51	316.55	1500.00
1.100	80983	774	0.00	300.00	300.27	302.14	306.97	315.53	1500.00
1.110	81757	774	0.00	300.00	300.24	301.94	306.46	314.55	1500.00
1.120	82531	774	0.00	300.00	300.21	301.77	305.98	313.64	1500.00
1.130	83305	774	0.00	300.00	300.18	301.60	305.54	312.78	1500.00
1.140	84079	774	0.00	300.00	300.16	301.46	305.13	311.96	1500.00
1.150	84853	774	0.00	300.00	300.14	301.32	304.74	311.20	1500.00
1.160	85627	774	0.00	300.00	300.12	301.20	304.39	310.48	1500.00
1.170	86401	774	0.00	300.00	300.11	301.09	304.05	309.80	1500.00
1.180	87174	773	0.00	300.00	300.09	300.98	303.74	309.16	1500.00
1.190	87948	774	0.00	300.00	300.08	300.89	303.45	308.56	1500.00
1.200	88721	773	0.00	300.00	300.07	300.80	303.19	308.00	1500.00
1.210	89495	774	0.00	300.00	300.06	300.73	302.94	307.47	1500.00
1.220	90268	773	0.00	300.00	300.05	300.65	302.71	306.97	1500.00
1.230	91041	773	0.00	300.00	300.05	300.59	302.50	306.50	1500.00
1.240	91815	774	0.00	300.00	300.04	300.53	302.30	306.07	1500.00

1.250	92588	773	0.00	300.00	300.03	300.48	302.11	305.65	1500.00
1.260	93361	773	0.00	300.00	300.03	300.43	301.94	305.27	1500.00
1.270	94134	773	0.00	300.00	300.03	300.39	301.79	304.91	1500.00
1.280	94907	773	0.00	300.00	300.02	300.35	301.64	304.57	1500.00
1.290	95680	773	0.00	300.00	300.02	300.31	301.51	304.25	1500.00
1.300	96453	773	0.00	300.00	300.02	300.28	301.38	303.96	1500.00
1.310	97226	773	0.00	300.00	300.01	300.25	301.27	303.68	1500.00
1.320	97999	773	0.00	300.00	300.01	300.23	301.16	303.42	1500.00
1.330	98771	772	0.00	300.00	300.01	300.20	301.06	303.18	1500.00
1.340	99544	773	0.00	300.00	300.01	300.18	300.97	302.95	1500.00
1.350	100317	773	0.00	300.00	300.01	300.16	300.89	302.74	1500.00
1.360	101089	772	0.00	300.00	300.01	300.14	300.82	302.54	1500.00
1.370	101862	773	0.00	300.00	300.01	300.13	300.75	302.36	1500.00
1.380	102634	772	0.00	300.00	300.00	300.11	300.68	302.18	1500.00
1.390	103407	773	0.00	300.00	300.00	300.10	300.62	302.02	1500.00
1.400	104179	772	0.00	300.00	300.00	300.09	300.57	301.87	1500.00
1.410	104952	773	0.00	300.00	300.00	300.08	300.52	301.74	1500.00
1.420	105724	772	0.00	300.00	300.00	300.07	300.47	301.61	1500.00
1.430	106496	772	0.00	300.00	300.00	300.06	300.43	301.49	1500.00
1.440	107269	773	0.00	300.00	300.00	300.06	300.39	301.37	1500.00
1.450	108041	772	0.00	300.00	300.00	300.05	300.36	301.27	1500.00
1.460	108813	772	0.00	300.00	300.00	300.04	300.32	301.17	1500.00
1.470	109585	772	0.00	300.00	300.00	300.04	300.29	301.08	1500.00
1.480	110357	772	0.00	300.00	300.00	300.03	300.27	301.00	1500.00
1.490	111129	772	0.00	300.00	300.00	300.03	300.24	300.92	1500.00
1.500	111901	772	0.00	300.00	300.00	300.03	300.22	300.85	1500.00
1.510	112673	772	0.00	300.00	300.00	300.02	300.20	300.78	1500.00
1.520	113445	772	0.00	300.00	300.00	300.02	300.18	300.72	1500.00
1.530	114217	772	0.00	300.00	300.00	300.02	300.16	300.67	1500.00
1.540	114989	772	0.00	300.00	300.00	300.02	300.15	300.61	1500.00
1.550	115761	772	0.00	300.00	300.00	300.01	300.13	300.56	1500.00
1.560	116533	772	0.00	300.00	300.00	300.01	300.12	300.52	1500.00
1.570	117305	772	0.00	300.00	300.00	300.01	300.11	300.48	1500.00
1.580	118077	772	0.00	300.00	300.00	300.01	300.10	300.44	1500.00
1.590	118849	772	0.00	300.00	300.00	300.01	300.09	300.40	1500.00
1.600	119620	771	0.00	300.00	300.00	300.01	300.08	300.37	1500.00
1.610	120392	772	0.00	300.00	300.00	300.01	300.07	300.34	1500.00
1.620	121164	772	0.00	300.00	300.00	300.01	300.07	300.31	1500.00
1.630	121936	772	0.00	300.00	300.00	300.01	300.06	300.28	1500.00
1.640	122707	771	0.00	300.00	300.00	300.00	300.05	300.26	1500.00
1.650	123479	772	0.00	300.00	300.00	300.00	300.05	300.24	1500.00
1.660	124251	772	0.00	300.00	300.00	300.00	300.04	300.22	1500.00
1.670	125022	771	0.00	300.00	300.00	300.00	300.04	300.20	1500.00
1.680	125794	772	0.00	300.00	300.00	300.00	300.03	300.18	1500.00
1.690	126565	771	0.00	300.00	300.00	300.00	300.03	300.17	1500.00
1.700	127337	772	0.00	300.00	300.00	300.00	300.03	300.15	1500.00
1.710	128108	771	0.00	300.00	300.00	300.00	300.02	300.14	1500.00
1.720	128880	772	0.00	300.00	300.00	300.00	300.02	300.13	1500.00
1.730	129651	771	0.00	300.00	300.00	300.00	300.02	300.12	1500.00
1.740	130423	772	0.00	300.00	300.00	300.00	300.02	300.11	1500.00
1.750	131194	771	0.00	300.00	300.00	300.00	300.02	300.10	1500.00
1.760	131966	772	0.00	300.00	300.00	300.00	300.01	300.09	1500.00
1.770	132737	771	0.00	300.00	300.00	300.00	300.01	300.08	1500.00
1.780	133508	771	0.00	300.00	300.00	300.00	300.01	300.07	1500.00
1.790	134280	772	0.00	300.00	300.00	300.00	300.01	300.07	1500.00
1.800	135051	771	0.00	300.00	300.00	300.00	300.01	300.06	1500.00
1.810	135822	771	0.00	300.00	300.00	300.00	300.01	300.06	1500.00
1.820	136594	772	0.00	300.00	300.00	300.00	300.01	300.05	1500.00
1.830	137365	771	0.00	300.00	300.00	300.00	300.01	300.05	1500.00
1.840	138136	771	0.00	300.00	300.00	300.00	300.01	300.04	1500.00
1.850	138908	772	0.00	300.00	300.00	300.00	300.01	300.04	1500.00
1.860	139679	771	0.00	0.00	300.00	300.00	300.00	300.03	1500.00
1.870	140450	771	0.00	0.00	300.00	300.00	300.00	300.03	1500.00
1.880	141221	771	0.00	0.00	300.00	300.00	300.00	300.03	1500.00
1.890	141993	772	0.00	0.00	300.00	300.00	300.00	300.03	1500.00
1.900	142764	771	0.00	0.00	300.00	300.00	300.00	300.02	1500.00
1.910	143535	771	0.00	0.00	300.00	300.00	300.00	300.02	1500.00
1.920	144306	771	0.00	0.00	300.00	300.00	300.00	300.02	1500.00
1.930	145077	771	0.00	0.00	300.00	300.00	300.00	300.02	1500.00

1.940	145848	771	0.00	0.00	300.00	300.00	300.00	300.02	1500.00
1.950	146619	771	0.00	0.00	300.00	300.00	300.00	300.01	1500.00
1.960	147391	772	0.00	0.00	300.00	300.00	300.00	300.01	1500.00
1.970	148162	771	0.00	0.00	300.00	300.00	300.00	300.01	1500.00
1.980	148933	771	0.00	0.00	300.00	300.00	300.00	300.01	1500.00
1.990	149704	771	0.00	0.00	300.00	300.00	300.00	300.01	1500.00
2.000	150475	771	0.00	0.00	300.00	300.00	300.00	300.01	1500.00
2.010	151246	771	0.00	0.00	300.00	300.00	300.00	300.01	1500.00
2.020	152017	771	0.00	0.00	300.00	300.00	300.00	300.01	1500.00
2.030	152788	771	0.00	0.00	300.00	300.00	300.00	300.01	1500.00
2.040	153559	771	0.00	0.00	300.00	300.00	300.00	300.01	1500.00
2.050	154330	771	0.00	0.00	300.00	300.00	300.00	300.00	1500.00
2.060	155101	771	0.00	0.00	300.00	300.00	300.00	300.00	1500.00
2.070	155872	771	0.00	0.00	300.00	300.00	300.00	300.00	1500.00
2.080	156643	771	0.00	0.00	300.00	300.00	300.00	300.00	1500.00
2.090	157414	771	0.00	0.00	300.00	300.00	300.00	300.00	1500.00
2.100	158185	771	0.00	0.00	300.00	300.00	300.00	300.00	1500.00
2.110	158956	771	0.00	0.00	300.00	300.00	300.00	300.00	1500.00
2.120	159727	771	0.00	0.00	300.00	300.00	300.00	300.00	1500.00
2.130	160498	771	0.00	0.00	300.00	300.00	300.00	300.00	1500.00
2.140	161269	771	0.00	0.00	300.00	300.00	300.00	300.00	1500.00
2.150	162040	771	0.00	0.00	300.00	300.00	300.00	300.00	1500.00
2.160	162811	771	0.00	0.00	300.00	300.00	300.00	300.00	1500.00
2.170	163582	771	0.00	0.00	300.00	300.00	300.00	300.00	1500.00
2.180	164353	771	0.00	0.00	300.00	300.00	300.00	300.00	1500.00
2.190	165123	770	0.00	0.00	300.00	300.00	300.00	300.00	1500.00
2.200	165894	771	0.00	0.00	300.00	300.00	300.00	300.00	1500.00
2.210	166665	771	0.00	0.00	300.00	300.00	300.00	300.00	1500.00
2.220	167436	771	0.00	0.00	300.00	300.00	300.00	300.00	1500.00
2.230	168207	771	0.00	0.00	300.00	300.00	300.00	300.00	1500.00
2.240	168978	771	0.00	0.00	300.00	300.00	300.00	300.00	1500.00
2.250	169749	771	0.00	0.00	300.00	300.00	300.00	300.00	1500.00
2.260	170519	770	0.00	0.00	300.00	300.00	300.00	300.00	1500.00
2.270	171290	771	0.00	0.00	300.00	300.00	300.00	300.00	1500.00
2.280	172061	771	0.00	0.00	300.00	300.00	300.00	300.00	1500.00
2.290	172832	771	0.00	0.00	300.00	300.00	300.00	300.00	1500.00
2.300	173603	771	0.00	0.00	300.00	300.00	300.00	300.00	1500.00
2.310	174373	770	0.00	0.00	300.00	300.00	300.00	300.00	1500.00
2.320	175144	771	0.00	0.00	300.00	300.00	300.00	300.00	1500.00
2.330	175915	771	0.00	0.00	300.00	300.00	300.00	300.00	1500.00
2.340	176686	771	0.00	0.00	300.00	300.00	300.00	300.00	1500.00
2.350	177457	771	0.00	0.00	300.00	300.00	300.00	300.00	1500.00
2.360	178227	770	0.00	0.00	300.00	300.00	300.00	300.00	1500.00
2.370	178998	771	0.00	0.00	300.00	300.00	300.00	300.00	1500.00
2.380	179769	771	0.00	0.00	300.00	300.00	300.00	300.00	1500.00
2.390	180540	771	0.00	0.00	0.00	300.00	300.00	300.00	1500.00
2.400	181310	770	0.00	0.00	0.00	300.00	300.00	300.00	1500.00
2.410	182081	771	0.00	0.00	0.00	300.00	300.00	300.00	1500.00
2.420	182852	771	0.00	0.00	0.00	300.00	300.00	300.00	1500.00
2.430	183623	771	0.00	0.00	0.00	300.00	300.00	300.00	1500.00
2.440	184393	770	0.00	0.00	0.00	300.00	300.00	300.00	1500.00
2.450	185164	771	0.00	0.00	0.00	300.00	300.00	300.00	1500.00
2.460	185935	771	0.00	0.00	0.00	300.00	300.00	300.00	1500.00
2.470	186705	770	0.00	0.00	0.00	300.00	300.00	300.00	1500.00
2.480	187476	771	0.00	0.00	0.00	300.00	300.00	300.00	1500.00
2.490	188247	771	0.00	0.00	0.00	300.00	300.00	300.00	1500.00
2.500	189017	770	0.00	0.00	0.00	300.00	300.00	300.00	1500.00
2.510	189788	771	0.00	0.00	0.00	300.00	300.00	300.00	1500.00
2.520	190559	771	0.00	0.00	0.00	300.00	300.00	300.00	1500.00
2.530	191329	770	0.00	0.00	0.00	300.00	300.00	300.00	1500.00
2.540	192100	771	0.00	0.00	0.00	300.00	300.00	300.00	1500.00
2.550	192871	771	0.00	0.00	0.00	300.00	300.00	300.00	1500.00
2.560	193641	770	0.00	0.00	0.00	300.00	300.00	300.00	1500.00
2.570	194412	771	0.00	0.00	0.00	300.00	300.00	300.00	1500.00
2.580	195183	771	0.00	0.00	0.00	300.00	300.00	300.00	1500.00
2.590	195953	770	0.00	0.00	0.00	300.00	300.00	300.00	1500.00
2.600	196724	771	0.00	0.00	0.00	300.00	300.00	300.00	1500.00
2.610	197495	771	0.00	0.00	0.00	300.00	300.00	300.00	1500.00
2.620	198265	770	0.00	0.00	0.00	300.00	300.00	300.00	1500.00

2.630	199036	771	0.00	0.00	0.00	300.00	300.00	300.00	1500.00
2.640	199807	771	0.00	0.00	0.00	300.00	300.00	300.00	1500.00
2.650	200577	770	0.00	0.00	0.00	300.00	300.00	300.00	1500.00
2.660	201348	771	0.00	0.00	0.00	300.00	300.00	300.00	1500.00
2.670	202118	770	0.00	0.00	0.00	300.00	300.00	300.00	1500.00
2.680	202889	771	0.00	0.00	0.00	300.00	300.00	300.00	1500.00
2.690	203660	771	0.00	0.00	0.00	300.00	300.00	300.00	1500.00
2.700	204430	770	0.00	0.00	0.00	300.00	300.00	300.00	1500.00
2.710	205201	771	0.00	0.00	0.00	300.00	300.00	300.00	1500.00
2.720	205971	770	0.00	0.00	0.00	300.00	300.00	300.00	1500.00
2.730	206742	771	0.00	0.00	0.00	300.00	300.00	300.00	1500.00
2.740	207513	771	0.00	0.00	0.00	300.00	300.00	300.00	1500.00
2.750	208283	770	0.00	0.00	0.00	300.00	300.00	300.00	1500.00
2.760	209054	771	0.00	0.00	0.00	300.00	300.00	300.00	1500.00
2.770	209824	770	0.00	0.00	0.00	300.00	300.00	300.00	1500.00
2.780	210595	771	0.00	0.00	0.00	300.00	300.00	300.00	1500.00
2.790	211366	771	0.00	0.00	0.00	300.00	300.00	300.00	1500.00
2.800	212136	770	0.00	0.00	0.00	300.00	300.00	300.00	1500.00
2.810	212907	771	0.00	0.00	0.00	300.00	300.00	300.00	1500.00
2.820	213677	770	0.00	0.00	0.00	0.00	300.00	300.00	1500.00
2.830	214448	771	0.00	0.00	0.00	0.00	300.00	300.00	1500.00
2.840	215218	770	0.00	0.00	0.00	0.00	300.00	300.00	1500.00
2.850	215989	771	0.00	0.00	0.00	0.00	300.00	300.00	1500.00
2.860	216760	771	0.00	0.00	0.00	0.00	300.00	300.00	1500.00
2.870	217530	770	0.00	0.00	0.00	0.00	300.00	300.00	1500.00
2.880	218301	771	0.00	0.00	0.00	0.00	300.00	300.00	1500.00
2.890	219071	770	0.00	0.00	0.00	0.00	300.00	300.00	1500.00
2.900	219842	771	0.00	0.00	0.00	0.00	300.00	300.00	1500.00
2.910	220612	770	0.00	0.00	0.00	0.00	300.00	300.00	1500.00
2.920	221383	771	0.00	0.00	0.00	0.00	300.00	300.00	1500.00
2.930	222153	770	0.00	0.00	0.00	0.00	300.00	300.00	1500.00
2.940	222924	771	0.00	0.00	0.00	0.00	300.00	300.00	1500.00
2.950	223694	770	0.00	0.00	0.00	0.00	300.00	300.00	1500.00
2.960	224465	771	0.00	0.00	0.00	0.00	300.00	300.00	1500.00
2.970	225236	771	0.00	0.00	0.00	0.00	300.00	300.00	1500.00
2.980	226006	770	0.00	0.00	0.00	0.00	300.00	300.00	1500.00
2.990	226777	771	0.00	0.00	0.00	0.00	300.00	300.00	1500.00
3.000	227547	770	0.00	0.00	0.00	0.00	300.00	300.00	1500.00
3.010	228318	771	0.00	0.00	0.00	0.00	300.00	300.00	1500.00
3.020	229088	770	0.00	0.00	0.00	0.00	300.00	300.00	1500.00
3.030	229859	771	0.00	0.00	0.00	0.00	300.00	300.00	1500.00
3.040	230629	770	0.00	0.00	0.00	0.00	300.00	300.00	1500.00
3.050	231400	771	0.00	0.00	0.00	0.00	300.00	300.00	1500.00
3.060	232170	770	0.00	0.00	0.00	0.00	300.00	300.00	1500.00
3.070	232941	771	0.00	0.00	0.00	0.00	300.00	300.00	1500.00
3.080	233711	770	0.00	0.00	0.00	0.00	300.00	300.00	1500.00
3.090	234482	771	0.00	0.00	0.00	0.00	300.00	300.00	1500.00
3.100	235252	770	0.00	0.00	0.00	0.00	300.00	300.00	1500.00
3.110	236023	771	0.00	0.00	0.00	0.00	300.00	300.00	1500.00
3.120	236793	770	0.00	0.00	0.00	0.00	300.00	300.00	1500.00
3.130	237564	771	0.00	0.00	0.00	0.00	300.00	300.00	1500.00
3.140	238334	770	0.00	0.00	0.00	0.00	300.00	300.00	1500.00
3.150	239105	771	0.00	0.00	0.00	0.00	300.00	300.00	1500.00
3.160	239875	770	0.00	0.00	0.00	0.00	300.00	300.00	1500.00
3.170	240646	771	0.00	0.00	0.00	0.00	300.00	300.00	1500.00
3.180	241416	770	0.00	0.00	0.00	0.00	0.00	300.00	1500.00
3.190	242187	771	0.00	0.00	0.00	0.00	0.00	300.00	1500.00
3.200	242957	770	0.00	0.00	0.00	0.00	0.00	300.00	1500.00
3.210	243728	771	0.00	0.00	0.00	0.00	0.00	300.00	1500.00
3.220	244498	770	0.00	0.00	0.00	0.00	0.00	300.00	1500.00
3.230	245269	771	0.00	0.00	0.00	0.00	0.00	300.00	1500.00
3.240	246039	770	0.00	0.00	0.00	0.00	0.00	300.00	1500.00
3.250	246810	771	0.00	0.00	0.00	0.00	0.00	300.00	1500.00
3.260	247580	770	0.00	0.00	0.00	0.00	0.00	300.00	1500.00
3.270	248351	771	0.00	0.00	0.00	0.00	0.00	300.00	1500.00
3.280	249121	770	0.00	0.00	0.00	0.00	0.00	300.00	1500.00
3.290	249892	771	0.00	0.00	0.00	0.00	0.00	300.00	1500.00
3.300	250662	770	0.00	0.00	0.00	0.00	0.00	300.00	1500.00
3.310	251433	771	0.00	0.00	0.00	0.00	0.00	300.00	1500.00

3.320	252203	770	0.00	0.00	0.00	0.00	0.00	300.00	1500.00
3.330	252974	771	0.00	0.00	0.00	0.00	0.00	300.00	1500.00
3.340	253744	770	0.00	0.00	0.00	0.00	0.00	300.00	1500.00
3.350	254515	771	0.00	0.00	0.00	0.00	0.00	300.00	1500.00
3.360	255285	770	0.00	0.00	0.00	0.00	0.00	300.00	1500.00
3.370	256056	771	0.00	0.00	0.00	0.00	0.00	300.00	1500.00
3.380	256826	770	0.00	0.00	0.00	0.00	0.00	300.00	1500.00
3.390	257597	771	0.00	0.00	0.00	0.00	0.00	300.00	1500.00
3.400	258367	770	0.00	0.00	0.00	0.00	0.00	300.00	1500.00
3.410	259138	771	0.00	0.00	0.00	0.00	0.00	300.00	1500.00
3.420	259908	770	0.00	0.00	0.00	0.00	0.00	300.00	1500.00
3.430	260679	771	0.00	0.00	0.00	0.00	0.00	300.00	1500.00
3.440	261449	770	0.00	0.00	0.00	0.00	0.00	300.00	1500.00
3.450	262220	771	0.00	0.00	0.00	0.00	0.00	300.00	1500.00
3.460	262990	770	0.00	0.00	0.00	0.00	0.00	300.00	1500.00
3.470	263761	771	0.00	0.00	0.00	0.00	0.00	300.00	1500.00
3.480	264531	770	0.00	0.00	0.00	0.00	0.00	300.00	1500.00
3.490	265301	770	0.00	0.00	0.00	0.00	0.00	300.00	1500.00
3.500	266072	771	0.00	0.00	0.00	0.00	0.00	300.00	1500.00
3.510	266842	770	0.00	0.00	0.00	0.00	0.00	0.00	1500.00
3.520	267613	771	0.00	0.00	0.00	0.00	0.00	0.00	1500.00
3.530	268383	770	0.00	0.00	0.00	0.00	0.00	0.00	1500.00
3.540	269154	771	0.00	0.00	0.00	0.00	0.00	0.00	1500.00
3.550	269924	770	0.00	0.00	0.00	0.00	0.00	0.00	1500.00
3.560	270695	771	0.00	0.00	0.00	0.00	0.00	0.00	1500.00
3.570	271465	770	0.00	0.00	0.00	0.00	0.00	0.00	1500.00
3.580	272236	771	0.00	0.00	0.00	0.00	0.00	0.00	1500.00
3.590	273006	770	0.00	0.00	0.00	0.00	0.00	0.00	1500.00
3.600	273777	771	0.00	0.00	0.00	0.00	0.00	0.00	1500.00
3.610	274547	770	0.00	0.00	0.00	0.00	0.00	0.00	1500.00
3.620	275317	770	0.00	0.00	0.00	0.00	0.00	0.00	1500.00
3.630	276088	771	0.00	0.00	0.00	0.00	0.00	0.00	1500.00
3.640	276858	770	0.00	0.00	0.00	0.00	0.00	0.00	1500.00
3.650	277629	771	0.00	0.00	0.00	0.00	0.00	0.00	1500.00
3.660	278399	770	0.00	0.00	0.00	0.00	0.00	0.00	1500.00
3.670	279170	771	0.00	0.00	0.00	0.00	0.00	0.00	1500.00
3.680	279940	770	0.00	0.00	0.00	0.00	0.00	0.00	1500.00
3.690	280711	771	0.00	0.00	0.00	0.00	0.00	0.00	1500.00
3.700	281481	770	0.00	0.00	0.00	0.00	0.00	0.00	1500.00
3.710	282252	771	0.00	0.00	0.00	0.00	0.00	0.00	1500.00
3.720	283022	770	0.00	0.00	0.00	0.00	0.00	0.00	1500.00
3.730	283792	770	0.00	0.00	0.00	0.00	0.00	0.00	1500.00
3.740	284563	771	0.00	0.00	0.00	0.00	0.00	0.00	1500.00
3.750	285333	770	0.00	0.00	0.00	0.00	0.00	0.00	1500.00
3.760	286104	771	0.00	0.00	0.00	0.00	0.00	0.00	1500.00
3.770	286874	770	0.00	0.00	0.00	0.00	0.00	0.00	1500.00
3.780	287645	771	0.00	0.00	0.00	0.00	0.00	0.00	1500.00
3.790	288415	770	0.00	0.00	0.00	0.00	0.00	0.00	1500.00
3.800	289186	771	0.00	0.00	0.00	0.00	0.00	0.00	1500.00
3.810	289956	770	0.00	0.00	0.00	0.00	0.00	0.00	1500.00
3.820	290726	770	0.00	0.00	0.00	0.00	0.00	0.00	1500.00
3.830	291497	771	0.00	0.00	0.00	0.00	0.00	0.00	1500.00
3.840	292267	770	0.00	0.00	0.00	0.00	0.00	0.00	1500.00
3.850	293038	771	0.00	0.00	0.00	0.00	0.00	0.00	1395.64
3.860	293808	770	0.00	0.00	0.00	0.00	0.00	0.00	1308.56
3.870	294579	771	0.00	0.00	0.00	0.00	0.00	0.00	1235.62
3.880	295349	770	0.00	0.00	0.00	0.00	0.00	0.00	1169.12
3.890	296119	770	0.00	0.00	0.00	0.00	0.00	0.00	1105.15
3.900	296890	771	0.00	0.00	0.00	0.00	0.00	0.00	1042.56
3.910	297660	770	0.00	0.00	0.00	0.00	0.00	0.00	981.21
3.920	298431	771	0.00	0.00	0.00	0.00	0.00	0.00	921.72
3.930	299201	770	0.00	0.00	0.00	0.00	0.00	0.00	866.53
3.940	299972	771	0.00	0.00	0.00	0.00	0.00	0.00	820.80
3.950	0	0	0.00	0.00	0.00	0.00	0.00	0.00	788.60
3.960	0	0	0.00	0.00	0.00	0.00	0.00	0.00	765.66
3.970	0	0	0.00	0.00	0.00	0.00	0.00	0.00	746.65
3.980	0	0	0.00	0.00	0.00	0.00	0.00	0.00	728.97
3.990	0	0	0.00	0.00	0.00	0.00	0.00	0.00	711.87
4.000	0	0	0.00	0.00	0.00	0.00	0.00	0.00	695.25

References

Adkins, C.J., Equilibrium Thermodynamics, 285pp, CUP, 1983.

Baker, V.R., G. Komatsu, T.J. Parker, V.C. Gulick, J.S. Kargel, J.S. Lewis, Channels and Valleys on Venus: Preliminary Analysis of Magellan Data, J. Geophys. Res., V.97, p 13421 - 13444, 1992.

Bevington, P.R., Data Reduction and Error Analysis for the Physical Sciences, 335 pp, McGraw-Hill, 1969.

Briggs, G.A., and F.W. Taylor, The Cambridge Photographic Atlas of the Planets, 256pp, CUP, 1982.

Bussey, D.B.J., and J.E. Guest, Erosion vs. Construction: The Origin of Venusian Channels, International Colloq. on Venus, Pasadena, LPI Contribution 789, 18-19, 1992.

Bussey, D.B.J., S-A Sörenesen, J.E. Guest, Factors Influencing the Capability of Lava to Erode its Substrate: Application to Venus, J. Geophys. Res., In Press, 1995.

Cameron, W.S., An Interpretation of Schroeter's Valley and Other Sinuous Rilles, J. Geophys. Res., V.69, p 2423 - 2430, 1964.

Carr, M.H., The Role of Lava Erosion in the Formation of Lunar Rilles and Martian Channels, Icarus, 22, p 1 - 23, 1974.

Dawson, J.B., P. Bowden, G.C. Clark, Activity of the Carbonatite Volcano Oldoinyo Lengai, 1966, Geol. Rund., 57, p 865 - 879, 1968.

Dragoni, M., M. Bonafede, E. Boschi, Downslope Flow Models of a Bingham Liquid: Implications for Lava Flows, J. Volc. Geotherm. Res., 30, p 305 - 325, 1986.

Fink, J.H., N.T. Bridges, R.E. Grimm, Shapes of Venusian "Pancake" Domes Imply Episodic Emplacement and Silicic Composition, Geophys. Res. Letts., V.20, No. 4, p 261 - 264, 1993.

Florensky, C.P., L.B. Ronca, A.T. Basilevsky, G.A. Burba, O.V. Nikolaeva, A.A. Pronin, A.M. Trakhtman, V.P. Volkov, V.V. Zazetsky, The Surface of Venus as revealed by Soviet Venera 9 and 10, Geol. Soc. Am. Bull., V.88, p 1537 - 1545, 1977.

Ford, J.P., R.G. Blom, J.A. Crisp, C. Elachi, T.G. Farr, R.S. Saunders, E.E. Theilig, S.D. Wall, S.B. Yewell, Spaceborne Radar Observations, 126pp, JPL Pub. 89-41, 1989.

Ford, J.P., and G.H. Pettengill, Venus Topography and Kilometer-Scale Slopes, J. Geophys, Res., V.97, p 13103 - 13114, 1992.

Ford, J.P., J.J. Plaut, C.M. Weitz, T.G. Farr, D.A. Senske, E.R. Stofan, G Michaels, T.J. Parker, Guide to Magellan Image Interpretation, 148pp, JPL Pub. 93-24, 1993.

Greeley, R., Lunar Hadley Rille: Considerations of it's Origin. Science, 172, p 722 - 725, 1971.

Gregg, T.K.P., and R. Greeley, Formation of Venusian Canali: Considerations of Lava Types and Their Thermal Behaviors, J. Geophys. Res., V.98, p 10873 - 10882, 1993.

Guest, J.E., M.H. Bulmer, J. Aubele, K. Beratan, R. Greeley, J.W. Head, G. Michaels, C. Weitz, C. Wiles, Small Volcanic Edifices and Volcanism in the Plains of Venus, J. Geophys. Res., V.97, p 15949 - 15966, 1992.

Head, J.W., and L. Wilson, The Formation of Eroded Depressions around the Sources of Lunar Sinuous Rilles: Observations, LPSC XI, p 426 - 428, 1980.

Head, J.W., and L. Wilson, Lunar Sinuous Rille Formation by Thermal Erosion: Eruption Conditions, Rates and Durations, LPSC XII, p 427 - 429, 1981.

Head, J.W., and L. Wilson, Volcanic Processes and Landforms on Venus: Theory, Predictions, and Observations, J. Geophys. Res., V.91, p 9407 - 9446, 1986.

Head, J.W., D.B. Campbell, C. Elachi, J.E. Guest, D.P., McKenzie, R.S. Saunders, G.G. Schaber, G. Schubert, Venus Volcanism: Initial Analysis fom Magellan Data, Science, V.252, p 276 -288, 1991.

Head, J.W., and L. Wilson, Magma Reservoirs and Neutral Buoyancy Zones on Venus: Implications for the Formation and Evolution of Volcanic Landforms, J. Geophys. Res., V.97, p 3877 - 3903, 1992.

Head, J.W., L.S. Crumpler, J.C. Aubele, J.E. Guest, R.S. Saunders, Venus Volcanism: Classification of Volcanic Features and Structures, Associations, and

Global Distribution from Magellan Data, J. Geophys. Res., V.97, p 13153 - 13197, 1992.

Heading, J., Mathematical Methods in Science and Engineering, 692pp, Arnold, 1970.

Holman, J.P., Heat Transfer, 676pp, McGraw Hill, Sigapore, 1989.

Hulme, G., Turbulent Lava Flow and the Formation of Lunar Sinuous Rilles, Mod. Geol., V.4, p 107 - 117, 1973.

Hulme, G., The Interpretation of Lava Flow Morphology, Geophys. J. Roy. Astr. Soc., 39, p 361 - 383, 1974.

Hulme, G., and G. Fielder, Effusion Rates and Rheology of Lunar Lavas, Phil. Trans. Roy. Soc. Lond. A., 285, p 227 - 234, 1977.

Hulme, G., A Review of Lava Flow Processes Related to the Formation of Lunar Sinuous Rilles, Geophys. Survs., 5, p 245 - 279, 1982.

Huppert, H.E., R.S.J. Sparks, J.S. Turner, N.T. Arndt, Emplacement and Cooling of Komatiite Lavas, Nature, 309, p 19 - 22, 1984.

Huppert, H.E., and R.S.J. Sparks, Komatiites I: Eruption and Flow, J. Petrol., 26, p 694 - 725, 1985.

Kargel, J.S., R.L. Kirk, B. Fegley, A.H. Treiman, Carbonate-Sulfate Volcanism on Venus?, Icarus, 112, p 219 - 252, 1994.

Keldysh, M.V., Venus Exploration with the Venera 9 and Venera 10 Spacecraft, Icarus, 30, p 605 - 625, 1977.

Komatsu, G., V.R. Baker, V.C. Gulick, T.J. Parker, Venusian Channels and Valleys: Distribution and Volcanological Implications, Icarus, 102, p 1 - 25, 1993.

Komatsu. G., and V.R. Baker, Meander Properties of Venusian Channels, Geology, V.22, p 67 - 70, 1994.

McCall, G.J.H., Lunar Rilles and a Possible Terrestrial Analogue, Nature, 225, p 714 - 716, 1970.

Moore, P., G. Hunt, The Atlas of the Solar System, 464pp, Mitchell Beazley, 1983.

Murase, T., and A.R. McBirney, Viscosity of Lunar Lavas, Science, 167, p 1491 - 1492, 1970.

Nikolayeva, O.V., Geochemistry of the Venera 8 Material Demonstrates the Presence of Continental Crust on Venus, Earth Moon Planets, 50, p 329 - 341, 1990.

Oberbeck, V.R., W.L. Quaide, R. Greeley, On the Origin of Lunar Sinuous Rilles, Mod. Geol., V.1, p 75 - 80, 1969.

Özisik, M.N., Boundary Layer Problems of Heat Conduction, pp 505, Int. Txt. Bk. Co., 1968.

Pettengill, G.H., E. Eliason, P.G. Ford, G.B. Loriot, H. Masurky, G.E. McGill, Pioneer Venus Radar Results: Altimetry and Surface Properties, J. Geophys. Res., V.85, p 8261 - 8270, 1980

Pettengill, G.H., P.G. Ford, W.T.K. Johnson, R.K. Raney, L.A. Soderblom, Magellan: Radar Performance and Data Products, Science, 252, p 261 -265, 1991.

Pieters C.M., J.W. Head, W. Patterson, S. Pratt, J. Garvin, V.L. Barsukov, A.T. Basilevsky, I.L. Khodakovsky, A.S. Panfilov, Yu.M. Getkin, Y.M. Narayeva, The Colour of the Surface of Venus, Science, 234, p 1379 - 1383, 1986.

Pinkerton, H., L. Wilson, G. Norton, Thermal Erosion - Obsrvations on Terrestrial Lava Flows and Implications for Planetary Volcanism, LPSC XXI, p 964 - 965, 1990.

Roberts, K., J.E. Guest, J.W. Head, M.G. Lancaster, Mylitta Fluctus, Venus: Rift-Related, Centralised Volcanism and the Emplacement of Large-Volume Flow Units, J. Geophys. Res., V.97, p 15991 - 16016, 1992.

Robson, G.R., Thickness of Etnean Lavas, Nature, 241, p 101 - 102, 1973.

Rogers, G.F.C., and Y.R. Mayhew, Engineering Thermodynamics Work and Heat Transfer, 667pp, Longman, 1980.

Roy, A.E., and D.C. Clarke, Astronomy; Principles and Practice, 357pp, Adam Hilger, 1988.

Saunders, R.S., and G Pettengill, Magellan: Mission Summary, Science, 252, p 247 -249, 1991.

Saunders, R.S., R.E. Arvidson, J.W. Head, G.G. Schaber, E.R. Stofan, S.C. Soloman, An Overview of Venus Geology, Science, 252, p 249 -252, 1991.

Saunders, R.S., A.J. Spear, P.C.Allin, R.S. Austin, A.L. Berman, R.C. Chandlee, J. Clark, A.V. deCharon, E.M. De Jong, D.G. Griffith, J.M. Gunn, S. Hensley, W.T.K. Johnson, C.E. Kirby, K.S. Leung, D.T. Lyons, G.A. Michaels, J. Miller, R.B. Morris, A.D. Morrison, R.G. Piereson, J.F. Scott, S.J. Shaffer, J.P. Slonski, E.R. Stofan, T.W. Thompson, S.D. Wall, Magellan Mission Summary, J. Geophys. Res., V.97, p 13067 - 13090, 1992.

Squyres, S.W., D.M. Janes, G. Baer, D.L. Bindschadler, G. Schubert, V.L. Sharpton, E.R. Stofan, The Morphology and Evolution of Coronae on Venus, J. Geophys. Res., V.97, p 13611 - 13634, 1992.

Stofan, E.R., V.L. Sharpton, G. Schubert, G. Baer, D.L. Bindschadler, D.M. Janes, S.W. Squyres, Global Distribution and Characteristics of Coronae and Related Features on Venus: Implications for Origin and Realtion to Mantle Processes, J. Geophys. Res., V.97, p 13347 - 13378, 1992.

Treiman, A.H., Comments on "Formation of Venusian Canali: Considerations of Lava Types and Their Thermal Behaviors" by T.K.P. Gregg and R. Greeley, J. Geophys., Res., V.99, p 17163 - 17186, 1994.

Turcotte, D.L., and G. Schubert, Geodynamics, 450pp, John Wiley, New York, 1982.

Urey, H.C., Water on the Moon, Nature, 213, p 484 - 485, 1967.

Wilson, L., and J.W. Head, The Formation of Eroded Depressions around the Sources of Lunar Sinuous Rilles: Theory, LPSC XI, p 1260 - 1262, 1980.

Young, C., The Magellan Venus Explorer's Guide, 197pp, JPL Pub. 90-24, 1990.